

# Electro-Weak Transitions in $A=2,3$ Nuclei in Pionless Effective Field Theory

Thesis submitted for the degree of  
"Doctor of Philosophy"

BY  
Hilla De-Leon

Submitted to the Senate of the Hebrew University  
February 2018

This work was carried out under the  
supervision of:

Prof. Doron Gazit  
**Electro-Weak**

# **Transitions in $A=2,3$ Nuclei in Pionless Effective Field Theory**

Thesis submitted for the degree of  
"Doctor of Philosophy"

BY

Hilla De-Leon

Submitted to the Senate of the Hebrew University  
February 2018



# Abstract

In this thesis, which is in the field of few-body systems, I am studying low-energy electro-weak interactions in light nuclear systems whose number of nucleons,  $A$ , is smaller than 4 (*i.e.*,  $d$ ,  ${}^3\text{H}$ ,  ${}^3\text{He}$ ), where the main purpose of this work is to calculate the proton-proton ( $pp$ ) fusion rate.

The main source of energy generated in the Sun is a set of exothermic reactions (named the  $pp$  chain) in which 4 protons are fused into  ${}^4\text{He}$ . The first and the slowest reaction of this set is the  $pp$  fusion, which is a two-nucleon weak reaction that fuses two protons into deuteron ( $d$ ) and determines the Sun's lifetime ( $\tau \sim 10^9$  years). However, due to its long lifetime it cannot be measured, so its rate, which is proportional to the matrix element squared of the weak interaction between initial and final nuclear states, has to be estimated from theory only.

The relevant theory of physics at low energies is Quantum Chromodynamics (QCD) but unfortunately, a direct calculation of the  $pp$  fusion matrix element is not trivial due to the non-perturbative character of QCD at low energies. In recent decades, many nuclear physicists faced the challenge of calculating the  $pp$  fusion rate, but these calculations, and in particular those conducted in the last years, are inconsistent with each other. This inconsistency emphasizes the necessity of deriving a new, simple calculation that should benchmark versus other past predictions and would provide a verified and validated prediction.

In the past two decades, a novel theoretical method, named Effective Field Theory (EFT), revolutionized nuclear physics. EFT is a simple, renormalizable and model independent theoretical method for describing low-energy reactions. The condition for describing a physical process using EFT is that its transfer momentum,  $Q$ , is small compared to a physical cutoff,  $\Lambda_{cut}$  (*i.e.*,  $Q/\Lambda_{cut} \ll 1$ ). In this thesis, I focus on electro-weak interactions that are characterized by momentum transfer,  $Q$ , which is much smaller than  $\Lambda_{cut} = m_\pi$ , the pion mass. In such cases, the corresponding EFT is the pionless EFT ( $\pi$ EFT), where

---

the pions are integrated out and only nucleons are left as effective degrees of freedom.

$\not{A}$ EFT weak Lagrangian includes a two-body low-energy constant (LEC), named  $L_{1,A}$ , which has to be calibrated from different well-measured, low-energy weak reaction that contains at least two nucleons. An appropriate well-measured, low-energy reaction for that calibration is the  ${}^3\text{H}$   $\beta$ -decay that involves  $L_{1,A}$ , so using  $\not{A}$ EFT for its calculation, enables the extraction of  $L_{1,A}$ .

Nevertheless, in contrast to the nuclear electro-weak interactions containing **two** nucleons that have been calculated over the last 20 years using  $\not{A}$ EFT, electro-weak interactions which involve **three** nucleons (such as  ${}^3\text{H}$   $\beta$ -decay) were not introduced until recently due to the complexity in describing these systems using  $\not{A}$ EFT formalism. Consequently, the consistency of  $\not{A}$ EFT for the transition between  $A = 3$  and  $A = 2$  nuclear systems, which is essential for the  $L_{1,A}$  extraction, could have never been examined. Since the  ${}^3\text{H}$   $\beta$ -decay is the only relevant low-energy  $1 < A < 4$  well-measured weak reaction, weak reactions cannot be used for examining the  $\not{A}$ EFT consistency, and therefore, another set of well-measured low-energy  $A < 4$  interactions with similar characteristics to the weak reactions, is needed for validation and verification of  $\not{A}$ EFT. The strong analogy between the **electromagnetic** to weak observables indicates that the four  $A < 4$  well-measured electromagnetic observables are the ones that serve as the required candidates.

Hence, in this thesis I develop a general perturbative diagrammatic approach for calculating the transition between  $A = 3$  bound-states of three-nucleon. This framework has been examined and found to be accurate not only for calculating electro-weak interactions, but also for other observables such as the binding energy difference between  ${}^3\text{H}$  and  ${}^3\text{He}$  due to the Coulomb interaction. I show that the electromagnetic calculations up to next-to-leading order (NLO) in  $Q/\Lambda_{cut}$  reproduce the experimental data very well, where the NLO contributions amount to a few percent only. The order-by-order analysis of those observables along with the high consistency between the  $A = 2$  and  $A = 3$  calculations lead to high theoretical uncertainty of less than 1%. This theoretical uncertainty estimate, accompanied by the strong analogy between the electromagnetic and weak observables, enables the extraction of  $L_{1,A}$  from the calculated  ${}^3\text{H}$   $\beta$ -decay and lead to the high accuracy calculation of the  $pp$  fusion rate.

This calculation, which is indeed simple and benchmarks versus past predictions, shows that the present prediction for the  $pp$  fusion cross-section is up to 5% bigger than previous estimations and contains 1.2% total uncertainty with 70% degree of belief. This might affect current models of solar evolution.

# Contents

<b>Abstract</b>	<b>i</b>
<b>1 Introduction</b>	<b>1</b>
1.1 Effective field theory: the modern approach to predictions in nuclear physics	3
1.2 $\chi$ EFT predictions of the $pp$ fusion matrix element . . . . .	3
1.3 The pionless EFT challenges for the $pp$ fusion . . . . .	6
1.4 Goals of this thesis . . . . .	8
1.5 Verification and validation of pionless EFT using electromagnetic observables	9
1.6 Structure of the thesis . . . . .	10
<b>2 The general formalism of pionless EFT</b>	<b>13</b>
2.1 A small parameter expansion of pionless EFT . . . . .	13
2.2 Pionless EFT at next-to-leading order . . . . .	14
2.2.1 $N - N$ scattering amplitude . . . . .	15
2.2.2 Coulomb corrections to N-N scattering amplitude . . . . .	17
2.3 Pionless EFT Lagrangian coupled to electro-weak fields . . . . .	22
2.3.1 Weak interaction in pionless EFT . . . . .	22
2.3.2 Electromagnetic interaction in pionless EFT . . . . .	23
2.4 Introducing dibaryon fields . . . . .	23
2.4.1 Hubbard-Stratonovich transformations for pionless EFT . . . . .	24
2.5 The dibaryon propagator . . . . .	26
2.5.1 The Coulomb propagator . . . . .	27
2.6 The deuteron normalization and $Z$ -parameterization . . . . .	28
2.7 Summary of Feynman Rules . . . . .	30

<b>3</b>	<b>Three nucleon system at leading order</b>	<b>35</b>
3.1	n-d scattering and ${}^3\text{H}$ bound-state . . . . .	35
3.1.1	Quartet channel . . . . .	35
3.1.2	Doublet channel . . . . .	37
3.1.3	The three-body force . . . . .	40
3.1.4	The n-d scattering with $E > 0$ . . . . .	43
3.2	$p - d$ scattering and ${}^3\text{He}$ bound-state . . . . .	46
3.2.1	The doublet channel . . . . .	48
3.2.2	${}^3\text{He}$ bound-state amplitude and three-body force . . . . .	50
<b>4</b>	<b>Normalization of the three-nucleon amplitude</b>	<b>53</b>
4.1	The Bethe-Salpeter wave function normalization . . . . .	53
4.2	The non-relativistic Bethe-Salpeter wave-function normalization . . . . .	55
4.3	The normalization of ${}^3\text{He}, {}^3\text{He}$ wave-functions . . . . .	56
4.4	The diagrammatic form of the normalization . . . . .	57
<b>5</b>	<b><math>A = 3</math> matrix element in pionless EFT</b>	<b>61</b>
5.1	The general form of an $A = 3$ matrix element . . . . .	61
5.2	Matrix elements of one-body operators . . . . .	63
5.2.1	Two-body matrix element . . . . .	65
5.3	Deuteron normalization and the matrix element in pionless EFT . . . . .	66
5.4	Example: ${}^3\text{He}$ - ${}^3\text{H}$ binding energy difference with a perturbative Coulomb . . . . .	66
<b>6</b>	<b>Perturbative correction to the three-body nuclear wave functions</b>	<b>71</b>
6.1	The NLO correction to the full scattering amplitude . . . . .	71
6.1.1	The NLO corrections to the three-nucleon bound-state pole position . . . . .	72
6.1.2	NLO three-body force . . . . .	74
6.1.3	${}^3\text{He}$ - correction to the three-body force and binding energy . . . . .	77
6.2	NLO corrections to the three-body wave function . . . . .	80
6.3	The NLO normalization . . . . .	82
<b>7</b>	<b><math>A = 2, 3</math> Electromagnetic reactions</b>	<b>85</b>
7.1	$M_1$ observables in the $A = 2, 3$ systems . . . . .	86
7.2	Magnetic photon currents in pionless EFT . . . . .	86
7.2.1	Diagrammatic representation of the electromagnetic matrix elements . . . . .	87
7.3	Results . . . . .	92

## CONTENTS

---

7.4	Magnetic interactions in Lattice QCD . . . . .	93
7.4.1	Calculation of $\sigma_{np}(Y'_{np})$ using $l_1^\infty$ from lattice QCD data . . . . .	95
7.4.2	Magnetic moments in Lattice QCD . . . . .	96
7.4.3	LQCD empirical uncertainties . . . . .	97
<b>8</b>	<b>Weak interactions and <math>^3\text{H}</math> <math>\beta</math>-decay in pionless EFT</b>	<b>99</b>
8.1	The weak interactions in pionless EFT . . . . .	99
8.2	$^3\text{H}$ $\beta$ -decay matrix elements . . . . .	100
8.2.1	$^3\text{H}$ $\beta$ -decay observables . . . . .	100
8.2.2	Fermi and Gamow-Teller matrix element: . . . . .	101
8.3	Fermi operator . . . . .	103
8.4	Gamow-Teller operator . . . . .	105
8.4.1	Gamow-Teller Transition for $\alpha = 0$ . . . . .	105
8.4.2	Numerical results for GT strength of triton decay . . . . .	106
8.5	Empirical extraction of Gamow-Teller strength and fixing $l_{1,A}$ . . . . .	107
<b>9</b>	<b>The proton-proton fusion matrix element</b>	<b>109</b>
9.1	$pp$ fusion matrix element . . . . .	110
9.2	Numerical results . . . . .	112
<b>10</b>	<b>Analysis of the results and a prediction for <math>pp</math> fusion</b>	<b>113</b>
10.1	An order-by-order analysis of the results and theoretical uncertainty . . . . .	113
10.1.1	$M_1$ observables as a case study . . . . .	115
10.1.2	Pionless EFT expansion and setting $l_2^\infty$ to zero . . . . .	115
10.1.3	Estimating pionless EFT theoretical uncertainty . . . . .	116
10.2	Analogy between $M_1$ observables and weak reactions . . . . .	118
10.3	Theoretical uncertainty of $pp$ fusion due to pionless EFT truncation . . . . .	119
10.4	Final results and comparison to previous calculations of $l_{1,A}$ and the $pp$ fusion	121
10.4.1	Previous extractions of $L_{1,A}$ . . . . .	122
10.4.2	$pp$ fusion past predictions . . . . .	124
<b>11</b>	<b>Summary and outlook</b>	<b>127</b>
11.1	Outlook . . . . .	128
<b>A</b>	<b>The Faddeev equations three-body scattering</b>	<b>129</b>
I	The Faddeev equations for $n - d$ scattering . . . . .	129



## CONTENTS

---

a	The Quartet channel for $n - d$ scattering . . . . .	129
b	The Doublet channel for $n - d$ scattering . . . . .	130
II	The Faddeev equations for $p - d$ scattering . . . . .	131
a	The Quartet channel for $p - d$ scattering . . . . .	131
b	The Doublet channel for the $p - d$ scattering . . . . .	135
<b>B</b>	<b>The analytic form of the NLO correction to the three-body force</b>	<b>137</b>
<b>C</b>	<b>The Hubbard-Stratonovich transformation with two-body electro-weak interaction</b>	<b>139</b>
<b>D</b>	<b>Appendix D - A Bayesian approach to estimate the convergence rate</b>	<b>143</b>
D.I	The Bayesian probability distribution of the expansion parameter .	143
D.II	The Bayesian probability distribution of the truncation error of an expansion, given a prior for the expansion parameter . . . . .	144

# List of Figures

1.1	Flow chart that demonstrates the main steps leading to the present $\not\equiv$ EFT calculation of the $pp$ fusion. . . . .	4
2.1	The $N - N$ scattering amplitude is a sum of the chains of $N - N$ bubbles. . . . .	15
2.2	The $N - N$ scattering amplitudes up to NLO. The blue squares denote the NLO insertion of the effective range. . . . .	17
2.3	The $pp$ scattering amplitude is a sum of chains of Coulomb-dressed bubbles. . . . .	17
2.4	The $pp$ dibaryon propagator up to NLO. The blue squares denote the NLO insertion of the effective range. . . . .	20
2.5	The dressed dibaryon propagator. The bare dibaryon propagator is dressed by nucleon bubbles to all orders. . . . .	26
3.1	Integral equation for the strong scattering matrix $T$ (red bubble), where $\mathcal{D}$ is the dibaryon propagator and $\mathcal{K}$ is the one-nucleon exchange propagator. . . . .	36
3.2	n-d scattering equations. The double lines are the propagators of the dibaryon fields $D_t$ (solid) and $D_s$ (dashed). The red bubbles (T) represent the triplet channel T=0, S=1, while the green bubbles (S) represent the singlet channel T=1, S=0. . . . .	37
3.3	The binding energy which solves eq. (3.20) as a function of cutoff ( $\Lambda$ ) (dots). The solid line is the experimental value of triton binding energy - 8.48 MeV. . . . .	41
3.4	The triton scattering equations with a three-body force. The double lines are the propagators of the dibaryon fields $D_t$ (solid) and $D_s$ (dashed). The red bubbles (T) represent the triplet channel T=0, S=1, while the green bubbles (S) represent the singlet channel T=1, S=0. The blue squares are the three-body force . . . . .	41
3.5	Values of the three-body force $H(\Lambda)$ as a function of the cutoff $\Lambda$ for ${}^3\text{H}$ . The dots show our numerical results for $H(\Lambda)$ and the solid line is the analytical result. . . . .	42

## LIST OF FIGURES

---

- 3.6 The full scattering equations for triton with a three-body force. The double lines are the propagators of the dibaryon fields  $D_t$  (solid) and  $D_s$  (dashed). The red bubbles (T) represent the triplet channel  $T=0, S=1$ , the green bubbles ( $S, S^\dagger$ ) represent the singlet channel  $T=1, S=0$  while the cyan bubbles ( $S'$ ) represent the singlet channel  $T=1, S=0$ . The blue squares are the three-body force. . . . . 44
- 3.7 The symmetry parameter  $\alpha$  as a function of  $\Lambda$  for  $E = 0$  MeV (a) and  $E = 8.48$  MeV (b). In both panels the solid line is  $\alpha^{\overleftarrow{T}}$ , the long dashed-dotted line is  $\alpha^{\overleftarrow{S}}$  and the short dashed-dotted line is  $\alpha^{\overleftarrow{S}^\dagger}$ . In addition we plotted the difference between  $\overleftarrow{S}$  and  $(\overleftarrow{S}^\dagger)^\dagger$  which is assumed to be zero (dashed line). . . . . 46
- 3.8 The possible one-photon exchange diagrams. . . . . 48
- 3.9 Diagrammatic form of the homogeneous part of  $p-d$  scattering that includes a three-body force. The double lines denote the dibaryon propagators  $D_t$  (solid),  $D_{np}$  (dashed) and  $D_{pp}$  (dotted). The red bubbles (T) represent the triplet channel ( $T=0, S=1$ ), the green bubbles (S) represent the singlet channel ( $T=1, S=0$ ) with  $np$  dibaryon while the blue bubbles (P) represent the singlet channel  $T=1, S=0$  with a  $pp$  dibaryon. The blue squares represent the three-body force. . . . . 51
- 3.10 Predictions for  $E_{3H}, E_{3He}$  binding energy as a function of the cutoff  $\Lambda$ . The solid line is the binding energy calculated using the non perturbative solution (subsection 3.2.2), the dashed-dotted line is the binding energy predicted using perturbation theory (eq. (5.21)). The short-dashed line is the experimental value,  $E_{3He} = 7.72$  MeV, and the long-dashed line is the experimental value,  $E_{3H} = 8.48$  MeV. . . . . 52
- 4.1 Diagrammatic representation of the two-body BS equation for the scattering matrix  $\mathcal{M}$ . 54
- 4.2 Diagrammatic representation of two possible connections between two identical three-nucleon wave-functions,  $\psi$ . The double lines are the propagators of the two dibaryon fields,  $\mathcal{D}$ . The solid lines represent one-nucleon propagators, while the dashed lines denote the delta functions. Diagram (a) is proportional to  $\frac{\partial}{\partial E} \hat{I}$ , while diagram (b) is proportional to  $\frac{\partial}{\partial E} \hat{\mathcal{K}}$ . . . . . 59
- 5.1 Diagrammatic representation of all the possible variations of  $\mathcal{O}^q$  between two three-nucleon wave-functions that involve a one-nucleon exchange. The RHS of each diagram is the final state,  $\psi^j$ , while the LHS is the initial state,  $\psi^i$ . The double lines are the propagators of the two dibaryon fields,  $\mathcal{D}$ . The probe represents the momentum and energy transfers due to the interaction. . . . . 69

## LIST OF FIGURES

---

- 6.1 The  $t$ -matrix describing a bound-state up to NLO (red bubbles). The LO  $t$ -matrix is the result of the LO homogeneous Faddeev equation - eq. (3.12). The NLO correction to the  $t$ -matrix includes the effective range  $\rho$  (black dot). The double lines are the propagators of the two dibaryon fields and the blue square is the three-body force. . . . . 73
- 6.2 The NLO correction for  $^3\text{H}$  binding energy. The double lines are propagators of the two intermediate auxiliary fields,  $D_t$  (solid) and  $D_t^{np}$  (dashed). The red bubbles ( $\Gamma_t$ ) represent the triplet channel  $T=0, S=1$ , the green bubbles represent ( $\Gamma_s$ ) the singlet channel  $T=1, S=0$ . The black circles denote the NLO correction to the dibaryon propagator, while the blue squares denote the NLO correction to the three-body force ( $H^{(1)}(\Lambda)$ ). . . 76
- 6.3 The three-body force,  $H(\Lambda)$ , at NLO as a function of the cutoff  $\Lambda$  in MeV for  $^3\text{H}$ . The solid curve is the analytical expression for  $H(\Lambda)$  taken from [44], while the dots are the numerical results based on eq. (6.20). . . . . 77
- 6.4 The NLO correction for  $^3\text{He}$  binding energy. The double lines are propagators of the two intermediate auxiliary fields,  $D_t$  (solid) and  $D_t^{np}$  (dashed) and  $D^{pp}$  (dotted). The red bubbles ( $\Gamma_t$ ) represent the triplet channel ( $T=0, S=1$ ), the green bubbles represent ( $\Gamma_s$ ) the singlet channel ( $T=1, S=0$ ) with an  $np$  dibaryon, while the blue bubbles ( $\Gamma_{pp}$ ) represent the singlet channel ( $T=1, S=0$ ) with  $pp$  dibaryon. The black circles denote the NLO correction to the dibaryon propagator, while the blue squares denote the NLO correction to the three-body force ( $H^{(1)}(\Lambda) + H^{(\alpha)}(\Lambda)$ ). . . . . 79
- 7.1 Diagrammatic representation of  $\hat{\mu}$  between two-body states, up to NLO.  $\hat{\mu}$  insertion is represented by the photon vertex. The double lines are the NLO propagator of the two dibaryon fields.  $D_t$  (solid) and  $D_s$  (dashed). The red lines represent the neutron propagator while the blue lines represent the proton propagator. A spin-singlet dibaryon-nucleon-nucleon vertex is proportional to  $y_s$  (blue diamond), while a spin-triplet dibaryon-nucleon-nucleon vertex is proportional to  $y_t$  (red diamond). . . . . 87
- 7.2 Different topologies of the diagrams contributing to the triton magnetic moment. The double lines are the propagators of the two dibaryon fields.  $D_t$  (solid) and  $D_s$  (dashed for  $nn$  and  $np$ ), where the red line is the neutron and the blue line is the proton. Most of the diagrams couple both the triplet and the singlet channels. The diagrams with one-body interactions are coupled to  $(\kappa_0 - \kappa_1) = \mu_n$  (upper) and  $(\kappa_0 + \kappa_1) = \mu_p$  (lower). The two-body interactions are coupled to both  $l'_1$  (upper) and  $l'_2$  (lower). . . . . 89

## LIST OF FIGURES

---

- 7.3 Three of the diagrams contributing to the triton magnetic moment. The one-body diagrams which are coupled to  $\mu_n \cdot \sigma$  (a) and  $\mu_p \cdot \sigma$  (b), diagram (c) is coupled to the two-body LEC  $l'_2$ . The double lines are the propagators of the two dibaryon field  $D_t$  (solid). The red lines represent the neutron propagator while the blue lines represent the proton propagator. . . . . 92
- 7.4 Numerical results for LECs  $l'_1$  (up) and  $l'_2$  (button), calibrated from  $\langle \hat{\mu}_{^3\text{H}} \rangle$  and  $\langle \hat{\mu}_{^3\text{He}} \rangle$  as a function of the cutoff  $\Lambda$ . The solid lines are the numerical results obtained from  $A = 3$  observables simultaneously, while the dashed lines are the numerical results obtained from  $A = 3$  observables separately. . . . . 94
- 8.1 Different topologies of the diagrams contributing to the triton  $\beta$ -decay amplitude. The LHS of each diagram is  $^3\text{H}$  while the RHS is  $^3\text{He}$ . The double line are the propagators of the two dibaryon fields  $D_t$  (solid),  $D_s$  (dashed for  $nn$  and  $np$ , dotted for  $pp$ ), where the red lines are the neutron and the blue lines are the proton. Most of the diagrams couple both the triplet and the singlet channels. The diagrams with one-body interactions are coupled to  $g_A$  while the two-body interaction are coupled to the effective ranges  $\rho_t$  and  $\rho_s$  and to  $l_{1,A}$ . . . . . 103
- 8.2 Numerical results for the Fermi transition. The solid line is the LO result for  $\langle F \rangle = 1$  with  $\alpha = 0$ . The dashed line is the numerical result for  $\alpha = 0$  with isospin breaking effects in the scattering lengths  $a_{np} \neq a_{pp}$  (LO). The dashed-dotted line shows the numerical result at NLO with  $\alpha \neq 0$ . The dotted line gives the value of  $\langle F \rangle = 0.9993$  from Ref. [31]. 104
- 8.3 Numerical results of the Gamow-Teller transition. The gray area is the full  $\langle GT \rangle$  matrix element with  $g_A = 1.273 \pm 0.003 \pm 0.005$  [95,96]. The short dashed lines are the numerical results of  $\langle GT \rangle^{\text{LO}}$ , the dashed-dotted lines are  $\langle GT \rangle$  with  $l_{1,A} = 0$ .  $Z$  refers to numerical results with the  $Z$ -parameterization:  $\rho'_t = \frac{Z_a - 1}{\gamma_t}$ . . . . . 106
- 8.4 Numerical results of the RG invariant,  $l_{1,A}$ , with  $g_A = 1.273(03)(05)$  [95,96]. The solid lines are the upper and lower limits of the ERE calculations while the dashed lines are the upper and lower limits of the  $Z$  calculations. . . . . 108
- 9.1 Diagrams for the  $pp$  fusion process, eq. (9.2), up to NLO. The double lines are the NLO propagators of the two dibaryon fields:  $D_t$  (solid) and  $D_{pp}$  (dotted). Two-nucleon propagator with a blue bubble denotes the Green's function including the Coulomb potential. A spin-singlet dibaryon-nucleon-nucleon (s-NN) vertex is proportional to  $y_s$  (blue diamond) while a spin-triplet dibaryon-nucleon-nucleon (t-NN) vertex is proportional to  $y_t$  (red diamond). The one-body diagrams are coupled to the one-body LEC,  $g_A$  where the two-body diagrams are coupled to the two-body LEC,  $L'_{1,A}$ . . . . . 111

## LIST OF FIGURES

---

10.1	Cumulative Density Functions (CDFs) of $\delta$ , the expansion parameter. The blue curve represents a calculation which takes into account the constraints of the NLO contributions of $\langle\hat{\mu}^3_{\text{H}}\rangle$ , $\langle\hat{\mu}^3_{\text{He}}\rangle$ , $Y_{np}$ , the N <sup>2</sup> LO contribution of $\langle\hat{\mu}_d\rangle$ , and the variation of $l_1'^\infty$ . The orange curve takes into account only the first four former constraints. The red lines limit the 10 – 90% probability range. . . . .	118
10.2	Cumulative Density Functions (CDFs) for the different observables, as calculated using eq. (D-2). Horizontal lines are the 70% and 90% degree of beliefs. We show CDFs relevant to expansion parameter priors with $n = 4$ (solid lines) and $n = 7$ (dashed lines) constraints, as explained in Fig. 10.1. . . . .	119
10.3	The strength of $A = 2, 3$ $M_1$ observables with 70% degree of belief. The bands correspond to the theoretical Z-parameterization uncertainty as shown in from Fig. 10.2. The stars are the experimental values. . . . .	120

## LIST OF FIGURES

---

# List of Tables

1.1	Estimations of $\Lambda_{pp}^2(0)$ from former calculations. The value in the first column is the ERE calculated by Bahcall and May in 1969 [1]. The second, third, and fourth columns are estimated from the $\not\{EFT$ calculations: up to NLO by Kong and Ravndal [29], up to N <sup>4</sup> LO by Butler and Chen [30] and the full calculation by Ando <i>et al.</i> [32], respectively. The fifth column is the NPLQCD calculation [34]. . . . .	6
1.2	Electro-weak LECs, operators and low-energy observables. . . . .	9
2.1	Experimental values for parameters used in the numerical calculation . . . . .	28
2.2	The Feynman rules for the NLO electro-weak interactions. a: the single nucleon propagator. b-d: the dibaryon propagator. e-f: : the dibaryon- nucleon interaction. g: the three-body force. h-j: the Coulomb interaction. k-m: the ERE correction to the dibaryon propagator. n-q: the weak interaction. r-x: the magnetic interaction. For all Feynman rules, a capital letter indicates the isospin index, while a small letter indicates the spin index. . . . .	33
7.1	Numerical results for our prediction for $l_1'^\infty, l_2'^\infty$ and $A = 2, 3$ $M_1$ observables. The nominal value is calculated using $Z$ -parameterization, while the number in brackets is calculated using the ERE-parameterization. Mean denotes the mean value of the $M_1$ observable based on its three predictions while $\Delta$ denotes the standard divination of these predictions. . . . .	93
7.2	Lattice nuclear parameters used in the numerical calculations. The values for the singlet and triplet effective ranges were taken from private communication with CalLAT. . . .	96
7.3	Numerical results for $\langle \hat{\mu}_{3H} \rangle$ and $\langle \hat{\mu}_{3He} \rangle$ with the non-physical pion mass. . . . .	97
7.4	The contribution of the calculated uncertainty in the physical observables to the uncertainty propagated to the electromagnetic observables. . . . .	98



## LIST OF TABLES

---

8.1	Numerical results of $\langle F \rangle$ . Note that the second row is without explicit Coulomb force ( $\alpha = 0$ ), but with isospin breaking in the scattering lengths, <i>i.e.</i> , with the physical values for the scattering lengths $a_{np} \neq a_{pp}$ . . . . .	105
8.2	Numerical results for $\langle GT \rangle$ . Note that the rows with the comment " $\alpha = 0, a_{np} \neq a_{pp}$ " are without explicit Coulomb force ( $\alpha = 0$ ), but with isospin breaking in the scattering lengths, <i>i.e.</i> , with physical values for the scattering lengths $a_{np} \neq a_{pp}$ . . . . .	107
10.1	The order-by-order expansion of the electro-weak matrix elements. The order-by-order expansion of the electromagnetic matrix elements is based on their mean values given in Tab. 7.1. The nominal value is calculated using $Z$ -parameterization, while the number in brackets is calculated using the ERE-parameterization. Mean denotes the mean value of the $M_1$ observable based on its three predictions while $\Delta$ denotes the standard deviation of these predictions. . . . .	114
10.2	Numerical results for our prediction for $l_1^\infty$ and $A = 2, 3$ $M_1$ observables with $l_2^\infty = 0$ . The $A = 3$ magnetic moments are given in units of nuclear magnetons ([nNM]). . . .	116

# Introduction

The evolution of the Sun, as well as other main sequence stars, remains one of the main theoretical questions in astrophysics. Our comprehensive understanding of this evolution has been used as a tool to reach many discoveries in other branches of physics, heralded by the discovery of the mass of the neutrino. The energy generated in the Sun comes from an exothermic set of reactions, the proton-proton ( $pp$ ) chain, by fusing four Hydrogen ions into  ${}^4\text{He}$ . The chain is initiated by the  $pp$  fusion reaction:  $p + p \rightarrow d + e^+ + \nu_e$ , which rules 99.76% of the proton reactions. The  $pp$  fusion is governed by the weak interaction, which makes it the slowest reaction in the chain ( $\tau \sim 10^9$  years), and therefore it determines the Sun's lifetime. However, its slow rate makes the measurement of its cross-section impossible, so it must be calculated theoretically.

The  $pp$  fusion cross-section,  $\sigma_{pp} = \frac{S^{11}(E)}{E} \exp[-2\pi\eta(E)]$ , consists of both the long-range Coulomb factor ( $\eta(E)$ ), and the short-range astrophysical  $S$ -factor ( $S^{11}(E)$ ), where  $E$  is the kinetic energy of the center of mass of the interacting protons, dictated by the temperature. In solar conditions, the magnitude of  $E$  is only a few keV and therefore  $S^{11}(E)$  can be expanded in a power series in  $E$  such that:  
 $S^{11}(E) = S^{11}(0) + \frac{dS^{11}(E)}{dE}|_{E=0}E + \dots$  At these solar energies this series expansion is dominated by the  $E = 0$  threshold value, *i.e.*,  $S^{11}(0)$  which is proportional to  $\Lambda_{pp}^2(0)$ , the square of the  $pp$  fusion matrix element.

The relevant theory of physics at these energies is Quantum ChromoDynamics (QCD). The challenge in theoretical calculation of the  $pp$  fusion matrix element stems from the non-perturbative character of QCD at the nuclear regime which makes a direct calculation non-trivial. This has led to many theoretical efforts to calculate the reaction rate.

In 1969, Bahcall and May have found that  $\Lambda_{pp}^2(0) = 7.08$  [1], using standard nuclear

physics effective range expansion (ERE) [2]. A review of all recent calculations of  $S^{11}(0)$  appeared in 2011, by Adelberger *et al.* [3], and recommended to use the value

$$S^{11}(0) = (4.011 \pm 0.04) \cdot 10^{-23} \text{ MeV} \cdot \text{fm}^2 \cdot \left( \frac{(ft)_{0^+ \rightarrow 0^+}}{3071.4 \text{ sec}} \right)^{-1} \left( \frac{g_A}{1.2695} \right)^2 \left( \frac{f_{pp}^R}{0.144} \right) \left( \frac{\Lambda_{pp}^2(0)}{7.035} \right), \quad (1.1)$$

representing an agreement between three different theoretical approaches that existed at that time, where  $(ft)_{0^+ \rightarrow 0^+} = (3071.4 \pm 0.8)s$ , is the value for superallowed  $0^+ \rightarrow 0^+$  transitions that has been determined from a comprehensive analysis of experimental rates corrected for radiative and Coulomb effects [4]. This value determines the weak mixing matrix element,  $|V_{ud}| = 0.97418(27)$  [5]. Ref. [6] used the then recommended PDG value for the weak axial constant:  $g_A = 1.2695 \pm 0.0029$  [5]. The phase-space factor  $f_{pp}^R$  takes into account 1.62% increase due to radiative corrections to the cross section [7].

However, in 2013, Marcucci *et al.* calculations for proton energies up to 100 keV [8], have yielded  $S^{11}(0) = (4.03 \pm 0.006) \cdot 10^{-23} \text{ MeV} \cdot \text{fm}^2$ , using the consistency of three-nucleon forces and two-body axial currents [9], while Acharya *et al.* recently yielded  $S^{11}(0) = (4.081_{-0.032}^{+0.024}) \cdot 10^{-23} \text{ MeV} \cdot \text{fm}^2$  [10].

These two predictions [8, 10] are inconsistent with each other. This inconsistency indicates that the uncertainties might be underestimated, and emphasizes the need for a new calculation which has a comprehensive error estimation. The main purpose of this thesis is to construct such a new calculation that will identify the theoretical and empirical uncertainties, preferably would be simple, should benchmark versus other past predictions, and must reproduce different experimentally measured reactions. This might enable us a verification of the theoretical method that is needed for prediction of the elusive  $pp$  fusion cross-section.

We focus on a novel theoretical method, which revolutionized nuclear physics in the past two decades, named Effective Field Theory (EFT). We are using the pionless version of this approach ( $\pi$ EFT) to calculate the  $pp$  fusion matrix element. In contrast to past works attempted to calculate the  $pp$  fusion within  $\pi$ EFT, e.g. J.W. Chen *et al.* [11], we use  $^3\text{H}$   $\beta$ -decay to calibrate the model. This is done by developing a perturbative diagrammatic approach to calculate the transition between  $A = 3$  bound-states (where  $A$  is the number of nucleons). A significant part of this work is dedicated to estimate the theoretical and empirical uncertainties relevant for calculating low-energy observables such as the  $pp$  fusion rate. We find a successful validation of this approach by studying the magnetic structure of  $A = 2, 3$  nuclei. The main steps leading to the  $\pi$ EFT calculation

of the  $pp$  fusion matrix element in this thesis are demonstrated in Fig. 1.1.

In the next sections we briefly review the basic principles of effective field theory, with emphasis on its chiral ( $\chi$ EFT) and pionless ( $\not\pi$ EFT) versions and the challenges of using  $\not\pi$ EFT for calculating the  $pp$  fusion matrix element. We examine the analogy between electromagnetic and weak observables in  $\not\pi$ EFT, which along with the comparison between the  $\not\pi$ EFT predictions of the electromagnetic interactions to their known experimental counterparts, are used for verification and validation of  $\not\pi$ EFT in calculating both electromagnetic and weak observables of  $A = 2, 3$  nuclei.

## 1.1 Effective field theory: the modern approach to predictions in nuclear physics

In recent years, an effort has begun to calculate low-energy observables such as the  $pp$  fusion matrix element, using EFT approaches. In EFT, the ratio of two separated scales is used as an expansion parameter in a systematic low-energy expansion in the calculation of observables. The first, which represents the low-energy scale is usually the typical momentum scale,  $Q$ , while the second and higher energy scale,  $\Lambda_{\text{cut}}$ , is frequently related to the lightest exchanged particle. The EFT has to preserve all symmetries of the fundamental theory, and the resulting Lagrangian includes only the relevant degrees of freedom while heavier excitations are integrated out of the theory. Thus, one can obtain an expression of non-renormalizable interactions which can be organized as a power series in  $Q/\Lambda_{\text{cut}}$  [12–16]. This method becomes useful when there is a significant scale separation between  $Q$  and  $\Lambda_{\text{cut}}$ , so only a small number of the effective operators corresponding to the leading powers in  $\frac{Q}{\Lambda_{\text{cut}}}$  needs to be retained to reproduce long wavelength observables with the desired accuracy.

Regarding the  $pp$  fusion matrix element calculations, one finds two main EFT approaches in the literature, which are relevant for this calculation: the chiral EFT ( $\chi$ EFT) and the pionless EFT ( $\not\pi$ EFT). In the last 15 years, most of the  $pp$  predictions used  $\chi$ EFT [8, 10].

## 1.2 $\chi$ EFT predictions of the $pp$ fusion matrix element

Chiral effective field theory ( $\chi$ EFT) identifies the pion as a Goldstone boson of the spontaneously broken chiral symmetry of QCD, stemming from the small masses of the up and

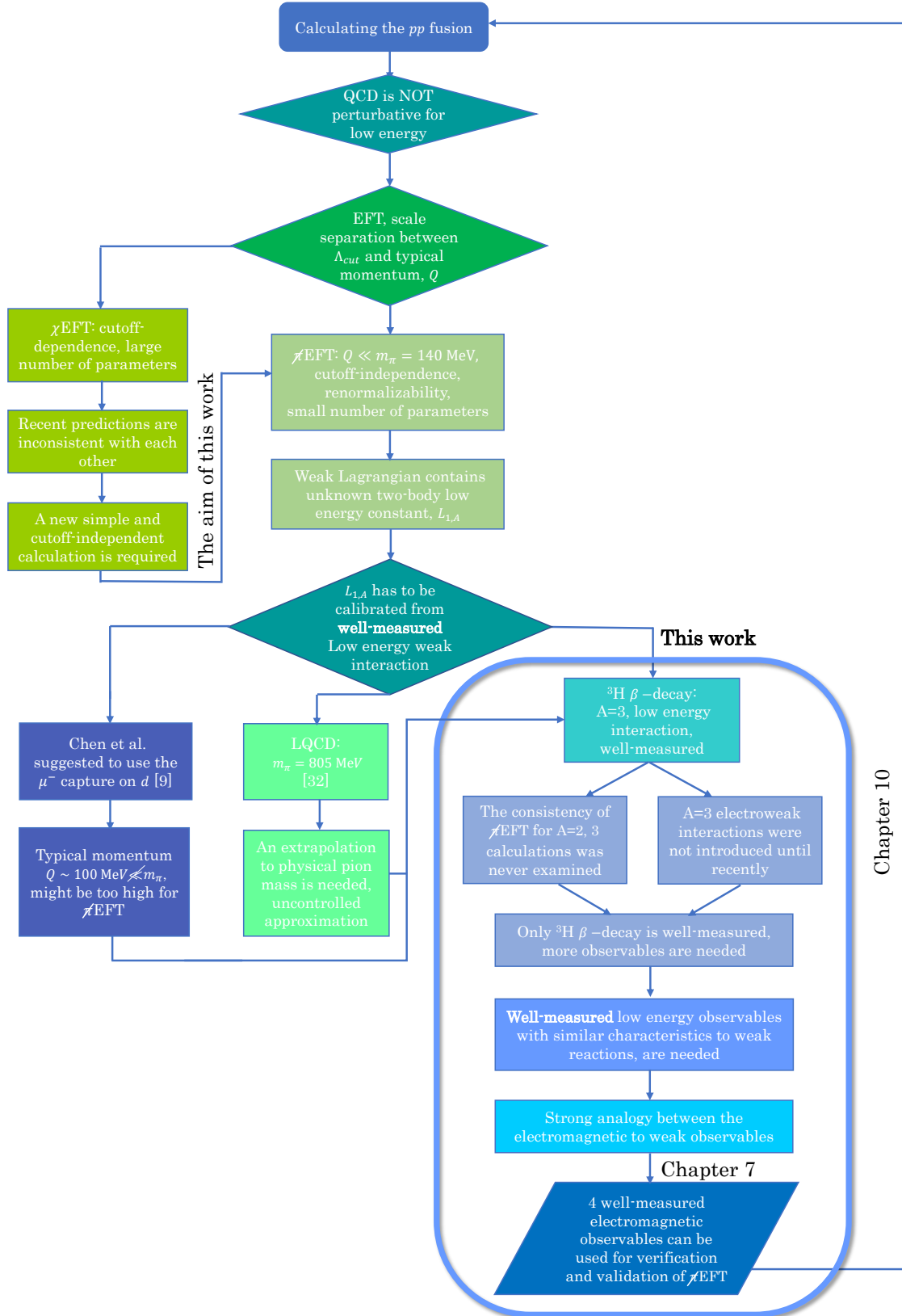


Figure 1.1: Flow chart that demonstrates the main steps leading to the present  $N^2$ EFT calculation of the  $pp$  fusion.

down quarks. The finite mass of the pion originates from the explicit chiral symmetry breaking, *i.e.*, the non-zero up and down quark masses. This framework has been used to construct a nuclear interaction that describes nuclear spectra and scattering observables to very high accuracy [17]. It has also been used to construct the nuclear electro-weak current operator and for subsequent calculations [18, 19]. These calculations have highlighted the benefit of an approach in which current operators and the interaction between nucleons are treated consistently.

As mentioned before,  $\chi$ EFT has been used by Marcucci *et al.* [8] to calculate the S-factor up to next-to-next-leading-order (NNLO),  $S^{11}(0) = (4.03 \pm 0.006) \cdot 10^{-23} \text{ MeV} \cdot \text{fm}^2$ . The uncertainty of their calculation, which is almost an order of magnitude smaller than a previous recommendation [3], is based only on the difference between two variants of  $\chi$ EFT potentials. Recently, Acharya *et al.* [10] have recalculated the S-factor of  $pp$  fusion reaction using  $\chi$ EFT up to NNLO:  $S^{11}(0) = (4.081_{-0.032}^{+0.024}) \cdot 10^{-23} \text{ MeV} \cdot \text{fm}^2$ . Similarly to Marcucci *et al.* [8], Acharya *et al.* [10] also used the consistency of three-nucleon forces and two-body axial currents, where the relevant low-energy constants (LECs) were calibrated using the triton  $\beta$ -decay and binding energies. Their uncertainty estimate is based mainly on the statistical uncertainties in the low-energy coupling constants of  $\chi$ EFT, on the systematic uncertainty due to limited  $\chi$ EFT cutoff dependence and on the variations in the database used to calibrate the nucleon-nucleon interaction.

In both Refs. [8, 10], the theoretical uncertainty due to the truncation of the EFT was taken into account, only in a very limited regime,  $\Lambda_{cut} \approx 400 - 600 \text{ MeV}$ , thus problematic for robust error estimate [20]. Moreover, the cutoff dependence of  $\chi$ EFT, as well as a large number of parameters sharpen the need to use a different approach for predicting the  $pp$  fusion and mainly its uncertainties.

In this work we use a **renormalizable** and **cutoff independent** EFT approach named pionless EFT ( $\pi$ EFT) which is an alternative EFT approach, that is particularly useful at low energies that are of interest for astrophysical processes, *i.e.*,  $Q \sim 10 \text{ MeV} \ll m_\pi = 140 \text{ MeV}$ , where  $m_\pi$  is the pion mass. The interactions in  $\pi$ EFT are only contact vertices, and the pion mass sets the breakdown scale of this approach (see for examples: [21–23]). Using this theory all particles but nucleons are “integrated out”. The renormalizability which ensures cutoff independence, the small number of parameters as well as their obvious relation to measured quantities (e.g., nucleon-nucleon scattering length and effective ranges), and the natural perturbative expansion are all making  $\pi$ EFT ideal for predictions of low-energy nuclear reactions with reliable uncertainty estimates such as the  $pp$  fusion [24].

### 1.3 The pionless EFT challenges for the $pp$ fusion

$\not\pi$ EFT is ideal for very light nuclei ( $A < 4$ ), since their typical momentum  $Q$  is smaller than  $m_\pi$ . However, the  $\not\pi$ EFT is limited in the number of observables that could be used for calibrating the relevant LECs of the interactions. Nuclear electro-weak interactions containing two nucleons have been calculated using  $\not\pi$ EFT with particular emphasis on the radiative capture ( $n + p \rightarrow d + \gamma$ ) and the  $pp$  fusion. This theoretical focus is due to the fact that the radiative capture is relevant to big-bang nucleosynthesis in energy regimes characterized by large experimental uncertainties [16, 25–28], while the great interest in  $pp$  fusion stems from solar physics.

For weak interactions, up to NLO,  $\not\pi$ EFT leaves a universal coupling LEC,  $L_{1,A}$ , unknown:  $L_{1,A} \approx \frac{l_{1,A}}{M\mu^2}$ , with  $|l_{1,A}|$  as a natural dimensionless number,  $\mu = m_\pi$ , the cutoff of the theory and  $M$  as the nucleon mass. Since the  $pp$  fusion cannot be measured,  $L_{1,A}$  has to be calibrated from other many-body low-energy observables.

Kong and Ravndal have calculated the  $pp$  fusion up to NLO [29]. Butler and Chen accomplished a calculation up to N<sup>4</sup>LO [30], where  $L_{1,A}$  was estimated from previous EFT predictions such as Ref. [31], with  $L_{1,A} = 6 \pm 2.5 \text{ fm}^3$ . Ando *et al.* have calculated the  $\Lambda_{pp}(0)$  while resumming range correction to all orders [32] where  $L_{1,A}$  was fixed indirectly from the two-body matrix element of Ref. [33], with  $L_{1,A} = 1.65 \pm 0.1 \text{ fm}^3$ , for  $\mu = m_\pi$ . In 2017, the Nuclear Physics with Lattice Quantum Chromo Dynamics (NPLQCD) collaboration has used direct lattice QCD calculation to find  $L_{1,A} = 3.9 \pm 1.4 \text{ fm}^3$  [34], for  $\mu = m_\pi$ . All previous  $\not\pi$ EFT predictions for the  $pp$  fusion matrix element are shown in Tab. 1.1.

	ERE [1]	NLO [29]	N <sup>4</sup> LO [30]	Ando <i>et al.</i> [32]	NPLQCD [34]
$\Lambda_{pp}^2(0)$	7.08	7.04~7.7	6.71~7.03	7.09±0.02	7.095±0.07

Table 1.1: Estimations of  $\Lambda_{pp}^2(0)$  from former calculations. The value in the first column is the ERE calculated by Bahcall and May in 1969 [1]. The second, third, and fourth columns are estimated from the  $\not\pi$ EFT calculations: up to NLO by Kong and Ravndal [29], up to N<sup>4</sup>LO by Butler and Chen [30] and the full calculation by Ando *et al.* [32], respectively. The fifth column is the NPLQCD calculation [34].

Tab. 1.1 show that all previous  $\not\pi$ EFT  $pp$  fusion predictions are consistent with each other while most of them have significant uncertainties. Also, neither one of the above predictions has used  $\not\pi$ EFT precisely to estimate  $L_{1,A}$ , which raises the question of the reliability of all these calculations.

Chen *et al.* [11] suggested to calibrate  $L_{1,A}$  using muon capture:

$$\mu^- + d \rightarrow \nu_\mu + n + n. \quad (1.2)$$

The problem in applying  $\not\pi$ EFT to the  $\mu^-d$  capture is that both energy and momentum transfer in this process are up to 100 MeV, which might be too high for  $\not\pi$ EFT, so it might affect the cutoff dependence and requires additional coupling constants, e.g., the axial radius of the nucleon, whose uncertainties were not taken into account. Their suggestion led to the MuSun experiment, measuring this observable, with the aim to reach accuracy of few percents in the determination of  $L_{1,A}$ , excluding the above mentioned uncertainty contribution. Results of MuSun are expected in the following months [35].

The NPLQCD collaboration has calibrated  $L_{1,A}$  using the triton  $\beta$ -decay [34], for the non-physical pion mass,  $m_\pi = 805$  MeV. This method includes an extrapolation to physical pion mass which leads to uncontrolled uncertainties.

In this work, we calibrate  $L_{1,A}$  using the triton ( ${}^3\text{H}$ )  $\beta$ -decay into Helium-3 ( ${}^3\text{He}$ ):

$${}^3\text{H} \rightarrow {}^3\text{He} + e^- + \bar{\nu}_e, \quad (1.3)$$

which is a well-measured, low-energy weak reaction, that also involves  $L_{1,A}$  and therefore can be used for calibrating it. Unlike  $\mu^-d$  capture, this decay is known to per-mill level accuracy [36], and its momentum and energy transfer lies well below the  $\not\pi$ EFT limit, so it is the perfect tool for  $\not\pi$ EFT calibration and predicting the  $pp$  fusion matrix element. Also, the similarity to previous  $\chi$ EFT [10] and LQCD [34] calculations, can serve as a benchmark for evaluating the accuracy of our calculation.

The calibration of LEC from a three-body interaction ( ${}^3\text{H}$   $\beta$ -decay) and the prediction of a two-nucleon interaction ( $pp$  fusion) is based on a hidden assumption that  $\not\pi$ EFT is consistent for calculating both  $A = 2$  and  $A = 3$  systems. However, this assumption is non-trivial for  $\not\pi$ EFT, since the deuteron ( ${}^2\text{H}$ ) wave function differs significantly from that of the three-nucleon ( ${}^3\text{H}$ ,  ${}^3\text{He}$ ) which is regularized by a high momentum, *i.e.*, ultraviolet cutoff  $\Lambda$  [24, 37–39].  $\not\pi$ EFT is renormalizable, *i.e.*, the theory has no dependence on the ultraviolet cutoff ( $\Lambda$ ). However, numerical and theoretical solutions of the integral equations reveal a strong dependence on this cutoff. To overcome this problem, a three-body force, which is allowed by symmetry, was added to the theory at leading order (LO) [38, 39] to remove this cutoff dependence. The question whether a similar behavior exists in a three-nucleon system coupled to an electro-weak field, cannot be answered straightforwardly



and has never been examined.

The Coulomb interaction in light nuclei is an additional complication: the Coulomb interaction is non-perturbative at low momenta  $\lesssim 10$  MeV, as expressed by the strong renormalization of the proton-proton scattering length, but should be perturbative in nuclei where the typical momenta are much higher.  $^3\text{He}$  is the lightest, and therefore simplest, nucleus to test the combination of  $\not\!\text{EFT}$  and Coulomb interaction [40–42] and many recent works have discussed the problem of such a combination. In particular, it was shown that while LO  $^3\text{He}$  is described correctly within  $\not\!\text{EFT}$ , at NLO the results are not so clear, and some approaches pointed out the need for additional, isospin dependent, three-body forces [43, 44]. Therefore, additional three-nucleon observables are needed to obtain predictive power within  $\not\!\text{EFT}$  at NLO such as  $^3\text{He}$  binding energy [43, 45–47].

## 1.4 Goals of this thesis

The primary goal of this work is to use  $\not\!\text{EFT}$  to predict and estimate the uncertainties in  $pp$  fusion rate, using the LEC,  $L_{1,A}$ , calibrated from the three-nucleon reaction  $^3\text{H}$   $\beta$ -decay. The corresponding subgoals needed for this calculations are:

1. To establish a general framework for calculating electro-weak interaction for three-nucleon systems up to NLO. By presenting the three-nucleon diagrammatic representation of the scattering amplitude, we construct a general  $A = 3$  matrix element. Apart from electro-weak observables, this matrix element can be used for calculating the energy difference between  $^3\text{H}$  and  $^3\text{He}$  due to the Coulomb interactions, and the NLO corrections to  $^3\text{H}$  and  $^3\text{He}$  scattering amplitudes due to effective range corrections [48].
2. To study the consistency of  $\not\!\text{EFT}$  for the transition between  $A = 2$  and  $A = 3$  systems and vice-versa up to NLO using the well-measured  $A < 4$ ,  $M_1$  **electromagnetic** observables at zero momentum transfer. By using two theoretical approaches for normalizing the deuteron wave function and comparing the two-body low-energy constants for both  $A = 2, 3$  we can find the nominal method that retains the consistency of the transition between three-nucleon system to two-nucleon system and vice versa. Validity is then checked against experimental data.
3. To evaluate  $\not\!\text{EFT}$  uncertainties due to theoretical and empirical sources.

## 1.5 Verification and validation of pionless EFT using electromagnetic observables

The extraction of the weak LEC  $L_{1,A}$ , could be done by the  $\not\pi$ EFT calculation of the half-life of the  ${}^3\text{H}$   $\beta$ -decay, which is a well-measured, low-energy reaction. This reaction, as well as other low-energy observables, is related to the matrix element of the interaction Hamiltonian between the initial and final nucleon states. However, the  $\not\pi$ EFT predictions of observables between  $A = 3$  **bound-states systems**, were not introduced until recently [49–52]. The primary challenge in describing these interactions stems from the fact that the three-nucleon wave functions are the numerical solution of coupled integral equations [38, 39].

The consistency of  $\not\pi$ EFT for calculating  $A = 2, 3$  electro-weak observables, which is crucial for the extraction of the weak LEC  $L_{1,A}$ , cannot be examined using the weak observables only, due to the small number of appropriate reactions. Instead, we are using the **four** electromagnetic well-measured observables applicable to the  $\not\pi$ EFT regime, which are very similar to weak observables. These observables are the three light nuclei magnetic moments:  $\langle\hat{\mu}_d\rangle$ ,  $\langle\hat{\mu}_{3\text{H}}\rangle$ ,  $\langle\hat{\mu}_{3\text{He}}\rangle$  [53, 54] and the radiative capture process  $n + p \rightarrow d + \gamma$ , whose cross-section is denoted by  $\sigma_{np}$  [55].

	Electromagnetic	weak
One-body LECs	$\kappa_0, \kappa_1$	$g_A$
Two-body LECs	$L_1, L_2$	$L_{1,A}$
One-body operator	$\sigma, \sigma\tau^0$	$\sigma\tau^{+,-}, \tau^{+,-}$
Two-body operator	$L_1 t^\dagger s, L_2 t^\dagger t$	$L_{1,A} t^\dagger s$
$A = 2, Q \approx 0$	$\sigma_{np} : n + p \rightarrow d + \gamma$	$pp$ fusion:
observables	$d$ magnetic moment $\langle\hat{\mu}_d\rangle$	$p + p \rightarrow d + e^+ + \nu_e$
$A = 3, Q \approx 0$	${}^3\text{H}, {}^3\text{He}$ magnetic moments:	${}^3\text{H}$ $\beta$ -decay into ${}^3\text{He}$ :
observables	$\langle\hat{\mu}_{3\text{H}}\rangle, \langle\hat{\mu}_{3\text{He}}\rangle$	${}^3\text{H} \rightarrow {}^3\text{He} + e^- \bar{\nu}_e$

Table 1.2: Electro-weak LECs, operators and low-energy observables.

Table 1.2 shows the similar  $\not\pi$ EFT characteristics of both electromagnetic and weak reactions of  $A = 2$  and  $A = 3$  systems. Up to NLO, the  $\not\pi$ EFT electro-weak Lagrangian contains two types of operators: one-body and two-body. The one-body operators are the Pauli matrices ( $\sigma, \tau, \sigma\tau$ ) and the two-body operators are the four-nucleon fields in term

of dibaryons fields:  $t^\dagger t$  and  $t^\dagger s$ . The  $\nabla$ EFT **electromagnetic** Lagrangian contains (up to NLO), two types of LECs: one-body and two-body. The one-body LECs which are coupled the Pauli matrices  $(\sigma, \tau)$ :  $\kappa_0$  (the isoscalar magnetic moment of the nucleon), and  $\kappa_1$  (the isovector magnetic moment of the nucleon), are both known with high accuracy from the proton and neutron magnetic moments. The two-body LECs,  $L_1$  and  $L_2$ , are known from  $A = 2$  electromagnetic reactions:  $L_1$ , which couples the spin-singlet channel to the spin-triplet channel, and while  $L_2$ , which couples the spin-triplet to another spin-triplet channel. Beside the unknown two-body LEC,  $L_{1,A}$  (which is the weak analogue to  $L_1$ ), the **weak**  $\nabla$ EFT Lagrangian contains the one-body axial low-energy constant,  $g_A$ , which is the weak analogue to  $\kappa_1$ .

the  $A = 2, 3$   $M_1$  observables depend on the values of the two-body electromagnetic LECs,  $L_1$  and  $L_2$ . In past works, the experimental values of the  $A = 2$  observables ( $\sigma_{np}$  and  $\langle \hat{\mu}_d \rangle$ ) were used to fix these LECs [28, 56]. Here, we calculate consistently the  $A = 2, 3$   $M_1$  observables ( $\langle \hat{\mu}_{3H} \rangle$ ,  $\langle \hat{\mu}_{3He} \rangle$ ,  $\langle \hat{\mu}_d \rangle$  and  $\sigma_{np}$ ), which depend on the same LECs, so we can extract these LECs from two observables and then use them to predict the remaining observables. Therefore, we have six independent ways for calibrating the LECs. These calibrations will be used later in this thesis for the evaluating the stability and consistency of  $\nabla$ EFT for  $A = 2$  and  $A = 3$  systems up to NLO and for estimating its theoretical uncertainty.

We argue that this similarity between the weak reactions to the electromagnetic ones, along with the comparison between the electromagnetic experimental data and the theoretical predictions of these observables, will enable us to examine the  $\nabla$ EFT consistency for both sectors (electromagnetic and weak) and to estimate its theoretical uncertainties.

## 1.6 Structure of the thesis

This thesis is organized as follows: The general formalism of  $\nabla$ EFT is presented in Chapter 2. The Faddeev equations describing the three-nucleon wave functions ( $^3\text{H}$  and  $^3\text{He}$ ) and a diagrammatic representation of the three-nucleon wave function are presented in Chapter 3, while the three-nucleon wave function normalization is presented in Chapter 4. The general form of the calculation of a matrix element between two  $A = 3$  bound-state amplitudes is detailed in Chapter 5, and the NLO corrections to the Faddeev equations are discussed in Chapter 6. The calculation of the  $A = 2$  and  $A = 3$  electromagnetic observables as well as the calibrations of the two-body LECs,  $L_1$  and  $L_2$  are presented in Chapter 7. The calculation of weak matrix elements, which are used for the extraction of

the two-body LEC,  $L_{1,A}$  is presented in Chapter 8, while the calculation of the  $pp$  fusion matrix element up to NLO is given in Chapter 9. We present an analysis of the results and calculate the theoretical uncertainty in Chapter 10, as well as giving our final results for the  $pp$  fusion matrix element. We then summarize and provide an outlook in Chapter 11.



# The general formalism of pionless EFT

In this chapter, we briefly summarize the general formalism of  $\pi$ EFT with strong, weak and electromagnetic interactions up to next-to-leading order (NLO).  $\pi$ EFT, as any other EFT, is based on scale separation between a typical momentum,  $Q$ , and high-energy scale,  $\Lambda_{\text{cut}}$ .  $\pi$ EFT is applicable for very low-energy interactions in which  $Q \ll m_\pi \approx 140$  MeV, where  $m_\pi$ , the pion mass, is used as the high-energy scale. The  $\pi$ EFT Lagrangian is, therefore, expanded in a power series of  $\frac{Q}{\Lambda_{\text{cut}}}$  [13], which includes only the contact interactions between the nucleons. In the next section, we present the typical  $\pi$ EFT scales, that are essential for building the  $\pi$ EFT Lagrangian and, as a result, the  $\pi$ EFT interactions matrix elements, up to NLO.

## 2.1 A small parameter expansion of pionless EFT

For light nuclei, the external momentum,  $p$ , and the deuteron binding momentum,  $\gamma_t$ , are formally considered as  $\mathcal{O}(Q)$ , while the renormalization scale,  $\mu$  (which will be introduced later in this chapter), is considered to be the cutoff,  $\Lambda_{\text{cut}}$ . In contrast to Beane and Savage [57] and similarly to Rupak and Kong power-counting [40], in this work we assume a scale separation between the scattering length,  $a$  (which is of the order of  $\frac{1}{Q}$ ) and the effective range,  $\rho$  (scaled as  $\frac{1}{\Lambda_{\text{cut}}}$ ). This scale separation enables us to use their ratio  $\left(\frac{\rho}{a}\right)$  as the small parameter that determines our order of expansion up to  $\frac{\rho}{a} = \mathcal{O}(Q/\Lambda_{\text{cut}})$ .

The  $\pi$ EFT power-counting of the present work is:

- The external nucleon momentum,  $p$ , scales as  $Q$ ;
- The deuteron binding momentum,  $\gamma_t$ , scales as  $Q$  ;

- The renormalization scale,  $\mu$ , scales as  $\Lambda_{\text{cut}}$ ;
- The scattering length,  $a$ , scales as  $\frac{1}{Q}$ ;
- The effective range,  $\rho$ , scales as  $\frac{1}{\Lambda_{\text{cut}}}$ ;
- The kinetic energy scales as  $Q^2/M$ ;
- The loop integration:  $\int d^3\mathbf{p}$  is scaled by  $Q^3$  and
- The nucleon propagator  $S(p_0, p) = \left[ p_0 - \frac{\mathbf{p}^2}{2M} + i\varepsilon \right]^{-1} \sim \mathcal{O}(M/Q^2)$ ,

where  $p$  and  $p_0$  refer to the inner momentum and its associated energy, respectively, and  $M$  is the nucleon mass. Similar to Ref. [40], the integration measure  $\int dq_0 d^3q$  scales as  $\mathcal{O}(Q^5/4\pi M)$ , as we include a factor of  $1/(4\pi)$  with every loop.

## 2.2 Pionless EFT at next-to-leading order

We consider the most general  $\not\pi$ EFT Lagrangian which involves only two nucleons (external electro-weak currents will be included later). A system with two nucleons with zero angular momentum  $L = 0$  can exist in two different channels: a spin singlet,  $s, {}^1S_0$ , (with spin 0 and isospin 1) or spin triplet,  $t, {}^3S_1$  (deuteron with spin 1 and isospin 0). The  $\not\pi$ EFT Lagrangian up to NLO in  $\frac{Q}{\Lambda_{\text{cut}}}$  can be written as [27]:

$$\begin{aligned} \mathcal{L} = & N^\dagger \left( i\partial_0 + \frac{\nabla^2}{2M} \right) N - C_0^t (N^T P_t N)^\dagger (N^T P_t N) - C_0^s (N^T P_s N)^\dagger (N^T P_s N) + \\ & \frac{C_2^t}{8} \left[ (N^T P_t N)^\dagger \left( N^T \left( \overleftrightarrow{\nabla} - \overrightarrow{\nabla} \right)^2 P_t N \right) + h.c. \right] + \frac{C_2^s}{8} \left[ (N^T P_s N)^\dagger \left( N^T \left( \overleftrightarrow{\nabla} - \overrightarrow{\nabla} \right)^2 P_s N \right) + h.c. \right]. \end{aligned} \quad (2.1)$$

Here  $M$  denotes the nucleon mass,  $N$  denotes the nucleon field, the subscripts  $s, t$  denote the spin-singlet and spin-triplet channels, respectively, and  $C_0^{t,s}, C_2^{t,s}$  are coupling constants defined using the nucleon-nucleon ( $N - N$ ) scattering amplitude,  $\mathcal{A}(p)$  which will be discussed later in the section. The projection operators are defined as:

$$P_t^i = \frac{1}{\sqrt{8}} \sigma^2 \sigma^i \tau^2, P_s^A = \frac{1}{\sqrt{8}} \sigma^2 \tau^2 \tau^A, \quad (2.2)$$

where  $\sigma, \tau$  are Pauli matrices.

The equations of motion of each channel in eq. (C-2) can be written as:

$$N^T \left( \overleftarrow{\nabla} - \overrightarrow{\nabla} \right)^2 P_{t,s} N = -4M \left( i\partial_0 + \frac{\nabla^2}{4M} \right) (N^T P_{t,s} N) , \quad (2.3)$$

where both time and space derivatives refer to the center of the mass of each channel, and the mass difference between the proton and the neutron is neglected.

Substituting eq. (2.3) in eq. (C-2) yields:

$$\begin{aligned} \mathcal{L} = & N^\dagger \left( i\partial_0 + \frac{\nabla^2}{2M} \right) N - C_0^t (N^T P_t N)^\dagger (N^T P_t N) - C_0^s (N^T P_s N)^\dagger (N^T P_s N) - \\ & - \frac{C_2^t}{2} M \left[ (N^T P_t N)^\dagger \left( i\partial_0 + \frac{\nabla^2}{4M} \right) (N^T P_t N) + h.c. \right] - \frac{C_2^s}{2} M \left[ (N^T P_s N)^\dagger \left( i\partial_0 + \frac{\nabla^2}{4M} \right) (N^T P_s N) + h.c. \right] . \end{aligned} \quad (2.4)$$

### 2.2.1 $N - N$ scattering amplitude

The nucleon-nucleon ( $N - N$ ) scattering amplitude,  $\mathcal{A}(p)$  (where  $p$  is the momentum in the center of mass frame), presented in this subsection, is the building block of the two-nucleon propagator, which is essential for calculating the  $\not\pi$ EFT interactions.

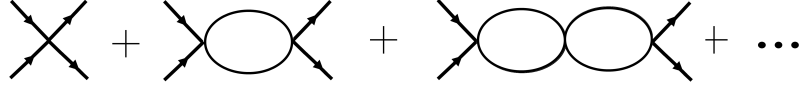


Figure 2.1: The  $N - N$  scattering amplitude is a sum of the chains of  $N - N$  bubbles.

$\mathcal{A}(p)$  can be written in terms of the coupling constants,  $C_0$  and  $C_2$ , up to NLO [13–15, 58]. The LO part of this scattering amplitude is given by the sum over all chains of bubbles (shown in Fig. 2.1), which can be written as:

$$\mathcal{A}_{t,s}^{\text{LO}}(p) = - \frac{C_0^{t,s}}{1 - C_0^{t,s} \mathcal{I}_B(p)} , \quad (2.5)$$

where  $t, s$  denote the nucleon-nucleon channel and  $\mathcal{I}_B(p)$  denotes the two-nucleon loop integral evaluated using the so-called power divergence subtraction (PDS) scheme (see Refs. [14–16]):

$$\mathcal{I}_B(p) = -i \left( \frac{\mu}{2} \right)^{4-D} \int \frac{d^D dq}{(2\pi)^D} \frac{1}{E/2 - p^2/M - p_0 + i\epsilon} \frac{1}{E/2 - p^2/M + p_0 + i\epsilon} , \quad (2.6)$$

where  $E = p^2/M$  is the total center-of-mass energy. This integral is linearly divergent for



$D > 2$ , but dimensional regularization in the space of dimensions makes it finite [13, 15]. When  $D = 3$ , this integral has a simple pole that can be subtracted while using the PDS scheme, which requires the introduction of the renormalization scale  $\mu$ . By analytic continuation of the dimension from  $D = 3$  to  $D = 4$ , one finds that:

$$\mathcal{I}_B(p) = -\frac{M}{4\pi}(\mu + ip) . \quad (2.7)$$

The (full) scattering amplitude  $\mathcal{A}_{t,s}$  is related also to the S-matrix by [15]:

$$S - 1 = e^{2i\delta_{t,s}} - 1 = i\frac{pM}{2\pi}\mathcal{A}_{t,s} , \quad (2.8)$$

where  $\delta_{t,s}$  is the phase shift, such that (up to NLO):

$$p \cot(\delta_{t,s}) = -\frac{1}{a_{t,s}} + \frac{1}{2}\rho_{t,s}p^2 , \quad (2.9)$$

where  $a_{t,s}$  is called the scattering length and  $\rho_{t,s}$  is the effective range. Given eq. (2.8), it is convenient to define  $p \cot(\delta)$  such that:

$$p \cot(\delta_{t,s}) = ip + \frac{4\pi}{\mathcal{A}_{t,s}M} . \quad (2.10)$$

By combining eqs. (2.5), (2.9) and (2.10), one finds that:

$$C_0^{t,s} = \frac{4\pi}{M} \frac{1}{\left(-\mu + \frac{1}{a_{t,s}}\right)} . \quad (2.11)$$

The NLO correction to the  $N-N$  scattering amplitude results in a single NLO insertion ( $C_2 p^2$ ) into the LO scattering amplitude. There are four different options for the locations of these insertions, as shown in Fig. 2.2. Summing over all NLO insertions yields [14]:

$$\mathcal{A}_{t,s}^{\text{NLO}}(p) = \mathcal{A}_{t,s}^{\text{LO}}(p) + \mathcal{A}_{t,s}^{(1)}(p) = \mathcal{A}_{t,s}^{\text{LO}}(p) + \frac{-C_2^{t,s} p^2}{(1 - C_0^{t,s} \mathcal{I}_B)^2} . \quad (2.12)$$

Using eqs. (2.8) to (2.10) up to NLO, one finds that:

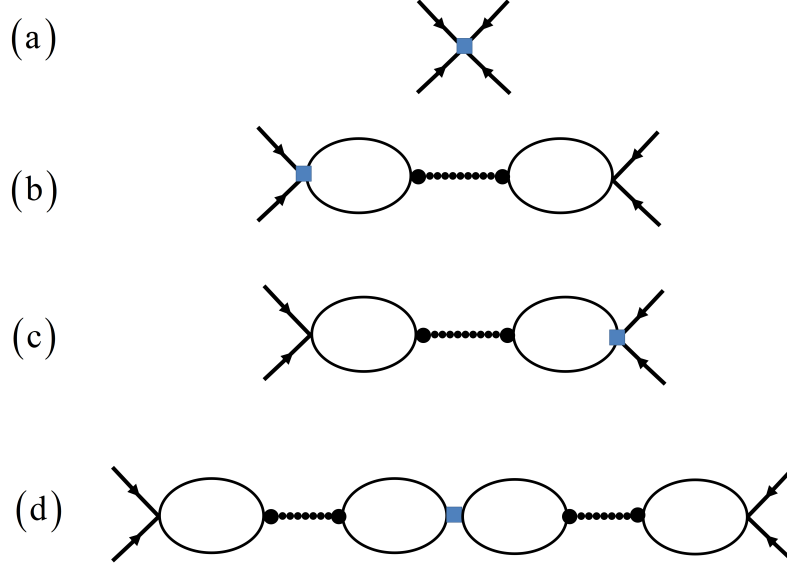


Figure 2.2: The  $N - N$  scattering amplitudes up to NLO. The blue squares denote the NLO insertion of the effective range.

$$p \cot(\delta_{t,s}^{\text{NLO}}) = p \cot(\delta_{t,s}^{\text{LO}}) + \frac{1}{2} \rho_{t,s} p^2 = ip + \frac{4\pi}{M \mathcal{A}_{t,s}^{\text{LO}}} + \frac{4\pi C_2^{t,s} p^2}{(C_0^{t,s})^2 M} \rightarrow C_2^{t,s} = \frac{4\pi}{M \left(-\mu + \frac{1}{a_{t,s}}\right)^2} \frac{\rho_{t,s}}{2}. \quad (2.13)$$

### 2.2.2 Coulomb corrections to N-N scattering amplitude

Some of the interactions discussed in this thesis, contain besides the strong interaction, the Coulomb interactions (*i.e.*,  $pp$  fusion and  ${}^3\text{He}$ ). The derivation of the proton-proton ( $pp$ ) scattering amplitude for these reactions is based on Refs. [29, 59, 60].

At LO, the  $pp$  nucleon bubble has an infinite series of ladder diagrams of a Coulomb photon exchange.

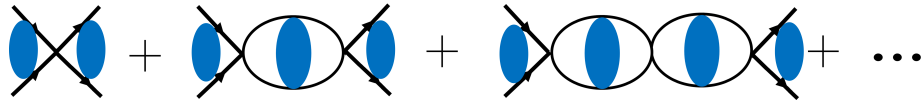


Figure 2.3: The  $pp$  scattering amplitude is a sum of chains of Coulomb-dressed bubbles.

The sum of all the bubbles yields the scattering amplitude shown in Fig. 2.3:

$$i\mathcal{A}_{pp}(p) = -iC_\eta^2 C_0^{pp} e^{2i\sigma_0} \frac{1}{1 - C_0^{pp} J_0(p)}, \quad (2.14)$$

where:

$$\sigma_l = \arg [\Gamma (1 + i\eta (p) + l)] , \quad C_\eta = \sqrt{\frac{2\pi\eta}{-1 + e^{2\pi\eta}}} , \quad \eta(p) = \frac{\alpha M}{2p} , \quad (2.15)$$

and  $\alpha \sim 1/137$  is the fine-structure constant.  $J_0(p)$ , the amplitude of an infinite photons exchange (without external energy and momentum transfer) is given by:

$$J_0(p) = M \int \frac{d^3k}{(2\pi)^3} \frac{\psi_0^* \psi_0}{p^2 - k^2} , \quad (2.16)$$

where

$$\psi_0 = \int \frac{d^3k}{(2\pi)^3} \langle k | \psi_p \rangle = C_\eta e^{i\sigma_0} , \quad (2.17)$$

and  $|\psi_p\rangle$  is the solution of the Schrödinger equation  $(\hat{H} - E) |\psi_p\rangle = 0$ , where  $\hat{H} = \hat{H} + \hat{V}_C$  is the full Hamiltonian with a Coulomb potential. Hence, eq. (2.16) has the form:

$$J_0(p) = M \int \frac{d^3k}{(2\pi)^3} \frac{2\pi\eta(k)}{e^{2\pi\eta(k)} - 1} \frac{1}{p^2 - k^2} = M \int \frac{d^3k}{(2\pi)^3} \frac{2\pi\eta(k)}{e^{2\pi\eta(k)} - 1} \frac{p^2}{k^2} \frac{1}{p^2 - k^2} - M \int \frac{d^3k}{(2\pi)^3} \frac{2\pi\eta(k)}{e^{2\pi\eta(k)} - 1} \frac{1}{k^2} . \quad (2.18)$$

The first integral ( $J_0^{\text{fin}}(p)$ , hereafter) converges and the second integral ( $J_0^{\text{div}}$ , hereafter) has no  $p$ -dependence, but it diverges with  $k \rightarrow \infty$ . Introducing a new variable  $x$ , we write:

$$J_0^{\text{fin}}(p) = M \int \frac{d^3k}{(2\pi)^3} \frac{2\pi\eta(k)}{e^{2\pi\eta(k)} - 1} \frac{p^2}{k^2} \frac{1}{p^2 - k^2} =_{k=\frac{\pi\alpha M}{x}} \int dx \frac{\alpha M^2 p^2}{2\pi} \frac{x}{(e^x - 1) (\pi^2 \alpha^2 M^2 - p^2 x^2)} , \quad (2.19)$$

and using the known integral

$$\int_0^\infty dx \frac{x}{e^x - 1} \frac{1}{x^2 + a^2} = \frac{1}{2} \left[ \log \left( \frac{a}{2\pi} \right) - \frac{\pi}{a} - \psi \left( \frac{a}{2\pi} \right) \right] , \quad (2.20)$$

we get that:

$$J_0^{\text{fin}}(p) = -\frac{\alpha M^2}{4\pi} \Phi(\eta) , \quad (2.21)$$

where

$$\Phi(x) = \psi(ix) + \frac{1}{2ix} - \log(ix) , \quad (2.22)$$

and  $\psi$  is the derivative of the  $\Gamma$  function.

Using  $\mu$  as the renormalization scale, the divergent part of  $J_0$  for  $D = 3 - \epsilon$  is given

by:

$$J_0^{\text{div}} = -M \int \frac{d^3k}{(2\pi)^3} \frac{2\pi\eta(k)}{e^{2\pi\eta(k)} - 1} \frac{1}{k^2} = \int dx \frac{\alpha M^2}{2\pi(e^x - 1)x} =$$

$$- \frac{\alpha M^2}{4\sqrt{\pi}\Gamma(\frac{d}{2})} \left( \frac{\mu}{M\alpha\sqrt{\pi}} \right)^\epsilon \int dx \frac{x^{\epsilon-1}}{(e^x - 1)} = - \frac{\alpha M^2}{4\sqrt{\pi}\Gamma(\frac{d}{2})} \left( \frac{\mu}{M\alpha\sqrt{\pi}} \right)^\epsilon \zeta(\epsilon)\Gamma(\epsilon), \quad (2.23)$$

where  $\zeta(x)$  is the Riemann zeta function.

For  $\epsilon \rightarrow 0$ , eq. (2.23) becomes:

$$J_0^{\text{div}} = \frac{\alpha M^2}{4\pi} \left[ \log\left(\frac{\mu}{\alpha}\right) + \frac{1}{\epsilon} - \frac{3C_E}{2} + 1 + \frac{\log(\pi)}{2} \right], \quad (2.24)$$

which includes a pole for  $\epsilon = 0$ . For  $D \rightarrow 2$ , the divergent part of eq. (2.18) has another pole:

$$J_0^{\text{div}}(D \rightarrow 2) = \frac{\mu M}{4\pi(D-2)}. \quad (2.25)$$

According to the PDS regularization scheme, the latter pole has to be subtracted from eq. (2.24), even when  $D \rightarrow 3$ , the result of which is:

$$J_0^{\text{div}} = \frac{\alpha M^2}{4\pi} \left[ \log\left(\frac{\mu\sqrt{\pi}}{\alpha M}\right) + 1 - \frac{3}{2}C_E + \frac{1}{\epsilon} \right] - \frac{\mu M}{4\pi}. \quad (2.26)$$

The Coulomb scattering length is thus contained in the ultraviolet divergent part of the Coulomb bubble:

$$\frac{1}{a_p} = \frac{4\pi}{M} \left( \frac{1}{C_0^{pp}} - J_0^{\text{div}} \right), \quad (2.27)$$

where  $a_p = -7.82$  fm is the measured  $pp$  scattering length. Since  $J_0^{\text{div}} = J_0(p) + \frac{\alpha M^2}{4\pi}\Phi(\eta)$ , eq. (2.27) can be written as:

$$\frac{1}{a_p} = \frac{4\pi}{M} \left( \frac{1}{C_0^{pp}} - J_0(p) - \frac{\alpha M^2}{4\pi}\Phi(\eta) \right), \quad (2.28)$$

and the  $pp$  scattering amplitude (eq. (2.14)) can be written as in Ref. [59]:

$$i\mathcal{A}_{pp}(p) = -iC_\eta^2 C_0^{pp} e^{2i\sigma_0} \frac{1}{1 - C_0^{pp} J_0(p)} = -iC_\eta^2 e^{2i\sigma_0} \frac{1}{\frac{1}{C_0^{pp}} - J_0(p)} = -iC_\eta^2 e^{2i\sigma_0} \frac{4\pi}{M \left( \frac{1}{a_p} + \alpha M \Phi(\eta) \right)}. \quad (2.29)$$

### The NLO correction to the Coulomb scattering amplitude

The NLO correction to the  $pp$  scattering amplitude is given by the diagrams shown in Fig. 2.4.

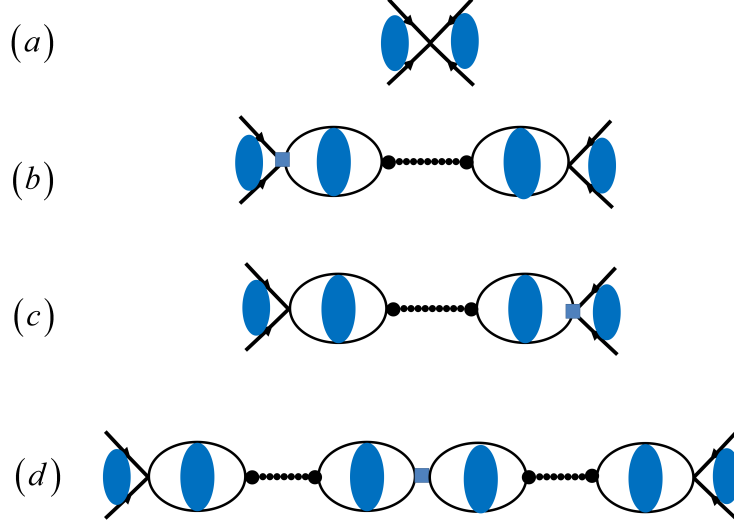


Figure 2.4: The  $pp$  dibaryon propagator up to NLO. The blue squares denote the NLO insertion of the effective range.

The contribution from the first diagram (Fig. 2.4 (a)) is:

$$T^a(p) = C_2^{pp} \psi_0(p) \psi_2(p) , \quad (2.30)$$

where

$$\psi_2(p) = \int \frac{d^3k}{(2\pi)^3} k^2 \psi_p(k) = C \eta e^{i\sigma_0} \left[ p^2 - \mu \alpha M - \frac{1}{2} (\alpha M)^2 \right] , \quad (2.31)$$

and

$$C_2^{pp} = \frac{M (C_0^{pp})^2}{8\pi} \rho_C , \quad (2.32)$$

with  $\rho_C$  denoting the Coulomb effective range.

The contribution from the second and third diagrams (Fig. 2.4 (b+c)) is given by (see [59]):

$$T^{b+c}(p) = C_2^{pp} \frac{C_0^{pp}}{1 - C_0 J_0(p)} \psi_0 [\psi_0(p) J_2(p) + \psi_2(p) J_0(p)] , \quad (2.33)$$

where:

$$\begin{aligned}
 J_2(p) &= M \int \frac{d^3k}{(2\pi)^3} \frac{\psi_2(k)\psi_0^*(k)}{p^2 - k^2} = M \int \frac{d^3k}{(2\pi)^3} \frac{e^{2\pi\eta(k)}}{e^{2\pi\eta(k)} - 1} \frac{k^2 - \mu\alpha M - \frac{1}{2}(\alpha M)^2}{p^2 - k^2} = \\
 &M \int \frac{d^3k}{(2\pi)^3} \frac{e^{2\pi\eta(k)}}{e^{2\pi\eta(k)} - 1} \frac{k^2 - p^2 + p^2 + \mu\alpha M - \frac{1}{2}(\alpha M)^2}{p^2 - k^2} = \\
 &\left[ p^2 - \mu\alpha M - \frac{1}{2}(\alpha M)^2 \right] J_0(p) - J,
 \end{aligned} \tag{2.34}$$

and

$$J = M \int \frac{d^3k}{(2\pi)^3} \frac{e^{2\pi\eta(k)}}{2\pi\eta(k) - 1} = M^4 \alpha^3 \int dx \frac{\pi e^x}{2x^3 (e^x - 1)}, \tag{2.35}$$

which has a  $p$ -independent ultraviolet divergence.

The contribution from the fourth diagram (Fig. 2.4 (d)) is:

$$T_d = \frac{C_2^{pp}(C_0^{pp})^2}{[1 - C_0^{pp}J_0(p)]^2} \psi_0^2(p) J_0(p) J_2(p). \tag{2.36}$$

The NLO correction to the  $pp$  scattering amplitude ( $\mathcal{A}_{pp}^{(1)}(p)$ ) is given by the summation over of the four contributions (eqs. (2.30), (2.33) and (2.36)):

$$\begin{aligned}
 \mathcal{A}_{pp}^{(1)}(p) &= \frac{C_2^{pp}\psi_0(p)}{[1 - C_0^{pp}J_0(p)]^2} \{ \psi_2(p) + C_0^{pp}[\psi_0(p)J_2(p) - \psi_2(p)J_0(p)] \} = \\
 &\frac{C_2^{pp}\psi_0^2}{[1 - C_0^{pp}J_0(p)]^2} \left[ p^2 - \mu\alpha M - \frac{1}{2}(\alpha M)^2 - C_0^{pp}J \right].
 \end{aligned} \tag{2.37}$$

Since  $\mu$  can be chosen such that  $\alpha M \ll \mu$ ;  $\frac{1}{2}(\alpha M)^2 + C_0^{pp}J$  is negligible in comparison to  $p^2 - \mu\alpha M$ . Therefore, eq. (2.37) becomes:

$$\begin{aligned}
 \mathcal{A}_{pp}^{(1)}(p) &= \frac{C_2^{pp}\psi_0^2}{[1 - C_0^{pp}J_0(p)]^2} (p^2 - \mu\alpha M) = C_\eta^2 e^{2i\sigma_0} \frac{M\rho_c}{8\pi \left( J_0(p) - \frac{1}{C_0^{pp}} \right)^2} (p^2 - \mu\alpha M) = \\
 &C_\eta^2 e^{2i\sigma_0} \frac{4\pi}{M} \frac{\rho_C}{2} \frac{1}{\left( \frac{1}{a_p} + \alpha M \Phi(\eta) \right)^2} (p^2 - \mu\alpha M).
 \end{aligned} \tag{2.38}$$

Up to NLO, the  $pp$  scattering amplitude is given by:

$$\begin{aligned}
 i\mathcal{A}_{pp}^{\text{NLO}}(p) &= i\mathcal{A}_{pp}^{\text{LO}}(p) + i\mathcal{A}_{pp}^{(1)}(p) = \\
 &-iC_\eta^2 e^{2i\sigma_0} \frac{4\pi}{M} \left[ \left( \frac{1}{a_p} + \alpha M \Phi(\eta) \right)^{-1} - \frac{\rho_C}{2} \frac{1}{\left( \frac{1}{a_p} + \alpha M \Phi(\eta) \right)^2} (p^2 - \mu\alpha M) \right] = \\
 &i\mathcal{A}_{pp}^{\text{LO}}(p) \left[ 1 - \frac{\rho_C}{2} \frac{p^2 - \mu\alpha M}{\frac{1}{a_p} + \alpha M \Phi(\eta)} \right]. \quad (2.39)
 \end{aligned}$$

## 2.3 Pionless EFT Lagrangian coupled to electro-weak fields

All interactions discussed in this thesis are either weak or electromagnetic, which should be added to  $\not\pi$ EFT Lagrangian, eq. (2.4).

### 2.3.1 Weak interaction in pionless EFT

For the low-energy process, the weak-interaction Lagrangian is:

$$\mathcal{L}_{\text{Weak}} = \frac{G_F V_{ud}}{\sqrt{2}} l_\mu^+ J_\mu^-, \quad (2.40)$$

where  $G_F$  is the Fermi constant and  $V_{ud}$  is the Cabibbo-Kobayashi-Maskawa (CKM) matrix element.  $l^\mu$  is the leptonic current and  $J_\mu$  is the hadronic current, which contains two parts, a polar-vector and axial-vector,  $J_\mu = V_\mu - A_\mu$ .

Up to NLO, the part of the polar vector current relevant to  $\beta$ -decay with a vanishing energy transfer is:

$$V_0^\pm = N^\dagger \frac{\tau^\pm}{2} N, \quad (2.41)$$

where  $\tau^\pm = \tau_1 \pm i\tau_2$ .

Here, we utilized the fact that the Conserved Vector Current (CVC) hypothesis is

accurate at this order of EFT. The axial-vector part is (see Ref. [32, 57]):

$$\mathbf{A}^\pm = \underbrace{\frac{g_A}{2} N^\dagger \boldsymbol{\sigma} \tau^\pm N}_{\text{LO}} + \underbrace{L_{1,A} \left[ (N^T P_t^i N)^\dagger (N^T P_s^A N) + h.c. \right]}_{\text{NLO}}, \quad (2.42)$$

where  $g_A$  is the axial coupling constant for a single nucleon, known from neutron  $\beta$ -decay and  $L_{1,A}$  is the unknown two-body weak LEC and  $\boldsymbol{\sigma}$  the Pauli matrix vector.

### 2.3.2 Electromagnetic interaction in pionless EFT

The one-body Lagrangian of the electromagnetic interaction is given by:

$$\mathcal{L}_{\text{magnetic}}^{(1)} = \frac{e}{2M} N^\dagger [(\kappa_0 + \kappa_1 \tau_3) \boldsymbol{\sigma} \cdot \mathbf{B}] N, \quad (2.43)$$

where  $\kappa_0 = 0.439902328(26)$  is the isoscalar magnetic moment of the nucleon and  $\kappa_1 = 2.352945028(26)$  is the isovector magnetic moment of the nucleon, both presented in units of nuclear magneton. The magnetic field is conventionally defined as  $\mathbf{B} = \nabla \cdot \mathbf{A}$ .

According to the  $\not\pi$ EFT naïve power-counting [40], at NLO there are two contributions to the two-body electromagnetic Lagrangian:

$$\mathcal{L}_{\text{magnetic}}^{(2)} = e \left[ L_1 (N^T P_s^A N)^\dagger (N^T P_t^i N) B_i - i \epsilon_{ijk} L_2 (N^T P_t^i N)^\dagger (N^T P_t^j N) B_k + h.c. \right], \quad (2.44)$$

where  $L_1$  and  $L_2$  are the two-body LECs of the electromagnetic interaction:  $L_1$  couples the spin-singlet channel to the spin-triplet channel and  $L_2$  couples two spin-triplet channels.

## 2.4 Introducing dibaryon fields

The Hubbard-Stratonovich (H-S) transformation is an exact mathematical transformation from a nucleon-nucleon field into a field of two nucleons (dibaryon). This transformation is most helpful in writing a three-particle system, as presented first in Refs. [38, 39, 57].

The transformation is defined using the integral:

$$\exp(ax^2) = \int_{-\infty}^{\infty} \frac{\exp\left(-\frac{y^2}{a} + 2x \cdot y\right)}{\sqrt{\pi a}} dy. \quad (2.45)$$



A general  $\psi^4$  Lagrangian (eq. (C-2)) has the form:

$$\mathcal{L} = N^T \left( i\partial_0 + \frac{\nabla^2}{2M} \right) N - C_0 (N^\dagger N)^2, \quad (2.46)$$

and the total path integral of the Lagrangian is defined as:

$$Z = \int \mathcal{D}[N^\dagger, N] \exp \left\{ - \left[ \int dx_0 \int d^d x N^T \left( i\partial_0 + \frac{\nabla^2}{2M} \right) N - C_0 (N^\dagger N)^2 \right] \right\}, \quad (2.47)$$

where:  $\mathcal{D}[N] = \prod_i dN_i$  over all the partials.

Using eq. (2.45), eq. (2.47) can be written as:

$$Z = \frac{1}{\sqrt{\pi C_0}} \int \mathcal{D}[N^\dagger, N] da \exp \left\{ - \int dx_0 \int d^d x \left[ N^T \left( i\partial_0 + \frac{\nabla^2}{2M} \right) N + \frac{1}{C_0} a^2 - 2 (N^\dagger N) a \right] \right\}, \quad (2.48)$$

where  $a$  is an auxiliary dibaryon field that contains two nucleons.

### 2.4.1 Hubbard-Stratonovich transformations for pionless EFT

In this subsection, we apply the H-S transformation to the  $\not\pi$ EFT Lagrangian [12, 57, 61] that leads to an equivalent Lagrangian in terms of two-body effective degrees of freedom. For simplification, we denote  $\left( i\partial_0 + \frac{\nabla^2}{4M} \right)$  of eq. (2.4) by  $\mathcal{O}_D$ , and by using the following notation:

$$(N^T P_{t,s} N) = \psi_{t,s}. \quad (2.49)$$

using this notation, eq. (2.4) has the form:

$$\mathcal{L} = N^\dagger \left( i\partial_0 + \frac{\nabla^2}{2M} \right) N - \sum_{a=t,s} \psi_a^\dagger (C_0^a + C_2^a M \cdot \mathcal{O}_D) \psi_a \quad (2.50)$$

and the path integral  $Z$  is given by:

$$Z = \int dN dN^\dagger d\psi_t d\psi_s \exp \left\{ - \int dx_0 \int d^d x \left[ N^\dagger \left( i\partial_0 + \frac{\nabla^2}{2M} \right) N - \sum_{a=t,s} \psi_a^\dagger (C_0^a + C_2^a M \mathcal{O}_D) \psi_a \right] \right\}. \quad (2.51)$$

By performing the H-S transformation and introducing two new dibaryon fields,  $t$  (with spin 1 and isospin 0) and  $s$  (with spin 0 and isospin 1), one can write path integral  $Z$  as:

$$\begin{aligned}
 Z = & \int dN dN^\dagger d\psi_t d\psi_s dt ds \exp \left\{ - \int dx_0 \int d^d x \left[ N^\dagger \left( i\partial_0 + \frac{\nabla^2}{2M} \right) N + \right. \right. \\
 & \left. \left. \sum_{a=t,s} -a^\dagger (\mathcal{O}_D - \sigma_a) a - y_a (\psi^\dagger a + a^\dagger \psi) \right] \right\} = \\
 & \int dN dN^\dagger \psi_t, d\psi_s \exp \left\{ - \int dx_0 \int d^d x \left[ N^\dagger \left( i\partial_0 + \frac{\nabla^2}{2M} \right) N - \sum_n \sum_{a=t,s} \psi_a^\dagger \left( \frac{y_a^2}{\sigma_a} \left( \frac{\mathcal{O}_D}{\sigma_a} \right)^n \right) \psi_a^\dagger \right] \right\}.
 \end{aligned} \tag{2.52}$$

Keeping up to first order in  $\mathcal{O}_D$ , eq. (2.53) becomes:

$$Z = \int dN dN^\dagger \psi_t d\psi_s \exp \left\{ - \int dx_0 \int d^d x \left[ N^\dagger \left( i\partial_0 + \frac{\nabla^2}{2M} \right) N - \sum_{a=t,s} \psi_a^\dagger \left( \frac{y_a^2}{\sigma_a} + \frac{\mathcal{O}_D y_a^2}{\sigma_a^2} \right) \psi_a^\dagger \right] \right\}. \tag{2.53}$$

Comparing eq. (2.53) with eq. (2.51) yields the following relations:

$$C_0^{t,s} = \frac{y_{t,s}^2}{\sigma_{t,s}}, \tag{2.54}$$

$$C_2^{t,s} = \frac{y_{t,s}^2}{M\sigma_{t,s}^2}. \tag{2.55}$$

From the comparison of eqs. (2.54) and (2.55) with eqs. (2.11) and (2.13), we introduce two new coupling constants for each channel:

$$y_{t,s} = \frac{\sqrt{8\pi}}{M\sqrt{\rho_{t,s}}}, \tag{2.56}$$

$$\sigma_{t,s} = \frac{2}{M\rho_{t,s}} \left( \frac{1}{a_{t,s}} - \mu \right), \tag{2.57}$$

such that eq. (2.4) has the form:

$$\begin{aligned}
 \mathcal{L} = & N^\dagger \left( i\partial_0 + \frac{\nabla^2}{2M} \right) N - t^{i\dagger} \left[ -\sigma_t + \left( i\partial_0 + \frac{\nabla^2}{4M} \right) \right] t^i - s^{A\dagger} \left[ -\sigma_s + \left( i\partial_0 + \frac{\nabla^2}{4M} \right) \right] s^i - \\
 & - y_t [t^{i\dagger} (N^T P_t^i N) + h.c.] - y_s [s^{A\dagger} (N^T P_s^i N) + h.c.] .
 \end{aligned} \tag{2.58}$$

## 2.5 The dibaryon propagator

The bare dibaryon propagator arising from the  $\pi$ EFT dibaryon Lagrangian, eq. (2.58) is:

$$i\mathcal{D}_{t,s}^{\text{bare}}(p_0, \mathbf{p}) = -i \left[ p_0 - \frac{\mathbf{p}^2}{4M} - \sigma_{t,s} \right]^{-1}. \quad (2.59)$$

We use a power-counting that is appropriate for systems with a scattering length  $a$  that is large compared to the range of the interaction  $\rho$  [15]. The *full* dibaryon propagator (Fig. 2.5) is therefore defined as the geometric sum of nucleon bubbles connected by bare dibaryon propagators (see Refs. [38, 39] for more details):

$$i\mathcal{D}_{t,s}^{\text{full}}(p_0, \mathbf{p}) = i\mathcal{D}_{t,s}^{\text{bare}}(p_0, \mathbf{p}) \cdot \sum_n (\mathcal{D}_{t,s}^{\text{bare}}(p_0, \mathbf{p}) \cdot \mathcal{I}_B \cdot (-2iy_{t,s})^2)^n, \quad (2.60)$$

where  $\mathcal{I}_B$  denotes the two-nucleon loop integral evaluated using the so-called power divergence subtraction (PDS) scheme (see [14–16]). The full (*unrenormalized*) propagator

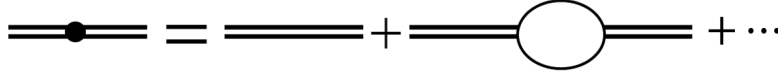


Figure 2.5: The dressed dibaryon propagator. The bare dibaryon propagator is dressed by nucleon bubbles to all orders.

becomes then

$$i\mathcal{D}_{t,s}^{\text{full}}(p_0, \mathbf{p}) = -i \left[ p_0 - \frac{\mathbf{p}^2}{4M} - \sigma_{t,s} + \frac{My_{t,s}^2}{4\pi} (\sqrt{-Mp_0 + \mathbf{p}^2/4 - i\epsilon} - \mu) \right]^{-1} = \\ i \frac{4\pi}{My_{t,s}^2} \left[ \frac{1}{a_{t,s}} - \sqrt{-Mp_0 + \frac{\mathbf{p}^2}{4}} + \frac{\rho_{t,s}}{2} (\mathbf{p}^2/4 - Mp_0) \right]^{-1}. \quad (2.61)$$

The dibaryon propagator shown above has two poles. One corresponds to the *physical* bound-state (virtual) pole that results from the large scattering length in the triplet (singlet) channel. The other pole is a spurious pole whose energy scale lies beyond the breakdown scale of the EFT. We expand the propagator in eq. (2.61) in powers of the effective range since the spurious pole causes problems in calculations for few-body systems. Through this expansion, we can also isolate the pieces that are dependent and independent of the effective range. Accordingly, we define the LO dibaryon propagator

as:

$$i\mathcal{D}_{t,s}^{\text{LO}}(p_0, \mathbf{p}) = i \frac{4\pi}{My_{t,s}^2} \left( \frac{1}{a_{t,s}} - \sqrt{-Mp_0 + \frac{\mathbf{p}^2}{4}} \right)^{-1}, \quad (2.62)$$

which is equal to (see Ref. [32]):

$$i\mathcal{D}_{t,s}^{\text{LO}}(p_0, \mathbf{p}) = \frac{-i}{y_{t,s}} i\mathcal{A}_{t,s}^{\text{LO}}(p') \frac{-i}{y_{t,s}}, \quad (2.63)$$

where:

$$p' = i\sqrt{\mathbf{p}^2/4 - Mp_0}. \quad (2.64)$$

In the case of a bound-state, we expand the triplet propagator (eq. (2.61)) about the deuteron pole. Up to NLO, the triplet propagator up is given by [43]:

$$i\mathcal{D}_t^{\text{NLO}}(p_0, \mathbf{p}) = i \frac{4\pi}{My_t^2} \left( \gamma_t - \sqrt{-Mp_0 + \frac{\mathbf{p}^2}{4}} \right)^{-1} \cdot \left[ 1 + \frac{\rho_t}{2} \left( \frac{\mathbf{p}^2/4 - Mp_0 - \gamma_t^2}{-\gamma_t + \sqrt{-Mp_0 + \frac{\mathbf{p}^2}{4}}} \right) \right]. \quad (2.65)$$

For the singlet channel, the singlet propagator up to NLO is given by:

$$i\mathcal{D}_s^{\text{NLO}}(p_0, \mathbf{p}) = i \frac{4\pi}{My_s^2} \left( \frac{1}{a_s} - \sqrt{-Mp_0 + \frac{\mathbf{p}^2}{4}} \right)^{-1} \cdot \left[ 1 + \frac{\rho_s}{2} \left( \frac{\mathbf{p}^2/4 - Mp_0}{-\frac{1}{a_s} + \sqrt{-Mp_0 + \frac{\mathbf{p}^2}{4}}} \right) \right] = \frac{-i}{y_s} i \left[ i\mathcal{A}_s^{\text{LO}}(p') + i\mathcal{A}_s^{(1)}(p') \right] \frac{-i}{y_s}. \quad (2.66)$$

### 2.5.1 The Coulomb propagator

At LO, the  $pp$  propagator contains an infinite series of ladder diagrams of Coulomb photon exchanges. Due to the non-perturbative nature of the Coulomb interaction at low energies, those diagrams have to be resummed up to infinity like that of the  $pp$  scattering amplitude (subsection 2.2.2). Similarly to eqs. (2.62) and (2.65), the LO Coulomb propagator is given by [32]:

$$i\mathcal{D}_{pp}^{\text{LO}}(p_0, \mathbf{p}) = - (C_\eta^2 e^{2i\sigma_0})^{-1} \frac{1}{y_s^2} i\mathcal{A}_{pp}^{\text{LO}}(p') = i \frac{4\pi}{My_s^2} \left[ \frac{1}{a_p} + 2\kappa\Phi(\kappa/p') \right]^{-1}, \quad (2.67)$$

where  $a_p$ ,  $\sigma_0$ ,  $C_\eta$  and  $\Phi$  are all defined in subsection 2.2.2,

$$\kappa = \frac{\alpha M}{2} . \quad (2.68)$$

Using eq. (2.39), the Coulomb propagator up to NLO is given by<sup>1</sup>:

$$i\mathcal{D}_{pp}^{\text{NLO}}(p_0, \mathbf{p}) = - (C_\eta^2 e^{2i\sigma_0})^{-1} \frac{1}{y_s^2} i\mathcal{A}_{pp}^{\text{NLO}} = i\mathcal{D}_{pp}^{\text{LO}}(p_0, \mathbf{p}) \left[ 1 - \frac{\rho_C}{2} \frac{p'^2 - \mu\alpha M}{\frac{1}{a_p} + 2\kappa\Phi(\kappa/p')} \right] . \quad (2.69)$$

## 2.6 The deuteron normalization and $Z$ -parameterization

The long range properties of the deuteron wave function are set by its residue [22, 62]:

$$Z_d = \left[ \frac{i\partial}{\partial E} \frac{1}{iD_t(E, p)} \Big|_{E=-\frac{\gamma_t^2}{M}, p=0} \right]^{-1} = \frac{1}{1 - \gamma_t \rho_t}, \quad (2.70)$$

which is a function of both the deuteron binding momentum ( $\gamma_t = \sqrt{ME_b(d)}$ ) and the effective range,  $\rho_t$ .

Parameter	Value	Parameter	Value
$\gamma_t$	45.701 MeV [63]	$\rho_t$	1.765 fm [64]
$a_s$	-23.714 fm [65]	$\rho_s$	2.73 fm [65]
$a_p$	-7.8063 fm [66]	$\rho_C$	2.794 fm [66]

Table 2.1: Experimental values for parameters used in the numerical calculation

Using the effective ranges that are fixed from scattering experiments we get (see Tab. 2.1):

$$Z_d^{\text{exp}} = \frac{1}{1 - \gamma_t \rho_t} \approx 1.690(3) . \quad (2.71)$$

In the effective range expansion (ERE), where  $\gamma_t \rho_t$  is the small parameter, the order-by-order expansion of  $Z_d$  is:

$$\begin{aligned} Z_d^{\text{LO}} &= 1 , \\ Z_d^{\text{NLO}} &= 1 + \gamma_t \rho_t \approx 1.408 . \end{aligned} \quad (2.72)$$

---

<sup>1</sup>Note that for the case of  $^3\text{He}$ , since  $p' \geq 70 \text{ MeV}$ ,  $\mu\alpha M$  can be neglected in comparison to  $p'^2$ .

However, for observables that include deuteron break-up or low-energy scattering, the normalization of the wave function prefactors the cross-section. In these cases, it was suggested that retaining the physical value of  $Z_d$  is more essential than fixing  $\rho_t$ , as this choice converges better and faster in the EFT expansion [67, 68]. Thus, the alternative NLO parameterization, known as the  $Z$ -parameterization in which  $Z_d - 1$  is the small parameter, is given by [22, 29, 50, 62, 69]:

$$\begin{aligned} Z_d^{\text{LO}} &= 1 , \\ Z_d^{\text{NLO}} &= 1 + (Z_d^{\text{exp}} - 1) = 1.690(3) . \end{aligned} \tag{2.73}$$





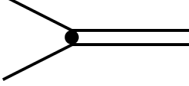
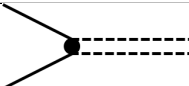

The price for retaining  $Z_d$  at its experimental value is that the value of the triplet effective range at NLO in this parameterization is:







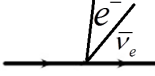
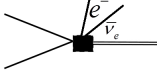
$$\rho'_t = \frac{Z_d^{\text{exp}} - 1}{\gamma_t} \approx \frac{0.690}{\gamma_t} , \tag{2.74}$$

rather than  $\rho_t$  of Tab. 2.1. These two alternatives are valid rearrangements of the perturbative expansion. In the following, we use these two NLO parameterizations, and the difference in their predictions is used as one of the measures for the theoretical uncertainty stemming from the EFT truncation.

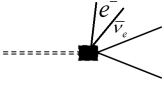
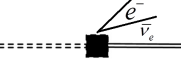

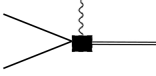
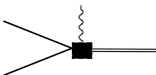
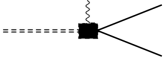
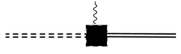
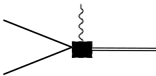
## 2.7 Summary of Feynman Rules

The Feynman rules for the electro-weak interactions are given in Tab. 2.2. These Feynman rules cover all aspects of the three-nucleon electro-weak interactions. Some of these rules were presented in the previous subsections while the others will be derived in the following chapters.

	Field structure	Diagrammatic structure	Feynman rule
Leading order			
(a)	single nucleon line		$iS_{\beta b}^{\alpha a} = i\delta_b^a \delta_\beta^\alpha \left( p_0 - \frac{\mathbf{p}^2}{2m} + i\varepsilon \right)^{-1}$
(b)	LO spin-triplet dibaryon propagator eq. (2.62)		$i\mathcal{D}_t^{ij}(p_0, \mathbf{p}) = i\delta^{ij} \frac{4\pi}{My_t^2} \left( \frac{1}{a_t} - \sqrt{-Mp_0 + \frac{\mathbf{p}^2}{4}} \right)^{-1}$
(c)	LO spin-singlet dibaryon propagator eq. (2.62)		$i\mathcal{D}_s^{AB}(p_0, \mathbf{p}) = i\delta^{AB} \frac{4\pi}{My_s^2} \left[ \frac{1}{a_s} - \sqrt{-Mp_0 + \frac{\mathbf{p}^2}{4}} \right]^{-1}$
(d)	LO $pp$ propagator eq. (2.67)		$i\mathcal{D}_{pp}^{AB}(p_0, \mathbf{p}) = i\delta^{AB} \frac{4\pi}{My_t^2} \left[ \frac{1}{a_p} + 2\kappa\Phi(\kappa/p') \right]^{-1}$
(e)	spin-triplet dibaryon vertex eq. (2.58)		$-2iy_t \frac{1}{\sqrt{8}} \sigma^2 \tau^2 \sigma^i$
(f)	spin-singlet dibaryon vertex eq. (2.58)		$-2iy_s \frac{1}{\sqrt{8}} \sigma^2 \tau^2 \tau^A$
(g)	three nucleons vertex eq. (3.24)		$\frac{2H(\Lambda)}{\Lambda^2}$

Coulomb interaction			
(h)	Coulomb propagator eq. (3.43)		$i\Delta_{\text{Coulomb}}(p) = \frac{i}{p^2 + \lambda^2}$
(i)	photon-nucleon vertex		$\pm ie$
(j)	photon-dibaryon vertex		$\pm ie$
Next to leading order			
(k)	NLO spin-triplet Effective range correction eq. (2.65)		$-i\delta^{ij} \frac{4\pi}{My_t^2} \frac{\rho_t}{2} \frac{\mathbf{p}^2/4 - Mp_0 - \gamma_t^2}{\left(\frac{1}{a_t} - \sqrt{-Mp_0 + \frac{\mathbf{p}^2}{4}}\right)^2}$
(l)	NLO spin-singlet Effective range correction eq. (2.66)		$-i\delta^{AB} \frac{4\pi}{My_s^2} \frac{\rho_s}{2} \frac{-Mp_0 + \frac{\mathbf{p}^2}{4}}{\left(\frac{1}{a_s} - \sqrt{-Mp_0 + \frac{\mathbf{p}^2}{4}}\right)^2}$
(m)	NLO Coulomb Effective range correction eq. (2.69)		$-i\delta^{AB} \frac{4\pi}{My_s^2} \frac{\rho_C}{2} \frac{\mathbf{p}^2/4 - Mp - \alpha\mu M}{\left[\frac{1}{a_p} + 2\kappa\Phi(\kappa/p')\right]^2}$
Weak Interaction - LO			
(n)	one-body weak interaction eq. (2.42)		$-i\frac{g_A}{2}\boldsymbol{\sigma}\boldsymbol{\tau}^\pm$
Weak Interaction - NLO			
(o)	$t^\dagger(N^T P_s N)/(N^T P_s N)^\dagger t$ interaction vertex eq. (8.2)		$i \left[ \pi \sqrt{\frac{\rho_t}{2\pi}} \frac{1}{\mu - \frac{1}{a_s}} g_A - L_{1,A} \frac{1}{\sqrt{2\pi\rho_t}} \left( \mu - \frac{1}{a_t} \right) \right] \cdot \left[ \frac{1}{\sqrt{8}} \sigma^2 \tau^2 \tau^A + \frac{1}{\sqrt{8}} (\sigma^2 \tau^2 \tau^A)^\dagger \right]$



(p)	$s^\dagger(N^T P_t N)/(N^T P_t N)^\dagger s$ interaction vertex eq. (8.2)		$i \left[ \pi \sqrt{\frac{\rho_s}{2\pi}} \frac{1}{\mu - \frac{1}{a_t}} g_A - L_{1,A} \frac{1}{\sqrt{2\pi\rho_s}} \left( \mu - \frac{1}{a_s} \right) \right] \cdot$ $\left[ \frac{1}{\sqrt{8}} \sigma^2 \tau^2 \sigma^i + \frac{1}{\sqrt{8}} (\sigma^2 \tau^2 \sigma^i)^\dagger \right].$
(q)	$s^\dagger t/t^\dagger s$ interaction vertex eq. (8.2)		$i \left[ \frac{1}{2} \frac{\rho_t + \rho_s}{\sqrt{\rho_t \rho_s}} g_A - \right.$ $\left. L_{1,A} \frac{1}{2\pi \sqrt{\rho_t \rho_s}} \left( \mu - \frac{1}{a_t} \right) \left( \mu - \frac{1}{a_s} \right) \right]$
Magnetic Interaction - LO			
(r)	one-body magnetic interactions eq. (2.43)		$-i \frac{e}{2M} (\kappa_0 + \kappa_1 \tau^3) \boldsymbol{\sigma}$
Magnetic interactions - NLO, $L_1$			
(s)	$t^\dagger(N^T P_s N)$ interaction vertex eq. (7.2)		$i \left[ \pi \sqrt{\frac{\rho_t}{2\pi}} \frac{1}{\mu - \frac{1}{a_s}} \frac{e}{2M} (2\kappa_1) - \right.$ $\left. - \frac{e L_1}{\sqrt{2\pi\rho_t}} \left( \mu - \frac{1}{a_t} \right) \right] \left[ \frac{1}{\sqrt{8}} \sigma^2 \tau^2 \tau^A \right]$
(t)	$(N^T P_s N)^\dagger t$ interaction vertex eq. (7.2)		$i \left[ \pi \sqrt{\frac{\rho_t}{2\pi}} \frac{1}{\mu - \frac{1}{a_s}} \frac{e}{2M} (2\kappa_1) - \right.$ $\left. \frac{e L_1}{\sqrt{2\pi\rho_t}} \left( \mu - \frac{1}{a_t} \right) \right] \cdot \left[ \frac{1}{\sqrt{8}} (\sigma^2 \tau^2 \tau^A)^\dagger \right]$
(u)	$s^\dagger(N^T P_t N)/(N^T P_t N)^\dagger s$ interaction vertex eq. (7.2)		$i \left[ \pi \sqrt{\frac{\rho_s}{2\pi}} \frac{1}{\mu - \frac{1}{a_t}} \frac{e}{2M} (2\kappa_1) - e L_1 \frac{1}{\sqrt{2\pi\rho_s}} \left( \mu - \frac{1}{a_s} \right) \right] \cdot$ $\left[ \frac{1}{\sqrt{8}} \sigma^2 \sigma^i \tau^A + \frac{1}{\sqrt{8}} (\sigma^2 \tau^2 \sigma^i)^\dagger \right]$
(v)	$s^\dagger t/t^\dagger s$ interaction vertex eq. (7.2)		$i \left[ \frac{1}{2} \frac{\rho_t + \rho_s}{\sqrt{\rho_t \rho_s}} \frac{e}{2M} (2\kappa_1) - \right.$ $\left. - e L_1 \frac{1}{2\pi \sqrt{\rho_t \rho_s}} \left( \mu - \frac{1}{a_t} \right) \left( \mu - \frac{1}{a_s} \right) \right]$
Magnetic interactions - NLO, $L_2$			
(w)	$t^\dagger(N^T P_t N)/(N^T P_t N)^\dagger t$ interaction vertex eq. (7.2)		$i \left[ \pi \sqrt{\frac{\rho_t}{2\pi}} \frac{1}{\mu - \frac{1}{a_t}} \frac{e}{2M} (2\kappa_0) - e L_2 \frac{2}{\sqrt{2\pi\rho_t}} \left( \mu - \frac{1}{a_t} \right) \right] \cdot$ $\left[ \frac{1}{\sqrt{8}} \sigma^2 \tau^2 \sigma^i + \frac{1}{\sqrt{8}} (\sigma^2 \tau^2 \sigma^i)^\dagger \right]$

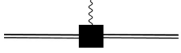
(x)	$t^\dagger t$ interaction vertex eq. (7.2)		$i \left[ \frac{e}{2M} (2\kappa_0) - eL_2 \frac{1}{\pi\rho_t} \left( \mu - \frac{1}{a_t} \right) \left( \mu - \frac{1}{a_s} \right) \right]$
-----	---	---	--

Table 2.2: The Feynman rules for the NLO electro-weak interactions. a: the single nucleon propagator. b-d: the dibaryon propagator. e-f: : the dibaryon- nucleon interaction. g: the three-body force. h-j: the Coulomb interaction. k-m: the ERE correction to the dibaryon propagator. n-q: the weak interaction. r-x: the magnetic interaction. For all Feynman rules, a capital letter indicates the isospin index, while a small letter indicates the spin index.



## Three nucleon system at leading order

In this chapter, we review the derivation of the Faddeev equation for nucleons and its projections on the quantum numbers relevant for  ${}^3\text{H}$  ( $n - d$ ) and  ${}^3\text{He}$  ( $p - d$ ) at LO. The derivation of the Faddeev equations for the three-nucleon has been widely studied in literature during the last twenty years, e.g., Refs. [38–41, 45–47, 70, 71]. In this chapter we redrive the general equations for three-nucleon system. In addition we show a new numerical solution for the unbound  $n - d$  scattering.

### 3.1 n-d scattering and ${}^3\text{H}$ bound-state

In this section, we derive the Faddeev equations for nucleons and their projections on the quantum numbers relevant for the doublet and quartet channels of the  $n - d$  scattering ( ${}^3\text{H}$ ), based on Refs. [39, 45, 47, 71].

This n-d scattering can be divided into two separate channels: the quartet channel in which the nucleon and the dibaryon are summed to total angular momentum  $J = 3/2$  and the doublet channel where the nucleon and the dibaryon are summed to a total angular momentum  $J = 1/2$ , while the doublet channel is a result of both  $n - d$  and  $N - s$  scattering. In the latter, one needs to solve coupled integrals equations for the two scattering matrices.

#### 3.1.1 Quartet channel

In the case of quartet channel, the three nucleons are coupled to a total spin of  $J = 3/2$  and  $T = 1/2$ . Hence the two-nucleon (dibaryon) channel has to be  ${}^3S_1$  (deuteron) only.

The Feynman diagrams leading  $n - d$  scattering integral equation are shown in Fig. 3.1. We use the Feynman rules presented in section 2.7 to write the three-nucleon scattering

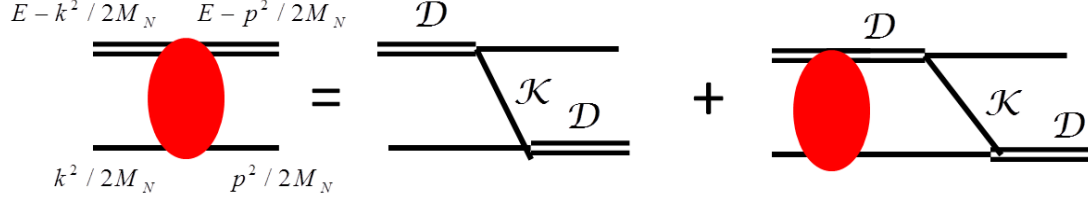


Figure 3.1: Integral equation for the strong scattering matrix  $T$  (red bubble), where  $\mathcal{D}$  is the dibaryon propagator and  $\mathcal{K}$  is the one-nucleon exchange propagator.

matrix,  $T$  (see Appendix A and Ref. [39, 45, 61, 71]):

$$(iT(E; \mathbf{p}, \mathbf{k})^{ij})_{\beta b}^{\alpha a} = -\frac{iMy_t^2}{2} (\sigma^j \sigma^i)_{\beta}^{\alpha} \delta_b^a \cdot \frac{1}{\mathbf{k}^2 + \mathbf{p}^2 - \mathbf{k} \cdot \mathbf{p} - ME} + \int \frac{d^4 q}{(2\pi)^4} \frac{My_t^2}{2} i\mathcal{D}_t(p_0, \mathbf{p}') i \left( T(E; \mathbf{p}, \mathbf{p}')^{kj} \right)_{\beta b}^{\gamma a} \cdot \frac{(\sigma^i \sigma^k)_{\gamma}^{\alpha} \delta_b^a}{\mathbf{p}'^2 + \mathbf{p}^2 - \mathbf{p}' \cdot \mathbf{p} - ME}, \quad (3.1)$$

where  $\alpha, \beta, \gamma$  indicate the elements in the  $\sigma$ 's matrices, while  $a, b$  indicate the elements in the  $\tau$ 's matrices.  $\delta_b^a$  is the Kronecker delta.  $\mathcal{D}_t$  and  $y_t$  are the dibaryon propagator and coupling constant, respectively and  $E$  is the three-nucleon energy.

Using the projection equation, one finds that:

$$iT(E; \mathbf{p}, \mathbf{k})_{\beta b}^{\alpha a} = \frac{1}{3} (\sigma^i)_{\alpha'}^{\alpha} i(T(E; \mathbf{p}, \mathbf{k})^{ij})_{\beta' b}^{\alpha' a} (\sigma^j)_{\beta}^{\beta'} \quad (3.2)$$

and for  $a = b = 1$ ,  $\alpha = \beta$ , eq. (3.2) becomes:

$$T(E, k, p) = -2My_t^2 K_0(k, p, E) + 2My_t^2 \int D_t(E, p') T(E, k, p') K_0(p', p, E) \frac{p'^2}{2\pi^2} dp', \quad (3.3)$$

where the one nucleon exchange propagator is defined as:

$$K_0(k, p, E) = \frac{1}{2pk} Q_0 \left( \frac{p^2 + k^2 - ME}{pk} \right), \quad (3.4)$$

$$Q_0(a) = \frac{1}{2} \int_{-1}^1 \frac{1}{x + a} dx \quad (3.5)$$

and

$$D_t(E, p) = \mathcal{D}_t \left( E - \frac{p^2}{2M}, \mathbf{p} \right) . \quad (3.6)$$

Equation (3.3) can be written in the following form:

$$T(E, k, p) = -2My_t^2 K_0(k, p, E) + 2T(E, k, p') \otimes K_0^S(p', p, E), \quad (3.7)$$

where

$$K_0^S(p', p, E) = My_t^2 K_0(p', p, E) \cdot D_t(E, p') \quad (3.8)$$

and

$$A(..., p) \otimes B(p, ...) = \int A(..., p) B(p, ...) \frac{p^2}{2\pi^2} dp. \quad (3.9)$$

### 3.1.2 Doublet channel

In contrast to the quartet channel, in the doublet channel the spins of the nucleon and the deuteron are coupled to a total spin of 1/2. The spin-singlet dibaryon can now appear in the intermediate state, which leads to two coupled amplitudes that differ in the type of the outgoing dibaryon as shown in Fig. 3.2. For the  $n-d$  scattering we set:  $a_{nn} = a_{np} = a_s$  and  $S_{np} = S_{nn} = S$ .

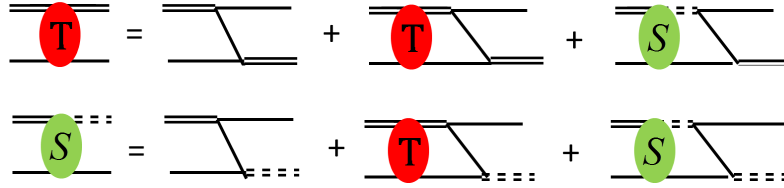


Figure 3.2:  $n-d$  scattering equations. The double lines are the propagators of the dibaryon fields  $D_t$  (solid) and  $D_s$  (dashed). The red bubbles (T) represent the triplet channel  $T=0, S=1$ , while the green bubbles (S) represent the singlet channel  $T=1, S=0$ .

The two coupled Faddeev integral equations for  $n-d$  scattering in the doublet channel are (see [39, 45, 47, 71] and Appendix A):

$$T(E, k, p) = My_t^2 K_0(k, p, E) - My_t^2 \int D_t(E, p') T(E, k, p') K_0(p', p, E) \frac{p'^2}{2\pi^2} dp' + \\ 3My_t y_s \int D_s(E, p') S(E, k, p') K_0(p', p, E) \frac{p'^2}{2\pi^2} dp' , \quad (3.10)$$

$$\begin{aligned}
 S(E, k, p) = & -3My_t y_s K_0 - My_s^2 \int D_s(E, p') S(E, k, p') K_0(p', p, E) \frac{p'^2}{2\pi^2} dp' + \\
 & 3My_s y_t \int D_t(E, p') T(E, k, p') K_0(p', p, E) \frac{p'^2}{2\pi^2} dp' . \quad (3.11)
 \end{aligned}$$

Equations (3.10) and (3.11) can be written in matrix form:

$$t^{nd}(E, k, p) = B_0(E, k, p) + t^{nd}(E, k, p') \otimes \hat{K}(p', p, E) , \quad (3.12)$$

where for n-d scattering:

$$t^{nd}(E, k, p) = \begin{pmatrix} T(E, k, p) \\ S(E, k, p) \end{pmatrix} , \quad (3.13)$$

the inhomogeneous part of the integral equation is given by:

$$B_0^{nd}(E, k, p) = K_0(k, p, E) \cdot \begin{pmatrix} My_t^2 \\ -3y_t y_s \end{pmatrix} \quad (3.14)$$

and the kernel is,

$$\hat{K}^{nd}(p', p, E) = K_0(p', p, E) \cdot \begin{pmatrix} -My_t^2 & 3My_t y_s \\ 3My_t y_s & -My_s^2 \end{pmatrix} \cdot \begin{pmatrix} D_t(E, p') \\ D_s(E, p') \end{pmatrix} . \quad (3.15)$$

### The Faddeev equation for the bound-state

The above sections describe the Faddeev equation for the three-nucleon system at an arbitrary energy. For energies close to the three-nucleon binding energy, *i.e.*, when  $E \sim E_B$ , the scattering amplitude takes the form

$$t(E, k, p) = \frac{\mathcal{B}^\dagger(k) \mathcal{B}(p)}{E - E_B} + \mathcal{R}(E, k, p) , \quad (3.16)$$

where the  $\mathcal{B}(E, k)$  are what we call *amputated* wave functions or vertex factors, whereas the  $\mathcal{R}(E, k, p)$  are terms that are regular at  $E = E_B$ , and thus can be neglected for

$E \rightarrow E_B$ <sup>1</sup>. By substituting eq. (3.16) into eq. (3.12), eq. (3.12) becomes

$$\mathcal{B}^{3\text{H}}(p) = \mathcal{B}^{3\text{H}}(p') \otimes \hat{K}^{3\text{H}}(p', p, E_{3\text{H}}), \quad (3.17)$$

where  $\hat{K}^{3\text{H}}(p', p, E_{3\text{H}}) = \hat{K}^{nd}(p', p, E_{3\text{H}})$ , *i.e.*, the homogeneous integral equation has the form of the non-relativistic Bethe-Salpeter equation [72, 73], with  $E_{3\text{H}}$ , the triton binding energy.

Specifically, for the case of the  ${}^3\text{H}$  bound-state, we express the amplitude as

$$\mathcal{B}^{3\text{H}}(p) = \begin{pmatrix} \Gamma_t^{3\text{H}}(p) \\ \Gamma_s^{3\text{H}}(p) \end{pmatrix}, \quad (3.18)$$

where  $\Gamma_t, \Gamma_s$  denote the two bound-state amplitudes that have a spin-triplet or spin-singlet dibaryon, respectively.

For the triton, one needs to solve the integral equation:

$$\begin{pmatrix} \Gamma_t^{3\text{H}}(p) \\ \Gamma_s^{3\text{H}}(p) \end{pmatrix} = K_0(p', p, E_{3\text{H}}) \begin{pmatrix} -My_t^2 D_t(E_{3\text{H}}, p') & 3My_t y_s D_s(E_{3\text{H}}, p') \\ 3My_t y_s D_t(E_{3\text{H}}, p') & -My_s^2 D_s(E_{3\text{H}}, p') \end{pmatrix} \otimes \begin{pmatrix} \Gamma_t^{3\text{H}}(p') \\ \Gamma_s^{3\text{H}}(p') \end{pmatrix}, \quad (3.19)$$

which can be written in compact form:

$$\Gamma_\mu^{3\text{H}}(p) = \sum_{\nu=t,s} My_\mu y_\nu a_{\mu\nu} K_0(p', p, E_{3\text{H}}) \otimes \left[ D_\nu(E_{3\text{H}}, p') \Gamma_\nu^{3\text{H}}(p') \right], \quad (3.20)$$

where  $\mu = t, s$  are the different triton channels and  $y_{\mu,\nu}$  are the nucleon-dibaryon coupling constants for the different channels. The  $a_{\mu\nu}$  and  $b_{\mu\nu}$  are a result of  $n-d$  doublet-channel

---

<sup>1</sup>Similar to the practice commonly used in the literature (see, for example, Refs. [44, 46]), we have neglected the contribution of a regular part for the scattering amplitude normalization for  $E \rightarrow E_B$ . The question of whether these parts might contribute to the three-nucleon amplitude was discussed in private conversation with Prof. Daniel Phillips of Ohio University and deserves a separate discussion, which is beyond the scope of the current work.



projection ( [71]), for example:

$$a_{tt} = \frac{4}{3} \left[ (\sigma^i)_\beta^\alpha (P_t^i)_{\gamma\delta}^\dagger (P_t^j)^{\delta\beta} (\sigma^j)_\chi^\gamma \right] = -1 \quad (3.21a)$$

$$a_{ts} = \frac{4}{3} \left[ (\sigma^i)_\beta^\alpha ((P_t^i)^\dagger)_{\gamma\delta}^{ab} (P_s^A)^{\delta\beta}_{bc} (\tau^A)_{da} \right]_{c,d=2} = 3 \quad (3.21b)$$

$$a_{st} = \frac{4}{3} \left[ (\tau^A)^{ab} ((P_t^A)^\dagger)_{\beta\alpha}^{dc} (P_t^i)_{bc}^{\chi\beta} (\sigma^i)_\alpha^\delta \right]_{a=d=2} = 3 \quad (3.21c)$$

$$a_{ss} = \frac{4}{3} \left[ (\tau^A)^{ab} (P_t^i)_{cd}^\dagger (P_t^B)^{db} (\tau^B)^{ec} \right]_{a=e=2} = -1, \quad (3.21d)$$

where  $i, j$  are the different spin projections and  $A, B$  are the isospin projections, the same as those in eq. (2.58).

All three-body equations in this work can be solved numerically only. We replace each integral by a sum of weighted functions on the interval  $[0, \Lambda]$  which is divided into  $n$  segments using Gaussian quadrature [74]:

$$\int_0^\Lambda f(x) dx = \sum_{i=1}^n w_i f(x_i), \quad (3.22)$$

where  $w_i$  are the weights. The three-body bound-state eq. (3.20) is then the solution of the homogeneous parts of Faddeev equations [72, 73], which can be solved as a coupled eigenvalue problem.

### 3.1.3 The three-body force

$\not{A}$ EFT is renormalizable, *i.e.*, the theory has no dependence on the ultraviolet cutoff ( $\Lambda$ ). In principle, the loop integration over all possible momenta should not be affected by the upper bound of the integral,  $\Lambda$ . However, a numerical solution of the integral equations reveals a strong dependence on  $\Lambda$ . In order to find the energy for each cutoff, we find the value of  $E$  for which:

$$\Gamma_\mu(p) = \sum_{\nu=t,s} M y_\mu y_\nu a_{\mu\nu} K_0(p', p, E) \otimes [D_\nu(E, p') \Gamma_\nu(p')] . \quad (3.23)$$

Figure. 3.3 shows that the  $^3\text{H}$  binding energy which solves eq. (3.20) has a strong cutoff dependency. To overcome this problem, one adds a three-body force counterterm to the

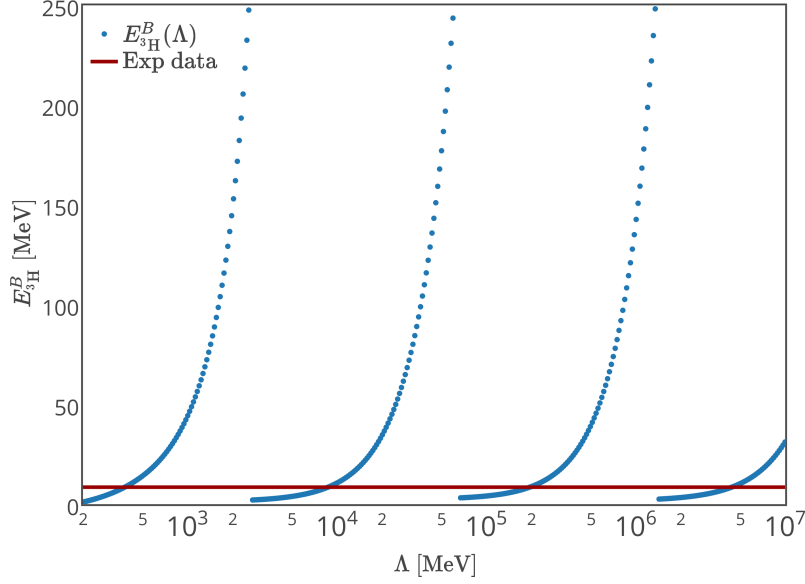


Figure 3.3: The binding energy which solves eq. (3.20) as a function of cutoff ( $\Lambda$ ) (dots). The solid line is the experimental value of triton binding energy - 8.48 MeV.

exchange nucleon propagator  $K_0(k, p, E)$  [38]:

$$K_0(k, p, E) \rightarrow K_0(k, p, E) + \frac{H(\Lambda)}{\Lambda^2}. \quad (3.24)$$

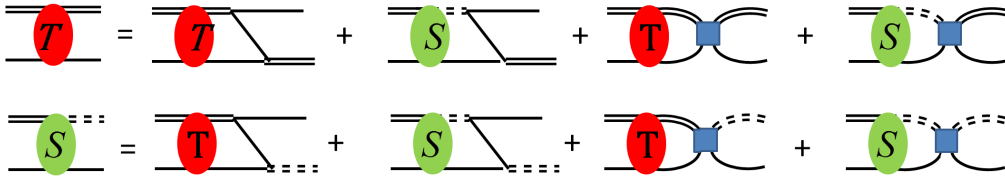


Figure 3.4: The triton scattering equations with a three-body force. The double lines are the propagators of the dibaryon fields  $D_t$  (solid) and  $D_s$  (dashed). The red bubbles (T) represent the triplet channel  $T=0, S=1$ , while the green bubbles (S) represent the singlet channel  $T=1, S=0$ . The blue squares are the three-body force

Formally, this three-body force term is obtained by adding [39]

$$\mathcal{L}_3 = M \frac{H(\Lambda)}{3\Lambda^2} \left\{ y_t^2 N^\dagger (\vec{t} \cdot \vec{\sigma})^\dagger (\vec{t} \cdot \vec{\sigma}) N + y_s^2 N^\dagger (\vec{s} \cdot \vec{\tau})^\dagger (\vec{s} \cdot \vec{\tau}) N - y_t y_s \left[ N^\dagger (\vec{t} \cdot \vec{\sigma})^\dagger (\vec{s} \cdot \vec{\tau}) N + h.c. \right] \right\}, \quad (3.25)$$

to the Lagrangian (eq. (2.58)).

To find  $H(\Lambda)$ , we solve the homogeneous equation (eq. (3.20)) numerically and use the known binding energy of triton  $-E_{3\text{H}} = -8.48$  MeV to remove the  $\Lambda$  dependence of  $-E_{3\text{H}}$ . For each cutoff we find the appropriate value of  $H(\Lambda)$  for which:

$$\Gamma_{\mu}^{3\text{He}}(p) = \sum_{\nu=t,s} M y_{\mu} y_{\nu} \left[ a_{\mu\nu} K_0(p', p, E_{3\text{H}}) + b_{\mu\nu} \frac{H(\Lambda)}{\Lambda^2} \right] \otimes \left[ D_{\nu}(E_{3\text{H}}, p') \Gamma_{\nu}^{3\text{H}}(p') \right], \Gamma_{\nu}^{3\text{He}}(E_{3\text{He}}, p') \quad (3.26)$$

where  $b_{tt} = b_{ss} = -1$  and  $b_{ts} = b_{st} = 1$ .

Equation (3.26) can be treated as a coupled eigenvectors equation, where for each  $\Lambda$  we find  $H(\Lambda)$  that solves eq. (3.26) numerically. The comparison between our numerical calculations of  $H(\Lambda)$  and the analytic result introduced in Refs. [38, 39],

$$H(\Lambda) = \frac{\sin \left[ s_0 \log \left( \frac{\Lambda}{\Lambda^*} \right) + \arctan \left( \frac{1}{s_0} \right) \right]}{\sin \left[ s_0 \log \left( \frac{\Lambda}{\Lambda^*} \right) - \arctan \left( \frac{1}{s_0} \right) \right]}, \quad (3.27)$$

with  $s_0 = 1.00624$  and  $\Lambda^* = 1.55$  MeV multiplied by  $c(\Lambda) = 0.879$  [75], is shown in Fig. 3.5. Our numerical results are in a good agreement with the analytical value.

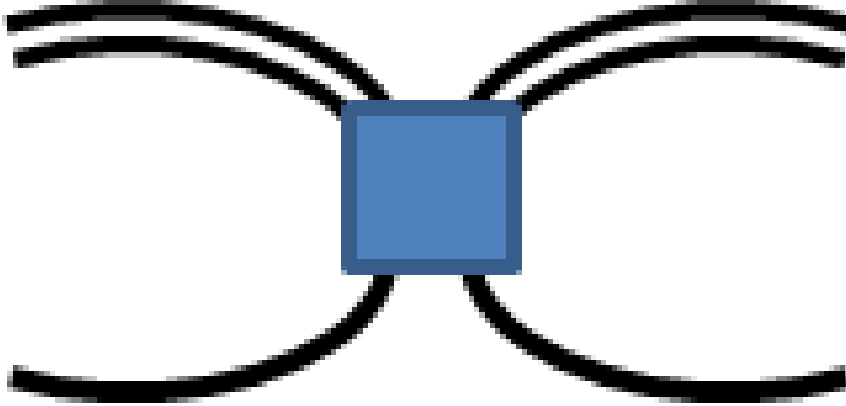


Figure 3.5: Values of the three-body force  $H(\Lambda)$  as a function of the cutoff  $\Lambda$  for  ${}^3\text{H}$ . The dots show our numerical results for  $H(\Lambda)$  and the solid line is the analytical result.

### 3.1.4 The n-d scattering with $E > 0$

In the case of the doublet channel, the spins of the nucleon and the deuteron are coupled to total spin of  $J = 1/2, T = 1/2$ . The spin-singlet dibaryon can now appear in the intermediate state, which leads to two coupled amplitudes that differ from each other in the type of the outgoing dibaryon as shown in Fig. 3.6. In the case of the unbound  $n - d$  scattering the three nucleons can be in both  $n - d$  and  $N - s$  ( $n - S_{np}$  states,  $p - S_{nn}$ ), and we set:  $a_{nn} = a_{np} = a_s$  and  $S_{np} = S_{nn} = S$ .

Fig. 3.6 shows a diagrammatic representation of the coupled-channel integral equations for the scattering amplitudes  $T, S', S$  and  $S^\dagger$  (which is the conjugate transpose of  $S$ ) in the doublet channel for the case that  $E > 0$  in which eq. (3.16) is not valid.

The full Faddeev equations for  $^3\text{H}$  can be written as (see Appendix A and Ref. [71]):

$$\overleftrightarrow{T}(E, k, p) = B_0 + K_0^S(E, p', p) \otimes \overleftrightarrow{T}(E, k, p), \quad (3.28)$$

where

$$\overleftrightarrow{T}(E, k, p) = \begin{pmatrix} T(E, k, p) & S^\dagger(E, k, p) \\ S(E, k, p) & S'(E, k, p) \end{pmatrix}, \quad (3.29)$$

$$B_0 = M \begin{pmatrix} y_t^2 \left[ K_0(p, k, E) + \frac{H(\Lambda)}{\Lambda^2} \right] & -y_t y_s \left[ 3K_0(p, k, E) + \frac{H(\Lambda)}{\Lambda^2} \right] \\ -y_t y_s \left[ 3K_0(p, k, E) + \frac{H(\Lambda)}{\Lambda^2} \right] & y_s^2 \left[ K_0(p, k, E) + \frac{H(\Lambda)}{\Lambda^2} \right] \end{pmatrix} \quad (3.30)$$

and

$$\begin{aligned} K_0^S(p, k, E) = & MK_0(p, k, E) \cdot \begin{pmatrix} -y_t^2 \cdot D_t(E, p) & 3y_t y_s \cdot D_s(E, p) \\ 3y_t y_s \cdot D_t(E, p) & -y_s^2 \cdot D_s(E, p) \end{pmatrix} + \\ & M \frac{H(\Lambda)}{\Lambda^2} \begin{pmatrix} -y_t^2 \cdot D_t(E, p) & y_t y_s \cdot D_s(E, p) \\ y_t y_s \cdot D_t(E, p) & -y_s^2 \cdot D_s(E, p) \end{pmatrix}. \end{aligned} \quad (3.31)$$

Fig. 3.6 shows that both  $T(E, k, p)$  and  $S'(E, k, p)$  are symmetric while  $S(E, k, p)$  and  $S^\dagger(E, k, p)$  are not symmetric. However, since the off diagonal terms of  $\overleftrightarrow{T}(E, k, p)$  are the transpose of each other, the overall matrix,  $\overleftrightarrow{T}(E, k, p)$ , is symmetric.

In the case of the inhomogeneous scattering amplitude, eq. (3.28) can be solved as a

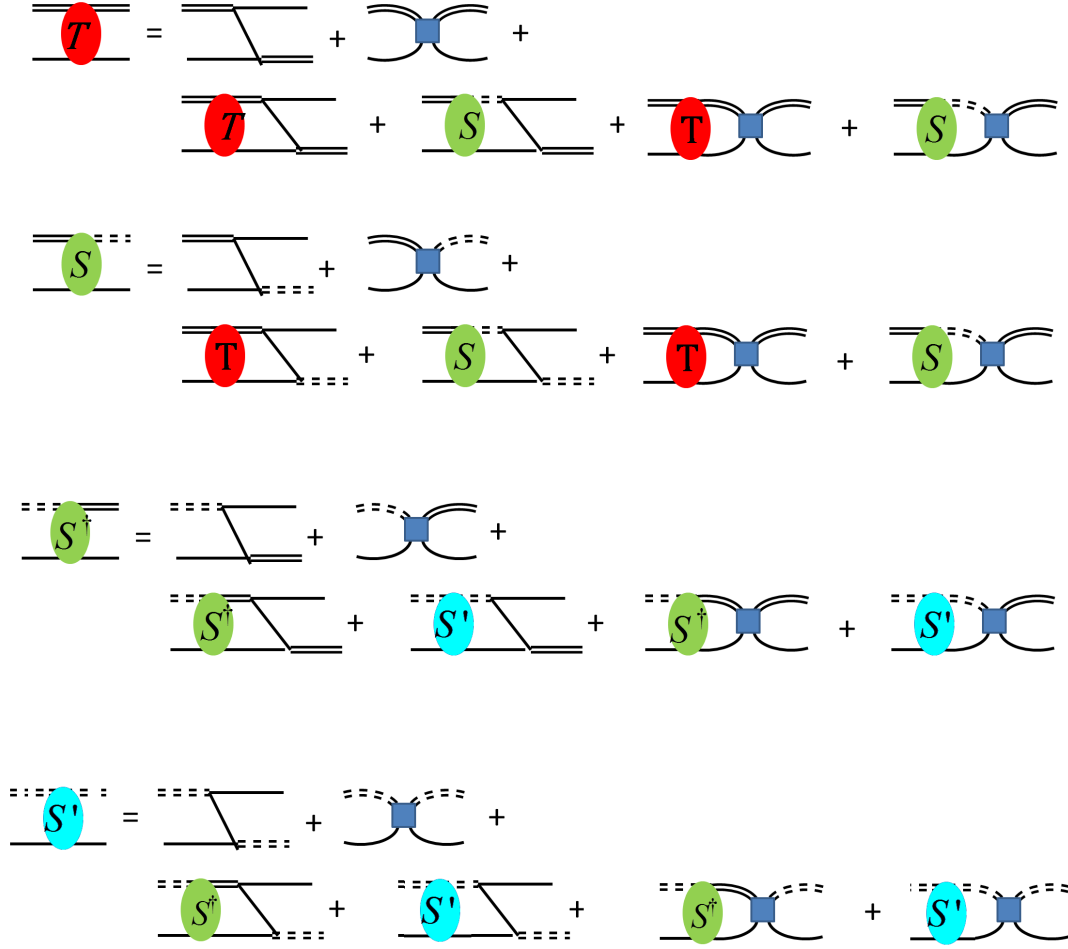


Figure 3.6: The full scattering equations for triton with a three-body force. The double lines are the propagators of the dibaryon fields  $D_t$  (solid) and  $D_s$  (dashed). The red bubbles (T) represent the triplet channel  $T=0$ ,  $S=1$ , the green bubbles ( $S, S^\dagger$ ) represent the singlet channel  $T=1$ ,  $S=0$  while the cyan bubbles ( $S'$ ) represent the singlet channel  $T=1$ ,  $S=0$ . The blue squares are the three-body force.

linear equation, where for each  $k_i$ :

$$\begin{pmatrix} T(E, k_i, p) \\ S(E, k_i, p) \\ S^\dagger(E, k_i, p) \\ S'(E, k_i, p) \end{pmatrix} = \begin{pmatrix} v_1(E, k_i, p) \\ v_3(E, k_i, p) \\ v_2(E, k_i, p) \\ v_4(E, k_i, p) \end{pmatrix} + \begin{pmatrix} M_1(E, p', p) & M_2(E, p', p) & 0 & 0 \\ M_3(E, p', p) & M_4(E, p', p) & 0 & 0 \\ 0 & 0 & M_1(E, p', p) & M_2(E, p', p) \\ 0 & 0 & M_3(E, p', p) & M_4(E, p', p) \end{pmatrix} \otimes \begin{pmatrix} T(E, k_i, p) \\ S(E, k_i, p) \\ S^\dagger(E, k_i, p) \\ S'(E, k_i, p) \end{pmatrix}, \quad (3.32)$$

where

$$M_1(E, p', p) = -\frac{My_t^2}{2} \left[ \frac{1}{pp'} Q_0 \left( \frac{p^2 + p'^2 - ME}{pp'} \right) + \frac{2H(\Lambda)}{\Lambda^2} \right] D_t(E, p) \frac{p'^2}{2\pi^2} \quad (3.33)$$

$$M_2(E, p', p) = \frac{My_t y_s}{2} \left[ \frac{3}{pp'} Q_0 \left( \frac{p^2 + p'^2 - ME}{pp'} \right) + \frac{2H(\Lambda)}{\Lambda^2} \right] D_s(E, p) \frac{p'^2}{2\pi^2} \quad (3.34)$$

$$M_3(E, p', p) = \frac{My_t y_s}{2} \left[ \frac{3}{pp'} Q_0 \left( \frac{p^2 + p'^2 - ME}{pp'} \right) + \frac{2H(\Lambda)}{\Lambda^2} \right] D_t(E, p) \frac{p'^2}{2\pi^2} \quad (3.35)$$

$$M_4(E, p', p) = -\frac{My_s^2}{2} \left[ \frac{1}{pp'} Q_0 \left( \frac{p^2 + p'^2 - ME}{pp'} \right) + \frac{2H(\Lambda)}{\Lambda^2} \right] D_s(E, p) \frac{p'^2}{2\pi^2} \quad (3.36)$$

and

$$v_1(E, k_i, p) = \frac{My_t^2}{2} \left[ \frac{1}{k_i p} Q_0 \left( \frac{p^2 + k_i^2 - ME}{k_i p} \right) + \frac{2H(\Lambda)}{\Lambda^2} \right] \quad (3.37)$$

$$v_2(E, k_i, p) = -\frac{My_t y_s}{2} \left[ \frac{3}{k_i p} Q_0 \left( \frac{p^2 + k_i^2 - ME}{k_i p} \right) + \frac{2H(\Lambda)}{\Lambda^2} \right] \quad (3.38)$$

$$v_3(E, k_i, p) = -\frac{My_t y_s}{2} \left[ \frac{3}{k_i p} Q_0 \left( \frac{p^2 + k_i^2 - ME}{k_i p} \right) + \frac{2H(\Lambda)}{\Lambda^2} \right] \quad (3.39)$$

$$v_4(E, k_i, p) = \frac{My_s^2}{2} \left[ \frac{1}{k_i p} Q_0 \left( \frac{p^2 + k_i^2 - ME}{k_i p} \right) + \frac{2H(\Lambda)}{\Lambda^2} \right], \quad (3.40)$$

and the experimental input parameters used for the numerical calculation, are taken from Tab. 2.1.

The linear solution of eq. (3.32) assumes nothing about the symmetry of the matrices  $T, S, S^\dagger$  and  $S'$  for all  $k$  and  $p$  a-priori. In order to verify our calculation, we define a new parameter  $\alpha$ , which enables us to estimate the symmetry of a general matrix  $\overleftrightarrow{M}$ :

$$\alpha^{\overleftrightarrow{M}}(E) = \sum_k \sum_p \left| \frac{\overleftrightarrow{M}(E, k, p) - \overleftrightarrow{M}^\dagger(E, k, p)}{\overleftrightarrow{M}(E, k, p)} \right| \quad (3.41)$$

where  $\alpha = 0$  implies that the matrix is symmetric. Fig. 3.7 shows the symmetry parameter  $\alpha$  for all relevant matrices ( $T, S, S^\dagger, S'$ ) as a function of the cutoff  $\Lambda$ , for two values of energy. For both energies,  $\alpha^T$  and  $\alpha^{S'}$  are smaller than  $10^{-13}$ , while  $\alpha^S, \alpha^{S^\dagger} \sim 1$ . However, the difference between  $S$  and  $(S^\dagger)^\dagger$ ,  $\sum_k \sum_p \left| \frac{\overleftrightarrow{S}(E, k, p) - (\overleftrightarrow{S}^\dagger)^\dagger(E, k, p)}{\overleftrightarrow{S}(E, k, p)} \right|$  is smaller than  $10^{-13}$ , so we conclude that our calculations are accurate also for the unbound case.

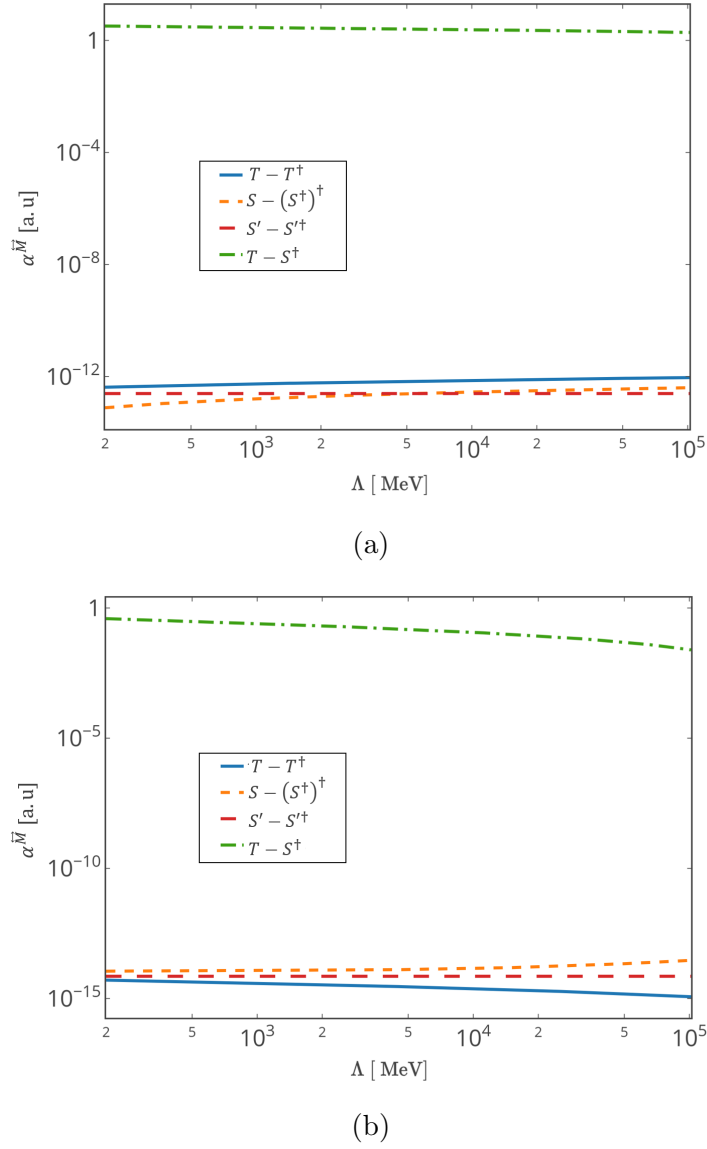


Figure 3.7: The symmetry parameter  $\alpha$  as a function of  $\Lambda$  for  $E = 0$  MeV (a) and  $E = 8.48$  MeV (b). In both panels the solid line is  $\alpha^{\overleftrightarrow{T}}$ , the long dashed-dotted line is  $\alpha^{\overleftrightarrow{S}}$  and the short dashed-dotted line is  $\alpha^{\overleftrightarrow{S'}}$ . In addition we plotted the difference between  $\overleftrightarrow{S}$  and  $(\overleftrightarrow{S^\dagger})^\dagger$  which is assumed to be zero (dashed line).

### 3.2 $p - d$ scattering and ${}^3\text{He}$ bound-state

In this section, we rederive the Faddeev equations for the bound-state  $p - d$  scattering ( ${}^3\text{He}$ ) for the doublet channel, based on Ref. [41, 43, 45–47, 76]. Similarly to the  $n - d$  scattering, the quartet channel, which is of higher orders, is not relevant for this work.

$^3\text{He}$ , contains one neutron and two protons, so the Coulomb interaction should be taken into account for accurately describing this system. The photon Lagrangian of the Coulomb interaction retains only contributions from the Coulomb photon that generate a static Coulomb potential between two charged particles, defined as :

$$\mathcal{L}_{\text{photon}} = -\frac{1}{4}F^{\mu\nu}F_{\mu\nu} - \frac{1}{\xi}(\partial_\mu A^\mu - \eta_\mu \eta_\nu \partial^\nu A^\mu)^2, \quad (3.42)$$

where  $F^{\mu\nu}$  is the electromagnetic tensor,  $A^\mu$  is the electromagnetic four-potential,  $\eta^\mu = (1, 0)$  is the unit timelike vector and the parameter  $\xi$  determines the choice of gauge. For convenience, we introduce the Feynman rule corresponding to the Coulomb photon propagator:

$$i\mathcal{D}_{\text{photon}}(\mathbf{k}) = \frac{i}{\mathbf{k}^2 + \lambda^2}, \quad (3.43)$$

where  $\lambda$  is an artificial small photon mass, added to regulate the singularity of the propagator when the momentum transfer vanishes [45].

Naïvely, proton-deuteron ( $p-d$ ) scattering should contain an infinite sum of photon exchanges [41]. The typical momentum scale for the  $^3\text{He}$  bound-state is  $Q \geq \sqrt{-2ME_{^3\text{He}}^B}/A$  and the Coulomb parameter  $\eta$  [59] is defined as:

$$\eta(Q) = \frac{\alpha M}{2Q}. \quad (3.44)$$

Therefore, for  $^3\text{He}$ , since  $E_{^3\text{H}}^B = -7.72 \text{ MeV}$ ,  $Q \simeq 70 \text{ MeV}$  and  $\eta(Q) \ll 1$ , the Coulomb interaction can be treated as only one-photon exchange diagrams. The Coulomb diagrams that contribute to  $p-d$  scattering are shown in Fig. 3.8, while the fine-structure constant  $\alpha \sim 1/137$  can be used as an additional expansion parameter.

The power-counting for the diagrams shown in Fig. 3.8 was discussed in Refs. [40, 46] whereas in Ref. [47] it was shown that diagram (e) is of a higher order than diagrams (a)-(d), and need not be taken into account at NLO.

Based on Chapter 2, we find that:

- Every nucleon-dibaryon vertex gives a factor of  $y_{t,s} = \frac{\Lambda_{\text{cut}}^{1/2}}{M}$
- Every nucleon-photon vertex gives a factor of  $\pm ie$
- Every  $q_0$  integral gives a factor of  $\frac{Q^2}{4\pi M}$
- Every  $q^2 dq$  integral gives a factor of  $Q^3$



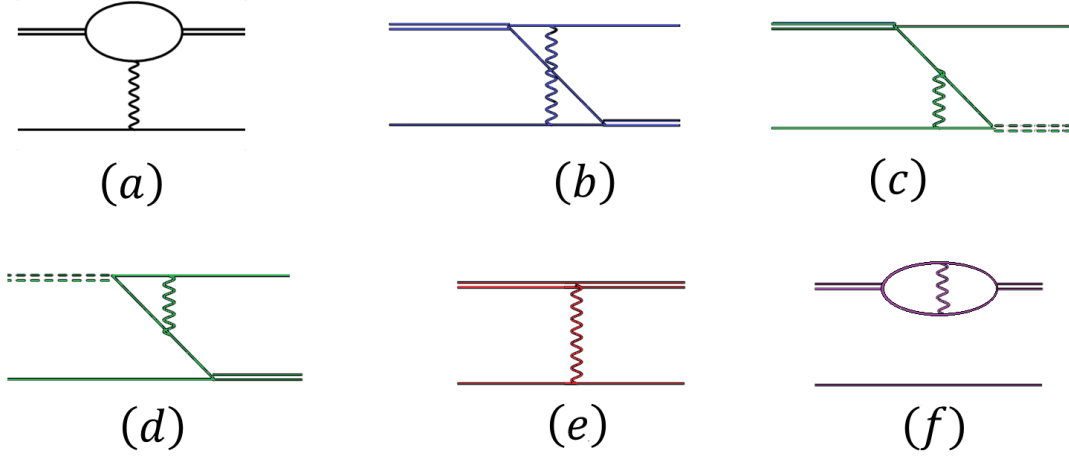


Figure 3.8: The possible one-photon exchange diagrams.

- Every photon propagator gives a factor of  $\frac{1}{Q^2}$
- Every nucleon propagator gives a factor of  $\frac{M}{Q^2}$ ,

therefore, we find that the power-counting for diagram (a) is:

$$\mathcal{O}(a) = \frac{\Lambda_{\text{cut}}}{M^2} \times \frac{\alpha}{Q^2} \times \left(\frac{M}{Q^2}\right)^3 \times Q^3 \times \frac{Q^2}{4\pi M} = \frac{\alpha}{Q^2} \times \frac{\Lambda_{\text{cut}}}{Q}, \quad (3.45)$$

similarly, we find that the power-counting for diagrams (b-c) is:

$$\mathcal{O}(b-d) = \frac{\Lambda_{\text{cut}}}{M^2} \times \frac{\alpha}{Q^2} \times \left(\frac{M}{Q^2}\right)^3 \times Q^3 \times \frac{Q^2}{4\pi M} = \frac{\alpha}{Q^2} \times \frac{\Lambda_{\text{cut}}}{Q}, \quad (3.46)$$

and the power-counting for diagrams (e) is:

$$\mathcal{O}(e) = \frac{\alpha}{Q^2} = \mathcal{O}(a-d) \times \frac{Q}{\Lambda_{\text{cut}}}. \quad (3.47)$$

Diagram (f) is the contribution from the non-perturbative proton-proton propagator, which affects the  ${}^3\text{H}$ - ${}^3\text{He}$  binding energy difference, as discussed in detail in [47], and will be shown later.

### 3.2.1 The doublet channel

The doublet channel in  $p-d$  scattering contains three coupled amplitudes as shown in Fig. 3.9. In contrast to the triton, for the  $p-d$  scattering the spin-singlet dibaryon has

two distinct isospin projections, *i.e.*, the  $np$  and  $pp$  spin-singlet states [45]. The Faddeev equations for  $p - d$  scattering, at LO, can be written as:

$$t^{pd}(E, k, p) = B_0^{pd}(E, k, p) + t^{pd}(E, k, p') \otimes [\hat{K}^{pd}(p', p, E) + \hat{K}_0^C(p', p, E)], \quad (3.48)$$

where the three individual components of the amplitude  $t$  are

$$t^{pd}(E, k, p) = \begin{pmatrix} T(E, k, p) \\ S(E, k, p) \\ P(E, k, p) \end{pmatrix}, \quad (3.49)$$

and:

$$B_0^{pd}(E, k, p) = \left[ K_0(k, p, E) + \frac{H}{\Lambda^2} \right] \cdot \begin{pmatrix} My_t^2 \\ -y_t y_s \\ -2y_t y_s \end{pmatrix} + \begin{pmatrix} My_t^2 [K_C^a(k, p, E) + K_C^b(k, p, E)] \\ -My_t y_s K_C^c(k, p, E) \\ -2My_t y_s K_C^b(k, p, E) \end{pmatrix}, \quad (3.50)$$

$$\begin{aligned} \hat{K}^{pd}(p', p, E) &= MK_0(p', p, E) \begin{pmatrix} -y_t^2 \cdot D_t(E, p') & 3y_t y_s \cdot D_s(E, p') & 3y_t y_s \cdot D_{pp}(E, p') \\ y_t y_s \cdot D_t(E, p') & y_s^2 \cdot D_s(E, p') & -y_s^2 \cdot D_{pp}(E, p') \\ 2y_t y_s \cdot D_t(E, p') & -2y_s^2 \cdot D_s(E, p') & 0 \end{pmatrix} + \\ &M \frac{H(\Lambda)}{\Lambda^2} \begin{pmatrix} -y_t^2 \cdot D_t(E, p') & y_t y_s \cdot D_s(E, p') & y_t y_s \cdot D_{pp}(E, p') \\ \frac{1}{3} y_t y_s \cdot D_t(E, p') & -\frac{1}{3} y_s^2 \cdot D_s(E, p') & -\frac{1}{3} y_s^2 \cdot D_{pp}(E, p') \\ \frac{2}{3} y_t y_s \cdot D_t(E, p') & -\frac{2}{3} y_s^2 \cdot D_s(E, p') & -\frac{2}{3} y_s^2 \cdot D_{pp}(E, p') \end{pmatrix}, \end{aligned} \quad (3.51)$$

and

$$\hat{K}_0^C(p', p, E) = MK^C(p', p, E) \cdot \begin{pmatrix} -y_t^2 D_t(E, p') & 3y_t y_s D_s(E, p') & 3y_t y_s D_{pp}(E, p') \\ y_t y_s D_t(E, p') & y_s^2 D_s(E, p') & -y_s^2 D_{pp}(E, p') \\ 2y_t y_s D_t(E, p') & -2y_s^2 D_s(E, p') & 0 \end{pmatrix}, \quad (3.52)$$

where

$$K^C(p', p, E) = \begin{pmatrix} K_C^a(p', p, E) + K_C^b(p', p, E) & K_C^b(p', p, E) & K_C^c(p', p, E) \\ K_C^b(p', p, E) & -K_C^a(p', p, E) + K_C^b(p', p, E) & K_C^c(p', p, E) \\ K_C^d(p', p, E) & K_C^d(p', p, E) & 0 \end{pmatrix} \quad (3.53)$$

and where:

$$D_{pp}(E, p) = \mathcal{D}_{pp} \left( E - \frac{p^2}{2M}, \mathbf{p} \right) \quad (3.54)$$

is the Coulomb propagator [32, 59].

The different one-photon exchange diagrams contributing to the Coulomb interaction (obtained by integrating eq. (3.42) multiplied by eq. (3.4)) are:

$$K_C^a(p', p, E) = \frac{M\alpha}{2p'p} Q_0 \left( -\frac{p'^2 + p^2 + \lambda^2}{2p'p} \right) \cdot \left[ \frac{\arctan \left( \frac{p'+2p}{\sqrt{3p'^2-4ME}} \right) - \arctan \left( \frac{2p'+p}{\sqrt{3p-4ME}} \right)}{p' - p} \right] \quad (3.55)$$

for Fig. 3.8 (a),

$$K_C^b(p', p, E) = \frac{M^2\alpha}{4(p'^2 - ME + p'p + p^2)} Q_0 \left( \frac{p'^2 + p^2 - ME}{p'p} \right) \left[ \frac{\arctan \left( \frac{p'+2p}{\sqrt{3p'^2-4ME}} \right) - \arctan \left( \frac{2p'+p}{\sqrt{3p-4ME}} \right)}{p' - p} \right] \quad (3.56)$$

for Fig. 3.8 (b), and

$$K_C^c(p', p, E) = K_C^d(p', p, E) = \alpha K_0(p', p, E) \cdot \frac{1}{4\pi(p' - p)} \log \left[ \frac{2ME - 2p'^2 + 2p'p - 2p^2}{-p'\sqrt{4ME - 3p'^2 + 2p'p - 3p^2} + p\sqrt{4ME - 3p'^2 + 2p'p - 3p^2} + 2ME - p'^2 - p^2} \right] \quad (3.57)$$

for Fig. 3.8 (c and d), where  $K_0$  was defined in eq. (3.4).

### 3.2.2 $^3\text{He}$ bound-state amplitude and three-body force

The above subsection provides all the information necessary to solve the homogeneous Faddeev equations for  $^3\text{He}$ , similarly to those corresponding to  $^3\text{H}$ . For  $^3\text{He}$ , the homoge-

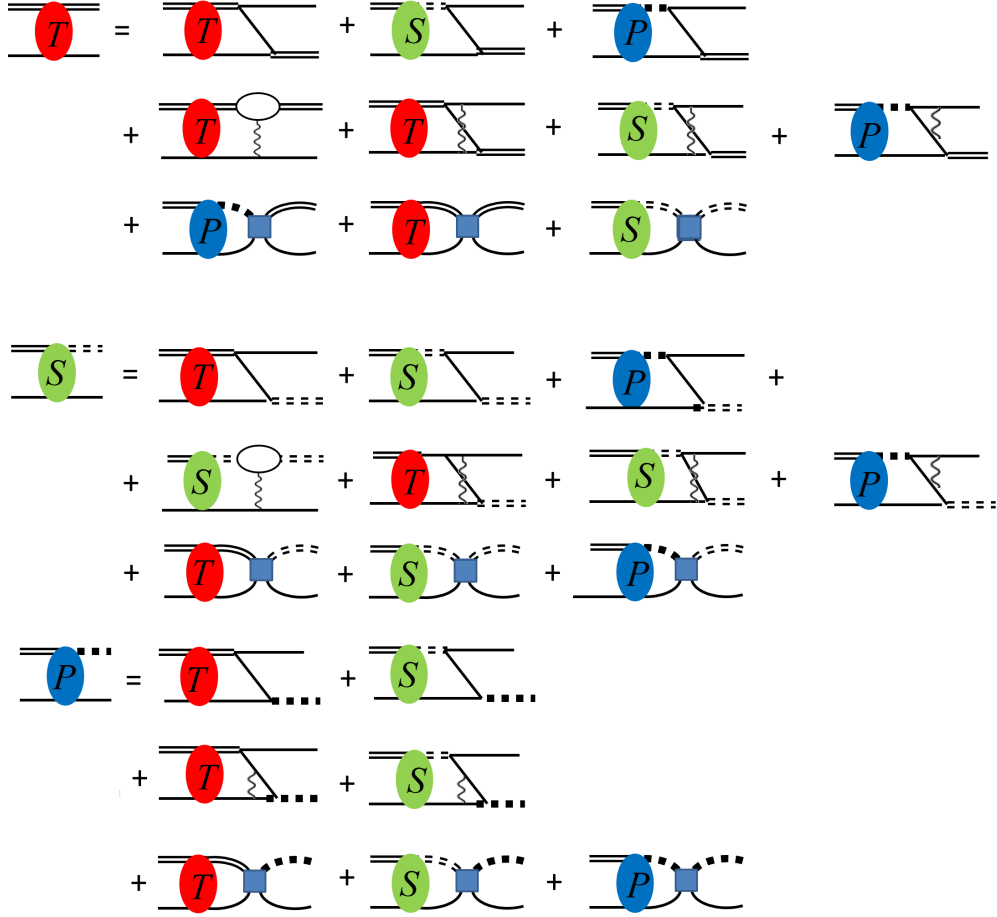


Figure 3.9: Diagrammatic form of the homogeneous part of  $p-d$  scattering that includes a three-body force. The double lines denote the dibaryon propagators  $D_t$  (solid),  $D_{np}$  (dashed) and  $D_{pp}$  (dotted). The red bubbles (T) represent the triplet channel ( $T=0$ ,  $S=1$ ), the green bubbles (S) represent the singlet channel ( $T=1$ ,  $S=0$ ) with  $np$  dibaryon while the blue bubbles (P) represent the singlet channel  $T=1$ ,  $S=0$  with a  $pp$  dibaryon. The blue squares represent the three-body force.

neous part of eq. (3.48) can be written as:

$$\Gamma_{\mu}^{3\text{He}}(p) = \sum_{\nu=t,s,pp} M y_{\mu} y_{\nu} \left[ a'_{\mu\nu} K_0(p', p, E_{3\text{He}}) + b'_{\mu\nu} \frac{H(\Lambda)}{\Lambda^2} + a'_{\mu\nu} K_{\mu\nu}^C(p', p, E_{3\text{He}}) \right] \otimes D_{\nu}(E_{3\text{He}}, p') \Gamma_{\nu}^{3\text{He}}(p'), \quad (3.58)$$

where  $\mu = t, s, pp$  are the different channels of  $^3\text{He}$  and  $K_0(p, p', E)$  and  $K_{\nu\mu}^C(p, p', E)$  is the  $\mu, \nu$  index of  $K^C(p, p', E)$  (eq. (3.53)). Notice that for the  $p-d$  doublet-channel projection,

the electromagnetic interaction does not couple to isospin eigenstates [45, 47], such that:

$$a'_{ts} = \frac{4}{3} \left[ (\sigma^i)_\beta^\alpha ((P_t^i)^\dagger)_{\gamma\delta}^{ab} (P_s^A)_{bc}^{\delta\beta} (1 \cdot i\delta^{A,3})_{da} \right]_{c,d=1} = 3, \quad (3.59a)$$

$$a'_{tpp} = \frac{4}{3} \left[ (\sigma^i)_\beta^\alpha ((P_t^i)^\dagger)_{\gamma\delta}^{ab} (P_s^A)_{bc}^{\delta\beta} (1 \cdot \delta^{A,1} + 1 \cdot i\delta^{A,2})_{da} \right]_{c,d=1} = 3. \quad (3.59b)$$

The three-body force  $H(\Lambda)$  has no isospin dependence, *i.e.*,  $H(\Lambda)_{^3\text{H}} = H(\Lambda)_{^3\text{He}}$ . Therefore, it is possible to calculate the binding energy of  $^3\text{He}$  using the three-body force  $H(\Lambda)$  obtained in the triton system. Similar to Ref. [46] we find the binding energy which solves the Faddeev equations for  $^3\text{He}$ , eq. (3.58), numerically, using the three-body force known from  $^3\text{H}$  at LO with for a large range of cutoffs as shown in Fig. 3.10. From now on, similarly to Ref. [47], we will use the numerical binding energies  $E_{^3\text{He}}(\Lambda)$  at LO as the binding energy of  $^3\text{He}$  rather than the experimental  $E_{^3\text{He}} = 7.72 \text{ MeV}$ . The high similarity between our results and Ref. [47] has been used as an additional check for our numerical calculations. Note that the non-perturbative calculation is the same as in Ref. [46]. The perturbative calculation is similar to the one in Ref. [47], except for the difference of definition of the two-body term, as presented in Chapter. 5.

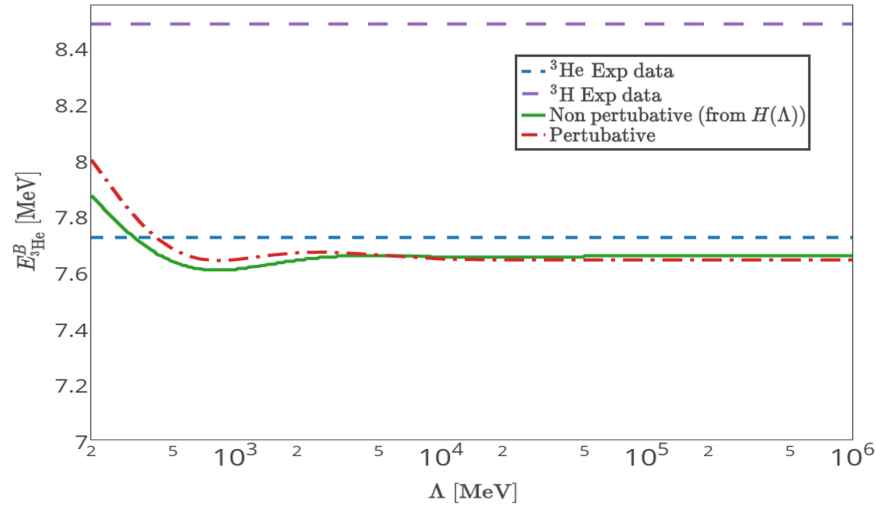


Figure 3.10: Predictions for  $E_{^3\text{H}}, E_{^3\text{He}}$  binding energy as a function of the cutoff  $\Lambda$ . The solid line is the binding energy calculated using the non perturbative solution (subsection 3.2.2), the dashed-dotted line is the binding energy predicted using perturbation theory (eq. (5.21)). The short-dashed line is the experimental value,  $E_{^3\text{He}} = 7.72 \text{ MeV}$ , and the long-dashed line is the experimental value,  $E_{^3\text{H}} = 8.48 \text{ MeV}$ .

# Normalization of the three-nucleon amplitude

In this chapter, we present the normalization of the three-nucleon (*i.e.*,  ${}^3\text{H}$  and  ${}^3\text{He}$ ) bound-state amplitude, in the form of the non-relativistic Bethe-Salpeter (BS) equation. This normalization, as introduced in Refs. [73, 78, 79] is found to have a diagrammatic representation as well. This diagrammatic representation is equivalent to the matrix element of the identity operator, and is found to be the sum over all the possible connections between two identical three-nucleon amplitudes. A similar diagrammatic representation is used later in this work for calculating the  ${}^3\text{H}$ - ${}^3\text{He}$  binding energy shift (Chapter 5), for the NLO contributions to the three-nucleon bound-state amplitude (Chapter 6) and for the three-nucleon electro-weak matrix elements (Chapters 7-9).

## 4.1 The Bethe-Salpeter wave function normalization

The three-nucleon Faddeev equations (eqs. (3.12) and (3.48)) have the same form as the non-relativistic BS equation [73, 76, 78, 79]:

$$\mathcal{M} = V - VG_{BS}\mathcal{M} = V - \mathcal{M}G_{BS}V , \quad (4.1)$$

where  $\mathcal{M}$  is the scattering matrix,  $V$  is the two-body interaction kernel and  $G_{BS}$  is the free two-body propagator. From eq. (4.1) we find:

$$V = \mathcal{M} + \mathcal{M}G_{BS}V , \quad (4.2)$$

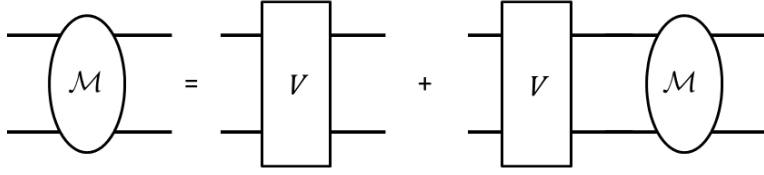


Figure 4.1: Diagrammatic representation of the two-body BS equation for the scattering matrix  $\mathcal{M}$ .

and upon substituting  $V$  in eq. (4.1), we get:

$$\mathcal{M} = V - \mathcal{M}G_{BS}\mathcal{M} - \mathcal{M}G_{BS}VG_{BS}\mathcal{M} . \quad (4.3)$$

For a bound-state,  $\mathcal{M}$  has a general form:

$$\mathcal{M} = \frac{|\Gamma\rangle\langle\Gamma|}{E - E_B} + \mathcal{R} , \quad (4.4)$$

where  $|\Gamma\rangle$  is the wave function amplitude,  $\langle\Gamma|$  is the representation of  $|\Gamma\rangle$  in the dual space (including Dirac conjugate) and  $\mathcal{R}$  is a regular part which is finite at  $E = E_B$  and therefore can be neglected for  $E \rightarrow E_B$  (see the footnote at subsection 3.1.2). Substituting eq. (4.4) into (eq. (4.1)), and equating residues at  $E = E_B$  yields the wave equation for  $|\Gamma\rangle$ :

$$|\Gamma\rangle = -VG_{BS}|\Gamma\rangle . \quad (4.5)$$

Substituting eq. (4.4) into eq. (4.3), multiplying the resulting equation by  $E - E_B$  and taking the limit  $E \rightarrow E_B$ , one finds that:

$$\begin{aligned} |\Gamma\rangle\langle\Gamma| &= - \lim_{E \rightarrow E_B} |\Gamma\rangle \frac{\langle\Gamma| G_{BS} (1 + VG_{BS}) |\Gamma\rangle}{E - E_B} \langle\Gamma| \\ \Rightarrow 1 &= - \lim_{E \rightarrow E_B} \frac{\langle\Gamma| G_{BS} (1 + VG_{BS}) |\Gamma\rangle}{E - E_B} = - \lim_{E \rightarrow E_B} \frac{\langle\Gamma| G_{BS} (G_{BS}^{-1} + V) G_{BS} |\Gamma\rangle}{E - E_B} . \end{aligned} \quad (4.6)$$

From eq. (4.5)  $\lim_{E \rightarrow E_B} \langle \Gamma | G_{BS} (1 + V G_{BS}) | \Gamma \rangle = 0$ , so the RHS of eq. (4.6) is of the form 0/0, so one can use the l'Hôpital's rule to evaluate the limit (which equals -1) explicitly:

$$\begin{aligned}
 & \frac{\lim_{E \rightarrow E_B} \frac{\partial}{\partial E} \langle \Gamma | G_{BS} (G_{BS}^{-1} + V) G_{BS} | \Gamma \rangle}{\lim_{E \rightarrow E_B} \partial_E (E - E_B)} = \lim_{E \rightarrow E_B} \frac{\partial}{\partial E} \langle \Gamma | G_{BS} (G_{BS}^{-1} + V) G_{BS} | \Gamma \rangle = \\
 & \quad \langle \Gamma | G'_{BS} G_{BS}^{-1} G_{BS} + G_{BS} (G_{BS}^{-1})' G_{BS} + G_{BS} G_{BS}^{-1} G'_{BS} | \Gamma \rangle|_{E=E_B} + \\
 & \quad \langle \Gamma | G'_{BS} V G_{BS} + G_{BS} V' G_{BS} + G_{BS} V G'_{BS} | \Gamma \rangle|_{E=E_B} = \\
 & \quad \langle \Gamma | G'_{BS} + G_{BS} (G_{BS}^{-1})' G_{BS} + G'_{BS} | \Gamma \rangle|_{E=E_B} + \langle \Gamma | -G'_{BS} + G_{BS} V' G_{BS} - V G'_{BS} | \Gamma \rangle|_{E=E_B} = \\
 & \quad \langle \Gamma | G_{BS} (G_{BS}^{-1})' G_{BS} + G_{BS} V' G_{BS} | \Gamma \rangle|_{E=E_B} = \langle \Gamma | G_{BS} \frac{\partial}{\partial E} (G_{BS}^{-1} + V) G_{BS} | \Gamma \rangle|_{E=E_B} = -1,
 \end{aligned} \tag{4.7}$$

where the terms proportional to  $\frac{\partial}{\partial E} | \Gamma \rangle$  vanish, due to the BS equation [79].

According to our notation,  $G_{BS} = -D(E, p)$ , the two-body propagator, and  $V = My^2 K_0(p, p', E)$ , the one-nucleon exchange matrix, such that the three-nucleon normalization condition is:

$$1 = \langle \mathcal{B} | G_{BS} \frac{\partial}{\partial E} (-G_{BS} - V) G_{BS} | \mathcal{B} \rangle|_{E=E_B}, \tag{4.8}$$

## 4.2 The non-relativistic Bethe-Salpeter wave-function normalization

The three-nucleon homogeneous integral equation (eq. (3.17)) was found to have the same form as the non-relativistic bound-state Bethe-Salpeter equation (eq. (4.5)):

$$\Gamma(p) = My^2 K_0(p, p', E) D(E, p') \otimes \Gamma(p'). \tag{4.9}$$

The normalization condition for the equation is given in Appendix A and in [76, 78, 79].

This is thus a representation of the normalization operator,  $\hat{Z}$ , such that:

$$\begin{aligned}
 \hat{Z}^{-1} = & \int \frac{d^4 p}{(2\pi)^4} \int \frac{d^4 p'}{(2\pi)^4} \Gamma(p) S(-p_0, -\mathbf{p}) \mathcal{D}(E + p_0, \mathbf{p}) \times \frac{\partial}{\partial E} \left[ \hat{I}(E, p, p') - My^2 K_0(p, p', E) \right]_{E=E_B} \\
 & \times \mathcal{D}(E + p'_0, \mathbf{p}') S(-p'_0, -\mathbf{p}') \Gamma(p'). \tag{4.10}
 \end{aligned}$$



Carrying out the angular and energy integrations gives

$$\hat{Z}^{-1} = \int \frac{p^2 dp}{2\pi^2} \int \frac{p'^2 dp'}{2\pi^2} \Gamma(p) D(E, p) \times M^2 y^2 \left\{ \frac{1}{4\pi \sqrt{3p^2 - 4EM}} \frac{2\pi^2}{p'^2} \delta(p - p') \right. \\ \left. \frac{-1}{2 [p'^2 (p^2 - 2EM) + (p^2 - EM)^2 + p'^4]} \right\} D(E, p') \Gamma(p') , \quad (4.11)$$

with:

$$\hat{I}(E, p, p') = \frac{2\pi^2}{p'^2} \delta(p - p') D^{-1}(E, p), \quad (4.12)$$

and  $S(p_0, \mathbf{p})$  as the one-nucleon propagator:

$$S(E, \mathbf{p}) = \frac{1}{p_0 - \frac{\mathbf{p}^2}{2M}} . \quad (4.13)$$

### 4.3 The normalization of ${}^3\text{H}$ , ${}^3\text{He}$ wave-functions

The homogeneous part of the Faddeev equation of both  ${}^3\text{H}$  and  ${}^3\text{He}$  has the form of a non-relativistic BS equation, which couples different channels.

Using eq. (3.26), the normalization condition that determines the wave-function factor  $Z^{3\text{H}}$  has the form:

$$1 = Z^{3\text{H}} \int \frac{d^3 p}{(2\pi)^3} \int \frac{d^3 p'}{(2\pi)^3} \sum_{\mu, \nu=t,s} \Gamma_\mu^{3\text{H}}(p) D_\mu(E_{3\text{H}}, p) \\ \times \left\{ \frac{\partial}{\partial E} \left[ \hat{I}_{\mu\nu}(E, p, p') - \hat{\mathcal{K}}_{\mu\nu}^{3\text{H}}(p, p', E) \right]_{E=E_{3\text{H}}} \right\} \times D_\nu(E_{3\text{H}}, p') \Gamma_\nu^{3\text{H}}(p') . \quad (4.14)$$

We rewrite the above equation in terms of the *wave-functions*  $\psi_\mu^{3\text{H}}(p)$  and obtain

$$1 = \int \frac{d^3 p}{(2\pi)^3} \int \frac{d^3 p'}{(2\pi)^3} \sum_{\mu, \nu=t,s} \psi_\mu^{3\text{H}}(p) \times \left\{ \frac{\partial}{\partial E} \left[ \hat{I}_{\mu\nu}(E, p, p') - \hat{\mathcal{K}}_{\mu\nu}^{3\text{H}}(p, p', E) \right]_{E=E_{3\text{H}}} \right\} \times \psi_\nu^{3\text{H}}(p') . \quad (4.15)$$

We recall that  $\psi^{3\text{H}}$  is the **normalized** three-nucleon wave-function

$$\langle \psi_\mu^{3\text{H}} | p \rangle = \sqrt{Z^{3\text{H}}} \int dp_0 \mathcal{D}_\mu(E_{3\text{H}} + p_0, p) \Gamma_\mu^{3\text{H}}(p) S(-p_0, -p) , \quad (4.16)$$

and

$$\hat{I}_{\mu\nu}(E, p, p') = \frac{2\pi^2}{p^2} \delta(p - p') D_\mu(E, p)^{-1} \delta_{\mu,\nu} , \quad (4.17)$$

$$\hat{\mathcal{K}}_{\mu\nu}^{3\text{H}}(p, p', E) = M y_\mu y_\nu a_{\mu\nu} K_0(p', p, E) , \quad (4.18)$$

where  $\delta_{\mu,\nu}$  is the Kronecker delta.

For  $^3\text{He}$ , the normalization condition that determines the wave-function factor  $Z^{3\text{He}}$  has the form:

$$1 = \int \frac{d^3p}{(2\pi)^3} \int \frac{d^3p'}{(2\pi)^3} \sum_{\mu,\nu=t,s,pp} \psi_\mu^{3\text{He}}(p) \times \left\{ \frac{\partial}{\partial E} \left[ \hat{I}_{\mu\nu}(E, p, p') - \hat{\mathcal{K}}_{\mu\nu}^{3\text{He}}(p, p', E) \right]_{E=E_{3\text{He}}} \right\} \psi_\nu^{3\text{He}}(p') , \quad (4.19)$$

where:

$$\langle \psi_\mu^{3\text{He}} | p \rangle = \sqrt{Z^{3\text{He}}} \int dp_0 \mathcal{D}_\mu(E_{3\text{He}} + p_0, p) \times \Gamma_\mu^{3\text{He}}(p) S(-p_0, -p) ,$$

$$\hat{\mathcal{K}}_{\mu\nu}^{3\text{He}}(p, p', E) = M y_\mu y_\nu a'_{\mu\nu} [K_0(p', p, E) + K_{\mu\nu}^C(p', p, E)] , \quad (4.20)$$

and  $K_{\mu\nu}^C(p', p, E)$  is the  $\mu, \nu$  index of the matrix  $K^C$  (eq. (3.53)).

## 4.4 The diagrammatic form of the normalization

The implication of the one-body unit operator is turning a single nucleon operator into two one-nucleon propagators under the assumption of energy and momentum conservation in the center-of-mass system:

$$\begin{aligned} \sum_i^A \mathbf{p}^i &= \sum_i^A \mathbf{p}'^i = 0 , \\ \sum_i^A p_0^i &= \sum_i^A p_0'^i = E , \end{aligned} \quad (4.21)$$

where  $i, j$  are the different nucleons indexes,  $\mathbf{p}^i, (\mathbf{p}'^i)$  refers to the one-nucleon incoming (outcoming) momentum and  $p_0^i(p_0'^i)$  refers to the  $i$ 's nucleon incoming (outcoming) energy.

The Jacobi momentum  $\mathbf{p}$  is defined as the relative momentum between the dimer and the one-nucleon of the incoming (outcoming) three-nucleon wave-function,  $\mathbf{p}(\mathbf{p}') = \frac{1}{2} [\mathbf{p}(\mathbf{p}') - (-\mathbf{p}(-\mathbf{p}'))]$  and  $E$  is the total three-nucleon energy.

Let us note that an energy derivative acting on a single nucleon propagator that contains the energy  $E$  can be written as two propagators:

$$\frac{\partial}{\partial E} S(E, \mathbf{p}) = - \int \frac{d^3 p'}{(2\pi)^3} S(E, \mathbf{p}) \times S(E, \mathbf{p}') (2\pi)^3 \delta(\mathbf{p} - \mathbf{p}') . \quad (4.22)$$

Therefore, the normalization operator for eq. (4.9) can be written as a multiplication of the one-nucleon propagators and the corresponding delta functions, under the assumption of energy and momentum conservation:

$$\begin{aligned} Z^{-1} = & - \int \frac{dp_0}{2\pi} \int \frac{d^3 p}{(2\pi)^3} \int \frac{dp'_0}{2\pi} \int \frac{d^3 p'}{(2\pi)^3} \Gamma(p) iS(-p_0, -\mathbf{p}) i\mathcal{D}(E + p_0, \mathbf{p}) \\ & \times \left\{ y^2 \int \frac{dk_0}{2\pi} \int \frac{d^3 k}{(2\pi)^3} \int \frac{dk'_0}{2\pi} \int \frac{d^3 k'}{(2\pi)^3} iS(E + p_0 + k_0, \mathbf{p} + \mathbf{k}) iS(E + p'_0 + k'_0, \mathbf{p}' + \mathbf{k}') iS(-k_0, -\mathbf{k}) iS(-k'_0, -\mathbf{k}') \right. \\ & \times \delta^3[\mathbf{p} + \mathbf{k} - (\mathbf{p}' + \mathbf{k}')] \left[ \delta^3(\mathbf{p}' - \mathbf{p}) \delta^3(\mathbf{k} - \mathbf{k}') + \frac{1}{2} \delta^3(\mathbf{k}' - \mathbf{p}) \delta^3(\mathbf{k} - \mathbf{p}') \right] \left. \right\} i\mathcal{D}(E + p'_0, \mathbf{p}') iS(-p'_0, -\mathbf{p}') \Gamma(p') . \end{aligned} \quad (4.23)$$

By performing the energy integration, eq. (4.23) becomes:

$$\begin{aligned} & \int \frac{p^2 dp}{2\pi^2} \int \frac{p'^2 dp'}{2\pi^2} \Gamma(p) D(E, p) \times M^2 y^2 \left[ \frac{-i}{4\pi(p - p')} \log \left( \frac{i\sqrt{3p'^2 - 4EM} - 2p - p'}{i\sqrt{3p^2 - 4EM} - p - 2p'} \right) \frac{2\pi^2 \delta(p - p')}{p'^2} \right. \\ & \quad \left. - \frac{1}{2p'^2 (p^2 - 2EM) + 2(p^2 - EM)^2 + 2p'^4} \right] \times D(E, p') \Gamma(p'), \end{aligned} \quad (4.24)$$

which is identical to eq. (4.10).

Figure 4.2 shows in detail the two topologies of the normalization diagrams. For the case in which the normalization insertion connects the two dimers in the three-nucleon systems, it is proportional to  $\frac{\partial}{\partial E} \hat{I}$  (Fig. 4.2 (a)). For the case in which the one-nucleon exchange propagator connects both one of the dimer nucleons and the single nucleon, the diagram is proportional to  $\frac{\partial}{\partial E} \hat{\mathcal{K}}$  (Fig. 4.2 (b)).

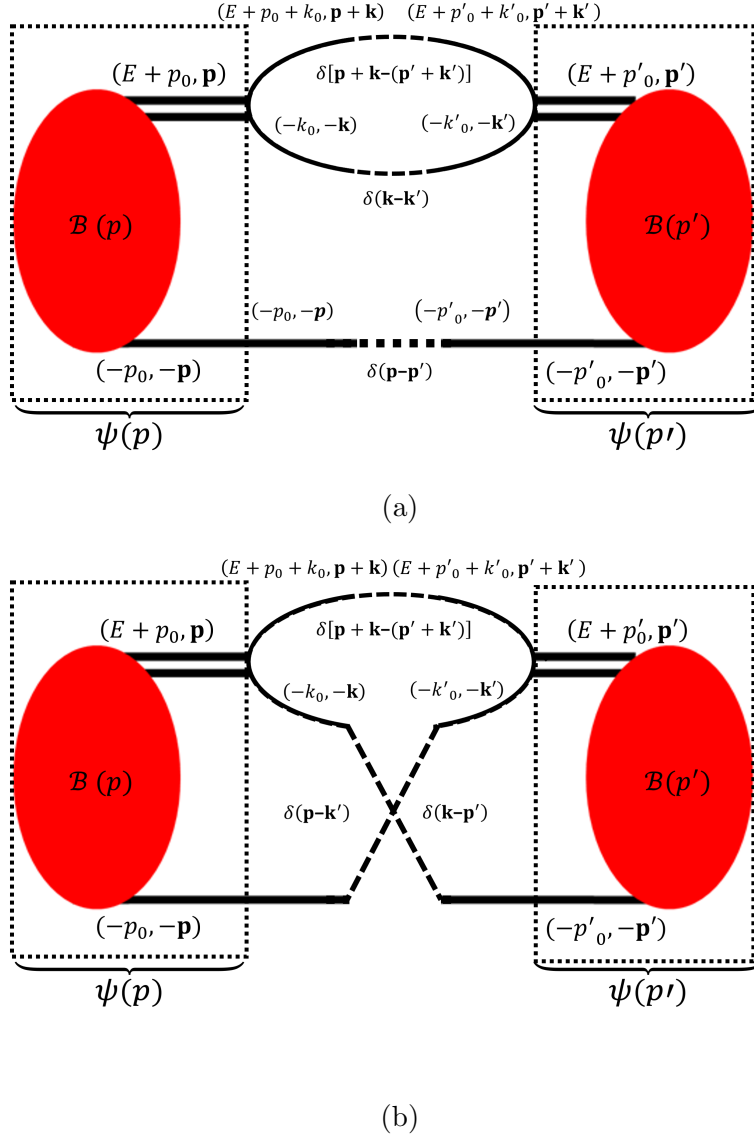


Figure 4.2: Diagrammatic representation of two possible connections between two identical three-nucleon wave-functions,  $\psi$ . The double lines are the propagators of the two dibaryon fields,  $\mathcal{D}$ . The solid lines represent one-nucleon propagators, while the dashed lines denote the delta functions. Diagram (a) is proportional to  $\frac{\partial}{\partial E} \hat{I}$ , while diagram (b) is proportional to  $\frac{\partial}{\partial E} \hat{\mathcal{K}}$ .

Note that since for both  ${}^3\text{H}$  and  ${}^3\text{He}$ ,  $\hat{\mathcal{K}}_{\mu\nu}$  is not diagonal, eqs. (4.14) and (4.19) involve different channels.



## A = 3 matrix element in pionless EFT

In this chapter, we present the general method for calculating an  $A = 3$  matrix element in  $\pi$ EFT. This method is used in this work for calculating the  $A = 3$  electro-weak observables, as well as the  ${}^3\text{He}$  energy shift perturbatively and the NLO contribution to the three-nucleon wave functions.

### 5.1 The general form of an $A = 3$ matrix element

In Chapter 4, we showed that the three-nucleon normalization can be written as:

$$1 = \sum_{\mu,\nu} \psi_{\mu}^i(p) \otimes \left\{ \frac{\partial}{\partial E} [\hat{I}_{\mu\nu}(E, p, p') - \hat{K}_{\mu\nu}^i(p, p', E)]_{E=E_i} \right\} \otimes \psi_{\nu}^i(p') \quad , \quad (5.1)$$

which can be written in terms of a matrix element:

$$1 = \sum_{\mu,\nu} \langle \psi_{\mu}^i | \mathcal{O}_{\mu\nu}^{\text{norm}}(E_i) | \psi_{\nu}^i \rangle \quad , \quad (5.2)$$

where  $\mathcal{O}_{\mu\nu}^{\text{norm}}(E_i)$  is the normalization operator such that:

$$\mathcal{O}_{\mu\nu}^{\text{norm}}(E_i) = \frac{\partial}{\partial E} \left[ \hat{I}_{\mu\nu}(E, p, p') - M y_{\mu} y_{\nu} a_{\mu\nu}^i \hat{K}_{\mu\nu}^i(p', p, E) \right] \Big|_{E=E_i} \quad , \quad (5.3)$$

where:

$$\hat{K}_{\mu\nu}^i = \begin{cases} K_0(p', p, E) & i = {}^3\text{H} \\ K_0(p', p, E) + K_{\mu\nu}^C(p', p, E) & i = {}^3\text{He} \end{cases} \quad (5.4)$$

and

$$a_{\mu\nu}^i = \begin{cases} a_{\mu\nu} & i = {}^3\text{H} \\ a'_{\mu\nu} & i = {}^3\text{He} \end{cases}, \quad (5.5)$$

which are a result of  $N - d$  doublet-channel projection (eqs. (3.21) and (3.59)). Note that we are considering here one-body operators that do not have additional momentum dependence. However, the formulas given here could easily be extended also to this case.

Equation (5.3) can be generalized to any operator,  $\mathcal{O}_{j,i}$ , between the initial (i) and final (j)  $A = 3$  bound-state wave-functions ( $\psi_{i,j}$ ), whose matrix element is evaluated as

$$\langle \mathcal{O}_{j,i}(q_0, q) \rangle = \langle S, S'_z, I, I'_z, E' | \mathcal{O}_{j,i}(q_0, q) | S, S_z, I, I_z, E \rangle, \quad (5.6)$$

where:

- $S$  denotes the total spin ( $\frac{1}{2}$ ) of the three-nucleon system.
- $S_z, S'_z$  denote the initial and final spin projections, respectively.
- $I$  denotes the total isospin ( $\frac{1}{2}$ ) of the three-nucleon
- $I_z, I'_z$  denote the initial and final isospin projections, respectively.
- $q$  is the momentum transfer of such an operator (assuming that for the initial state, the three-nucleon total momentum is zero).
- The energy transfer is defined as:  $q_0 = E' - E$ .

Therefore, a general operator that connects two three-nucleon bound-states with  $I = \frac{1}{2}$ ,  $S = \frac{1}{2}$ , factorizes into the following parts:

$$\mathcal{O}_{j,i} = \mathcal{O}^J \mathcal{O}^T \mathcal{O}_{j,i}(q_0, q), \quad (5.7)$$

where  $\mathcal{O}^J$ , the spin part of the operator whose total spin is  $J$ , and  $\mathcal{O}^T$ , the isospin part of the operator, depend on the initial and final quantum numbers. The spatial part of the operator,  $\mathcal{O}_{j,i}(q_0, q)$ , is a function of the three-nucleon wave-function's binding energies ( $E_i, E_j$ ) and the energy and momentum transfer ( $q_0, q$ , respectively).

The observable associated with the above matrix element is also related to a reduced matrix element between  $A = 3$  bound-state wave functions:

$$\langle \|\mathcal{O}_{j,i}(q_0, q)\| \rangle = \langle S, I, E', q | \mathcal{O}^J \mathcal{O}^T \mathcal{O}_{j,i}(q_0, q) | S, I, E \rangle.$$

In the next subsection, we write explicitly the reduce matrix element term for a general one-body operator. Note that the amplitude  $\Gamma^i(p)$  (and as a result,  $\psi^i(p)$ ) still carries implicit spin and isospin indices,  $S_z$  and  $I_z$ , respectively. We calculate the reduced matrix element shown above by performing the spin algebra with the afore-mentioned spin and isospin projectors and the spin- and isospin part of the operator under consideration for one particular choice of external spin projections. Then we use the Wigner-Eckhart theorem to combine this matrix element with a Clebsch-Gordan coefficient to obtain the reduced matrix element.

## 5.2 Matrix elements of one-body operators

The one-body normalization operator,  $\mathcal{O}_{\mu\nu}^{\text{norm}}(E_i)$  (eq. (5.3)), is a result of  $N - d$  doublet-channel projection (eqs. (3.21) and (3.59)). For the case that the one-body spin and isospin operators are combinations of Pauli matrices, the general matrix element will be a result of the different  $N - d$  doublet-channel projections coupled to a spin-isospin operator. To evaluate the reduced matrix element of a general one-body operator, one needs to calculate explicitly one component of the spin operator,  $\mathcal{O}^J$ . For an operator whose spin part is proportional to  $\sigma$ , for example, the zero-component of  $\langle \mathcal{O}^J \rangle$ ,  $\langle \mathcal{O}_0^J \rangle$  is given by:

$$\langle \mathcal{O}_{j,i}^{1\text{B}}(q_0, q) \rangle_0 = \sum_{\mu,\nu} y_\mu y_\nu \langle \psi_\mu^j | \left\{ d_{\mu\nu}^{ij} \hat{\mathcal{I}}(q_0, q) + a_{\mu\nu}^{ij} \left[ \hat{\mathcal{K}}(q_0, q) + \hat{\mathcal{K}}_{\mu\nu}^C(E, q_0, q) \right] \right\} | \psi_\nu^i \rangle, \quad (5.8)$$

where  $\hat{\mathcal{I}}(E, q_0, q)$  and  $\hat{\mathcal{K}}(E, q_0, q)$  represent all the possible connections between two three-nucleon wave-functions ( $\psi^i, \psi^j$ ) that contain a **one-body** insertion of momentum and energy transfer without a Coulomb interaction. The spatial parts that do not contain a one-nucleon exchange are denoted by  $\hat{\mathcal{I}}(q_0, q)$ , and the spatial parts that do contain a one-nucleon exchange are denoted by  $\hat{\mathcal{K}}(q_0, q)$ ; the full expressions for  $\hat{\mathcal{I}}(E, q_0, q)$  and  $\hat{\mathcal{K}}(q_0, q)$  are given eqs. (5.9) and (5.10).  $a_{\mu\nu}^{ij}$  and  $d_{\mu\nu}^{ij}$  are a result of the  $N - d$  doublet-channel projection coupled to  $\mathcal{O}_0^J \mathcal{O}^T$ .  $\hat{\mathcal{K}}_{\mu\nu}^C(E, q_0, q)$  are the diagrams that contain a one-photon interaction in addition to the energy and momentum transfer. A derivation of an analytical expression for these diagrams is too complex, so they were calculated numerically only.



$$\begin{aligned}
 \hat{\mathcal{I}}(q_0, q) &= \frac{M^2 i}{4\pi(q - p + p')}. \\
 &\left\{ \log \left[ q \left( \sqrt{4EM - 3p'^2} - 2p + p' \right) + (p' - p) \left( \sqrt{4EM - 3p'^2} - 2p - p' \right) + q^2 + 2q_0 M \right] \right. \\
 &\quad \left. - \sqrt{4EM - q^2 + 2qp - 4q_0 M - 3p^2} \sqrt{\frac{-1}{-4EM + q^2 - 2qp + 4q_0 M + 3p^2}} \right. \\
 &\log \left[ -(p - p') \left( \sqrt{4EM - q^2 + 2qp - 4q_0 M - 3p^2} - p - 2p' \right) + q \left( \sqrt{4EM - q^2 + 2qp - 4q_0 M - 3p^2} - p' \right) \right] \\
 &\quad \left. \delta(q_0 - E + E') \delta(p' - p) \frac{2\pi^2}{p'^2} \right\} \quad (5.9)
 \end{aligned}$$

and:

$$\begin{aligned}
 \hat{\mathcal{K}}(q_0, q) &= \frac{M^2}{2pp' [q(2(p + p') - q) - 2Mq_0]} \times \\
 &\left\{ \log \left[ (-EM + p^2 + pp' + p'^2) (2EM - 2Mq_0 - 2(p^2 - pp' + p'^2) + 2q(p + p') - q^2) \right] \right. \\
 &\left. - \log \left[ (-EM + p^2 - pp' + p'^2) (2EM - 2Mq_0 - 2(p^2 + pp' + p'^2) + 2q(p + p') - q^2) \right] \right\} \cdot \\
 &\quad \delta(q_0 - E + E') \delta(q - p + p') \quad (5.10)
 \end{aligned}$$

Figure 5.1 shows all possible diagrams of a one-body insertion of momentum and energy transfer between two three-nucleon wave-functions that contain a one-nucleon exchange.

The one-body reduced matrix element,  $\langle \|\mathcal{O}_{j,i}^{1B}(E, q_0, q)\| \rangle$ , can be easily calculated as a function of the three-nucleon quantum total spin and isospin numbers, using the Wigner-Eckart theorem. Since these calculations are not dependent on the spatial structure of the three-nucleon wave function, one can isolate the spin and isospin matrix elements in terms of the three-nucleon quantum numbers such that (again for the zero component):

$$\langle \|\mathcal{O}_{j,i}^{1B}(q_0, q)\| \rangle = \frac{\sqrt{2}}{\langle \frac{1}{2}S_z J 0 | \frac{1}{2}S'_z \rangle} \sum_{\mu, \nu} \langle \psi_\mu^j | y_\mu y_\nu \left[ d_{\mu\nu}^{ij} \hat{\mathcal{I}}(q_0, q) + a_{\mu\nu}^{ij} \hat{\mathcal{K}}(q_0, q) \right] | \psi_\nu^i \rangle, \quad (5.11)$$

that can be written as:

$$\begin{aligned} \langle \|\mathcal{O}_{j,i}^{1B}(q_0, q)\| \rangle &= \left\langle \frac{1}{2} \|\mathcal{O}^J\| \frac{1}{2} \right\rangle \left\langle \frac{1}{2}, I'_z | \mathcal{O}^T | I_z, \frac{1}{2} \right\rangle \\ &\times \sum_{\mu, \nu} \langle \psi_\mu^j | y_\mu y_\nu \left\{ d_{\mu\nu}^{ij} \hat{\mathcal{I}}(q_0, q) + a_{\mu\nu}^{ij} \left[ \hat{\mathcal{K}}(p, p', E, q_0) + \hat{\mathcal{K}}_{\mu\nu}^C(q_0, q) \right] \right\} | \psi_\nu^i \rangle \quad , \quad (5.12) \end{aligned}$$

such that for  $i = j$ :

$$d_{\mu\nu}^{ii} = \delta_{\mu, \nu} \quad (5.13)$$

$$a_{\mu\nu}^{ii} = \begin{cases} a_{\mu\nu} & i = {}^3\text{H} \\ a'_{\mu\nu} & i = {}^3\text{He} \end{cases} \quad , \quad (5.14)$$

where  $\hat{\mathcal{K}}_{\mu\nu}^C(q_0, q) = 0$  for  ${}^3\text{H}$ .

The reduced matrix element of the spin part of the operator,  $\langle \frac{1}{2} \|\mathcal{O}^J\| \frac{1}{2} \rangle$ , is a function of the initial and final total spin of the  $A = 3$  nucleon wave-function. For the case that  $\mathcal{O}^J = \boldsymbol{\sigma}$ , the reduced matrix element,  $\langle \frac{1}{2} \|\mathcal{O}^J\| \frac{1}{2} \rangle$ , is calculated using the Wigner-Eckart theorem such that:

$$\left\langle \frac{1}{2} \|\boldsymbol{\sigma}\| \frac{1}{2} \right\rangle = 2 \left\langle \frac{1}{2} \|\mathbf{s}\| \frac{1}{2} \right\rangle = \sqrt{6} \quad . \quad (5.15)$$

### 5.2.1 Two-body matrix element

In contrast to the normalization operator given in eq. (5.3), which contains only one-body interactions, a typical  $\not\!A$ EFT electroweak interaction contains also the following two-body interactions up to NLO:

$$t^\dagger t, s^\dagger s, (s^\dagger t + h.c) \quad , \quad (5.16)$$

under the assumption of energy and momentum conservation. The diagrammatic form of the different two-body interactions, given in Tab. 2.2 (( $o$ ) – ( $q$ ) are the two-body weak interactions while ( $s$ ) – ( $x$ ) are the two-body magnetic interactions), is a result of the Hubbard-Stratonovich transformation of a four-nucleon interaction vertex (see, for example, Refs. [28, 32] and Appendix C).

### 5.3 Deuteron normalization and the matrix element in pionless EFT

The calculation of matrix elements is significantly harder in the three-body sector than in the two-body sector due to the more complicated structure of three-body diagrams [38, 39]. However, a closer look at the deuteron wave-function normalization reveals that the deuteron wave-function normalization can also be written in the same manner as discussed above, since

$$Z_d^{-1} = i \frac{\partial}{\partial E} \frac{1}{iD_t(E, p)} \Big|_{E=\frac{\gamma_t^2}{M}, p=0}, \quad Z_d = \frac{1}{1 - \gamma_t \rho_t}, \quad (5.17)$$

where the energy derivative of  $i \frac{1}{iD_t(E, p)}$  is equivalent to the addition of a one-nucleon propagator, as discussed in Chapter 4. Hence, a general deuteron matrix element that contains energy and momentum transfer (such as the deuteron magnetic moment) can be written as the sum over all possible connections [16]:

$$\langle S, p' | \mathcal{O}_{j,i}(q_0, q) | S, p \rangle = \langle 1 | \mathcal{O}^J | 1 \rangle \left( \frac{M^2}{8\pi\gamma_t} \right)^{-1} \langle p' | \hat{\mathcal{I}}(q_0, q) | p \rangle. \quad (5.18)$$

For the case that  $O^J = 1$  and  $q_0, q = 0$ , eq. (5.18) gives the deuteron form factor,  $F_C(0)$ , which is equal to 1:

$$\langle \mathcal{O}_{j,i}(q_0, q) \rangle = \left( \frac{M^2}{8\pi\gamma_t} \right)^{-1} \hat{\mathcal{I}}(E_d, 0, 0) = \left( \frac{M^2}{8\pi\gamma_t} \right)^{-1} \frac{M^2}{8\pi\gamma_t} = 1. \quad (5.19)$$

This matrix element form, which is very similar to the general three-body matrix element (eq. (5.11)), implies that in the case of bound-state matrix elements, our *wave-function* approach can be applied in the two- and the three-nucleon systems, consistently.

### 5.4 Example: ${}^3\text{He}$ - ${}^3\text{H}$ binding energy difference with a perturbative Coulomb

In this subsection, we apply the formalism introduced above to the so-called Coulomb energy shift in the three-nucleon system. We define the Coulomb-induced energy shift,

$\Delta E$ , as [45–47]:

$$-E_{3\text{He}} = -E_{3\text{H}} + \Delta E. \quad (5.20)$$

The energy difference between  ${}^3\text{H}$  and  ${}^3\text{He}$  due to the Coulomb interaction can be calculated perturbatively at LO as a matrix element of one-photon exchange diagrams (Fig. 3.8 a-d) and the  $pp$  propagator (diagram f) between two triton bubbles, as described in detail in [46, 47]. In our notation, these Coulomb interactions can be treated as a special case of a general matrix element, despite the fact that the Coulomb interaction does not conserve the three-nucleon isospin. This representation is possible since we divided the contribution to the energy shift into a one-body (1B) term and a two-body (2B) term. The one-body term originates from the one-photon exchange diagrams being calculated as a one-body interaction between two  ${}^3\text{H}$  bound-state wave-functions and does not affect the three-nucleon isospin. The two-body term originates from the difference between the proton-proton propagator and the spin singlet propagator (which is a two-body operator).

In terms of eq. (5.6),  $\Delta E$  has the form:

$$\begin{aligned} \Delta E(\Lambda) = & Z^{3\text{H}} \sum_{\mu, \nu=t,s} y_\mu y_\nu \left[ \Gamma_\mu^{3\text{H}}(p) D_\mu(E_{3\text{H}}, p) \right] \otimes c_{\mu\nu} K_{\mu\nu}^C(p, p', E_{3\text{H}}) \otimes \left[ D_\nu(E_{3\text{H}}, p') \Gamma_\nu^{3\text{H}}(p') \right] \\ & + Z^{3\text{H}} \sum_{\mu=t,s} \left[ \Gamma_\mu^{3\text{H}}(p) D_\mu(E_{3\text{H}}, p) \right] \otimes \left[ a_{\mu s} K_0(p, p', E_{3\text{H}}) + b_{\mu s} \frac{H(\Lambda)}{\Lambda^2} \right] \otimes \left\{ [D_{pp}(E_{3\text{H}}, p') - D_s(E_{3\text{H}}, p')] \Gamma_s^{3\text{H}}(p') \right\} \end{aligned} \quad (5.21)$$

Using the fact that:

$$\Gamma_s^{3\text{H}}(p') = \sum_{\mu=t,s} \left[ \Gamma_\mu^{3\text{H}}(p) D_\mu(E_{3\text{H}}, p) \right] \otimes \left[ a_{\mu s} K_0(p, p', E_{3\text{H}}) + b_{\mu s} \frac{H(\Lambda)}{\Lambda^2} \right], \quad (5.22)$$

eq. (5.21) becomes:

$$\begin{aligned} \Delta E(\Lambda) = & \sum_{\mu, \nu=t,s} \psi_\mu^{3\text{H}}(p) \otimes \underbrace{c_{\mu\nu} K_{\mu\nu}^C(p, p', E_{3\text{H}})}_{\text{one body}} \otimes \psi_\nu^{3\text{H}}(p') \\ & + \sum_{\mu=t,s} \psi_\mu^{3\text{H}}(p) \otimes \underbrace{\left[ \frac{D_{pp}(E_{3\text{H}}, p) - D_s(E_{3\text{H}}, p)}{D_s(E_{3\text{H}}, p)^2} \right] \times \frac{\delta(p - p')}{p'^2} 2\pi^2 \delta_{\mu,s}}_{\text{two-body}} \otimes \psi_s^{3\text{H}}(p') \\ = & \sum_{\mu=t,s} \psi_\mu^{3\text{H}}(p) \otimes [\mathcal{O}_{\mu\nu}^{q(1\text{B})}(E_{3\text{H}}, p, p') + \mathcal{O}_{\mu\nu}^{q(2\text{B})}(E_{3\text{H}}, p, p')] \otimes \psi_\mu^{3\text{H}}(p'), \end{aligned} \quad (5.23)$$

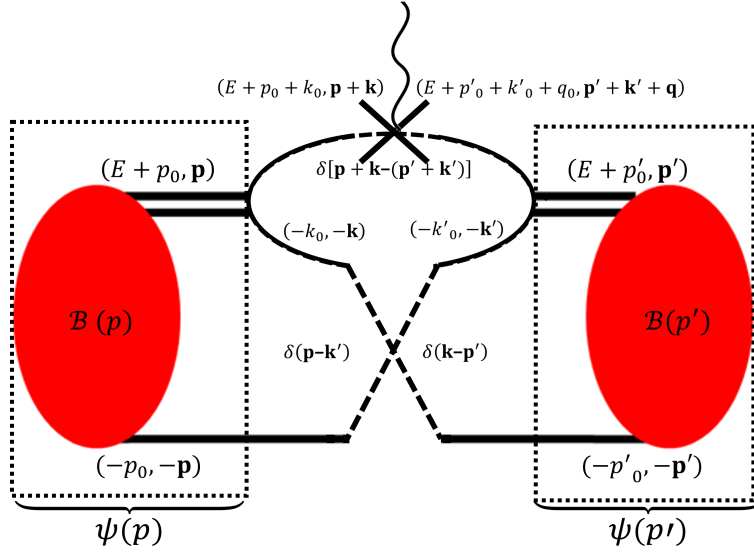
where  $Z^{3\text{H}}$  is the  $^3\text{H}$  normalization, and

$$\mathcal{O}_{\mu\nu}^{q(1\text{B})}(E, p, p') = c_{\mu\nu} K_{\mu\nu}^C(p, p', E) \delta(q - p + p'), \quad (5.24)$$

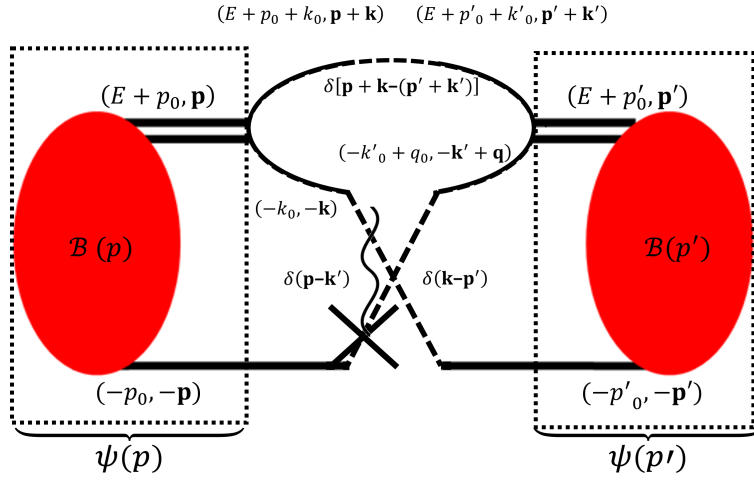
$$\begin{aligned} \mathcal{O}_{\mu\nu}^{q(2\text{B})}(E, p, p') = & \left[ \frac{D_{pp}(E, p) - D_s(E, p)}{D_s(E, p)^2} \right] \\ & \times \frac{\delta(p - p')}{p'^2} 2\pi^2 \delta_{\mu,s} \delta_{\nu,s}, \end{aligned} \quad (5.25)$$

where  $K_{\mu\nu}^C(p, p', E)$  is given in eq. (3.53) and  $c_{\mu\nu} = a_{\mu\nu}$  under the assumption that  $\Gamma_s = \Gamma_{np}, \Gamma_{pp}$ ;  $D_{pp}(E, p), D_s(E, p)$  were defined in Chapter 2.

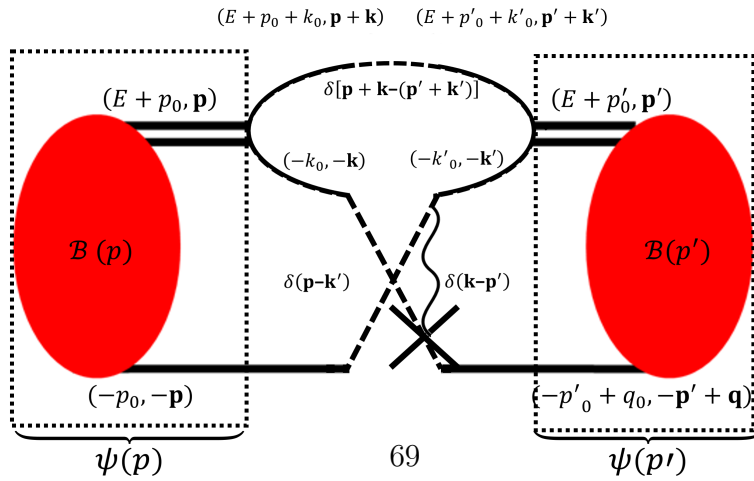
Figure. 3.10 shows that summing over all possible one- and two-body Coulomb diagrams (eq. (5.21)) is consistent with the non-perturbative calculation presented in section 3.2.2. Both calculations reproduce the predictions presented in Refs. [46, 47], and this fact serves as a validation of the numerical calculation presented here.



(a)



(b)



(c)



# Perturbative correction to the three-body nuclear wave functions

The components needed for a consistent calculation of an  $A = 3$  matrix element up to NLO (*i.e.*, retaining terms of order  $\frac{Q}{\Lambda_{cut}}$ ) are the interaction operator,  $\mathcal{O}_{j,i}(q_0, q)$ , and the bound-state amplitudes up to this order. In this section, we present how the NLO contributions to the three-nucleon bound-state amplitude can be calculated using the method presented in Chapter 5. Specifically, we follow the NLO bound-state calculation of Vanasse et al. [43, 50], except that we consider  $y_t \neq y_s$ .

In our notation we distinguish between the NLO correction to the scattering matrix  $t(E, k, p)$  and the NLO correction to the bound-state scattering amplitude ( $\mathcal{B}(k)$ ) which is the homogeneous solution of the Faddeev equations.

## 6.1 The NLO correction to the full scattering amplitude

In this section, we use the formalism introduced in Chapter 5 to calculate the NLO correction to the full scattering amplitude.

For simplicity, in a similar manner to that presented in Chapter 4, we first write the NLO correction for the case that the  $t$ -matrix contains only one channel, *i.e.*,  $t(E, k, p) = T(E, k, p)$ , and then extend this formalism for  ${}^3\text{H}$  and  ${}^3\text{He}$ .

The full  $t$ -matrix can be expanded order-by-order:

$$T(E, k, p) = T^{\text{LO}}(E, k, p) + T^{(1)}(E, k, p) + \dots, \quad (6.1)$$



## CHAPTER 6. PERTURBATIVE CORRECTION TO THE THREE-BODY NUCLEAR WAVE FUNCTIONS

---

where  $T^{\text{LO}}(E, k, p)$  is given by eq. (3.12) and  $T^{(1)}$ , which contains the effective range corrections up to NLO, is derived next. Based on Chapter. 5 and Ref. [43], eq. (6.1) for a bound-state (eq. (3.16)) can be written as:

$$T(E, k, p) = T^{\text{LO}}(E, k, p) + T^{\text{LO}}(E, k, p') D^{\text{LO}}(E, p') \otimes \mathcal{O}^{(1)}(E, p', p'') \otimes D^{\text{LO}}(E, p'') T^{\text{LO}}(E, p'', p), \quad (6.2)$$

where the operator  $\mathcal{O}^{(1)}(E, p', p'')$  contains all NLO corrections to the  $T$ -matrix (see Fig. 6.1). Using eq. (6.2), the NLO correction to the  $T$ -matrix is given by:

$$T^{(1)}(E, k, p) = -T^{\text{LO}}(E, k, p') D^{\text{LO}}(E, p') \otimes \left\{ \frac{My^2}{2} \left[ K_0(p', p'', E) + \frac{H(\Lambda)}{\Lambda^2} \right] \times [\Delta(E, p'') + \Delta(E, p')] \right\} \otimes D^{\text{LO}}(E, p'') T^{\text{LO}}(E, p'', p). \quad (6.3)$$

By using the STM equation (eq. (3.10)), eq. (6.3) becomes:

$$\begin{aligned} T^{(1)}(E, k, p) &= \int \frac{p'^2 dp'}{2\pi^2} T^{\text{LO}}(E, k, p') \Delta(E, p') D^{\text{LO}}(E, p') T^{\text{LO}}(E, p', p) \\ &= -\frac{2\pi}{My^2} \rho \int \frac{p'^2 dp'}{2\pi^2} T^{\text{LO}}(E, k, p') \frac{3p'^2/4 - EM - 1/a_2^2}{\left( \sqrt{3p'^2/4 - EM} - 1/a_2 \right)^2} \times T^{\text{LO}}(E, p', p), \end{aligned} \quad (6.4)$$

where  $\rho$  is the effective range,  $a_2$  is the dibaryon scattering length,  $K_0$  is defined in eq. (3.4),

$$\Delta(E, p) = \frac{D^{\text{NLO}}(E, p) - D^{\text{LO}}(E, p)}{D^{\text{LO}}(E, p)}, \quad (6.5)$$

and  $D^{\text{NLO}}(E, p)$  is defined in eq. (2.65).

### 6.1.1 The NLO corrections to the three-nucleon bound-state pole position

Following Vanasse et al. [43], we use eq. (6.3) to predict the NLO correction to the three-nucleon binding energy. We extend the method developed by Ji, Phillips and Platter [44] to include complications due to the isospin. The scattering amplitude possesses a pole at

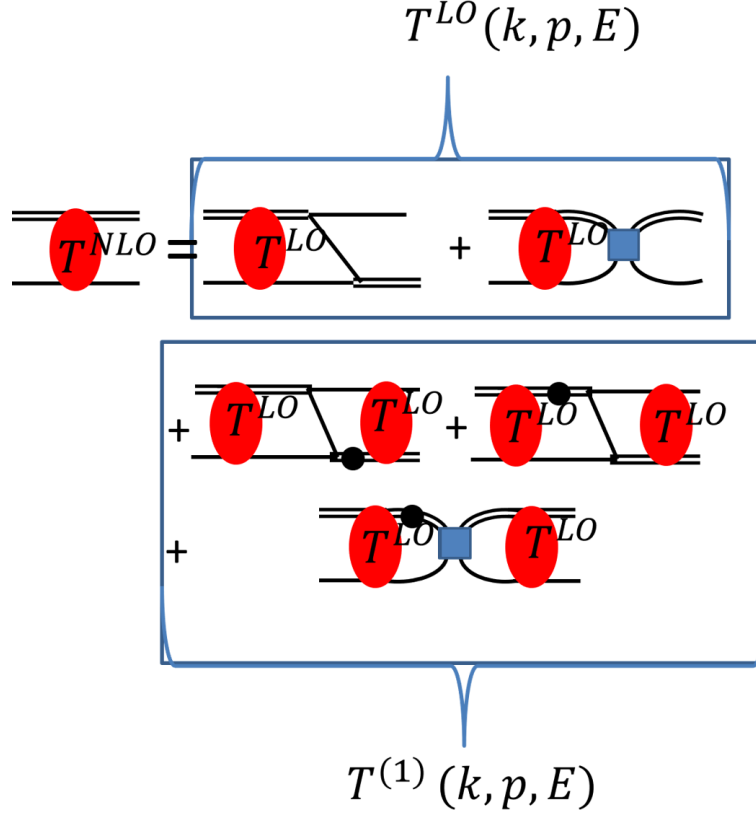


Figure 6.1: The  $t$ -matrix describing a bound-state up to NLO (red bubbles). The LO  $t$ -matrix is the result of the LO homogeneous Faddeev equation - eq. (3.12). The NLO correction to the  $t$ -matrix includes the effective range  $\rho$  (black dot). The double lines are the propagators of the two dibaryon fields and the blue square is the three-body force.

the binding energy and can be written as:

$$\begin{aligned}
 T(E, k, p) &= T^{LO}(E, k, p) + T^{(1)}(E, k, p) \\
 &= \frac{\mathcal{Z}^{LO}(k, p) + \mathcal{Z}^{(1)}(k, p)}{E - (E_B + \Delta E_B)} + \mathcal{R}_0(E, k, p) + \mathcal{R}_1(E, k, p),
 \end{aligned} \tag{6.6}$$

where  $\mathcal{Z}^{LO}, \mathcal{Z}^{(1)}$  are the residue vector functions and  $\Delta E_B$  is the NLO correction to the binding energy. Both  $\mathcal{R}_0(E, k, p)$  and  $\mathcal{R}_1(E, k, p)$  are regular at  $E = E_B$ , so they can be neglected. At the first order in ERE (NLO) of eq. (6.6), one finds that [80]:

$$T^{(1)}(E, k, p) = \frac{\mathcal{Z}^{(1)}(k, p)}{E - E_B} + \Delta E_B \frac{\mathcal{Z}^{LO}(k, p)}{(E - E_B)^2}, \tag{6.7}$$

where  $\mathcal{Z}^{\text{LO}}$  is defined around the pole ( $E \rightarrow E_B$ ) from eq. (6.6) as:

$$\mathcal{Z}^{\text{LO}}(k, p) = \lim_{E \rightarrow E_B} (E - E_B) T^{\text{LO}}(E, k, p). \quad (6.8)$$

For  $E \rightarrow E_B$ ,  $\Delta E_B$  is given by:

$$\Delta E_B = \lim_{E \rightarrow E_B} \frac{T^{(1)}(E, k, p)(E - E_B)^2}{\mathcal{Z}^{\text{LO}}(k, p)}. \quad (6.9)$$

It might seem that the binding energy correction ( $\Delta E_B$ ) depends on the incoming and outgoing momenta ( $k, p$ ). However, we would expect the NLO binding energy,  $E_B^{\text{NLO}} = E_B + \Delta E_B$ , to depend on the cutoff  $\Lambda$  only, similarly to LO (as shown in Fig. 3.10), so it is essential to examine its momentum dependence. Since for a bound-state (eq. (3.16)):

$$T(E, k, p) = \frac{\Gamma(k)\Gamma(p)}{E - E_B}, \quad (6.10)$$

eq. (6.3) becomes:

$$\begin{aligned} T^{(1)}(E, k, p)(E - E_B)^2 &= \Gamma^{\text{LO}}(k)\Gamma^{\text{LO}}(p')D^{\text{LO}}(E, p') \otimes \mathcal{O}^{(1)}(E, p', p'') \otimes D^{\text{LO}}(E, p'')\Gamma^{\text{LO}}(p'')\Gamma^{\text{LO}}(p) = \\ &\Gamma^{\text{LO}}(k)\psi^{\text{LO}}(p') \otimes \mathcal{O}^{(1)}(E, p', p'') \otimes \psi^{\text{LO}}(p'')\Gamma^{\text{LO}}(p), \end{aligned} \quad (6.11)$$

where  $\psi^{\text{LO}}(p)$  is the three-nucleon wave-function (eq. (4.16) for  ${}^3\text{H}$  and eq. (4.20) for  ${}^3\text{He}$ ) and  $D_t^{\text{LO}}(E, p)$  is the dibaryon propagator at LO (eq. (2.62)). Since  $\mathcal{Z}^{\text{LO}}(k, p) = \lim_{E \rightarrow E_B} \Gamma_t^{\text{LO}}(k)\Gamma_t^{\text{LO}}(p)$ , substituting eq. (6.11) into eq. (6.9) yields:

$$\Delta E_B = \psi^{\text{LO}}(p') \otimes \mathcal{O}^{(1)}(E, p', p'') \otimes \psi^{\text{LO}} = f(\Lambda), \quad (6.12)$$

which is a function of the cutoff  $\Lambda$  only, *i.e.*, it has no dependence on the momenta  $k$  and  $p$ .

### 6.1.2 NLO three-body force

From eq. (6.12), we find that the NLO correction to  ${}^3\text{H}$  has a cutoff dependence that needs to be removed [81]. Similarly to the LO case, this  $\Lambda$ -dependence is removed by adding a term that includes an NLO correction to the LO three-body force,  $H^{(1)}(\Lambda)$ , such that  $T^{(1)}$

## CHAPTER 6. PERTURBATIVE CORRECTION TO THE THREE-BODY NUCLEAR WAVE FUNCTIONS

---

becomes:

$$\begin{aligned}
T^{(1)}(E, k, p) = & -T^{\text{LO}}(E, k, p')D^{\text{LO}}(E, p') \otimes \left\{ \frac{My^2}{2} \left[ K_0(p', p'', E) + \frac{H(\Lambda)}{\Lambda^2} \right] \right. \\
& \left. \otimes [\Delta(E, p'') + \Delta(E, p')] \right\} \otimes D^{\text{LO}}(E, p'')T^{\text{LO}}(E, p'', p) \\
& - T^{\text{LO}}(E, k, p')D^{\text{LO}}(E, p') \otimes \frac{H^{(1)}(\Lambda)}{\Lambda^2} My^2 \otimes D^{\text{LO}}(E, p'')T^{\text{LO}}(E, p'', p) . \quad (6.13)
\end{aligned}$$

Using the STM equation (eq. (3.10)) yields:

$$\begin{aligned}
T^{(1)}(E, k, p) = & -\frac{\rho}{My^2} \int \frac{p'^2 dp'}{\pi} T^{\text{LO}}(E, k, p') \times \frac{3p^2/4 - EM - 1/a_2^2}{\left( \sqrt{3p^2/4 - EM} - 1/a_2 \right)^2} T^{\text{LO}}(E, p', p) \\
& - T^{\text{LO}}(E, k, p')D^{\text{LO}}(E, p') \otimes \frac{H^{(1)}(\Lambda)}{\Lambda^2} My^2 \otimes D^{\text{LO}}(E, p'') \\
& \times T^{\text{LO}}(E, p'', p) . \quad (6.14)
\end{aligned}$$

Using eq. (6.13),  $\Delta E_B$  is now given by:

$$\begin{aligned}
\Delta E_B(\Lambda) = & -\frac{1}{2} My^2 \psi^{\text{LO}}(p') \otimes \left\{ \left[ K_0(p', p'', E) + \frac{H(\Lambda)}{\Lambda^2} \right] \right. \\
& \left. \times [\Delta(E, p'') + \Delta(E, p')] \right\} \otimes \psi^{\text{LO}}(p'') - My^2 \psi^{\text{LO}}(p') \otimes \frac{H^{(1)}(\Lambda)}{\Lambda^2} \otimes \psi^{\text{LO}}(p'') . \quad (6.15)
\end{aligned}$$

Let us now consider the three-nucleon case and set eq. (6.15) to zero for  $^3\text{H}$  [43], with

$$\mathcal{B}(p) = \mathcal{B}^{3\text{H}}(p) \quad (6.16)$$

and

$$\psi(p) = \psi^{3\text{H}}(p) = \begin{pmatrix} \psi_t^{3\text{H}}(p) \\ \psi_s^{3\text{H}}(p) \end{pmatrix} . \quad (6.17)$$

The NLO correction to the  $^3\text{H}$  binding energy is given by:

$$\Delta E_B(\Lambda) = \sum_{\mu, \nu} \psi^{\text{LO}}(p) \otimes \mathcal{O}_{\mu\nu}^{(1)}(E_{3\text{H}}, p, p') \otimes \psi^{\text{LO}}(p') , \quad (6.18)$$

## CHAPTER 6. PERTURBATIVE CORRECTION TO THE THREE-BODY NUCLEAR WAVE FUNCTIONS

with

$$\mathcal{O}_{\mu\nu}^{(1)}(E_{3\text{H}}, p, p') = My_\mu y_\nu \left\{ \frac{1}{2} \left[ a_{\mu\nu} K_0(p, p', E_{3\text{H}}) + b_{\mu\nu} \frac{H(\Lambda)}{\Lambda^2} \right] \times \left[ \Delta_\mu(E_{3\text{H}}, p) + \Delta_\nu(E_{3\text{H}}, p') \right] + b_{\mu\nu} \frac{H^{(1)}(\Lambda)}{\Lambda^2} \right\}. \quad (6.19)$$

Where the diagrammatic representation of  $\Delta E_B(\Lambda)$  for the case of  $^3\text{H}$ , is shown in Fig. 6.2.

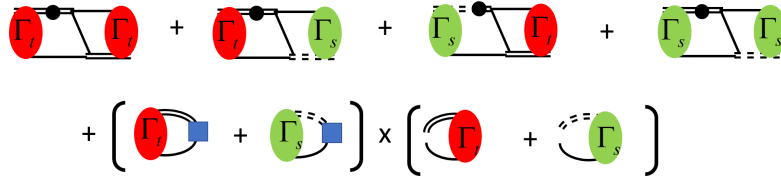


Figure 6.2: The NLO correction for  $^3\text{H}$  binding energy. The double lines are propagators of the two intermediate auxiliary fields,  $D_t$  (solid) and  $D_t^{np}$  (dashed). The red bubbles ( $\Gamma_t$ ) represent the triplet channel  $T=0, S=1$ , the green bubbles represent ( $\Gamma_s$ ) the singlet channel  $T=1, S=0$ . The black circles denote the NLO correction to the dibaryon propagator, while the blue squares denote the NLO correction to the three-body force ( $H^{(1)}(\Lambda)$ ).

Therefore, we find that the NLO three-body force has the form:

$$-\frac{H^{(1)}(\Lambda)}{\Lambda^2} = M \sum_{\mu, \nu=t,s} \psi_\mu^{3\text{H}}(p) \otimes \left\{ \frac{1}{2} y_\mu y_\nu \left[ a_{\mu\nu} K_0(p, p', E_{3\text{H}}) + b_{\mu\nu} \frac{H(\Lambda)}{\Lambda^2} \right] \times \left[ \Delta_\mu(E_{3\text{H}}, p) + \Delta_\nu(E_{3\text{H}}, p') \right] \right\} \otimes \psi_\nu^{3\text{H}}(p') \times \left[ M \sum_{\mu, \nu=t,s} y_\mu y_\nu \psi_\mu^{3\text{H}}(p) \otimes b_{\mu\nu} \otimes \psi_\nu^{3\text{H}}(p') \right]^{-1}. \quad (6.20)$$

Using the fact that:

$$\Gamma_\nu^{3\text{H}}(p') = M \sum_{\mu=t,s} y_\mu y_\nu \psi_\mu^{3\text{H}}(p) \otimes \left[ a_{\mu\nu} K_0(p, p', E_{3\text{H}}) + b_{\mu\nu} \frac{H(\Lambda)}{\Lambda^2} \right] \quad (6.21)$$

and

$$\Gamma_\mu^{3\text{H}}(p) = M \sum_{\nu=t,s} y_\mu y_\nu \left[ a_{\mu\nu} K_0(p, p', E_{3\text{H}}) + b_{\mu\nu} \frac{H(\Lambda)}{\Lambda^2} \right] \otimes \psi_\nu^{3\text{H}}(p'), \quad (6.22)$$

Equation (6.20) becomes:

$$\begin{aligned}
 -\frac{H^{(1)}[\Lambda]}{\Lambda^2} = & \frac{1}{2}M \sum_{\mu=t,s} \psi_{\mu}^{3\text{H}}(p) \otimes \left\{ \left[ \frac{\Delta_{\mu}(E_{3\text{H}}, p)}{D_{\mu}(E_{3\text{H}}, p)} + \frac{\Delta_{\mu}(E_{3\text{H}}, p')}{D_{\mu}(E_{3\text{H}}, p')} \right] 2\pi^2 \frac{\delta(p-p')}{p^2} \right\} \otimes \psi_{\mu}^{3\text{H}}(p') \\
 & \times \left[ M \sum_{\mu,\nu=t,s} y_{\mu}y_{\nu} \psi_{\mu}^{3\text{H}}(p) \otimes b_{\mu\nu} \otimes \psi_{\nu}^{3\text{H}}(E_{3\text{H}}, p') \right]^{-1}. \quad (6.23)
 \end{aligned}$$

A comparison of the analytical [44] and the numerical results of the NLO three-body force,  $H^{(1)}(\Lambda)$  of eq. (6.20), reveals that they are in good agreement, as shown in Fig. 6.3. The diagrammatic representation of  $\Delta E_B(\Lambda)$  is given in Appendix D.

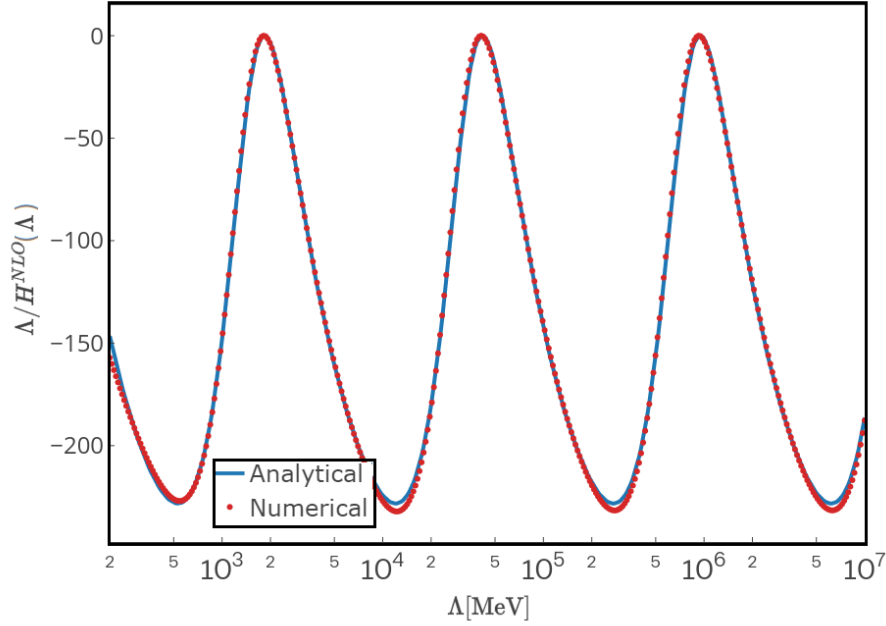


Figure 6.3: The three-body force,  $H(\Lambda)$ , at NLO as a function of the cutoff  $\Lambda$  in MeV for  ${}^3\text{H}$ . The solid curve is the analytical expression for  $H(\Lambda)$  taken from [44], while the dots are the numerical results based on eq. (6.20).

### 6.1.3 ${}^3\text{He}$ - correction to the three-body force and binding energy

The prediction of  $H^{(1)}(\Lambda)$  for  ${}^3\text{H}$  (see subsection 6.1.2) enables us to calculate the NLO corrections to  ${}^3\text{He}$  as well. Similarly to the LO calculation, we are using the three-body

## CHAPTER 6. PERTURBATIVE CORRECTION TO THE THREE-BODY NUCLEAR WAVE FUNCTIONS

force to determine the NLO correction to  ${}^3\text{He}$  binding energy, by assuming that  $H^{(1)}(\Lambda)$  has no isospin dependence [43]. The diagrammatic representation of  $\Delta E_B(\Lambda)$  for the case of  ${}^3\text{He}$ , is shown in Fig. 6.4. Similarly to  ${}^3\text{H}$ , the correction to the binding energy of  ${}^3\text{He}$  is a function of  $\Lambda$  only [43]:

$$\Delta E_B(\Lambda) = \sum_{\mu,\nu=t,s,pp} \psi_\mu^{3\text{He}}(p) \otimes \mathcal{O}_{\mu\nu}^{(1)}(E_{3\text{He}}, p, p') \otimes \psi_\nu^{3\text{He}}(p') , \quad (6.24)$$

$$\begin{aligned} \mathcal{O}_{\mu\nu}^{(1)}(E_{3\text{He}}, p, p') = & My_\mu y_\nu \left\{ \frac{1}{2} \left[ a'_{\mu\nu} K_0(p, p', E_{3\text{He}}) + a'_{\mu\nu} K_{\mu\nu}^C(p, p', E_{3\text{He}}) + b'_{\mu\nu} \frac{2H(\Lambda)}{\Lambda^2} \right] \right. \\ & \times [\Delta_\nu(E_{3\text{He}}, p) + \Delta_\nu(E_{3\text{He}}, p')] + b'_{\mu\nu} \frac{H^{(1)}(\Lambda)}{\Lambda^2} \Big\} \\ & + \alpha Q_0 \left( \frac{p^2 + p'^2 + \lambda^2}{2pp'} \right) \times (\delta_{\mu,t} \delta_{\nu,t} + 3\delta_{\mu,s} \delta_{\nu,s}) , \end{aligned} \quad (6.25)$$

where  $\alpha Q_0 \left( \frac{p^2 + p'^2 + \lambda^2}{2pp'} \right)$  originates from diagram (f) in Fig. 3.8.

In contrast to  ${}^3\text{H}$  and to  ${}^3\text{He}$  at LO, the numerical result of eq. (6.25) reveals that  $\Delta E_B$  for  ${}^3\text{He}$  diverges with the cutoff  $\Lambda$  (see Ref. [43]) and does not vanish. This contradicts the assumption that the addition of an isospin independent  $H^{\text{NLO}}(\Lambda)$  to  $T^{\text{NLO}}$  removes the cutoff dependence of  $\Delta E_B$  for both  ${}^3\text{H}$  and  ${}^3\text{He}$ . The solution to this issue is obtained by defining a different three-body force for  ${}^3\text{He}$ , such that:

$$E_{3\text{He}}^{\text{NLO}} = E_{3\text{He}}^{\text{LO}}(\Lambda) + \Delta E_B(\Lambda) = 7.72 \text{ MeV}, \quad (6.26)$$

which equals to the experimental binding energy of  ${}^3\text{He}$ , where  $E_{3\text{He}}^{\text{LO}}(\Lambda)$  is shown in Fig. 3.10.

Accordingly, the new three-body force,  $H^\alpha(\Lambda)$ , is defined and can be calculated numerically as:

$$\begin{aligned} \frac{H^\alpha(\Lambda)}{\Lambda^2} = & \left[ \frac{7.72 \text{ MeV} - E_{3\text{He}}^{\text{LO}}(\Lambda)}{\Lambda^2} - \sum_{\mu,\nu=t,s,pp} \psi_\mu^{3\text{He}}(p) \otimes \mathcal{O}_{\mu\nu}^{(1)}(E_{3\text{He}}, p, p') \otimes \psi_\nu^{3\text{He}}(p') \right] \\ & \times \left[ \sum_{\mu,\nu=t,s,pp} \psi_\mu^{3\text{He}}(p) \otimes b'_{\mu\nu}(E_{3\text{He}}, p, p') \otimes \psi_\nu^{3\text{He}}(p') \right]^{-1} \end{aligned} \quad (6.27)$$

while its analytical form is given in Refs. [43, 44].

## CHAPTER 6. PERTURBATIVE CORRECTION TO THE THREE-BODY NUCLEAR WAVE FUNCTIONS

The diagrammatic representation of  $\Delta E_B(\Lambda)$  for the case of  ${}^3\text{He}$ , is shown in Fig. 6.4.

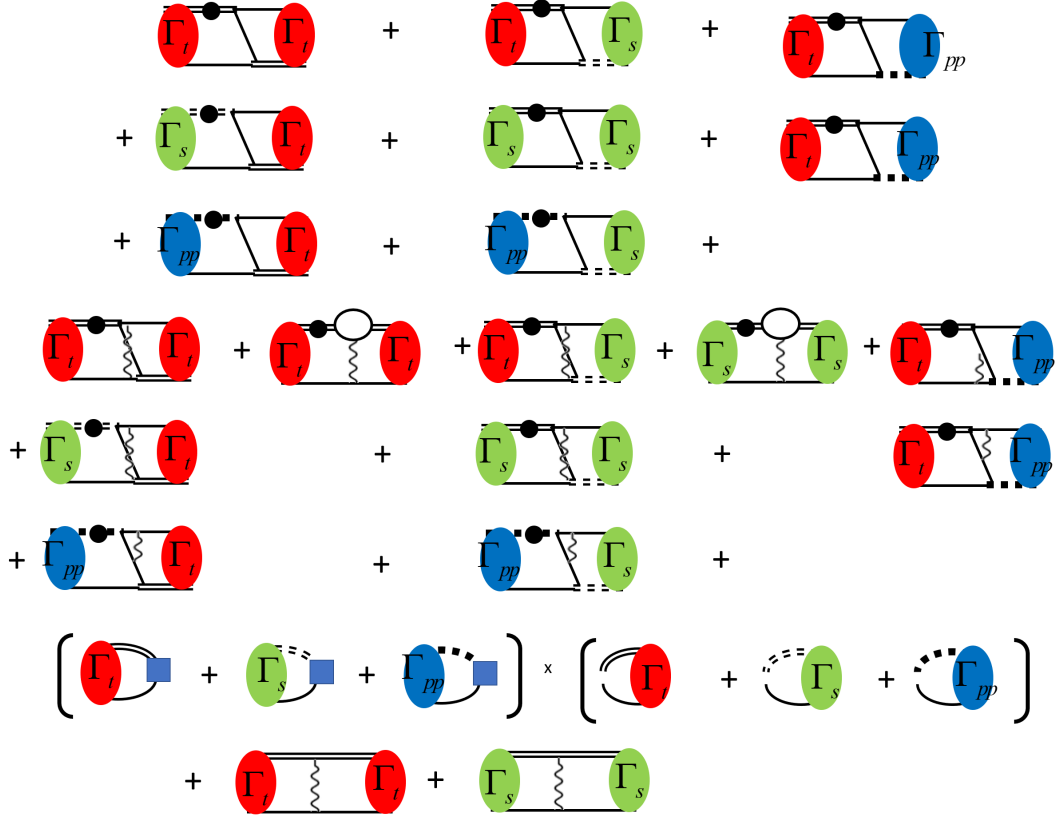


Figure 6.4: The NLO correction for  ${}^3\text{He}$  binding energy. The double lines are propagators of the two intermediate auxiliary fields,  $D_t$  (solid) and  $D_t^{np}$  (dashed) and  $D^{pp}$  (dotted). The red bubbles ( $\Gamma_t$ ) represent the triplet channel ( $T=0$ ,  $S=1$ ), the green bubbles represent ( $\Gamma_s$ ) the singlet channel ( $T=1$ ,  $S=0$ ) with an  $np$  dibaryon, while the blue bubbles ( $\Gamma_{pp}$ ) represent the singlet channel ( $T=1$ ,  $S=0$ ) with  $pp$  dibaryon. The black circles denote the NLO correction to the dibaryon propagator, while the blue squares denote the NLO correction to the three-body force ( $H^{(1)}(\Lambda) + H^{(\alpha)}(\Lambda)$ ).



## 6.2 NLO corrections to the three-body wave function

The **full** (non-perturbative in  $\alpha$ ) Faddeev equations for  ${}^3\text{He}$  (at LO in ERE) consist of two parts - the strong part and the Coulomb interaction part:

$$\begin{aligned} \Gamma_\mu^{3\text{He}}(p) = \sum_{\nu=t,s} My_\mu y_\nu \times & \left[ a'_{\mu\nu} K_0(p', p, E_{3\text{He}}) + b'_{\mu\nu} \frac{H(\Lambda)}{\Lambda^2} + c'_{\mu\nu} K_{\mu\nu}^C(p', p, E_{3\text{He}}) \right] \\ & \otimes D_\nu(E_{3\text{He}}, p') \Gamma_\nu^{3\text{He}}(E_{3\text{He}}, p') \\ & + My_\mu y_s \left[ a'_{\mu pp} K_0(p', p, E_{3\text{He}}) + b'_{\mu pp} \frac{H(\Lambda)}{\Lambda^2} \right] \otimes D_{pp}(E_{3\text{He}}, p') \Gamma_{pp}^{3\text{He}}(p'). \end{aligned} \quad (6.28)$$

Faddeev equations for  ${}^3\text{H}$  at LO are:

$$\Gamma_\mu^{3\text{H}}(p) = \sum_{\nu=t,s} My_\mu y_\nu \left[ a_{\mu\nu} K_0(p', p, E_{3\text{H}}) + b_{\mu\nu} \frac{H(\Lambda)}{\Lambda^2} \right] \otimes D_\nu(E_{3\text{H}}, p') \Gamma_\nu^{3\text{H}}(p'). \quad (6.29)$$

Using eq. (6.28), the  ${}^3\text{He}$ - ${}^3\text{H}$  binding energy difference, defined in subsection 5.4, is a function of the Coulomb part of eq. (6.28), using  ${}^3\text{H}$  wave-functions and assuming that  $\psi_s(E, p) = \psi_{nn}(E, p) = \psi_{np}(E, p) = \psi(E, p)_{pp}$ .

This implies that the  ${}^3\text{He}$ - ${}^3\text{H}$  binding energy difference can be written as a first-order perturbation in  $\alpha$ :

$$\Delta E(\Lambda) = \sum_{\mu,\nu} \psi_\mu^0(p) \otimes \mathcal{O}_{\mu\nu}^C(E, p, p') \otimes \psi_\nu^0(p'), \quad (6.30)$$

where  $\psi_{\mu,\nu}^0 = \psi_{\mu,\nu}^{3H}$  is the three-nucleon wave-function without the Coulomb interaction, and  $\mathcal{O}_{\mu,\nu}^C(E, p, p')$  are the Coulomb parts of eq. (6.28):

$$\mathcal{O}_{\mu\nu}^C(E, p, p') = c_{\mu\nu} K_{\mu\nu}^C(p, p, E) + \left[ a_{\mu\nu} K_0(p, p', E) + b_{\mu\nu} \frac{H(\Lambda)}{\Lambda^2} \right] \times \left[ \frac{D_{pp}(E, p) - D_s(E, p)}{D_s(E, p)^2} \right] \delta_{\nu,s}. \quad (6.31)$$

The NLO correction to the binding energy can also be written as a first-order pertur-

## CHAPTER 6. PERTURBATIVE CORRECTION TO THE THREE-BODY NUCLEAR WAVE FUNCTIONS

---

bation in  $Q/\Lambda_{\text{cut}}$ :

$$\begin{aligned}\Delta E_B(\Lambda) &= \sum_{\mu,\nu} \psi_\mu^{\text{LO}}(p) \otimes \mathcal{O}_{\mu\nu}^{(1)}(E, p, p') \otimes \psi_\nu^{\text{LO}}(p') \\ &= Z^{\text{LO}} \sum_{\mu,\nu} [\Gamma_\mu^{\text{LO}}(p) D_\mu^{\text{LO}}(E, p)] \otimes \mathcal{O}_{\mu\nu}^{(1)}(E, p, p') \otimes [D_\nu^{\text{LO}}(E, p') \Gamma_\nu^{\text{LO}}(p')] , \quad (6.32)\end{aligned}$$

where  $\mu, \nu$  are the different dibaryon channels and  $\mathcal{O}_{\mu\nu}^{(1)}(E, p, p')$  (defined in eq. (6.19)) is the NLO correction to the binding energy in terms of the different dibaryon channels. Since eqs. (6.30) and (6.32) have the same form, we can define the homogeneous scattering amplitude up to NLO such that for  $^3\text{H}$ :

$$\begin{aligned}\Gamma_\mu^{\text{NLO}}(p) &= \Gamma_\mu^{\text{LO}}(p) + \Gamma_\mu^{(1)}(p) = \\ &= \sum_{\nu=t,s} \left[ a_{\mu\nu} K_0(p, p', E_{^3\text{H}}) + b_{\mu\nu} \frac{H(\Lambda)}{\Lambda^2} + \mathcal{O}_{\mu\nu}^{(1)}(E_{^3\text{H}}, p, p') \right] \otimes D_\nu^{\text{LO}}(E_{^3\text{H}}, p') \Gamma_\nu^{\text{LO}}(p') , \quad (6.33)\end{aligned}$$

and for  $^3\text{He}$ ,

$$\begin{aligned}\Gamma_\mu^{\text{NLO}}(p) &= \Gamma_\mu^{\text{LO}}(p) + \Gamma_\mu^{(1)}(E_{^3\text{He}}, p) \\ &= \sum_{\nu=t,s,pp} \left\{ a'_{\mu\nu} [K_0(p, p', E_{^3\text{He}}) + K_{\mu\nu}^C(p, p', E_{^3\text{He}})] + b'_{\mu\nu} \frac{H(\Lambda)}{\Lambda^2} + \mathcal{O}_{\mu\nu}^{(1)}(E_{^3\text{He}}, p, p') \right\} \otimes D_\nu^{\text{LO}}(E_{^3\text{He}}, p') \Gamma_\nu^{\text{LO}}(p') , \quad (6.34)\end{aligned}$$

which are no longer Bethe-Salpeter equations, therefore, the Bethe-Salpeter normalization condition is not valid.

Having defined the NLO correction for the bound-state scattering amplitude,  $\Gamma_\mu$ , it is now possible to define the general form of a three-nucleon matrix element (such as an electroweak (EW) interaction) up to NLO:

$$\langle \mathcal{O}_{\text{EW}}^{\text{LO}} \rangle + \langle \mathcal{O}_{\text{EW}}^{(1)} \rangle = \sum_{\mu,\nu} \underbrace{\langle \psi_\mu^{\text{LO}} | \mathcal{O}_{\mu\nu}^{\text{LO}} | \psi_\nu^{\text{LO}} \rangle}_{\mathcal{O}_{\text{EW}}^{\text{LO}}} + \underbrace{\langle \psi_\mu^{\text{LO}} | \mathcal{O}_{\mu\nu}^{(1)} | \psi_\nu^{\text{LO}} \rangle + \langle \psi_\mu^{(1)} | \mathcal{O}_{\mu\nu}^{\text{LO}} | \psi_\nu^{\text{LO}} \rangle + \langle \psi_\mu^{\text{LO}} | \mathcal{O}_{\mu\nu}^{\text{LO}} | \psi_\nu^{(1)} \rangle}_{\mathcal{O}_{\text{EW}}^{(1)}} , \quad (6.35)$$

where:

$$\psi_\mu^{(1)}(p) = \sqrt{Z_1} \left\{ [D_\mu^{\text{NLO}}(E, p) - D_\mu^{\text{LO}}(E, p)] \Gamma_\mu^{\text{LO}}(p) + D_\mu^{\text{LO}}(E, p) \Gamma_\mu^{(1)}(p) \right\}, \quad (6.36)$$

where  $Z_1$  is the NLO correction to the three-nucleon normalization, which is determined by the  $A=3$  form factor, as will be discussed next.

### 6.3 The NLO normalization

Charge conservation puts strong constraints on the zero-momentum limit of the electric form factor. In this subsection, we, therefore, want to relate the three-nucleon charge form factor to the three-nucleon normalization procedure discussed here. Following Ref. [16], we expand the charge form factor of the deuteron up to NLO

$$F_C = F_C^{\text{LO}} + F_C^{(1)}, \quad (6.37)$$

where for the deuteron:

$$F_C^{\text{LO}}(0) = Z_d^{\text{LO}} \lim_{q \rightarrow 0} \frac{4\gamma_t}{q} \arctan\left(\frac{q}{4\gamma_t}\right) = 1. \quad (6.38)$$

Up to NLO, one finds that:

$$F_C(0) = Z_d^{\text{NLO}} \lim_{q \rightarrow 0} \frac{4\gamma_t}{q} \arctan\left(\frac{q}{4\gamma_t}\right) - Z_d^{\text{LO}} \lim_{q \rightarrow 0} \gamma_t \rho_t \frac{4\gamma_t}{q} \arctan\left(\frac{q}{4\gamma_t}\right). \quad (6.39)$$

We can rewrite this as:

$$\left( Z_d^{\text{LO}} + Z_d^{(1)} \right) F_C^{(0)} - Z_d^{\text{LO}} \gamma_t \rho_t F_C^{(0)} = 1 \rightarrow Z_d^{(1)} - \gamma_t \rho_t = 0. \quad (6.40)$$

From eq. (6.39), it is easy to show that up to NLO:

$$Z_d^{\text{NLO}} - \gamma_t \rho_t = 1 \rightarrow Z_d^{\text{NLO}} = 1 + \gamma_t \rho_t, \quad (6.41)$$

which equals 1.408, as discussed in Chapter 2.

Similarly, the  $A = 3$  NLO normalization is obtained from the  $^3\text{H}$  and  $^3\text{He}$  form factor up to NLO [16, 50, 52]. Based on eq. (5.11), it is easy to show that at LO, the  $A = 3$  form

## CHAPTER 6. PERTURBATIVE CORRECTION TO THE THREE-BODY NUCLEAR WAVE FUNCTIONS

---

factor is given by:

$$F_C^{(0)}(q) = \sum_{\mu,\nu} \psi_\mu^{\text{LO}}(E', p') \otimes \mathcal{O}_{\mu\nu}^{FC(1B)}(q) \otimes \psi_\nu^{\text{LO}}(E, p) , \quad (6.42)$$

where:

$$\mathcal{O}_{\mu\nu}^{FC(1B)}(q) = y_\mu y_\nu \left\{ d_{\mu\nu}^{ii} \hat{\mathcal{I}}(q_0, q) + a_{\mu\nu}^{ii} \left[ \hat{\mathcal{K}}(q_0, q) + \hat{\mathcal{K}}_{\mu\nu}^C(q_0, q) \right] \right\} , \quad (6.43)$$

and  $d_{\mu\nu}^{ii}, a_{\mu\nu}^{ii}$  were defined in eqs. (5.13) and (5.14).

Based on eq. (6.35), up to NLO,  $F_C(0)$  is given by:

$$\begin{aligned} F_C^{\text{NLO}}(0) &= F_C^{(0)}(0) + F_C^{(1)}(0) = \sum_{\mu,\nu} \psi_\mu^{\text{LO}}(E, p') \otimes \mathcal{O}_{\mu\nu}^{FC(1B)}(0) \otimes \psi_\nu^{\text{LO}}(E, p) \\ &+ \frac{1}{2} \left[ \psi_\mu^{(1)}(E, p') \otimes \mathcal{O}_{\mu\nu}^{FC(1B)}(0) \otimes \psi_\nu^{\text{LO}}(E, p) + \psi_\mu^{\text{LO}}(E, p') \otimes \mathcal{O}_{\mu\nu}^{FC(1B)}(0) \otimes \psi_\nu^{(1)}(E, p) \right] \\ &+ \psi_\mu^{\text{LO}}(E, p') \otimes \mathcal{O}_{\mu\nu}^{FC(2B)}(0) \otimes \psi_\nu^{\text{LO}}(E, p) = F_C^{(0)}(0) = 1 , \end{aligned} \quad (6.44)$$

where:

$$\mathcal{O}_{\mu\nu}^{FC(1B)}(0) = \mathcal{O}_{\mu\nu}^{\text{norm}}(E_i) , \quad (6.45)$$

and  $i = {}^3\text{H}, {}^3\text{He}$ .

Since the two-body term is a result of the  $A_0$  photons, which couple only the triplet channel, the two-body term can be written as [52]:

$$\mathcal{O}_{\mu\nu}^{FC(2B)}(0) = \frac{2\pi^2}{p^2} \delta(p - p') \delta_{\mu,t} \delta_{\nu,t} . \quad (6.46)$$

By substituting eqs. (6.45) and (6.46) in eq. (6.44), one finds that the NLO correction to the triton form factor,  $F_C^{(1)}(0)$ , is given by:

$$\begin{aligned} F_C^{(1)}(0) &= \frac{1}{2} \sum_{\nu=t,s} \left\{ \psi_\mu^{(1)}(p) \otimes \mathcal{O}_{\mu\nu}^{\text{norm}}(E_{3\text{H}}) \otimes \psi_\nu^{\text{LO}}(p') + \psi_\mu^{\text{LO}}(p) \otimes \mathcal{O}_{\mu\nu}^{\text{norm}}(E_{3\text{H}}) \otimes \psi_\nu^{(1)}(p') \right\} \\ &- \frac{2}{3} \psi_t^{\text{LO}}(p) \otimes \frac{2\pi^2}{p^2} \delta(p - p') \otimes \psi_t^{\text{LO}}(p') = 0 , \end{aligned} \quad (6.47)$$

## CHAPTER 6. PERTURBATIVE CORRECTION TO THE THREE-BODY NUCLEAR WAVE FUNCTIONS

---

and similarly for  ${}^3\text{He}$ :

$$F_C^{(1)}(0) = \frac{1}{2} \sum_{\nu=t,s} \left\{ \psi_\mu^{(1)}(p) \otimes \mathcal{O}_{\mu\nu}^{\text{norm}}(E_{3\text{He}}) \otimes \psi_\nu^{\text{LO}}(p') + \psi_\mu^{\text{LO}}(p) \otimes \mathcal{O}_{\mu\nu}^{\text{norm}}(E_{3\text{He}}) \otimes \psi_\nu^{(1)}(p') \right\} \\ - \frac{2}{3} \psi_t^{\text{LO}}(p) \otimes \frac{2\pi^2}{p'^2} \delta(p - p') \otimes \psi_t^{\text{LO}}(p') = 0, \quad (6.48)$$

where for both  ${}^3\text{H}$  and  ${}^3\text{He}$ ,  $\psi_\mu^{(1)}(p)$  is the **normalized** NLO correction to the three-nucleon wave-function<sup>1</sup>.

---

<sup>1</sup>Note that by defining eqs. (6.47) and (6.48) to be equal to 0, we are consistent with Refs. [50, 52] in which  $F_1(0) = F^{\text{LO}}(0) + F^{\text{NLO}}(0) = 1$ , where  $F_1(0)$  is the three-nucleon triton charge form factor up to NLO.

## $A = 2, 3$ Electromagnetic reactions

In this chapter, we present our calculations for low-energy electromagnetic reactions, which will be used later (chapter 10) to study the consistency of  $\not\pi$ EFT in the transition from  $A = 2$  to  $A = 3$  nuclei and vice-versa. These reactions are essential for understanding the nuclear structure and the dynamics of light nuclei, and therefore a comparison between  $\not\pi$ EFT prediction and available experimental data can confirm the validity of  $\not\pi$ EFT for both physical and non-physical pion mass.

In this thesis, we focus on four well-measured low-energy electromagnetic “ $M_1$ ” reactions, *i.e.*, the magnetic moments of the bound nuclei  $\langle \hat{\mu}_d \rangle$ ,  $\langle \hat{\mu}^3_{\text{H}} \rangle$ ,  $\langle \hat{\mu}^3_{\text{He}} \rangle$  [53, 54], and the cross-section  $\sigma_{np}$  for the radiative capture  $n + p \rightarrow d + \gamma$  for thermal neutrons [55]. While the matrix elements of the  $A = 2$  reactions (  $\langle \hat{\mu}_d \rangle$  and  $\sigma_{np}$  ) were predicted using  $\not\pi$ EFT up to NLO [16, 28, 82], the matrix elements of the  $A = 3$  reactions ( $^3\text{H}$  and  $^3\text{He}$  magnetic moments) haven’t been predicted using  $\not\pi$ EFT until recently. However, recent studies have shown much progress in this front. First, a recent calculation employing configuration space Schrödinger equation representation of  $\not\pi$ EFT hinted a regular behavior of the  $A = 3$  magnetic properties, at least at small cutoffs of the theory [83]. Second, a new method to calculate  $A = 3$  form-factors has been used to calculate  $A = 3$  magnetic moments, using an  $\text{SU}(4)$  symmetry approximation for the nucleon, without including the Coulomb interactions for  $^3\text{He}$  [52, 84].

In this chapter we use the formalism developed in Chapter 5 to calculate the  $A = 3$  matrix elements of the magnetic moments within  $\not\pi$ EFT.

## 7.1 $M_1$ observables in the $A = 2, 3$ systems

$M_1$  observables at vanishing momentum transfer are related to the electromagnetic nuclear current density  $\hat{\mathcal{J}}(\vec{q})$  at vanishing momentum transfer  $\vec{q}$ . Explicitly, the magnetic moment of a state is just the expectation value of the operator:

$$\hat{\mu} = -\frac{i}{2} \vec{\nabla}_q \times \hat{\mathcal{J}}(\vec{q})|_{q=0}, \quad (7.1)$$

while the cross-section of the thermal neutron radiative capture  $n + p \rightarrow d + \gamma$  is proportional to the transition matrix element of the same operator between the neutron and proton,  $S = 0$  state, to the deuteron,  $S = 1$  state [16, 28, 57].

Thus, to calculate these observables, one needs the nuclear amplitudes of the  $A = 2, 3$  nuclei, as well as the nuclear current in response to a magnetic photon. The resulting  $M_1$  strengths are just matrix elements of the nuclear current between the nuclear amplitudes.

## 7.2 Magnetic photon currents in pionless EFT

A magnetic photon interaction with a nucleus can be modeled effectively as an interaction with ever growing clusters of nucleons. In  $\not\pi$ EFT, LO includes a single nucleon interaction with a photon, while the interaction of a magnetic photon with two-body clusters appearing first at NLO. The electromagnetic Lagrangian is given in Chapter 2 by eqs. (2.43) and (2.44).

Applying the H-S transformation on eq. (2.44) leads to the interaction in terms of the dibaryon fields (see Ref. [28] and Appendix C):

$$\mathcal{L}_{\text{magnetic}}^\mu = \frac{e}{2M} \left[ N^\dagger (\kappa_0 + \kappa_1 \tau_3) \vec{\sigma} \cdot \vec{B} N - L'_1(t^\dagger s + s^\dagger t) \cdot \vec{B} + L'_2(t^\dagger t) \cdot \vec{B} \right], \quad (7.2)$$

where the two-dibaryons-one-photon coefficients are given by:

$$L'_1(\mu) = -\frac{\rho_t + \rho_s}{\sqrt{\rho_t \rho_s}} \kappa_1 + l_1(\mu), \quad (7.3)$$

$$L'_2(\mu) = l_2(\mu) - 2\kappa_0, \quad (7.4)$$

where  $l_1$  and  $l_2$  are RG invariant combinations:

$$l_1(\mu) = \frac{M}{\pi\sqrt{\rho_t\rho_s}} L_1 \left( \mu - \frac{1}{a_t} \right) \left( \mu - \frac{1}{a_s} \right), \quad (7.5)$$

$$l_2(\mu) = \frac{2M}{\pi\rho_t} L_2 \left( \mu - \frac{1}{a_t} \right)^2 \quad (7.6)$$

and  $a_{t,s}$  are the spin-triplet and -singlet scattering lengths,  $\rho_{t,s}$  are the respective effective ranges and  $\mu$  is the renormalization scale. Note that since  $[L_1, L_2] = \text{fm}^{-4}$ ,  $l_1(\mu), l_2(\mu)$  are dimensionless. Here  $\mu$  is taken consistently as the three-body regularization scale  $\Lambda = \mu$ , contrary to past works, where it was taken at the  $\pi$ EFT breakdown scale  $\mu = m_\pi$ . We note that since the photon field  $\vec{\mathcal{A}}$  fulfills  $\vec{B} = \vec{\nabla} \cdot \vec{\mathcal{A}}(\vec{x})$ , then the scattering operator  $\hat{\mu}$  is given by the prefactor of  $\vec{B}$  in eqs. (2.43) and (7.2). Feynman rules are extracted trivially, using this fact.

### 7.2.1 Diagrammatic representation of the electromagnetic matrix elements

#### Two-nucleon electromagnetic matrix elements

The matrix element of  $\hat{\mu}$  (Eq. 7.1) between two-nucleon states is represented diagrammatically in Fig. 7.1. This matrix element represents  $\sigma_{np} (\langle \hat{\mu}_d \rangle)$  if the initial state is in relative  $^1S_0$  ( $^3S_1$ ) state, respectively.

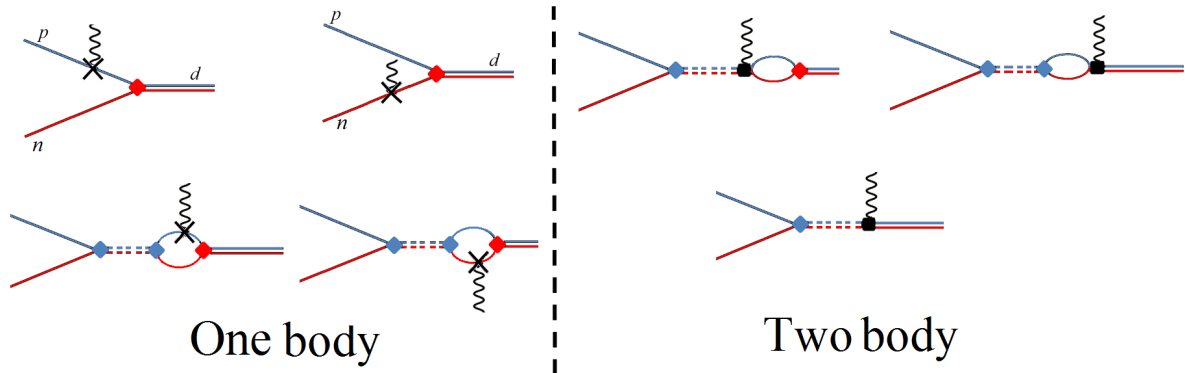


Figure 7.1: Diagrammatic representation of  $\hat{\mu}$  between two-body states, up to NLO.  $\hat{\mu}$  insertion is represented by the photon vertex. The double lines are the NLO propagator of the two dibaryon fields.  $D_t$  (solid) and  $D_s$  (dashed). The red lines represent the neutron propagator while the blue lines represent the proton propagator. A spin-singlet dibaryon-nucleon-nucleon vertex is proportional to  $y_s$  (blue diamond), while a spin-triplet dibaryon-nucleon-nucleon vertex is proportional to  $y_t$  (red diamond).



From Fig. 7.1, one concludes that up to NLO, the magnetic moment of the deuteron is given by:

$$\langle \hat{\mu}_d \rangle = Z_d^{\text{NLO}}(2\kappa_0) + Z_d^{\text{LO}}[\gamma_t \rho_t L'_2(\mu)] = 2\kappa_0 + \gamma_t \rho_t l_2(\mu) = 2\kappa_0(1 + l'_2(\mu)), \quad (7.7)$$

where we implicitly define the net NLO two-body contribution as:  $l'_2(\mu) \equiv \gamma_t \rho_t \frac{l_2(\mu)}{2\kappa_0}$ . We note that  $l'_2$  and  $l_2$  are not of the same order of magnitude, since  $\frac{\gamma_t \rho_t}{2\kappa_0} = \mathcal{O}\left(\frac{Q}{\Lambda_{\text{cut}}}\right)$ .

The cross-section of thermal neutron capture on a proton is related to the matrix element  $Y$  by:

$$\sigma_{np} = 2\alpha\pi \frac{(\gamma_t^2 + q^2/4)^3 a_s^2}{M^4 q \gamma_t} Y_{np}^2 \approx 2\alpha\pi \frac{\gamma_t^5 a_s^2}{M^4 q} (2\kappa_1)^2 (Y'_{np})^2, \quad (7.8)$$

where  $Y_{np}$  is the sum over all the diagrams of Fig. 7.1 and  $q = 0.0069$  MeV is the momentum transfer [52, 85]<sup>1</sup>.

Since  $\langle \hat{\mu}_d \rangle$  is approximately 1, we define the normalized matrix element,  $Y'_{np} = Y_{np}/(2\kappa_1)$ , so that both  $A = 2$  matrix elements and their associated LECs,  $l'_1(\mu)$  and  $l'_2(\mu)$  can be compared with each other. This normalized matrix element is also obtained by Fig. 7.1 to yield:

$$Y'_{np} = \sqrt{Z_d} \left[ \left(1 - \frac{1}{\gamma_t a_s}\right) + \frac{\gamma_t \sqrt{\rho_t \rho_s}}{4\kappa_1} L'_1(\mu) \right], \quad (7.9)$$

and up to NLO is given by:

$$Y'_{np} = \sqrt{Z_d^{\text{NLO}}} \left(1 - \frac{1}{\gamma_t a_s}\right) + \sqrt{Z_d^{\text{LO}}} \frac{\gamma_t \sqrt{\rho_t \rho_s}}{4\kappa_1} L'_1(\mu) = \sqrt{Z_d^{\text{NLO}}} \left(1 - \frac{1}{\gamma_t a_s}\right) - \gamma_t \frac{\rho_t + \rho_s}{4} + l'_1(\mu), \quad (7.10)$$

where here the net NLO two-body contribution is defined by  $l'_1(\mu) \equiv \gamma_t \sqrt{\rho_t \rho_s} \frac{l_1(\mu)}{4\kappa_1}$ . We note that  $l'_1$  is about an order of magnitude smaller than  $l_1$ , due to a (numerical) suppression originating in  $4\kappa_1 \approx 10$ .

The above expressions up to higher order corrections can be found in the literature (see, e.g., Refs. [28, 82]).

---

<sup>1</sup>In this work, similar to Refs. [52, 85], we use  $q = 2Mv_{\text{lab}} = 2 \cdot M2200\text{M/s} = 0.0069$  MeV. This value is higher than the value used in Refs. [28, 82],  $q = 0.068$  MeV. We found that  $l'_1(q = 0.0069 \text{ MeV})$  is higher than  $l'_1(q = 0.0068 \text{ MeV})$  by 20%(10%) for the Z- (ERE-) parameterization.

### Three-nucleon electromagnetic matrix elements

The three-body diagrams representing the matrix elements of  $\hat{\mu}$  appear in Fig. 7.2. At LO, only the diagrams that include a one-body electromagnetic interaction coupled to  $\kappa_0 - \kappa_1 = \mu_n$  and  $\kappa_1 + \kappa_0 = \mu_p$  contribute to the magnetic moment (left panels of Fig. 7.2). At NLO, these interactions are augmented with a single NLO insertion, in the nuclear amplitude or in the propagators, as well as with the diagrams that include the two-body interactions coupled to the two-body LECs:  $l'_1$  and  $l'_2$  (right panels of Fig. 7.2). As the latter interactions are at NLO, the bubbles and propagators are taken at LO.

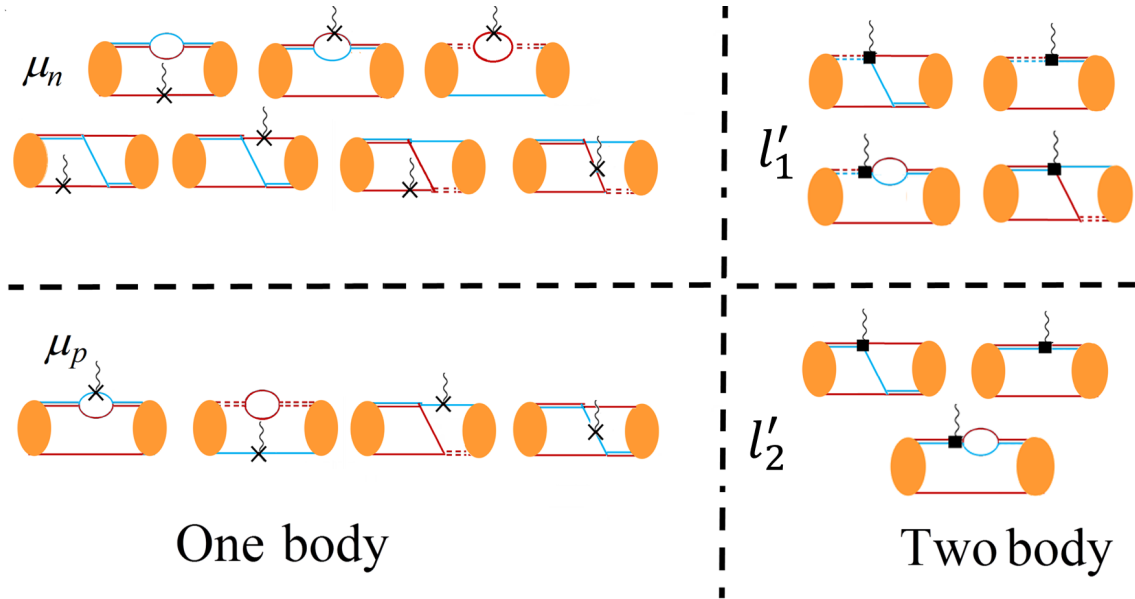


Figure 7.2: Different topologies of the diagrams contributing to the triton magnetic moment. The double lines are the propagators of the two dibaryon fields.  $D_t$  (solid) and  $D_s$  (dashed for  $nn$  and  $np$ ), where the red line is the neutron and the blue line is the proton. Most of the diagrams couple both the triplet and the singlet channels. The diagrams with one-body interactions are coupled to  $(\kappa_0 - \kappa_1) = \mu_n$  (upper) and  $(\kappa_0 + \kappa_1) = \mu_p$  (lower). The two-body interactions are coupled to both  $l'_1$  (upper) and  $l'_2$  (lower).

The  $A = 3$  magnetic moment expectation value,  $\langle \hat{\mu} \rangle = \underbrace{\langle \hat{\mu}^{(1B)} \rangle}_{\text{one-body}} + \underbrace{\langle \hat{\mu}^{(2B)} \rangle}_{\text{two-body}}$ , can be calculated numerically (with the experimental input parameters shown in Tab. 2.1) by summing over all diagrams up to NLO, as shown in Fig. 7.2.

$$\begin{aligned}
 \langle \hat{\mu}^{(1B)} \rangle &= \frac{\langle \frac{1}{2} \|\boldsymbol{\sigma}\| \frac{1}{2} \rangle}{\sqrt{6}} \times \\
 &\sum_{\mu, \nu} \psi_{\mu}^j(p') \otimes y_{\mu} y_{\nu} (\kappa_0 + \kappa_1 \tau_3) \left[ d_{\mu\nu}^{ij} \hat{\mathcal{I}}(0, 0) \right. \\
 &\quad \left. + a_{\mu\nu}^{ij} \hat{\mathcal{K}}(0, 0) \right] \otimes \psi_{\nu}^i(p) , \quad (7.11)
 \end{aligned}$$

where for  ${}^3\text{H}$ :

$$\begin{array}{c|ccc}
 & \mu & & \\
 & \nu & & \\
 \hline
 d_{\mu\nu}^{ii} = & t & \frac{2}{3}\mu_n + \frac{1}{3}\mu_p & \mu_n - \mu_p & 0 \\
 & np & \frac{\mu_n - \mu_p}{3} & \mu_p & 0 \\
 & nn & 0 & 0 & \mu_n
 \end{array} , \quad (7.12)$$

and

$$\begin{array}{c|ccc}
 & \nu & & \\
 & \mu & & \\
 \hline
 a_{\mu\nu}^{ii} = & t & -\left(\frac{5}{3}\mu_p - \frac{2}{3}\mu_n\right) & \mu_p + 2\mu_n & 3\mu_p \\
 & np & \frac{2}{3}\mu_n + \frac{1}{3}\mu_p & 2\mu_n - \mu_p & -\mu_p \\
 & nn & 2\mu_p & -2\mu_p & 0
 \end{array} , \quad (7.13)$$

and for  ${}^3\text{He}$ :

$$\begin{array}{c|ccc}
 & \mu & & \\
 & \nu & & \\
 \hline
 d_{\mu\nu}^{ii} = & t & \frac{2}{3}\mu_p + \frac{1}{3}\mu_n & \mu_p - \mu_n & 0 \\
 & np & \frac{\mu_p - \mu_n}{3} & \mu_n & 0 \\
 & nn & 0 & 0 & \mu_p
 \end{array} \quad (7.14)$$

and

$$\begin{array}{c|ccc}
 & \nu & & \\
 & \mu & & \\
 \hline
 a_{\mu\nu}^{ii} = & t & -\left(\frac{5}{3}\mu_n - \frac{2}{3}\mu_p\right) & \mu_n + 2\mu_p & 3\mu_n \\
 & np & \frac{2}{3}\mu_p + \frac{1}{3}\mu_n & 2\mu_p - \mu_n & -\mu_n \\
 & nn & 2\mu_n & -2\mu_n & 0
 \end{array} . \quad (7.15)$$

Note that for  $^3\text{H}$  and  $^3\text{He}$ , eq. (7.11) is defined such that:

$$\begin{aligned} \langle \hat{\mu}^{(1\text{B})} \rangle = \kappa_0 \sum_{\mu, \nu} \psi_{\mu}^j(p') \otimes y_{\mu} y_{\nu} \left[ d_{\mu\nu}^{ii} \hat{\mathcal{I}}(0, 0) \right. \\ \left. + a_{\mu\nu}^{ii} \hat{\mathcal{K}}(0, 0) \right] \otimes \psi_{\nu}^i(p) = \kappa_0, \end{aligned} \quad (7.16)$$

for the case that  $\mu_n = \mu_p = \kappa_0$ , since:

$$\begin{aligned} \sum_{\mu, \nu} \psi_{\mu}^i(p') \otimes y_{\mu} y_{\nu} \left[ d_{\mu\nu}^{ii} \hat{\mathcal{I}}(0, 0) + \right. \\ \left. a_{\mu\nu}^{ii} \hat{\mathcal{K}}(0, 0) \right] \otimes \psi_{\nu}^i(p) = 1. \end{aligned} \quad (7.17)$$

The three-nucleon magnetic moment matrix element that contains **two-body** interactions,  $\hat{\mu}^{(2\text{B})}$ , can be written as the sum of all two-body interactions (see Ref. [48]):

$$\begin{aligned} \langle \mu^{(2\text{B})} \rangle = + \frac{2}{3} L'_2 \langle \psi_t(p) | \psi_t(p) \rangle \\ + L'_1 a_{ts}^{(2)} [\langle \psi_t(p) | \psi_{np}(p) \rangle + h.c.], \end{aligned} \quad (7.18)$$

where

$$a_{ts}^{(2)} = \begin{cases} -\frac{2}{3} & ^3\text{H} \\ 1 & ^3\text{He}. \end{cases} \quad (7.19)$$

Figure 7.3 (a)+(b) present a one-body  $A = 3$  matrix element coupled to  $i \frac{e}{2M} (\kappa_0 + \kappa_1 \tau_3) \boldsymbol{\sigma}$ ,  $\mu_n$  in the case of neutron and  $\mu_p$  in the case of proton.

At LO, Fig. 7.3 (a) is given by:

$$\begin{aligned} \mu_n y_t^2 \int \frac{d^3 p}{(2\pi)^3} \frac{d^3 p'}{(2\pi)^3} \frac{2\pi^2}{p^2} \psi_t(E_{3\text{H}}, p) \frac{M^2}{4\pi \sqrt{3p^2 - 4ME_{3\text{H}}}} \delta(p - p') \cdot \psi_t(E_{3\text{H}}, p') = \\ \mu_n M y_t^2 \langle \psi_{\mu}^i(E_{3\text{H}}, p') | \mathcal{I}^{q=0}(E_{3\text{H}}, 0, p, p') | \psi_{\nu}^i(E_{3\text{H}}, p) \rangle, \end{aligned} \quad (7.20)$$

Fig. 7.3 (b) is given by:

$$\begin{aligned} \mu_p y_t^2 \int \frac{d^3 p}{(2\pi)^3} \frac{d^3 p'}{(2\pi)^3} \psi_t(E_{3\text{H}}, p) \cdot \frac{M^2}{p^2 (p^2 - 2ME_{3\text{H}}) + (p^2 - ME_{3\text{H}})^2 + p'^4} \psi_t(E_{3\text{H}}, p') = \\ \mu_p M y_t^2 \langle \psi_{\mu}^i(E_{3\text{H}}, p') | \mathcal{K}^{q=0}(p, p', E_{3\text{H}}, 0) | \psi_{\nu}^i(E_{3\text{H}}, p) \rangle, \end{aligned} \quad (7.21)$$

where  $i = {}^3\text{H}$ .

Figure 7.3 (c) (two-body operator) is given by:

$$l'_2 \int \frac{d^3p}{(2\pi)^3} \psi_t(E_{3\text{H}}, p)^2. \quad (7.22)$$

The  $A = 3$  magnetic moment expectation value,  $\langle \hat{\mu} \rangle = \langle \hat{\mu}^{(1\text{B})} \rangle + \langle \hat{\mu}^{(2\text{B})} \rangle$ , can be calculated

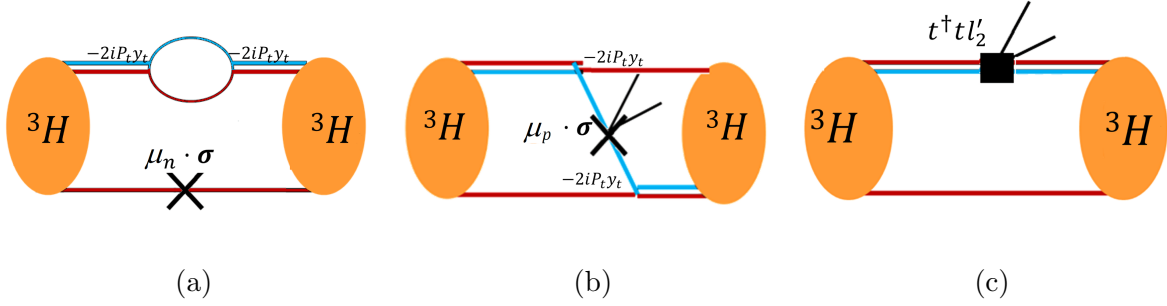


Figure 7.3: Three of the diagrams contributing to the triton magnetic moment. The one-body diagrams which are coupled to  $\mu_n \cdot \sigma$  (a) and  $\mu_p \cdot \sigma$  (b), diagram (c) is coupled to the two-body LEC  $l'_2$ . The double lines are the propagators of the two dibaryon field  $D_t$  (solid). The red lines represent the neutron propagator while the blue lines represent the proton propagator.

numerically (with experimental input parameters shown in Tab. 2.1)) by summing over all diagrams up to NLO as shown in Fig. 7.2.

## 7.3 Results

Evidently, the  $A = 2, 3$   $M_1$  observables depend on the physical (RG invariant) values of the LECs, *i.e.*,  $l'_1{}^\infty \equiv l'_1(\mu = \Lambda \rightarrow \infty)$  and  $l'_2{}^\infty \equiv l'_2(\mu = \Lambda \rightarrow \infty)$ . In past works, the experimental values of the  $A = 2$  observables ( $\sigma_{np}$  and  $\langle \hat{\mu}_d \rangle$ ) were used to fix these LECs [28, 56]. Here, we calculate consistently the  $A = 2, 3$   $M_1$  observables ( $\langle \hat{\mu}_{3\text{H}} \rangle$ ,  $\langle \hat{\mu}_{3\text{He}} \rangle$ ,  $\langle \hat{\mu}_d \rangle$  and  $Y'_{np}$ ), which depend on the same LECs, so we can extract these LECs from two observables and then use them to predict the remaining observables. Therefore, we have six independent ways for calibrating the LECs. These calibrations will be used later in this thesis for the evaluating the stability and consistency of  $\not\pi$ EFT for the simultaneous description of  $A = 2$  and  $A = 3$  systems up to NLO and for estimating theoretical uncertainty (Chapter 10).

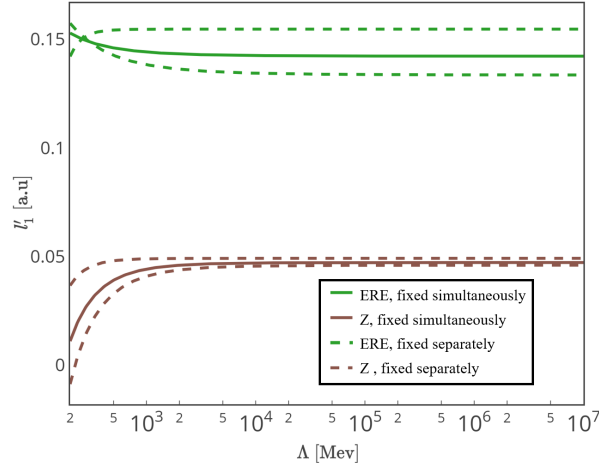
Table 7.1 summarizes our predictions for  $l_1^\infty$ ,  $l_2^\infty$  and  $M_1$  observables up to NLO in both  $Z$ - and ERE- parameterization. For each row, the ' $\star$ ' denotes the  $M_1$  observables used for  $l_1^\infty$ ,  $l_2^\infty$  calibration, by comparing our calculation to the experimental data. For example, the first row of Tab. 7.1 shows the LECs fixed from  $A = 3$  observables and our prediction of  $A = 2$  magnetic observables, while the second row of Tab. 7.1 shows the LECs fixed from  $A = 2$  observables and the prediction of  $A = 3$  magnetic observables. Note that for each  $M_1$  observable we have three predictions.

	$l_1^\infty/10^{-2}$	$l_2^\infty/10^{-2}$	$\langle\hat{\mu}_{3H}\rangle[\text{nNM}]$	$\langle\hat{\mu}_{3He}\rangle[\text{nNM}]$	$\langle\hat{\mu}_d\rangle[\text{nNM}]$	$Y'_{np}$
	4.72 (14.2)	-1.55 ( 4.1 )	$\star$	$\star$	0.87 (0.92)	1.253 (1.31)
	4.66 (9.0)	-2.55 (-2.55)	2.978 (2.76)	-2.145 (-1.89)	$\star$	$\star$
	4.66 (9.0)	-2.4 (29)	$\star$	-2.144 (-1.66)	0.86 (1.17)	$\star$
	4.66 (9.0)	-0.13 (-31)	2.996 (2.59)	$\star$	0.88 (0.61)	$\star$
	4.92 (15.2)	-2.55 (-2.55)	$\star$	-2.143 (-2.23)	$\star$	1.255 (1.32)
	4.60 (13.4)	-2.55 (-2.55)	2.967 (2.91)	$\star$	$\star$	1.253 (1.30)
Mean	4.73 (13.0)	-1.66 ( -0.04)	2.98 (2.75)	-2.144 (-1.93)	0.87 ( 0.89)	1.253 (1.31)
$\Delta$	0.2 (2.8)	1.11 (25)	0.015 ( 0.16)	0.001 ( 0.28)	0.01 (0.26)	0.001 (0.01)
Exp data			2.979	-2.128	0.857	1.253

Table 7.1: Numerical results for our prediction for  $l_1^\infty, l_2^\infty$  and  $A = 2, 3$   $M_1$  observables. The nominal value is calculated using  $Z$ -parameterization, while the number in brackets is calculated using the ERE-parameterization. Mean denotes the mean value of the  $M_1$  observable based on its three predictions while  $\Delta$  denotes the standard deviation of these predictions.

A closer examination of the LECs mean and standard deviation reveals big differences between the LECs. For the case of the  $Z$ -parameterization we find that while  $l_1^\infty$  has minor dependence on the  $M_1$  observables used for its calibration, *i.e.*,  $\Delta l_1^\infty/l_1^\infty \approx 3\%$ , the stranded deviation of  $l_2^\infty$  is of the same order of magnitude as  $l_2^\infty$ , *i.e.*,  $\Delta l_2^\infty/l_2^\infty \approx 70\%$ . For the case of the ERE-parameterization, we find that the differences between  $l_1^\infty$  and  $l_2^\infty$  are more significant; while  $\Delta l_{1ERE}^\infty/l_{1ERE}^\infty \approx 21\%$ ,  $\Delta l_{2ERE}^\infty$  is two orders of magnitude larger than  $l_{2ERE}^\infty$ . This behavior of  $l_1^\infty, l_2^\infty$  will be discussed later in this thesis (Chapter 10), and will use for estimating the theoretical uncertainty of  $\not\sim\text{EFT}$ .

## 7.4 Magnetic interactions in Lattice QCD



(a)

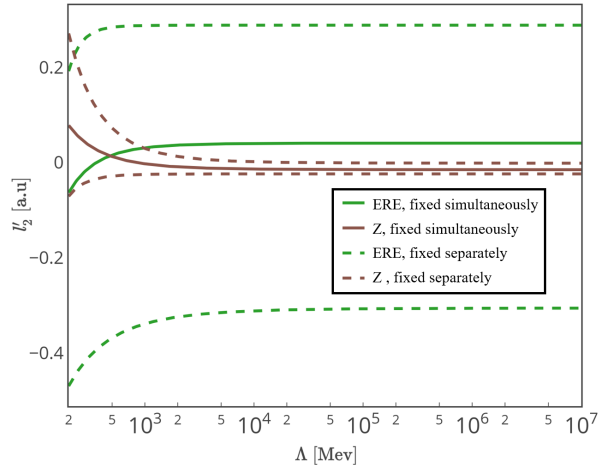


Figure 7.4: Numerical results for LECs  $l'_1$  (up) and  $l'_2$  (bution), calibrated from  $\langle \hat{\mu}_{3\text{H}} \rangle$  and  $\langle \hat{\mu}_{3\text{He}} \rangle$  as a function of the cutoff  $\Lambda$ . The solid lines are the numerical results obtained from  $A = 3$  observables simultaneously, while the dashed lines are the numerical results obtained from  $A = 3$  observables separately.

In previous sections, we used experimental data to calibrate the value of the electromagnetic LECs,  $l'_1$  and  $l'_2$ . An alternative way was accomplished recently by the Nuclear Physics with Lattice Quantum Chromo Dynamics (NPLQCD) collaboration, as reported in Ref. [85,86]. In this section we will calculate  $Y'_{np}$  using  $l'^{\infty}_1$  extracted from lattice QCD

data (subsection 7.4.1) and will extract  $l_2^\infty$  using the lattice magnetic moments of both  $^3\text{H}$  and  $^3\text{He}$  (subsection 7.4.2).

### 7.4.1 Calculation of $\sigma_{np}(Y'_{np})$ using $l_1^\infty$ from lattice QCD data

In previous sections, we used experimental data to calibrate the value of the electromagnetic LECs,  $l'_1$  and  $l'_2$ . An alternative way was accomplished recently by the Nuclear Physics with Lattice Quantum Chromo Dynamics (NPLQCD) collaboration, as reported in Ref. [85]. They have performed large scale lattice QCD calculations of a system of neutron and a proton coupled to a strong electromagnetic field  $\vec{B}$ . The energy difference between the  $^1S_0$  and  $^3S_1$  eigenstates of this two-nucleon system is then given by  $\Delta E = 2(\kappa_1 + \bar{L}_1) \frac{e}{M} |\vec{B}|$  [87–89], with  $\bar{L}_1 = Z_d \kappa_1 [2l'_1(\mu) + \gamma_t \sqrt{\rho_s \rho_t} - \frac{\gamma_t}{2} (\rho_s + \rho_t)]$ .

The results of the simulations allow them to extract  $\bar{L}_1 = 0.285^{+63}_{-60}$  nNM, or:

$$l_1^{\text{NPLQCD}} = 6.06^{+14}_{-13Z} (6.66^{+14}_{-13\text{ERE}}) / 10^{-2}. \quad (7.23)$$

The uncertainties here are related to the lattice calculation and to the uncertainty introduced in the extrapolation of the simulations (done at large non-physical quark masses) to the natural values of the quark masses. Comparing to Tab. 7.1, a  $2\sigma$  deviation is found. This translates to about 2% deviation from experimental matrix element,  $Y'_{np}$ :

$$Y'_{np} = 1.267^{+0.013}_{-0.013} (1.230^{+0.013}_{-0.013}), \quad (7.24)$$

where nominal value is the one produced using the  $Z$ -parameterization, and the ERE-parameterization value is given in brackets. This result is in some contrast with the conclusions of Ref. [85], where a perfect fit with experiment was found, since the power-counting used in that paper is different than the one we use here. e.g., the deuteron normalization is taken at its nature value ( $Z_d \approx 1.69$ ) at all orders, and not perturbatively, as in eq. (7.10). In addition, no theoretical uncertainty due to the EFT truncation in the calculation of  $\sigma_{np}$  is given in that paper. Interestingly, when we use recent lattice QCD calculation of  $d$ ,  $^3\text{H}$  and  $^3\text{He}$  magnetic moments [86], we find that the result is inconsistent with the experiment by more than two standard deviations of the numerical calculations. The LQCD “experimental” value for  $\langle \hat{\mu}_{^3\text{H}} \rangle$  is  $3.56 \pm 0.23$  nNM so it contains  $\sim 7\%$  uncertainty, in addition to the inconsistency with the measured magnetic moments of 2.9789 nNM [53]. The difference given here is not sufficient to draw any definite conclusions. Therefore, in the next section, we will try to reproduce the lattice QCD



magnetic moments using the  $\not\pi$ EFT diagrammatic method introduced in this work, with the non-physical pion mass:  $m_\pi = 805$  MeV, up to NLO.

### 7.4.2 Magnetic moments in Lattice QCD

In recent years, physical observables of low-energy electromagnetic interactions have been calculated (with large uncertainties) using lattice QCD for a non-physical pion mass (and then have been extrapolated to the physical pion mass) [86, 90]. They found that for the non-physical pion mass,  $m_\pi = 805$  MeV, the magnetic moments are:  $\kappa_p = 3.119(33)(64)$  nNM and  $\kappa_n = -1.981(05)(18)$  nNM. Their calculations yielded the following results:  $\langle \hat{\mu}_d \rangle = 1.218(38)(87)$  nNM for the deuteron,  $\langle \hat{\mu}_{^3\text{He}} \rangle = 2.29(03)(12)$  nNM for  $^3\text{He}$  and  $\langle \hat{\mu}_{^3\text{H}} \rangle = 3.56(05)(18)$  nNM for the triton. Since for non-physical pion mass, the Coulomb interaction is ignored, the radiative capture,  $\sigma_{np}$ , cannot be accounted for consistently *i.e.*, the Coulomb interaction is ignored.

In this section, we use our numerical and analytical methods for the extraction of  $l'_1$  and  $l'_2$  from our prediction to the  $A = 3$  magnetic moment in  $\not\pi$ EFT by repeating all numerical calculations with the non-physical pion mass,  $m_\pi = 805$  MeV. In contrast to the physical world, there are different approaches for calculating physical inputs. The values of the lattice nuclear parameters used in the calculation are detailed in Tab. 7.3.

Parameter	Nature $m_\pi = 139$ MeV (Tab. 2.1)	LQCD $m_\pi = 805$ MeV [83, 89, 91]
$M$ [MeV]	938.9	1634(18)
$B_{np}$ [MeV]		15.9(40)
$a_{np}^s$ [fm]	-23.75	
$a_{pp}$ [fm]	-7.806	
$\gamma_t$ [MeV]	45.701	180(44)
$E_{^3\text{H}}^B$ [MeV]	8.482	54(11)
$E_{^3\text{He}}^B$ [MeV]	7.718	
$\rho_t$	1.765 fm	$3.96(20)/m_\pi$
$\rho_s$	2.73 fm	$5.89(45)/m_\pi$
$\rho_C$	2.794 fm	$5.89(45)/m_\pi$

Table 7.2: Lattice nuclear parameters used in the numerical calculations. The values for the singlet and triplet effective ranges were taken from private communication with CalLAT.

These new non-physical inputs require a new calculation for both three-body force and three-body scattering amplitudes, up to NLO. Repeating the same calculations for

both  ${}^3\text{H}$  and  ${}^3\text{He}$  magnetic moments with the physical input taken from Tab. 7.3, along with the non-physical magnetic moments:  $\mu_p=3.119(33)(64)$  nNM and  $\mu_n=-1.981(05)(18)$  nNM, we find that the  $A = 3$  magnetic moments are (Tab. 7.3):

	${}^3\text{H}[\text{nNM}]$	${}^3\text{He}[\text{nNM}]$
One-body, LO	$3.1195 \pm 0.002$	$-1.981 \pm 0.001$
NLO range corrections	$2.38 \pm 0.02$	$-0.92 \pm 0.02$
Experimental “data” [86]	$3.56 \pm 0.23$	$-2.29 \pm 0.15$

Table 7.3: Numerical results for  $\langle \hat{\mu}_{3\text{H}} \rangle$  and  $\langle \hat{\mu}_{3\text{He}} \rangle$  with the non-physical pion mass.

In this section, we use the difference between our numerical results of NLO with range corrections to the ”experimental” values of Beane *et al.* [86], to extract  $l'_1$  and  $l'_2$  and to recalculate the deuteron magnetic moment,  $\langle \hat{\mu}_d \rangle$ :

$$\langle \hat{\mu}_d \rangle = 1.5 \pm 0.3 \pm 0.13[\text{nNM}] \quad (7.25)$$

with

$$l'_2 = 3.5 \pm 3 \pm 1.3 \cdot 10^{-2}, \quad (7.26)$$

where the first uncertainty originates from the  ${}^3\text{H}$  magnetic moment uncertainty, while the second uncertainty originates from the  ${}^3\text{He}$  magnetic moment uncertainty ([86]). We note that  ${}^3\text{H}$  and  ${}^3\text{He}$  magnetic moment uncertainties are translate into large uncertainties of the LEC,  $l'_2$ .

The LEC,  $l'_2$  as being calibrated from  ${}^3\text{H}$  and  ${}^3\text{H}$  magnetic simultaneously, holds many uncertainties originating from the different LQCD parameters given in Tab. 7.3 in addition to the ones presented in eq. (7.26). In the next subsection, we will analyze the effects of these uncertainties on the  $A = 3$  magnetic moments and as a result, on  $l'_2$  and  $\langle \hat{\mu}_d \rangle$ .

### 7.4.3 LQCD empirical uncertainties

In contrast to the physical pion mass, for the non-physical pion mass the physical parameters ( $\gamma_t, a_s, E_3^B, \rho_t, \rho_s$ ) hold large uncertainties, originating from the character of the LQCD calculation as shown in Tab. 7.3.

In Tab. 7.5, we show the contribution of each such uncertainty to the uncertainty propagated to the electromagnetic observables.

Physical observable		$E_{3\text{H}}^B$	$a_s$	$\gamma_t$	$\rho_t$	$\rho_s$	$\mu_p$	$\mu_n$
Quoted uncertainty		18.5%	25.16%	22.22%	5.05%	7.64%	3.11%	1.16%
Effect on magnetic observable	$\Delta\langle\hat{\mu}_{3\text{H}}\rangle$	0.01%	0.05%	0.2%	0.01%	0.02%	3.11%	0%
	$\Delta\langle\hat{\mu}_{3\text{He}}\rangle$	0.02%	0.08%	0.31%	0.02%	0.03%	0%	1.16%
	$\Delta\langle\hat{\mu}_d\rangle$	2.76%	0.83%	6.06%	1.5%	0.75%	18.42%	9.54%
	$\Delta l'_2$	11.34%	3.44%	24.94%	6.48%	3.15%	91.33%	22.77%

Table 7.4: The contribution of the calculated uncertainty in the physical observables to the uncertainty propagated to the electromagnetic observables.

The physical inputs of Tab .7.5 are divided into two categories: on-shell parameters ( $\mu_n$  and  $\mu_p$ ) and off-shell parameters ( $E_{3\text{H}}^B$   $a_s$   $\gamma_t$   $\rho_s$   $\rho_t$ ), which effect the three-body force and three-nucleon wave functions. It clear that for the on-shell parameters,  $\langle\mu_{3\text{H}}\rangle$  and  $\langle\mu_{3\text{He}}\rangle$  uncertainties are proportional to the relevant parameter has a minor effect on  $\langle\mu_{3\text{H}}\rangle$  and  $\langle\mu_{3\text{He}}\rangle$  uncertainty, *i.e.*,  $\Delta\langle\mu_{3\text{H}}\rangle \propto \Delta\kappa_p$  and  $\Delta\langle\mu_{3\text{He}}\rangle \propto \Delta\kappa_n$ . Since  $\langle\mu_{3\text{H}}\rangle$  depends mostly on  $\kappa_p$  and  $\mu_{3\text{He}}$  depends mostly on  $\kappa_n$ , the total effect of  $\kappa_p, \kappa_n$  uncertainties on  $l'_2$  (and as a result, on  $\langle\hat{\mu}_d\rangle$ ) is much larger than the effect of  $E_B, \rho_s, a_s$ . Since  $l'_2 = \gamma_t \rho_t \frac{l_2}{2\kappa_0} \rho_t$ ;  $\gamma_t$  uncertainty more affects  $\Delta\langle\hat{\mu}_d\rangle$  and  $\Delta l'_2$  than  $E_B, \rho_s, a_s$  as shown in Tab. 7.3. Also, we note that for the off-shell parameters, the uncertainty stems mainly from the  $A = 3$  wave function, and therefore, we expect that off-shell parameters uncertainty will effect  $\langle\mu_{3\text{H}}\rangle$  and  $\langle\mu_{3\text{He}}\rangle$  in a similar way. The fact that  $\mu_p$  and  $\mu_n$  uncertainty is not symmetric to  $\langle\mu_{3\text{H}}\rangle$  and  $\langle\mu_{3\text{He}}\rangle$ , increases their effect on  $l'_2$  and  $\langle\hat{\mu}_d\rangle$  comparing to the off-shell parmters.

Summarizing, the  $\not\pi$ EFT procedure of calculating the electromagnetic observables creates a significant sensitivity of these observables to uncertainties in the calculations of the binding energies, and, mainly in the deuteron case, in calculated lattice values of the single nucleon magnetic moments.

# Weak interactions and ${}^3\text{H}$ $\beta$ -decay in pionless EFT

In this chapter we outline the calculation of the matrix element of the weak reaction:

$${}^3\text{H} \rightarrow {}^3\text{He} + e^- + \bar{\nu}_e, \quad (8.1)$$

which is well-measured weak reaction that contains more than one nucleon and its energy transfer is applicable for the  $\not\pi$ EFT regime. As mention before, we are using this calculation of  ${}^3\text{H}$   $\beta$ -decay for extracting the unknown LEC,  $L_{1,A}$ , which is essential for predicting the  $pp$  fusion rate.

## 8.1 The weak interactions in pionless EFT

The weak interaction Lagrangian is given in Chapter 2 by eqs. (2.40) and (2.42). The axial-vector part (after Hubbard-Stratonovich transformation) is (see Appendix C):

$$\mathbf{A}^\pm = \frac{g_A}{2} N^\dagger \boldsymbol{\sigma} \tau^\pm N + g_A L'_{1,A} (t^\dagger s + s^\dagger t) , \quad (8.2)$$

where  $g_A$  is the axial coupling constant for a single nucleon, known from neutron  $\beta$ -decay. In two-nucleon calculations, the renormalization scale  $\mu$  is frequently assumed to be comparable to the breakdown scale of theory, usually at  $m_\pi$ . In the current case, it is set to  $\mu = \Lambda$ . One expects that by taking  $\Lambda \rightarrow \infty$  numerically, regularization effects from the treatment of the  $A = 3$  system vanish. This causes an asymptotic behavior of  $L_{1,A}$ , which cancels the cutoff dependence in the NLO term, leaving it RG invariant. Testing

this is part of the validation process of our numerical calculation. We therefore define:

$$L'_{1,A}(\mu) = \frac{\rho_t + \rho_s}{2\sqrt{\rho_s\rho_t}} - l_{1,A}(\mu) , \quad (8.3)$$

where  $l_{1,A}$  is an RG invariant combination (in arbitrary units).

$$l_{1,A}(\mu) = \frac{L_{1,A}}{2\pi g_A} \frac{1}{\sqrt{\rho_s\rho_t}} \left( \mu - \frac{1}{a_t} \right) \left( \mu - \frac{1}{a_s} \right) , \quad (8.4)$$

and  $\mu$  is the renormalization scale. Similar to the electromagnetic LEC (Chapter. 7), we take the limit  $\mu = \Lambda \rightarrow \infty$ , such that:

$$l_{1,A}(\Lambda) = \frac{L_{1,A}}{2\pi g_A} \frac{1}{\sqrt{\rho_s\rho_t}} \left( \Lambda - \frac{1}{a_t} \right) \left( \Lambda - \frac{1}{a_s} \right) . \quad (8.5)$$

The operator  $\mathbf{A}^\pm$  (eq. (8.2)) is written up to NLO. To maintain consistency, the LO interaction is coupled to the NLO three-body wave functions, while the NLO interactions are coupled to the LO wave functions as discussed in Chapter 6.

## 8.2 $^3\text{H}$ $\beta$ -decay matrix elements

The triton  $\beta$ -decay to  $^3\text{He}$  matrix element eq. (8.1), can be calculated using the LO and NLO  $A = 3$  bound-state wave functions as introduced in Chapter 5.

### 8.2.1 $^3\text{H}$ $\beta$ -decay observables

The half-life of  $^3\text{H}$   $\beta$ -decay can be expressed as [31]:

$$fT_{1/2} = \frac{K/G_V^2}{\langle F \rangle^2 + \frac{f_A}{f_V} \langle GT \rangle^2} ; \quad (8.6)$$

where  $(fT_{1/2})_t = 1129.6 \pm 3$  s [92] is the triton comparative half-life,  $K = 2\pi^3 \log 2/m_e^5$  (with  $m_e$  denoting the electron mass),  $G_V$  is the weak interaction vector coupling constant (such that  $K/G_V^2 = 6146.66 \pm 0.6$  [93]),  $f_V = 2.8355 \cdot 10^{-6}$  and  $f_A = 2.8506 \cdot 10^{-6}$  are the Fermi functions calculated by Towner, as reported by Simpson in Ref. [94]. The weak transitions  $\langle GT \rangle, \langle F \rangle$  are a result of weak interaction matrix, which can be calculated using the method introduced in Chapter 5.

### 8.2.2 Fermi and Gamow-Teller matrix element:

For the case of triton  $\beta$  decay, it is better to separate the triton into 3 different channels - $d, np, nn$ , under the the assumption that for the scattering lengths  $a_{nn} = a_{np} = a_s$ ). Given that, one finds that:

$$1 = \sum_{\mu, \nu=t, s, nn} \left\langle \psi_{\mu}^{3\text{H}}(E_{3\text{H}}, p') \left| \frac{d}{dE} \left[ \hat{I}_{\mu\nu} - M y_{\mu} y_{\nu} a_{\mu\nu} K_0(p'', p', E) \right]_{E=E_{3\text{H}}} \right| \psi_{\nu}^{3\text{H}}(E_{3\text{H}}, p'') \right\rangle, \quad (8.7)$$

where:

$$a_{\mu\nu} = \begin{array}{c|ccc} & \nu & & & \\ & \mu & & & \\ \hline t & -1 & 3 & 3 \\ np & 1 & 1 & -1 \\ nn & 2 & -2 & 0 \end{array}. \quad (8.8)$$

is a result of the different projection operators [46].

The Gamow-Teller operator of the triton beta decay, ( $\langle GT \rangle$ ) matrix element is given by:

$$\begin{aligned} \langle GT \rangle &= \frac{\langle \psi^{3\text{He}} \| \mathbf{A}^+ \| \psi^{3\text{He}} \rangle}{\sqrt{2}} = \\ &\left\langle \frac{1}{2} \left\| \tau^+ \right\| \frac{1}{2} \right\rangle \frac{\langle \frac{1}{2} \| \boldsymbol{\sigma} \| \frac{1}{2} \rangle}{\sqrt{2}} g_A \sum_{\mu, \nu} \left\langle \psi_{\mu}^{3\text{He}}(E_{3\text{He}}, p') \left| y_{\mu} y_{\nu} \left[ d'_{\mu\nu}{}^{ij} \mathcal{I}^q(E_{3\text{H}}, q_0, p, p') + \right. \right. \right. \\ &\left. \left. \left. a'_{\mu\nu}{}^{ij} \mathcal{K}^q(p, p', E_{3\text{H}}, q_0) \right] \right| \psi_{\nu}^{3\text{H}}(E_{3\text{H}}, p) \right\rangle - g_A L'_{1,A} \left( \langle \psi_{nn}^{3\text{H}} | \psi_t^{3\text{He}} \rangle + \langle \psi_t^{3\text{H}} | \psi_{pp}^{3\text{He}} \rangle \right), \quad (8.9) \end{aligned}$$

where:

$$d'_{\mu\nu} = \begin{array}{c|ccc} & \mu & & & \\ & \nu & & & \\ \hline t & 1/3 & 0 & -1 \\ np & 0 & 1/3 & 0 \\ nn & -2/3 & 0 & 0 \end{array} \quad (8.10)$$

and

$$a_{\mu\nu}^{ij} = \begin{array}{c|ccc} & \nu & & & \\ & \mu & & & \\ \hline & t & np & pp & \\ \hline t & -7/3 & 1 & 3 & \\ np & 1 & 1 & -1 & \\ nn & 2/3 & -2 & -2 & \end{array} \quad (8.11)$$

denotes the Gamow-Teller transition.

The Fermi matrix element ( $\langle F \rangle$ ) is given by:

$$\begin{aligned} \langle F \rangle &= \frac{\langle \psi^{3\text{He}} \| V^+ \| \psi^{3\text{He}} \rangle}{\sqrt{2}} = \\ &\left\langle \frac{1}{2} \left\| \tau^+ \right\| \frac{1}{2} \right\rangle \sum_{\mu, \nu} \left\langle \psi_{\mu}^{3\text{He}}(E_{3\text{He}}, p') \right| y_{\mu} y_{\nu} \left[ d_{\mu\nu}^{ij} \mathcal{I}^q(E_{3\text{H}}, q_0, p, p') + a_{\mu\nu}^{ij} \mathcal{K}^q(p, p', E_{3\text{H}}, q_0) \right] \left| \psi_{\nu}^{3\text{H}}(E_{3\text{H}}, p) \right\rangle \end{aligned} \quad (8.12)$$

where:

$$d_{\mu\nu}^{ij} = \begin{array}{c|ccc} & \mu & & & \\ & \nu & & & \\ \hline & t & np & pp & \\ \hline t & 1 & 0 & 0 & \\ np & 0 & 1 & -1 & \\ nn & 0 & 2 & 0 & \end{array} \quad (8.13)$$

and

$$a_{\mu\nu}^{ij} = \begin{array}{c|ccc} & \nu & & & \\ & \mu & & & \\ \hline & t & np & pp & \\ \hline t & -1 & 3 & 3 & \\ np & 1 & 1 & 1 & \\ nn & 2 & -2 & -2 & \end{array}, \quad (8.14)$$

$\mu, \nu$  denote the different channels of the three-nucleon wave function ( $t, np, pp$  for  ${}^3\text{He}$  and  $t, np, nn$  for  ${}^3\text{H}$ ), where  $\psi_{\mu}, \psi_{\nu}$  are the three-nucleon wave functions for the different channels, defined using the homogeneous solution of the three-nucleon scattering amplitude [48] and  $q_0 = E_{3\text{He}} - E_{3\text{H}}$  is the energy transfer. The general diagrammatic form of  ${}^3\text{H}$   $\beta$ -decay, shown in Fig. 8.1, is similar to the general matrix element introduced in Chapter 5. For both  $\langle F \rangle$  and  $\langle GT \rangle$  transitions, the left hand side bubbles of the diagrams are  ${}^3\text{H}$ , while the right hand side bubbles are  ${}^3\text{He}$ .

The one-body diagrams which contain a one-body weak interaction are coupled to the

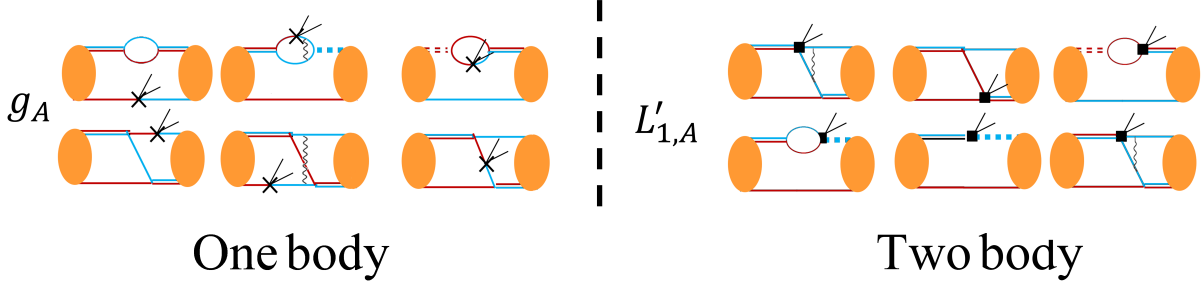


Figure 8.1: Different topologies of the diagrams contributing to the triton  $\beta$ -decay amplitude. The LHS of each diagram is  $^3\text{H}$  while the RHS is  $^3\text{He}$ . The double line are the propagators of the two dibaryon fields  $D_t$  (solid),  $D_s$  (dashed for  $nn$  and  $np$ , dotted for  $pp$ ), where the red lines are the neutron and the blue lines are the proton. Most of the diagrams couple both the triplet and the singlet channels. The diagrams with one-body interactions are coupled to  $g_A$  while the two-body interaction are coupled to the effective ranges  $\rho_t$  and  $\rho_s$  and to  $l'_{1,A}$ .

weak axial LEC,  $g_A$ , and contribute to both  $\langle F \rangle$  and  $\langle GT \rangle$  transitions. Similarly to  $A = 3$  magnetic moments, this one-body diagrams are taken up to NLO, and therefore contain the NLO insertion for the one-body diagrams as discussed in Chapter 6. The two-body diagrams include a two-body term originating from the ERE term in the Lagrangian:  $\frac{1}{2} \frac{\rho_t + \rho_s}{\sqrt{\rho_t \rho_s}} g_A$ , and a two-body weak interaction which is coupled to the unknown LEC  $l'_{1,A}$ . The two-body diagrams contribute to the  $\langle GT \rangle$  transition only.

### 8.3 Fermi operator

In the absence of the Coulomb interaction,  $^3\text{H}$  is identical to  $^3\text{He}$  and the Fermi transition is equal to the triton wave function normalization as defined in Chapter 5:

$$\begin{aligned} \langle F \rangle^0 &= \frac{\langle \psi^{3\text{H}} | \tau^0 | \psi^{3\text{H}} \rangle}{\sqrt{2}} = \left\langle \frac{1}{2} \left\| \tau^0 \right\| \frac{1}{2} \right\rangle. \\ \sum_{\mu, \nu} \left\langle \psi_{\mu}^{3\text{H}}(E_{3\text{H}}, p') \right| y_{\mu} y_{\nu} \left[ d_{\mu\nu}^{ij} \mathcal{I}^{q=0}(E_{3\text{H}}, q_0 = 0, p, p') + a_{\mu\nu}^{ij} \mathcal{K}^{q=0}(p, p', E_{3\text{H}}, q_0 = 0) \right] \left| \psi_{\nu}^{3\text{H}}(E_{3\text{H}}, p) \right\rangle &= 1, \end{aligned} \quad (8.15)$$

where:

$$d_{\mu, \nu}^{ij} = \delta_{\mu, \nu} \quad (8.16)$$

$$a_{\mu\nu}^{ij} = a_{\mu\nu} \quad (8.17)$$



From comparison between eqs. (8.8) and (8.16) and eqs. (8.13) and (8.14) we expect that  $\langle F \rangle = 1 - \epsilon$  [31], where  $\epsilon \ll 1$ , originates mostly from the isospin breaking due to the Coulomb interaction. We can therefore isolate the effect of isospin breaking and the one-photon exchange diagrams on the Fermi transition and compare them later to the Gamow-Teller calculations. In this section, we present our calculations of the Fermi transition. First, we calculate the Fermi transition in the absence of Coulomb interaction, but under the assumption that  $a_{nn,np} \neq a_{pp}$ . Second, we calculate the Fermi transition with  $\alpha \neq 0$ , and, obviously,  $a_{nn,np} \neq a_{pp}$ , as a result for both Z- and ERE-parameterization. All these calculations result from the left hand side of the diagrams in Fig. 8.1.

We use the experimental data shown in Tab. 2.1 as input for our numerical calculations shown in Fig. 8.2 and Tab. 8.1.

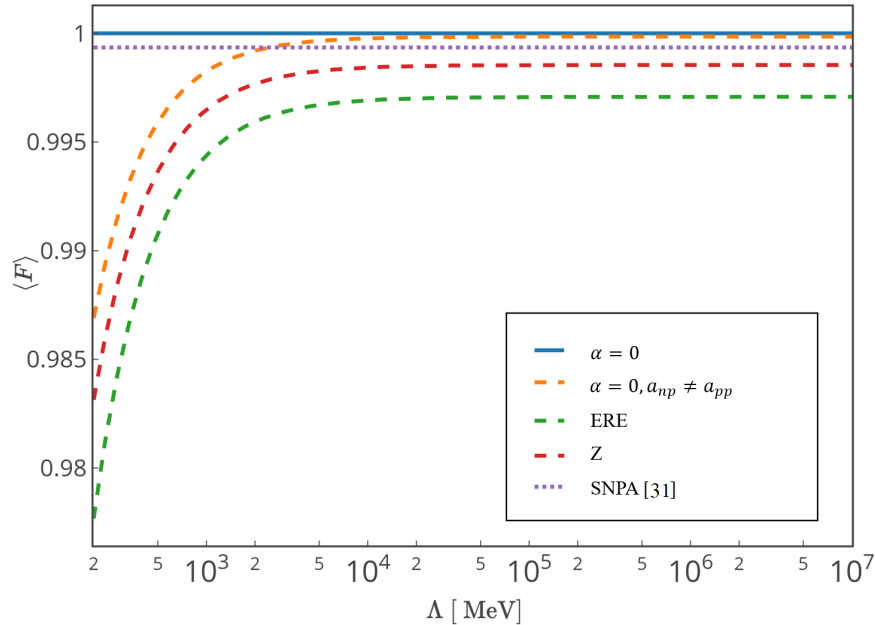


Figure 8.2: Numerical results for the Fermi transition. The solid line is the LO result for  $\langle F \rangle = 1$  with  $\alpha = 0$ . The dashed line is the numerical result for  $\alpha = 0$  with isospin breaking effects in the scattering lengths  $a_{np} \neq a_{pp}$  (LO). The dashed-dotted line shows the numerical result at NLO with  $\alpha \neq 0$ . The dotted line gives the value of  $\langle F \rangle = 0.9993$  from Ref. [31].

	$\langle F \rangle$
One-body, LO $\alpha = 0$	1
One-body, LO $\alpha = 0, a_{np} \neq a_{pp}$	0.9999
LO, ERE	0.9971
LO, Z	0.9985
SNPA [31]	0.9993

Table 8.1: Numerical results of  $\langle F \rangle$ . Note that the second row is without explicit Coulomb force ( $\alpha = 0$ ), but with isospin breaking in the scattering lengths, *i.e.*, with the physical values for the scattering lengths  $a_{np} \neq a_{pp}$ .

Our numerical result compares well to the  $\langle F \rangle$  standard nuclear physics approach (SNPA) calculation by Schiavilla *et al.* [31]. The SNPA calculation involves nuclear wave functions derived from high-precision phenomenological nuclear potentials, and one-nucleon and two-nucleon electro-weak currents.

## 8.4 Gamow-Teller operator

In contrast to the Fermi transition, the Gamow-Teller transition also involves two-body operators at NLO. The diagrams which contain a one-body weak interaction are coupled to  $g_A$  and contain one ERE insertion up to NLO. The two-body diagrams are coupled to  $\frac{\rho_t + \rho_s}{2\sqrt{\rho_s \rho_t}} - l_{1,A}(\Lambda)$ . By summing over all diagrams and comparing the resulting sum to the triton half-life, [36],  $l_{1,A}(\Lambda)$  can be extracted, as will be discussed later in this chapter. We used the experimental input parameters shown in Tab. 2.1 for all numerical calculations.

### 8.4.1 Gamow-Teller Transition for $\alpha = 0$

As mentioned before, in the absence of Coulomb interaction, the Fermi transition matrix element at LO is 1 (*i.e.*  $\alpha = 0$ ). Similarly, the LO matrix element of the Gamow-Teller transition with  $\alpha = 0$ , easily found to be:

$$\begin{aligned}
 \langle GT \rangle_{\alpha=0}^{\text{LO}} &= \frac{\langle \frac{1}{2} \| \boldsymbol{\sigma} \| \frac{1}{2} \rangle}{\sqrt{2}} \left\langle \frac{1}{2} \| \tau^0 \| \frac{1}{2} \right\rangle. \\
 \sum_{\mu, \nu} \left\langle \psi_{\mu}^{{}^3\text{H}}(E_{{}^3\text{H}}, p') \right| y_{\mu} y_{\nu} \left[ \delta_{\mu, \nu} \mathcal{I}^{q=0}(E_{{}^3\text{H}}, q_0 = 0, p, p') + a_{\mu\nu} \mathcal{K}^{q=0}(p, p', E_{{}^3\text{H}}, q_0 = 0) \right] \left| \psi_{\nu}^{{}^3\text{H}}(E_{{}^3\text{H}}, p) \right\rangle &= \\
 \frac{\sqrt{6}}{\sqrt{2}} &= \sqrt{3},
 \end{aligned} \tag{8.18}$$

where  $a_{\mu\nu}$  is given in eq. (8.8). We have performed this calculation in two ways: one with  $\alpha = 0$  for both the scattering amplitude and the matrix element, and second with  $\alpha = 0$  for the matrix element, but for different scattering lengths, similarly to the Fermi case. From Tab. 8.2, one sees that the effect of different scattering lengths leads to  $< 0.6\%$  difference for both Fermi and Gamow-Teller transitions. These results imply that for the Fermi and Gamow-Teller transitions, the Coulomb interaction has to be taken non-perturbatively, since its contribution for the matrix element is not neglectable. As for the scattering length difference, Tabs. 8.1 and 8.2 indicate that up to LO, the scattering length difference has a small effect on both transitions, which can be estimated perturbatively.

### 8.4.2 Numerical results for GT strength of triton decay

Our  $\langle GT \rangle$  numerical results for both NLO arrangements are shown in Tab. 8.2 and in Fig. 8.3. The full NLO result with  $l_{1,A} = 0$  includes both, one-body and two-body terms which contribute to  $\langle GT \rangle$ , without the diagrams that are coupled to  $l_{1,A}$ .

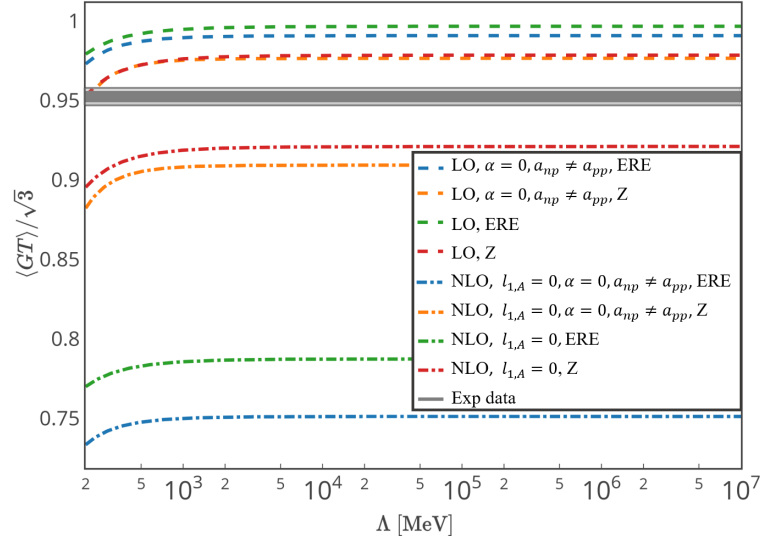


Figure 8.3: Numerical results of the Gamow-Teller transition. The gray area is the full  $\langle GT \rangle$  matrix element with  $g_A = 1.273 \pm 0.003 \pm 0.005$  [95, 96]. The short dashed lines are the numerical results of  $\langle GT \rangle^{\text{LO}}$ , the dashed-dotted lines are  $\langle GT \rangle$  with  $l_{1,A} = 0$ . Z refers to numerical results with the Z-parameterization:  $\rho'_t = \frac{Z_d - 1}{\gamma_t}$ .

	$\langle GT \rangle, \text{ERE}$	$\langle GT \rangle, Z$
One-body, LO $\alpha = 0$	$\sqrt{3}$	$\sqrt{3}$
One-body, LO $\alpha = 0, a_{np} \neq a_{pp}$	1.716	1.692
One-body, LO	1.727	1.695
Full NLO, $l_{1,A} = 0, \alpha = 0, a_{np} \neq a_{pp}$	1.301	1.575
Full NLO, $l_{1,A} = 0$	1.383	1.596

Table 8.2: Numerical results for  $\langle GT \rangle$ . Note that the rows with the comment " $\alpha = 0, a_{np} \neq a_{pp}$ " are without explicit Coulomb force ( $\alpha = 0$ ), but with isospin breaking in the scattering lengths, *i.e.*, with physical values for the scattering lengths  $a_{np} \neq a_{pp}$ .

## 8.5 Empirical extraction of Gamow-Teller strength and fixing $l_{1,A}$

The GT matrix element can be extracted from a triton half-life calculation using eq. (8.6). The axial coupling constant  $g_A$  has been remeasured recently, leading to results whose range is much bigger than the current recommendation. To be on the safe side, we take  $g_A = 1.273 \pm 0.003 \pm 0.005$  [95, 96]. The first uncertainty in  $g_A$  arises from the difference between the measurements of Refs. [95, 96], and the second uncertainty is the statistical experimental uncertainty. In order to extract the Gamow-Teller strength, we use our prediction for the Fermi transition:  $\langle F \rangle = 0.9993$  [31]. At large cutoff values we find that the empirical GT strength is  $\langle GT \rangle_{\text{emp}} = \sqrt{3} \frac{1.213 \pm 0.002}{g_A}$  [31]. The uncertainty here originates mainly from the uncertainty in the triton half-life.

The difference between the empirical GT strength and the numerical result for the GT-transition at NLO is used to fix  $l_{1,A}$  such that:

$$l_{1,A}(\Lambda) = \frac{\langle GT \rangle_{\text{emp}} - \langle GT \rangle_{l_{1,A}=0}^{\text{NLO}}}{\langle GT \rangle_{l_{1,A}}^{\text{NLO}}}, \quad (8.19)$$

where  $\langle GT \rangle_{l_{1,A}}^{\text{NLO}}$  are the two-body diagrams that contribute to the triton  $\beta$ -decay and coupled to  $l_{1,A}$ , while  $\langle GT \rangle_{l_{1,A}=0}^{\text{NLO}}$  is the sum over all the diagrams that contribute to the triton  $\beta$ -decay **without** the diagrams coupled to  $l_{1,A}$ . The numerical results for  $l_{1,A}$  for both ERE- and  $Z$ -parameterizations are shown in Fig. 8.4.

Importantly, we find numerically, that for both parameterizations,  $l_{1,A}$  is RG invariant,

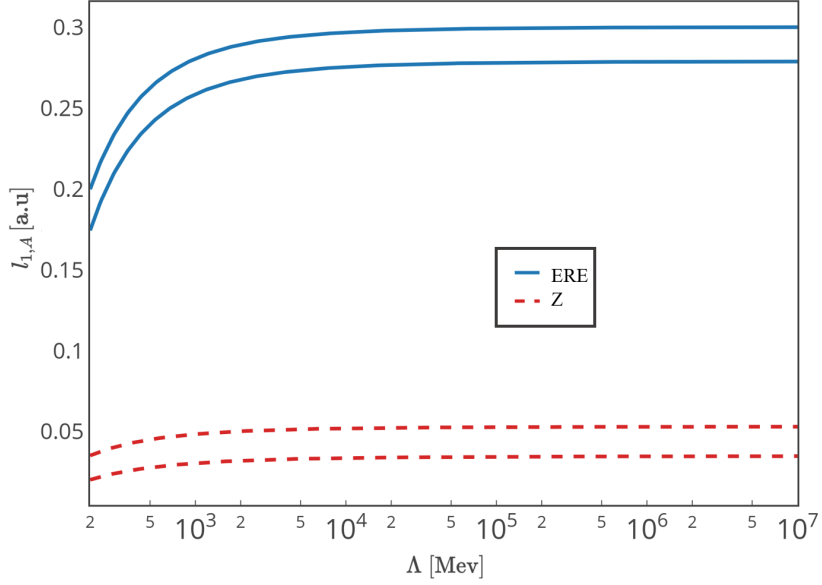


Figure 8.4: Numerical results of the RG invariant,  $l_{1,A}$ , with  $g_A = 1.273(03)(05)$  [95, 96]. The solid lines are the upper and lower limits of the ERE calculations while the dashed lines are the upper and lower limits of the  $Z$  calculations.

a fact that has been already predicted by theory [97], where for  $\Lambda \rightarrow \infty$ :

$$l_{1,A}^\infty = 0.055(0.317) \pm 0.004 \pm 0.001, \quad g_A = 1.2701, \quad (8.20a)$$

$$l_{1,A}^\infty = 0.047(0.308) \pm 0.004 \pm 0.001, \quad g_A = 1.2767, \quad (8.20b)$$

The nominal value is calculated using  $Z$ -parameterization, while the number in brackets is calculated using the ERE-parameterization. The first uncertainty comes from  $g_A$  experimental uncertainty and the second uncertainty comes from the rest of the experimental uncertainties, such as the statistical uncertainties in the measured triton half-life.

## The proton-proton fusion matrix element

The energy generated in the Sun comes from an exothermic set of reactions, named the proton-proton ( $pp$ ) chain, which fuses four Hydrogen ions into  ${}^4\text{He}$ :



The leading reaction in this chain is the  $pp$  fusion:



This reaction is governed by the weak interaction, which makes it the slowest reaction (by far) in the whole chain, and therefore it determines the Sun's lifetime. This fusion is the main contributor to the solar neutrinos [6, 98, 99]. Since a direct measurement of its cross-section is impossible, the fusion rate estimates depend entirely on theory [3]. Since the  $pp$  fusion is a weak reaction, calibrating  $L_{1,A}$  with sufficient accuracy is crucial for predicting its rate.

The  $pp$  fusion rate, i.e. the number of reactions per unit of time per volume, is given by:

$$R_{pp} = \frac{N_p}{2} \langle \sigma \nu \rangle, \quad (9.3)$$

where  $N_p$  is the proton number density,  $\sigma$  is the cross-section in the center of the mass and  $\nu$  is the proton center-of-mass thermal average velocity, assuming a Boltzmann distribution with temperature of the solar core, *i.e.*, approximately 15 million degrees. This defines low-energy scale in the nuclear regime ( $\approx 1.5\text{keV} \ll E_d$ ).

The astrophysical  $S$ -Factor is defined in the terms of the cross-section [6]:

$$S^{11}(E) = (\sigma E) e^{2\pi\eta(E)} \quad (9.4)$$

where  $\eta(E) = \frac{2\pi}{h\nu}$  is the Coulomb parameter in terms of  $E$ , where  $E$  is the kinetic energy of the center of mass of the interacting protons, dictated by the temperature. In solar conditions, the magnitude of  $E$  is only a few keVs and therefore  $S^{11}(E)$  can be expanded in a power series in  $E$ :

$$S^{11}(E) = S^{11}(0) + S^{11'}(0)E + \frac{S^{11''}(0)E^2}{2} + \dots \quad (9.5)$$

where ( [3]):

$$S^{11}(0) = 4.01 \left( \frac{g_A}{1.2695} \right)^2 \frac{\Lambda_{pp}(0)^2}{7.035} 10^{-23} \text{ MeV} \cdot \text{fm}^2, \quad (9.6)$$

where  $\Lambda_{pp}(0)$  is the weak interaction matrix element:

$$\Lambda_{pp}(0) \propto \langle d | \mathcal{L}_{weak} | pp \rangle, \quad (9.7)$$

$\mathcal{L}_{weak}$  is the  $\pi$ EFT interaction Lagrangian, introduced in Chapter 8.

## 9.1 $pp$ fusion matrix element

The diagrams contributing to the  $pp$  fusion matrix element,  $\Lambda_{pp}(0)$  (up to NLO) are shown in Fig 9.1. The sum over all  $pp$  fusion diagrams up to NLO in  $\frac{Q}{\Lambda_{cut}}$  is given by (see Refs. [30, 32]):

$$T_{fi} = \langle d | \vec{\mathcal{A}}^- | pp \rangle = \sqrt{\frac{8\pi}{\gamma_t^3}} C_\eta e^{i\sigma_0} \left\{ \sqrt{Z_d^{\text{NLO}}} [e^\chi - M\alpha a_p I(\chi)] + \sqrt{Z_d^{\text{LO}}} \frac{a_p \gamma_t^2}{2} \sqrt{\rho_t \rho_s} \left( \frac{\rho_t + \rho_s}{2\sqrt{\rho_t \rho_s}} - l_{1,A} \right) \right\}, \quad (9.8)$$

where  $Z_d^{\text{LO}}, Z_d^{\text{NLO}}$  are the deuteron LO and NLO normalizations, respectively (eqs. (2.72) and (2.73)),  $\chi = \frac{\alpha M}{\gamma_t}$  and  $\sigma_0, C_\eta, a_p, \rho_{t,s}, \alpha, M$  and  $\gamma_t$  were introduced in Chapter 2. The integral  $I(\chi)$  is defined as:

$$I(\chi) = \int dx \frac{\chi e^{\frac{x}{\pi} \arctan\left(\frac{\pi x}{x}\right)}}{(e^x - 1)(\pi^2 \chi^2 + x^2)}, \quad (9.9)$$

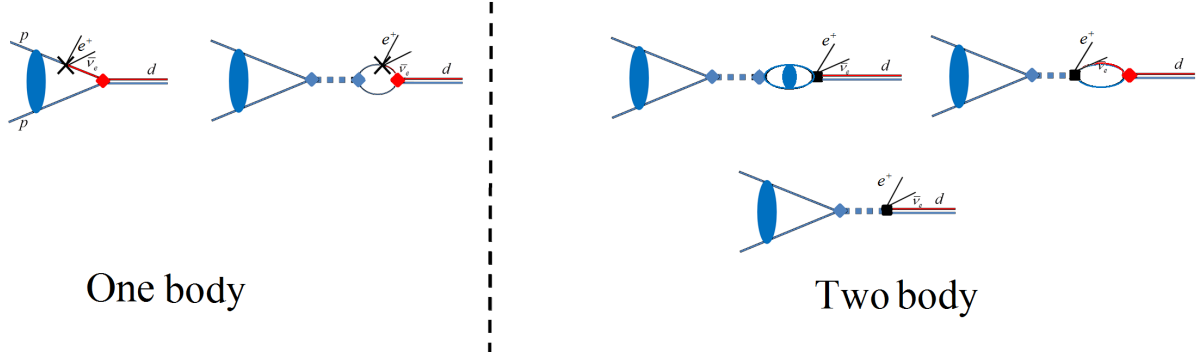


Figure 9.1: Diagrams for the  $pp$  fusion process, eq. (9.2), up to NLO. The double lines are the NLO propagators of the two dibaryon fields:  $D_t$  (solid) and  $D_{pp}$  (dotted). Two-nucleon propagator with a blue bubble denotes the Green's function including the Coulomb potential. A spin-singlet dibaryon-nucleon-nucleon (s-NN) vertex is proportional to  $y_s$  (blue diamond) while a spin-triplet dibaryon-nucleon-nucleon (t-NN) vertex is proportional to  $y_t$  (red diamond). The one-body diagrams are coupled to the one-body LEC,  $g_A$  where the two-body diagrams are coupled to the two-body LEC,  $L'_{1,A}$ .

and  $\Lambda_{pp}(0)$  is given by [24, 29]:

$$\Lambda_{pp}(0, \mu) = \gamma_t^2 \sqrt{\frac{\rho_t}{8\pi C_\eta^2}} |T_{fi}(0, \mu)| = \sqrt{Z_d^{\text{NLO}}} [e^\chi - M\alpha a_p I(\chi)] + \sqrt{Z_d^{\text{LO}}} \frac{a_p \gamma_t^2}{2} \sqrt{\rho_t \rho_s} \left( \frac{\rho_t + \rho_s}{2\sqrt{\rho_t \rho_s}} - l_{1,A} \right). \quad (9.10)$$

For the ERE-parameterization, eq. (9.10) becomes:

$$\Lambda_{pp}(0, \mu) = \left( 1 + \frac{\gamma_t \rho_t}{2} \right) [e^\chi - M\alpha a_p I(\chi)] + \frac{a_p \gamma_t^2}{2} \sqrt{\rho_t \rho_s} \left( \frac{\rho_t + \rho_s}{2\sqrt{\rho_t \rho_s}} - l_{1,A} \right), \quad (9.11)$$

while for the  $Z$ -parameterization, we find that:

$$\Lambda_{pp}(0, \mu) = \sqrt{Z_d} [e^\chi - M\alpha a_p I(\chi)] + \frac{a_p \gamma_t^2}{2} \sqrt{\rho_t \rho_s} \left( \frac{\rho_t + \rho_s}{2\sqrt{\rho_t \rho_s}} - l_{1,A} \right). \quad (9.12)$$

Similarly to the electromagnetic observables we define  $l'_{1,A}$  such that:

$$\Lambda_{pp}^{\text{ERE}}(0, \mu) = \left( 1 + \frac{\gamma_t \rho_t}{2} \right) [e^\chi - a_p \gamma_t \chi I(\chi)] + \frac{a_p \gamma_t^2}{4} (\rho_t + \rho_s) - l'_{1,A}(\mu) \quad (9.13)$$

$$\Lambda_{pp}^Z(0, \mu) = \sqrt{Z_d} [e^\chi - a_p \gamma_t \chi I(\chi)] + \frac{a_p \gamma_t^2}{4} (\rho_t + \rho_s) - l'_{1,A}(\mu), \quad (9.14)$$



with

$$l'_{1,A}(\mu) = \frac{a_p \gamma_t^2}{2} \sqrt{\rho_t \rho_s} l_{1,A}(\mu). \quad (9.15)$$

## 9.2 Numerical results

We calculate the matrix element,  $\Lambda_{pp}(0)$ , of eq. (9.10) using the parameters introduced in Tab. 2.1 and for  $\chi = 0.1494$ , so  $I(\chi) = 4.97311$ .

For  $l'_{1,A} = 0$  we get:

$$\Lambda_{pp}(0) = 2.67(2.55), \quad (9.16)$$

where the nominal value is the one produced using the  $Z$ -parameterization, and the ERE-parameterization value is given in brackets. For  $l'_{1,A} = -0.025(-0.146) \pm 0.002 \pm 0.001$   $g_A = 1.2701$ ,  $l'_{1,A} = -0.021(-0.141) \pm 0.002 \pm 0.001$   $g_A = 1.2769$ , calculated from eq. (8.20), we can predict the  $pp$  fusion rate, accompanied by theoretical and empirical uncertainties. In the next chapter, we will analyze the  $\not\pi$ EFT uncertainties due to both sources using the electromagnetic observables, which will enable us to predict the  $pp$  fusion.

# Chapter 10

## Analysis of the results and a prediction for $pp$ fusion

The purpose of this work is to establish a consistent method for calculating electro-weak (EW) matrix elements of  $A < 4$  nuclei, focusing on the prediction for the  $pp$  fusion rate. The approach used in this work, the  $\nabla$ EFT, like any other EFT, is useful for robust and reliable theoretical uncertainty estimates due to the neglected orders in the EFT expansion. The results presented in the previous chapters show that  $\nabla$ EFT is both viable and attractive theory for describing electromagnetic observables of the  $A = 2, 3$  systems and for predicting RG invariant electro-weak LECs up to NLO with high accuracy. In this chapter we use these results to provide a theoretical uncertainty estimate for the electromagnetic observables [49, 100]. Also, this chapter presents an analysis of the similarity between the  $\nabla$ EFT characteristics of electromagnetic and weak observables which enables us to estimate the theoretical uncertainty for the weak observables and to predict the  $pp$  fusion rate with sufficient certainty.

### 10.1 An order-by-order analysis of the results and theoretical uncertainty

The  $\nabla$ EFT presented here is purely perturbative in effective range expansion, *i.e.*, consistently organizes the expansion in a perturbative manner without including any higher order terms. Moreover, an order-by-order renormalization was obtained, as shown numerically, by the cutoff invariance. In chiral effective field theory ( $\chi$ EFT), a cutoff variation is

## CHAPTER 10. ANALYSIS OF THE RESULTS AND A PREDICTION FOR $PP$ FUSION

frequently used to obtain an uncertainty estimate for any calculation. A main advantage of using  $\not\epsilon$ EFT is the cutoff invariance, which is obtained at a natural scale of no more than a few times the physical breakdown scale ( $\Lambda \sim \text{few } m_\pi$ ). This is a measure of the irrelevance of regularization effects and does not only remove questions regarding residual cutoff dependencies that might contribute to the total uncertainty [42, 83], but also allows giving a physical meaning to the size of the NLO contribution. Since, in a non-renormalizable theory, strength can be shifted from one order to the other via similarity transformations [101].

The order-by-order RG invariance indicates that analyzing the results can be accomplished by studying the order-by-order contributions. We divide the calculation to three contributions: LO, NLO range corrections, and short-range contributions, proportional to  $l'_{1,2}^\infty$  and  $l_{1,A}$ . Table. 10.1 presents these three contributions to the different electro-weak matrix elements, for two NLO arrangements: the ERE- and  $Z$ -parameterizations (see section 2.6). For the  $pp$  fusion ( $A = 2, \Lambda_{pp}(0)$ ), the short-range corrections were calculated using  $l_{1,A}$  fixed by the  $A = 3$  observables ( $\langle GT \rangle, \langle F \rangle$ ) while the electromagnetic  $A = 2, 3$  observables were calculated using  $l'_{1,2}^\infty$  fixed by comparing our numerical results with experimental data of all combinations of two of the four  $A = 2, 3$  observables (see Chapter 7). The Gamow-Teller (GT) range correction is given by the difference between  $\langle GT \rangle_{\text{emp}}$  and our NLO predictions as discussed in Chapter 8.

	EW matrix element	NLO/LO total	NLO/LO range corrections	NLO/LO, LECs contributions
Electro- magnetic observable	$\langle \hat{\mu}_{3H} \rangle$ [nNM]	7% (0.1%)	3% (11%)	5% (10%)
	$\langle \hat{\mu}_{3He} \rangle$ [nNM]	16% (4%)	4% (25%)	12% (29%)
	$\langle \hat{\mu}_d \rangle$ [nNM]	1% (1%)	0% (0%)	1% (1%)
	$Y'_{np}$	6% (9%)	2% (2%)	4% (12%)
Weak observable	$A = 3 \langle GT \rangle, g_A = 1.2701$	2% (4%)	6% (21%)	3% (16%)
	$A = 3 \langle GT \rangle, g_A = 1.2769$	3% (5%)	6% (21%)	3% (16%)
	$\Lambda_{pp}(0), g_A = 1.2701$	6% (6%)	4.8% (0.3%)	1.3% (5.6%)
	$\Lambda_{pp}(0), g_A = 1.2769$	6% (6%)	4.8% (0.3%)	1.1% (5.4%)

Table 10.1: The order-by-order expansion of the electro-weak matrix elements. The order-by-order expansion of the electromagnetic matrix elements is based on their mean values given in Tab. 7.1. The nominal value is calculated using  $Z$ -parameterization, while the number in brackets is calculated using the ERE-parameterization. Mean denotes the mean value of the  $M_1$  observable based on its three predictions while  $\Delta$  denotes the standard deviation of these predictions.

From Tab 10.1 we find that the NLO contributions for all electro-weak matrix elements

are smaller than the LO part, and in particular for the case of the Z-parameterization, which leads to a better convergence up to NLO.

Thus, in the next subsections, we examine the  $\not\pi$ EFT NLO contributions and estimate its truncation error using the well-measured electromagnetic observables:  $\langle\hat{\mu}_{3\text{H}}\rangle$ ,  $\langle\hat{\mu}_{3\text{He}}\rangle$ ,  $\langle\hat{\mu}_d\rangle$ ,  $\sigma_{np}$  only for the Z-parameterization, which shows more natural convergence pattern, and therefore has a better predictive power. The large variations and fluctuations of the ERE-parameterization raise questions about its relevance at NLO for predictions of electro-weak observables.

### 10.1.1 $M_1$ observables as a case study

The electromagnetic observables: the three magnetic moments,  $\langle\hat{\mu}_{3\text{H}}\rangle$ ,  $\langle\hat{\mu}_{3\text{He}}\rangle$ ,  $\langle\hat{\mu}_d\rangle$ , and the radiative capture cross-section,  $\sigma_{np}$ , are all well-measured, which makes them a perfect tool for verifying and validating  $\not\pi$ EFT at NLO. In this section, we examine the two-body electromagnetic LECs calibrated from  $A = 2, 3$  observables (see Tab. 7.1 in Chapter 7) for better understanding the consistency of  $\not\pi$ EFT in making predictions, as well as in estimating theoretical uncertainties and truncation errors.

### 10.1.2 Pionless EFT expansion and setting $l_2'^\infty$ to zero

We found (in Chapter 7) qualitative differences between the  $l_1'^\infty$  and  $l_2'^\infty$  standard deviation. While  $\Delta l_1'^\infty/l_1' \approx 3\%$ , the standard deviation of  $l_2'^\infty$  is of the same order of magnitude as  $l_2'^\infty$ , *i.e.*,  $\Delta l_2'^\infty/l_2'^\infty \approx 70\%$ , so  $l_2'^\infty$  is consistent with zero. In addition, the NLO contribution to  $\langle\hat{\mu}_d\rangle$  (the  $M_1$  observable that depends on  $l_2'^\infty$  only) originates from LECs, is much smaller compared to other  $M_1$  observables, as shown in Tab. 10.1. This means that  $l_2'^\infty$  might be regarded as higher order than NLO. This is an amazing result, which will be discussed also in future publications.

Table 10.2 shows our predictions for  $l_1'^\infty$  and  $M_1$  observables up to NLO for the case in which  $l_2'^\infty = 0$ . Similarly to Tab. 7.1, for each row, the ' $\star$ ' notes the  $M_1$  observable used for  $l_1'^\infty$  calibration.

	$l_1^\infty \cdot 10^{-2}$	$\langle \hat{\mu}_{3\text{H}} \rangle$	$\langle \hat{\mu}_{3\text{He}} \rangle$	$Y'_{np}$
	4.36	★	-2.10	1.250
	4.97	2.996	★	1.256
	4.66	2.987	-2.11	★
Mean	4.7	2.99	-2.11	1.253
$\Delta$	0.6	0.01	0.01	0.006
%NLO/LO		7%	13%	5%
Exp data		2.979	-2.128	1.253

Table 10.2: Numerical results for our prediction for  $l_1^\infty$  and  $A = 2, 3$   $M_1$  observables with  $l_2^\infty = 0$ . The  $A = 3$  magnetic moments are given in units of nuclear magnetons ([nNM]).

It is clear that setting  $l_2'^\infty$  to zero does not reduce the precision and accuracy of  $l_1^\infty$  and  $M_1$  predictions. This implies that the  $l_2'^\infty$  contribution to the  $M_1$  matrix element is suppressed compared to NLO contributions. This fundamental point would be studied better in a study following this thesis.

### 10.1.3 Estimating pionless EFT theoretical uncertainty

As aforementioned, EFT is a systematic expansion in some small parameter. In order to judge whether the EFT describes well the observables, one needs to make sure that the expansion converges order-by-order. The theory presented here is purely perturbative, i.e., consistently organizes the expansion in a perturbative manner.

Since  $\not\!EFT$  is RG invariance, the  $\not\!EFT$  expansion for any  $M_1$  observable can be written as:

$$\langle M_1 \rangle = \langle M_1 \rangle_{\text{LO}} \cdot (1 + a_{M_1}^{\text{NLO}} + \mathcal{O}(\delta^2)). \quad (10.1)$$

EFT suggests that  $c_{M_1}^{\text{NLO}} = a_{M_1}^{\text{NLO}}/\delta$  are of natural size, and thus the truncation error is dictated by  $\delta$ . In  $\not\!EFT$ , the naïve expansion parameter is  $\delta \approx \frac{1}{3}$ . This expansion parameter, however, can be estimated directly from the numerical results we have presented. Firstly, in Tab. 10.2 we calculate the ratio of NLO to LO contribution for each matrix element. These ratios are found to be in the range of 0.05–0.13. Secondly, since  $\langle \hat{\mu}_d \rangle$  has vanishing NLO contribution, its deviation from experiment can be regarded as N<sup>2</sup>LO, and assuming a natural convergence we expect the ratio of this contribution to the LO contribution to be  $(\text{N}^2\text{LO}/\text{LO}) \approx (\text{NLO}/\text{LO})^2$ . This leads to  $(\text{NLO}/\text{LO}) \approx 0.1$ . Lastly, the variation of  $l_1^\infty$  (see Tab. 10.2) leads to a variation in the predictions for the different  $l_1'^\infty$  dependent

## CHAPTER 10. ANALYSIS OF THE RESULTS AND A PREDICTION FOR $PP$ FUSION

observables. This variation represents the contribution of higher orders, thus the ratio of the variation to the NLO contribution should be of the order of the expansion parameter. Using Tab. 10.2 this leads to  $(N^2\text{LO}/\text{NLO}) \approx 0.04 - 0.1$ .

If one assumes that the expansion parameter  $\delta$  is common to all  $M_1$  observables, then one can use the results to assess the value of  $\delta$ . In order to do this, let us take the log average of all the aforementioned samples:  $\log \left| a_{M_1}^{\text{N}^k\text{LO}} / a_{M_1}^{\text{N}^{k-1}\text{LO}} \right| = \log \delta + \log R$ . The numbers  $R$  are positive natural numbers and are not biased, thus should be distributed about "1", and summing over their logarithms should vanish. The log average of many such samples should converge to  $\log \delta$ . The fact that this is a finite sized sample, means that there remains a measure of uncertainty, represented in a distribution, which we find that at a 95% degree of belief the expansion parameter is in the range,  $0.05 < \delta < 0.1$ .

These suggest that the expansion converges faster, by about a factor of 3, than the naïve  $\not{p}$ EFT estimate.

The truncation error of a given expansion, given a prior which represents the naturalness of the expansion, follows a posterior that was calculated in Refs. [102–104]. In the current case, since the expansion parameter is unknown, *i.e.*, follows the aforementioned prior distribution, one should fold these two distributions to find the posterior distribution of these two distribution. The formalism is further explained in Appendix D.

In order to check the sensitivity of the expansion parameter to the number of observables, we calculate the Cumulative Density Functions (CDF) of  $\delta$ , the expansion parameter, with all the  $n = 7$  constraints: the NLO contributions of  $\langle \mu_{3\text{H}} \rangle$ ,  $\langle \hat{\mu}_{3\text{He}} \rangle$ ,  $Y_{np}$ , the  $N^2\text{LO}$  contribution of  $\langle \hat{\mu}_d \rangle$ , and the variation of  $l_1^\infty$  stems from the three electromagnetic observables. Also, we calculate the CDF of  $\delta$  only with the  $n = 4$  first constraints stemming from the order of the calculation and not from the LEC variation. As shown in Fig. 10.1, at 70% degree of belief, the effect of the change is rather small (a change of about 20% in the estimated truncation error). At higher degrees of belief, especially above 90%, the truncation error depends significantly on the number of constraints, as can be expected.

Figure 10.2 shows that at about 70% degree of belief, the  $M_1$  obesrables' uncertainty does not exceed 1%<sup>1</sup>. Also shown a similar analysis for the proton-proton fusion, assuming that this reaction has the same expansion parameter as the magnetic observables. This will be discussed further in the next section.

Comparing our theoretical prediction (including the uncertainty calculated above) with experimental results, we find that the theory well reproduces the electromagnetic observables within the estimated uncertainties, as is graphically summarized in Fig. 10.3.

<sup>1</sup>The uncertainty varies with the observable. 1% is the maximal value, to be on the conservative side.

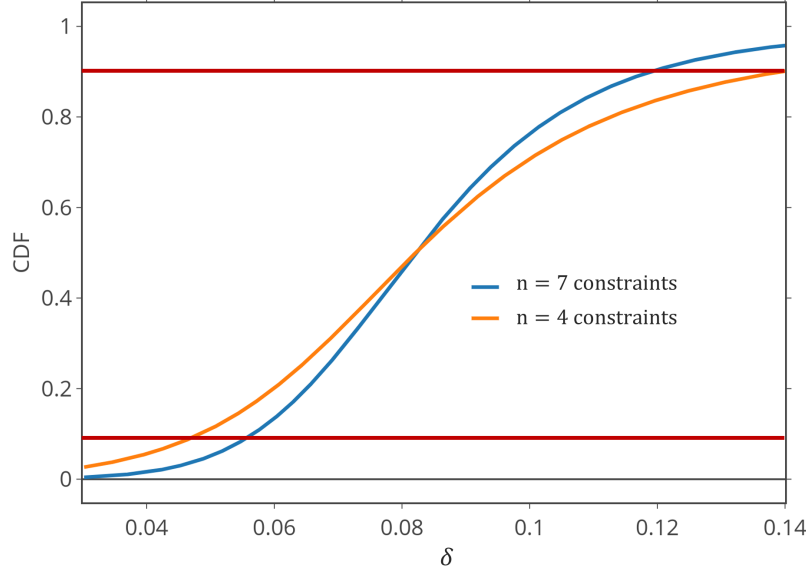


Figure 10.1: Cumulative Density Functions (CDFs) of  $\delta$ , the expansion parameter. The blue curve represents a calculation which takes into account the constraints of the NLO contributions of  $\langle \hat{\mu}_{3\text{H}} \rangle$ ,  $\langle \hat{\mu}_{3\text{He}} \rangle$ ,  $Y_{np}$ , the N<sup>2</sup>LO contribution of  $\langle \hat{\mu}_d \rangle$ , and the variation of  $l_1^\infty$ . The orange curve takes into account only the first four former constraints. The red lines limit the 10 – 90% probability range.

## 10.2 Analogy between $M_1$ observables and weak reactions

A significant conclusion arises in this work, is the similar structure of the weak and electromagnetic observables in  $\not{A}$ EFT (see Tab. 1.2 and Chapter 5). As shown in Tab. 1.2, the one-body operators of the weak and electromagnetic interactions have the same structure, *i.e.*, one-body LECs coupled to Pauli matrices.

The electromagnetic LEC,  $l_1$ , which couples the spin-singlet to spin-triplet channel, has a weak analogue,  $l_{1,A}$ . We found that electromagnetic LEC,  $l_2$ , which couples two spin-triplet channels (and has no weak analogue) to be of a higher order than  $l_1$  and  $l_{1,A}$ . This result emphasizes the qualitative similarity between the two interactions.

This similarity goes beyond this qualitative statement. In Chapter 8 we have calculated the triton  $\beta$ -decay into  $^3\text{He}$ , which contains both the Fermi and the Gamow-Teller transitions. The Fermi transition, which is the weak analogue to the three-body normalization is found to be nearly one. Also, the Gamow-Teller transition, which is the weak analogue to the three-body magnetic moments is also found to be nearly  $\sqrt{3}$  at LO,

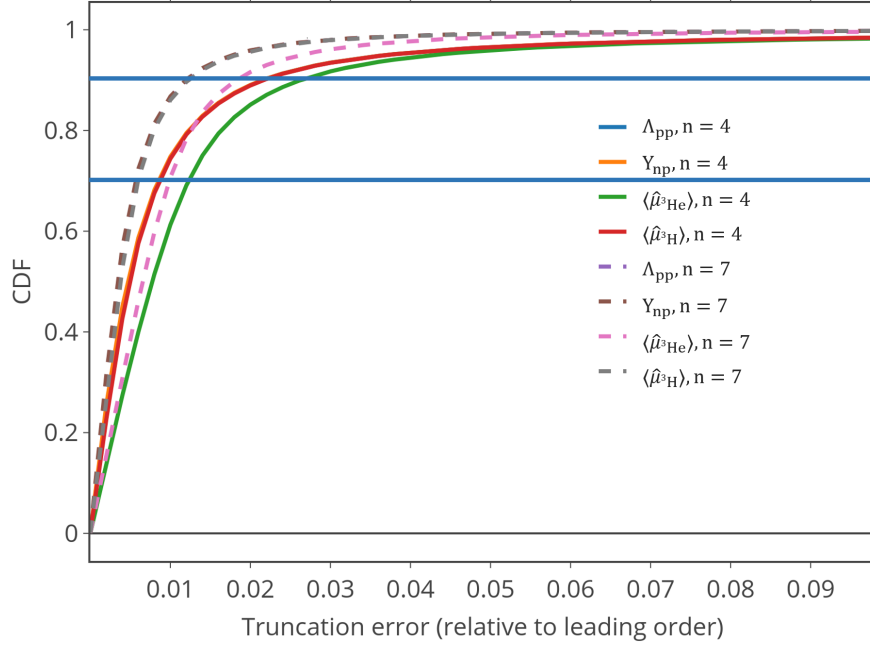


Figure 10.2: Cumulative Density Functions (CDFs) for the different observables, as calculated using eq. (D-2). Horizontal lines are the 70% and 90% degree of beliefs. We show CDFs relevant to expansion parameter priors with  $n = 4$  (solid lines) and  $n = 7$  (dashed lines) constraints, as explained in Fig. 10.1.

*i.e.*,  $\langle GT^{\text{LO}} \rangle = \langle \psi^{\text{LO}}(E_{3\text{He}}, p) | \sigma \tau^+ | \psi^{\text{LO}}(E_{3\text{H}}, p) \rangle = 0.99(1)\sqrt{3}$ . This is consistent with the electromagnetic matrix moments at LO where  $\langle \hat{\mu}_{3\text{H}}^{\text{LO}} \rangle \approx \mu_p$  and  $\langle \hat{\mu}_{3\text{He}}^{\text{LO}} \rangle \approx \mu_n$ .

These similar characters of the electromagnetic and weak interactions along with the perturbative character of the Coulomb interaction, presented in Chapters 5 and 8 are reflecting the small effect of the Coulomb interaction on the  $^3\text{He}$  wave-function and implies that the expansion parameter,  $\delta$ , calculated from the electromagnetic observables is the same for the weak interactions and in particular, the  $pp$ -fusion.

### 10.3 Theoretical uncertainty of $pp$ fusion due to pionless EFT truncation

As mentioned above, for the weak interaction only the triton  $\beta$ -decay is low-energy, well-measured reaction. Therefore, we cannot estimate the theoretical uncertainty of the weak  $\nexists$ EFT calculation in the same method used for the electromagnetic case. Nevertheless, we can use the analogy between the electromagnetic to weak observables for estimating the theoretical uncertainty of the  $pp$  fusion and alluding to their nominal NLO arrangement. In the previous sections we showed that both  $pp$  fusion and  $np$ -radiative capture have



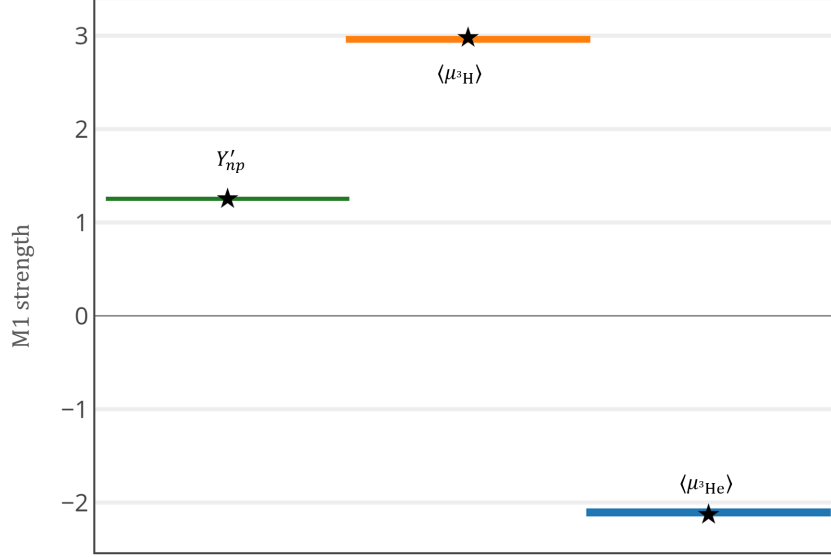


Figure 10.3: The strength of  $A = 2, 3$   $M_1$  observables with 70% degree of belief. The bands correspond to the theoretical  $Z$ -parameterization uncertainty as shown in from Fig. 10.2. The stars are the experimental values.

similar small NLO contributions as shown in Tab. 10.1. This behavior, as well as the similar  $\overline{\text{N}}\text{EFT}$  characteristics presented above, indicate that the electromagnetic theoretical uncertainty originating in  $\overline{\text{N}}\text{EFT}$  truncation is valid also for the weak observables, which is 1% for the  $Z$ -parameterization (see Fig. 10.2). We note that this is not inconsistent. The uncertainty estimate relies upon the small expansion parameter, implied by the ratio of the NLO contribution, compared to the LO result. The uncertainty should then be of the order of the expansion parameter squared. The similarities between the electromagnetic and the weak calculations bring us to two separate conclusions: (i) the expansion parameter of both should be the same, and thus the uncertainty analysis should lead to the same results, (ii) the  $Z$ -parameterization is more appropriate for such long distance observables at NLO. Thus, in the following we consider only the  $Z$ -parameterization predictions for the  $pp$  fusion, and assume 0.6% of theoretical uncertainty in the calculation of the weak matrix element with 70% degree of belief.

## 10.4 Final results and comparison to previous calculations of $l_{1,A}$ and the $pp$ fusion

As discussed above, the analogy between the electromagnetic and the weak observables enables us to use the Z-parameterization as the preferred parameterization for LECs calibration up to NLO. Therefore we find that:

$$l_{1,A} = 0.055 \pm 0.004 \pm 0.001, \quad g_A = 1.2701 \quad (10.2)$$

$$l_{1,A} = 0.049 \pm 0.004 \pm 0.001, \quad g_A = 1.2767 \quad (10.3)$$

where the first uncertainty comes from  $g_A$  experimental uncertainty and the second uncertainty comes from the rest of the experimental uncertainties, such as the statistical uncertainties in the measured triton half-life.

The  $pp$  fusion matrix element is given by:

$$\Lambda_{pp}(0) = 2.66 + 0.6l_{1,A}. \quad (10.4)$$

Since the astrophysical  $S^{11}(0)$  is given by:

$$S^{11}(0) = 4.01 \left( \frac{g_A}{1.2695} \right)^2 \frac{\Lambda_{pp}^2(0)}{7.035}, \quad (10.5)$$

one gets

$$S_{pp}(0, g_A = 1.2701) = (4.14 \pm 0.05 \pm 0.012 \pm 0.002) \cdot 10^{-23} \text{MeV} \cdot \text{fm}^2, \quad (10.6)$$

and

$$S_{pp}(0, g_A = 1.2766) = (4.17 \pm 0.05 \pm 0.012 \pm 0.002) \cdot 10^{-23} \text{MeV} \cdot \text{fm}^2, \quad (10.7)$$

The first uncertainty originates in the theoretical uncertainty estimated as 0.6% for the weak matrix element with 70% degree of belief (see Fig. 10.2). The second uncertainty originates in the experimental uncertainty of  $g_A$  ( $1\sigma$ ), while the third uncertainty originates from the experimental value of  $^3\text{H}$  half-life ( $1\sigma$ ). Since the theoretical uncertainty of  $S_{pp}(0)$  is more dominant than the other two, we get at about 70% degree of belief, combining

them quadratically (assuming Gaussian pdfs for the experimental uncertainties):

$$S_{pp}(0, g_A = 1.2701) = (4.14 \pm 0.05 \pm 0.012 \pm 0.002) \cdot 10^{-23} \text{MeV} \cdot \text{fm}^2, \quad (10.8a)$$

$$S_{pp}(0, g_A = 1.2766) = (4.17 \pm 0.05 \pm 0.012 \pm 0.002) \cdot 10^{-23} \text{MeV} \cdot \text{fm}^2, \quad (10.8b)$$

eqs. (10.8a) and (10.8b) are the main results of this thesis.

### 10.4.1 Previous extractions of $L_{1,A}$

Due to the importance of  $L_{1,A}$ , as the only counterterm that appears in the pionless description of  $pp$  fusion, its evaluation has attracted much attention in the literature. In this subsection, we review the previous extraction of  $l_{1,A}$  in the  $\not\pi$ EFT and the latest predictions of the  $pp$  fusion rate.

Two main approaches were taken in previous studies to match  $l_{1,A}$ . In the first, an experimental value of a two-body weak interaction process, usually at cutoff of  $\mu = m_\pi$  has been used for matching. Among these reactions are deuteron dissociation by anti-neutrinos from reactors [105], and neutrino reactions with the deuteron, as measured in SNO [106], both lead to similar RG invariant combinations of the two-body axial strength,  $l_{1,A} \approx 0.13 \pm 0.26$ . In both cases, the large uncertainties originate from statistical errors in the experiments, due to the small cross-section for neutrino-deuteron reactions. The authors of Ref. [11] proposed, therefore, a precision measurement of muon capture on the deuteron, with the aim of reducing the uncertainties by a factor of 3, reflecting an estimated 2-3% experimental uncertainty in the (then proposed) ongoing MuSun experiment [107]. It is important to note that the  $\mu^- d$  capture has a large energy transfer, possibly too large for an application of  $\not\pi$ EFT, which might impact the convergence pattern of any calculation. In all these, the uncertainties are mainly experimental, due to the uncertainty in the observable, i.e. neglecting the truncation error.

A different approach was taken by Ando and collaborators in Ref. [32]. They used the hybrid calculation of the  $pp$  fusion rate from Park, Marcucci *et al.* [33]. As a constraint, the ratio of the two-body strength over the one-body strength was taken from that calculation and matched  $L_{1,A}$  to reproduce this ratio in the  $\not\pi$ EFT regime. Their result was  $l_{1,A} = 0.038 \pm 0.002$ . Their small uncertainties is due to the accurate triton half-life measurement that is used to fix undetermined counterterms in Ref. [33]. However, this work highlights a few criticisms of Ref. [32]. Firstly, a three-body constraint should be taken at a sufficiently large cutoff, to make sure no regularization effects affect the cutoff invariance. Secondly,

## CHAPTER 10. ANALYSIS OF THE RESULTS AND A PREDICTION FOR $PP$ FUSION

---

they take a phenomenological approach which leads to contributions from higher orders to the NLO calculation, as they take the non-perturbative deuteron normalization at all orders. These two reasons entail that a robust theoretical uncertainty estimate is very hard within this approach, and indeed it is missing from the  $L_{1,A}$  result in this case. Lastly, and most important, the constraint they take is not an observable, as one can use hermitian transformations to shift strengths from the two-body sector to the one-body, and vice versa.

In 2017, the Nuclear Physics with Lattice Quantum Chromo Dynamics (NPLQCD) collaboration has calibrated  $L_{1,A}$  using the triton  $\beta$ -decay [34], with

$$l_{1,A} = 0.068(0.003)(0.017)(0.006)(0.016).$$

The four uncertainties are: the statistical uncertainty, the fitting and analysis systematic uncertainty, the mass extrapolation systematic uncertainty, and a power-counting estimate of higher order corrections in  $\not{P}$ EFT, respectively. Their value matches our  $Z$ -parameterization value, while considering all uncertainties. Similarly to the electromagnetic calculation of  $l_1$ , we find that their value for the two-body LEC is larger than our  $Z$ -parameterization prediction. We assume that this difference between these values comes from the different power-counting of the two works. As discussed in Chapter 7, the power-counting used in that paper, is different from the one we use here, e.g., the deuteron normalization is taken at its nature value ( $Z_d \approx 1.69$ ) at all orders, and not perturbatively, as in this work. For both electromagnetic weak interaction, the lattice QCD (LQCD) matrix elements have the form:  $Y = \sqrt{Z_d} (Y^{\text{LO}} + Y^{\text{NLO}})$ , where  $\sqrt{Z_d} = \frac{1}{\sqrt{1-\gamma_t \rho_t}}$ . This form is inconsistent with our power-counting that assumes  $\frac{\rho}{a} \ll 1$ . The disadvantage of the power-counting used in Ref. [34], arises from the fact that for this power-counting, the deuteron propagator is taken at all orders, (eq. (2.61)) and therefore it contains a pole at  $q \sim 150 \text{ MeV}$ , which is around the breakup scale  $\mu = m_\pi$ . This pole makes it very difficult to calculate the  $A = 3$  observables at cutoffs greater than the breakup scale ( $\mu \sim \text{few } m_\pi$ ), and therefore the two-body LEC,  $l_{1,A}$ , calibrated from the  ${}^3\text{H}$   $\beta$ -decay was calculated at  $\mu = m_\pi$ . This calculation stands in contrast to the  $\not{P}$ EFT used here, which was found to be RG invariant for  $\Lambda \sim \text{few } m_\pi$  and according to what is known today, cannot be achieved without assuming that  $\frac{\rho}{a} \ll 1$ .

### 10.4.2 $pp$ fusion past predictions

The validity of our  $\not\chi$ EFT prediction for the  $pp$  fusion rate is obtained also by benchmarking with previous calculations, where the relevant past predictions were calculated by Marcucci *et al.* in 2013 [8], Acharya *et al.* in 2016 [10] and LQCD in 2017 [34].

The comparison between our predictions to that of Marcucci *et al.* [8] (pure Coulomb  $\chi$ EFT S-calculation) has to be made for the same  ${}^3\text{H}$  decay rate,  $g_A$  and for the same  $\langle F \rangle$  value. Our prediction, assuming their values for the needed parameters, is:

$$S_{pp}^{\not\chi\text{EFT}}(0, g_A = 1.2695) = (4.14 \pm 0.05) \cdot 10^{-23} \text{MeV} \cdot \text{fm}^2, \quad (10.9)$$

while that of Marcucci *et al.* is:

$$S_{pp}^{\chi\text{EFT}}({}^3S_1, \text{pure Coulomb}) = (4.030 \pm 0.006) \cdot 10^{-23} \text{MeV} \cdot \text{fm}^2. \quad (10.10)$$

This interesting tension was found also by Acharya *et al.* [10] and was explained in the following way. According to Acharya *et al.* [10], this inconsistency can arise from the infrared convergence of the matrix elements between a bound-state and a scattering state wave function of Marcucci *et al.* calculation. In their work, Acharya *et al.* [10] have recalculated the S-factor of  $pp$  fusion reaction using  $\chi$ EFT up to NNLO:

$$S_{pp}^{\text{NNLO}}(0) = (4.081_{-0.032}^{+0.024}) \cdot 10^{-23} \text{MeV} \cdot \text{fm}^2, \quad (10.11)$$

where the uncertainty originates from optimizing 42 different NNLO interactions used in that work, as well as the statistical uncertainties of all LECs used for that calculation, including  $g_A$ .

Finally, for the LQCD calculating [34], we find that:

$$S_{pp}^{\text{LQCD}}(0) = 4.052(0.006)(0.03)(0.012)(0.027) \cdot 10^{-23} \text{MeV} \cdot \text{fm}^2, \quad (10.12)$$

(where the four uncertainties are the statistical uncertainty, the fitting and analysis systematic uncertainty, the mass extrapolation systematic uncertainty, and a power-counting estimate of higher order corrections in  $\not\chi$ EFT, respectively [34]). As discussed above, the different power-counting of Ref. [34] makes the comparison between the two predictions, problematic. Moreover, the NPLQCD method, based on extrapolating the quark mass up to its natural value is still partially controlled and has big uncertainties.

Among the four estimates (Marccuci, Acharya, LQCD and this work), only the predictions done by Acharya *et al.* can serve as a benchmark for our prediction, due to wrong calculation of wave functions in Ref. [8] and the uncontrolled extrapolation and approximations in the lattice calculation of Ref. [34]. The comparison between the two calculations shows a good agreement, taking the uncertainties into account (eq. (10.8a)). Moreover, since both calculations have used the triton  $\beta$ -decay for calibrating the two-body LEC ( $l_{1,A}$ ), the overlapping of the two predictions is another confirmation to the validity of the theory. This consistency has a great significance due to the distinct differences of the recent predictions for the  $pp$  fusion in the last decade.

In conclusion, by comparison to the electromagnetic predictions, we find that the  $Z$ -parameterization is the more appropriate parameterization for calculating  $A = 2, 3$  observables in  $\pi$ EFT at NLO, for these long distance observables. We note that for very low-energy interactions, the deuteron normalization must include the deuteron tail of the wave function, which is not possible up to NLO in the ERE-parameterization.

Our final predictions for the  $pp$  fusion rate derived in this work, are:

$$S_{pp}(0, g_A = 1.2701) = (4.14 \pm 0.05) \cdot 10^{-23} \text{ MeV} \cdot \text{fm}^2, \quad (10.13)$$

$$S_{pp}(0, g_A = 1.2766) = (4.17 \pm 0.05) \cdot 10^{-23} \text{ MeV} \cdot \text{fm}^2. \quad (10.14)$$

which are consistent with chiral EFT predictions, and especially with Acharya *et al.* [10]. However, the current calculation, apart from including an estimate for the theoretical uncertainty, is RG invariant, fully perturbative, and includes about a factor of 3 less parameters. In addition, each parameter is related to a measured specific observable, such as the scattering lengths, the effective ranges, and the axial constant.



## Summary and outlook

In this thesis, we presented a detailed study of low-energy electro-weak  $A = 2, 3$  observables using  $\not\pi$ EFT to next-to-leading order (NLO). The main purpose of the thesis was to calculate and estimate the theoretical and empirical uncertainties of the  $pp$  fusion rate.

This was done by establishing a perturbative and consistent framework to calculate transitions between three-body bound-states, up to NLO. This method is based on a diagrammatic expansion of both the nuclear amplitudes (wave functions) and the matrix elements which are proportional to the electro-weak observables. For these electro-weak matrix elements, the NLO contributions amount less than 10% correction, which is smaller than the naïve expansion parameter of  $\not\pi$ EFT. The similar NLO contributions of both the electromagnetic and weak observables have strengthened the premise that the two sectors (weak and electromagnetic) share similar properties. Therefore we have used our predictions for the well-measured electromagnetic observables to estimate the theoretical and empirical  $\not\pi$ EFT uncertainties of  $A = 2, 3$  electro-weak interactions.

We showed that by using the so-called  $Z$ -parameterization, that correctly describes the deuteron wave function at large distances, the values of the short-range strengths are consistent in the  $A = 2$  and  $A = 3$  systems, up to 1%, as estimated by the robust order-by-order convergence. We found that  $\not\pi$ EFT predictions for the electromagnetic observables have unprecedented precision and accuracy, which, as summarized in Fig. 10.3, verify and validate the way we applied  $\not\pi$ EFT at NLO. Using the  $Z$ -parameterization, our final predictions for the electromagnetic interactions are, to 70% degree of belief:



	This work [nNM]	Experiment [nNM]	
$Y'_{np}$	$= 1.253 \pm 0.006$	$1.2532 \pm 0.0019$	[55]
$\langle \hat{\mu}_{3\text{H}} \rangle$	$= 2.992 \pm 0.015$	$2.97896\dots$	[53]
$\langle \hat{\mu}_{3\text{He}} \rangle$	$= -2.11 \pm 0.02$	$-2.12750\dots$	[53]

Our predictions for the electromagnetic observables, which perfectly match the experimental data, point out that by using the  $Z$ -parameterization,  $\not\!Z$ EFT is consistent for a simultaneous description of  $A = 2$  and  $A = 3$  systems up to NLO. This consistency enabled us to calibrate the unknown weak low-energy constant  $l_{1,A}$ , needed for the calculation of the  $pp$  fusion rate, from the well-measured  ${}^3\text{H}$   $\beta$ -decay.

$$S_{pp}(0) = (4.15 \pm 0.06) \cdot 10^{-23} \text{ MeV} \cdot \text{fm}^2, \quad (11.1)$$

Our result is 1.5%-4.5% higher than recent predictions of the  $pp$  fusion rate [3, 8], which have been used for theoretical computations of stellar models [108, 109]. Our new predictions will affect the stellar models and will be checked in future work.

## 11.1 Outlook

A natural continuation of this Ph.D. research outlined above, is a study of other aspects of  $\not\!Z$ EFT. The NLO contributions of the electro-weak observables are smaller than our naïve estimations and in our opinion, this requires further examination which is beyond the scope of this thesis.

An interesting result, which was found at the ending stages of this thesis, is that the isoscalar two-body strength  $l_2$ , should enter at higher order than  $l_1$ , *i.e.*, than its naïve dimensional analysis suggested order. This might be related to the fact that in chiral EFT the isovector two-body electromagnetic current is an NLO term, while the isoscalar two-body contribution is further suppressed. In addition, the small NLO contributions to the  $M_1$   $A = 2, 3$  observables lead to the famous approximate shell model structure of the magnetic moments. These unexpected signatures of pion physics and shell model naturally stem from pionless EFT. This seems to be a first example for a connection between these three approaches to nuclear structure. This fundamental point would be studied better in a study following this thesis.

# Appendix A

## The Faddeev equations three-body scattering

### I The Faddeev equations for $n - d$ scattering

#### a The Quartet channel for $n - d$ scattering

Using the Feynman rules that follow from the Lagrangian, eq. (2.58), and inserting appropriate symmetry factors, we get:

$$\begin{aligned}
 iT^{ij}(E; \mathbf{p}, \mathbf{k})_{\beta b}^{\alpha a} &= (-2iy_t)^2 \frac{1}{\sqrt{8}} (\sigma^2 \sigma^i)_{\alpha'}^{\alpha} (\tau^2)_{a'}^a iS(k_0 - p_0, \mathbf{k} - \mathbf{p}) \delta_{\beta'}^{\alpha'} \delta_{b'}^{a'} \frac{1}{\sqrt{8}} (\sigma^j \sigma^2)_{\beta}^{\beta'} (\tau^2)_b^{b'} \\
 &\quad + \int \frac{d^4 q}{(2\pi)^4} (-2iy_t)^2 \frac{1}{\sqrt{8}} (\sigma^2 \sigma^i)_{\alpha'}^{\alpha} (\tau^2)_{a'}^a iS(q_0 - p_0, \mathbf{q} - \mathbf{p}) i\mathcal{D}_t(q_0, q) \delta_{b'}^{a'} \times \\
 &\quad \quad \quad iT^{ik}(E; \mathbf{q}, \mathbf{k})_{\beta' b}^{\alpha' c} \frac{1}{\sqrt{8}} (\sigma^k \sigma^2)_{\beta}^{\beta'} (\tau^2)_b^{b'} = \\
 iT^{ij}(E; \mathbf{p}, \mathbf{k})_{\alpha b}^{\beta a} &= (-iy_t)^2 \frac{1}{2} (\sigma^j \sigma^i)_{\alpha}^{\beta} iS(k_0 - p_0, \mathbf{k} - \mathbf{p}) \delta_b^a \\
 &\quad + \int \frac{d^4 q}{(2\pi)^4} (-iy_t)^2 \frac{1}{2} (\sigma^j \sigma^k)_{\alpha'}^{\beta} iS(q_0 - p_0, \mathbf{q} - \mathbf{p}) i\mathcal{D}_t(q_0, q) \delta_c^a iT^{ik}(E; \mathbf{q}, \mathbf{k})_{\alpha b}^{\alpha' c}.
 \end{aligned} \tag{A-1}$$

Integration over  $q_0$  yields:

$$\begin{aligned}
 iT^{ij}(E; \mathbf{p}, \mathbf{k})_{\alpha b}^{\beta a} &= -i \frac{My_t^2}{2} (\sigma^j \sigma^i)_{\alpha}^{\beta} \delta_b^a \frac{1}{\mathbf{k}^2 + \mathbf{p}^2 + \mathbf{k} \cdot \mathbf{p} - ME} \\
 &\quad + i \int \frac{d^3 q}{(2\pi)^3} \frac{My_t^2}{2} (\sigma^j \sigma^k)_{\alpha'}^{\beta} \delta_c^a \mathcal{D}_d \left( E - \frac{q^2}{2M}, q \right) \frac{iT^{ik}(E; \mathbf{q}, \mathbf{k})_{\alpha b}^{\alpha' c}}{\mathbf{q}^2 + \mathbf{p}^2 + \mathbf{q} \cdot \mathbf{p} - ME}.
 \end{aligned} \tag{A-2}$$

## b The Doublet channel for $n - d$ scattering

The Faddeev equations for  $n - d$  scattering are given by:

$$\begin{aligned}
 (iT^{i,j})_{\alpha\alpha}^{\beta b}(E; \mathbf{k}, \mathbf{p}) &= -\frac{iMy_t^2}{2} \cdot (\sigma^j \sigma^i)_\alpha^\beta \delta_a^b \frac{1}{\mathbf{k}^2 + \mathbf{k} \cdot \mathbf{p} + \mathbf{p}^2 - ME} \\
 &+ \frac{My_t^2}{2} \int \frac{d^3q}{(2\pi)^3} D_t(E, q) \frac{(\sigma^j \sigma^k)_\gamma^\beta \delta_c^b}{\mathbf{q}^2 + \mathbf{q} \cdot \mathbf{p} + \mathbf{p}^2 - ME} (iT^{ik})_{\alpha\alpha}^{\gamma c} \\
 &+ \frac{My_t y_s}{2} \int \frac{d^3q}{(2\pi)^3} D_s^{np}(E, q) \frac{(\sigma^k)_\gamma^\beta (\tau^3)_c^b}{\mathbf{q}^2 + \mathbf{q} \cdot \mathbf{p} + \mathbf{p}^2 - ME} (iS_{nn}^i)_{\alpha\alpha}^{\gamma c} \\
 &+ \frac{My_t y_s}{2} \int \frac{d^3q}{(2\pi)^3} \mathcal{D}_t^{nn}(E - \frac{\mathbf{q}^2}{2M}, \mathbf{q}) \frac{(\sigma^k)_\gamma^\beta (\tau^{1+2i})_c^b}{\mathbf{q}^2 + \mathbf{q} \cdot \mathbf{p} + \mathbf{p}^2 - ME} (iS_{nn}^i)_{\alpha\alpha}^{\gamma c} \\
 (iS_{np})_{\alpha\alpha}^{\beta b}(\mathbf{k}, \mathbf{p}; E) &= -\frac{iMy_s^2}{2} \cdot (\sigma^i)_\alpha^\beta (\tau^3)_a^b \cdot \frac{1}{\mathbf{k}^2 + \mathbf{k} \cdot \mathbf{p} + \mathbf{p}^2 - MME} \\
 &+ \frac{My_t y_s}{2} \int \frac{d^3q}{(2\pi)^3} \mathcal{D}_d(E - \frac{\mathbf{q}^2}{2M}, \mathbf{q}) \frac{(\sigma^k)_\alpha^\gamma (\tau^3)_c^b}{\mathbf{q}^2 + \mathbf{q} \cdot \mathbf{p} + \mathbf{p}^2 - ME} (iT^{ik})_{\alpha\alpha}^{\gamma c} \\
 &+ \frac{My_s^2}{2} \int \frac{d^3q}{(2\pi)^3} D_s^{np}(E, q) \frac{(\tau^3)_c^b (\tau^3)_d^c}{\mathbf{q}^2 + \mathbf{q} \cdot \mathbf{p} + \mathbf{p}^2 - ME} (iS_{np}^i)_{\alpha\alpha}^{\beta d} \\
 &+ \frac{My_s^2}{2} \int \frac{d^3q}{(2\pi)^3} \mathcal{D}_t^{nn}(E - \frac{\mathbf{q}^2}{2M}, \mathbf{q}) \frac{(\tau^{C=i+i \cdot 2})_c^b (\tau^3)_d^c}{\mathbf{q}^2 + \mathbf{q} \cdot \mathbf{p} + \mathbf{p}^2 - ME} (iS_{nn}^i)_{\alpha\alpha}^{\beta d} \\
 (iS_{nn}^i)_{\alpha\alpha}^{\beta b}(\mathbf{k}, \mathbf{p}; E) &= -\frac{iMy_t y_s}{2} \cdot (\sigma^i)_\alpha^\beta (\tau^{B=1+i \cdot 2})_a^b \cdot \frac{1}{\mathbf{k}^2 + \mathbf{k} \cdot \mathbf{p} + \mathbf{p}^2 - ME} \\
 &+ \frac{My_t y_s}{2} \int \frac{d^3q}{(2\pi)^3} D_t(E, q) \frac{(\sigma^k)_\alpha^\gamma (\tau^{B=1+i \cdot 2})_c^b}{\mathbf{q}^2 + \mathbf{q} \cdot \mathbf{p} + \mathbf{p}^2 - ME} (iT^{ik})_{\alpha\alpha}^{\gamma c} \\
 &+ \frac{My_s^2}{2} \int \frac{d^3q}{(2\pi)^3} D_s^{np}(E, q) \frac{(\tau^3)_c^b (\tau^{B=1+i \cdot 2})_d^c}{\mathbf{q}^2 + \mathbf{q} \cdot \mathbf{p} + \mathbf{p}^2 - ME} (iS_{nn}^i)_{\alpha\alpha}^{\beta d},
 \end{aligned} \tag{A-3}$$

where the superscripts  $i, j$  denote the Cartesian indexes of the incoming and outgoing dibaryon fields and the amplitudes are not projected on definite  $J$  and  $T$ . The projector is given by  $\frac{1}{\sqrt{3}}\sigma_i$  for deuteron channel and by  $\frac{1}{\sqrt{3}}\tau_i$  for the triplet channel [71]:

$$iT(E; \mathbf{p}, \mathbf{k})_{\beta b}^{\alpha a} = \frac{1}{3} (\sigma^i)_\alpha^\alpha iT(E; \mathbf{p}, \mathbf{k})^{ij}_{\beta' b} \alpha'^a_{\beta'} (\sigma^j)_\beta^{\beta'}, \tag{A-4}$$

$$iS(E; \mathbf{p}, \mathbf{k})_{\beta b}^{\alpha a} = \frac{1}{3} (\sigma^i)_\alpha^\alpha i(S(E; \mathbf{p}, \mathbf{k})^{iC})_{\beta' a'}^{\alpha' a} (\tau^C)_b^{a'}, \tag{A-5}$$

where for  $n - d$  scattering  $a = b = 1$ ,  $\alpha = \beta$  and  $a_{nn} = a_{np} = a_s$  and  $S_{np} = S_{nn}$ .

## II The Faddeev equations for $p - d$ scattering

### a The Quartet channel for $p - d$ scattering

Using the Feynman rules (Tab. 2.2) which follow from the Lagrangian eq. (2.58) and inserting appropriate symmetry factors, we get:

$$\begin{aligned}
 iT^{ij}(E; \mathbf{p}, \mathbf{k})_{\beta b}^{\alpha a} = & (-2iy_t)^2 \frac{1}{\sqrt{8}} (\sigma^2 \sigma^i)_{\alpha'}^{\alpha} (\tau^2)_{a'}^a iS(k_0 - p_0, \mathbf{k} - \mathbf{p}) \delta_{\beta'}^{\alpha'} \delta_{b'}^{a'} \frac{1}{\sqrt{8}} (\sigma^j \sigma^2)_{\beta}^{\beta'} (\tau^2)_b^{b'} + \\
 & (-2iy_t)^2 \frac{1}{\sqrt{8}} (\sigma^2 \sigma^i)_{\alpha'}^{\alpha} (\tau^2)_{a'}^a i\mathcal{I}_B(E, \mathbf{k}, \mathbf{p}) i\mathcal{D}_{photon}(\mathbf{k} - \mathbf{p}) \delta_{\beta'}^{\alpha'} \delta_{b'}^{a'} \frac{1}{\sqrt{8}} (\sigma^j \sigma^2)_{\beta}^{\beta'} (\tau^2)_b^{b'} + \\
 & (-2iy_t)^2 \frac{1}{\sqrt{8}} (\sigma^2 \sigma^i)_{\alpha'}^{\alpha} (\tau^2)_{a'}^a i\mathcal{I}_b(\mathbf{k}, \mathbf{p}) \delta_{\beta'}^{\alpha'} \delta_{b'}^{a'} \frac{1}{\sqrt{8}} (\sigma^j \sigma^2)_{\beta}^{\beta'} (\tau^2)_b^{b'} + \\
 & + \int \frac{d^4 q}{(2\pi)^4} (-2iy_t)^2 \frac{1}{\sqrt{8}} (\sigma^2 \sigma^i)_{\alpha'}^{\alpha} (\tau^2)_{a'}^a iS(q_0 - p_0, \mathbf{q} - \mathbf{p}) i\mathcal{D}_t(q_0, q) \delta_{b'}^{a'} \times \\
 & \quad iT^{ik}(E; \mathbf{q}, \mathbf{k})_{\beta' b}^{\alpha' c} \frac{1}{\sqrt{8}} (\sigma^{\mathbf{k}} \sigma^2)_{\beta}^{\beta'} (\tau^2)_b^{b'} + \\
 & + \int \frac{d^4 q}{(2\pi)^4} (-2iy_t)^2 \frac{1}{\sqrt{8}} (\sigma^2 \sigma^i)_{\alpha'}^{\alpha} (\tau^2)_{a'}^a iS(q_0 - p_0, \mathbf{q} - \mathbf{p}) i\mathcal{D}_t(q_0, q) \delta_{b'}^{a'} \times \\
 & \quad iT^{ik}(E; \mathbf{q}, \mathbf{k})_{\beta b}^{\alpha' c} i\mathcal{I}_B(E, \mathbf{q}, \mathbf{p}) i\mathcal{D}_{photon}(\mathbf{q}) \frac{1}{\sqrt{8}} (\sigma^{\mathbf{k}} \sigma^2)_{\beta}^{\beta'} (\tau^2)_b^{b'} \\
 & + \int \frac{d^4 q}{(2\pi)^4} (-2iy_t)^2 \frac{1}{\sqrt{8}} (\sigma^2 \sigma^i)_{\alpha'}^{\alpha} (\tau^2)_{a'}^a iS(q_0 - p_0, \mathbf{q} - \mathbf{p}) i\mathcal{D}_t(q_0, q) \delta_{b'}^{a'} \times \\
 & \quad iT^{ik}(E; \mathbf{q}, \mathbf{k})_{\beta' b}^{\alpha' c} i\mathcal{I}_b(E, ) \frac{1}{\sqrt{8}} (\sigma^{\mathbf{k}} \sigma^2)_{\beta}^{\beta'} (\tau^2)_b^{b'},
 \end{aligned} \tag{A-6}$$

where

$$i\mathcal{D}_{photon}(\mathbf{k}) = \frac{i}{\mathbf{k}^2 + \lambda} \tag{A-7}$$

where  $\lambda$  is a small photon added to regulate the singularity of the propagator at zero momentum transfer.

The bubble integral (Figure 3.8(a)) is given by:

$$\begin{aligned}
 i\mathcal{I}_B(\mathbf{k}, p) = & \int \frac{d^4 q}{(2\pi)^4} iS(q_0, -\mathbf{q}) \cdot iS(E - k_0 + q_0, \mathbf{k} + \mathbf{q}_0) \cdot iS(p_0 - q_0, p - \mathbf{q}) = \\
 & \int \frac{d^3 q}{(2\pi)^3} \frac{M^2}{(2ME - p^2 + 2Mp_0 - 2p\mathbf{q} - 2\mathbf{q}^2)(\mathbf{k}^2 - 2ME - 2k_0M + 2\mathbf{k}\mathbf{q} + 2\mathbf{q}^2)},
 \end{aligned} \tag{A-8}$$

## APPENDIX A. THE FADDEEV EQUATIONS THREE-BODY SCATTERING

---

where eq. (A-8) can be written as:

$$i\mathcal{I}_B^{ij}(E, \mathbf{k}, \mathbf{p}) = \int \frac{d^3q}{(2\pi)^3} \frac{4M^2}{A(\mathbf{q}) \cdot B(\mathbf{q})}, \quad (\text{A-9})$$

and  $A(q), B(q)$  are:

$$A(\mathbf{q}) = (2ME - \mathbf{p}^2 + 2Mp_0 - 2\mathbf{p} \cdot \mathbf{q} - 2\mathbf{q}^2) \quad (\text{A-10})$$

$$B(\mathbf{q}) = -((\mathbf{k}^2 - 2ME - 2k_0M + 2\mathbf{k} \cdot \mathbf{q} + 2\mathbf{q}^2)). \quad (\text{A-11})$$

Using Feynman integrals, one find that:

$$i\mathcal{I}_B(\mathbf{k}, \mathbf{p}) = \int \frac{d^3q}{(2\pi)^3} \int_0^1 dx \frac{4M^2}{(xA(\mathbf{q}) + B(\mathbf{q}) \cdot (1-x))^2}, \quad (\text{A-12})$$

by performing a d-dimensional integrals in Minkowski space, the final expression for eq. (A-8), is:

$$\begin{aligned} i\mathcal{I}_B(\mathbf{k}, \mathbf{p}) = & - \int_0^1 dx \frac{iM^2}{2\pi} \times ( -\mathbf{k}^2 + 4ME + 4k_0M - 4k_0Mx + 2\mathbf{k}\mathbf{p}x - 2\mathbf{p}^2x + 4Mp_0x \\ & + \mathbf{k}^2x^2 - 2\mathbf{k}\mathbf{p}x^2 + \mathbf{p}^2x^2 )^{-1/2} = \\ & \frac{iM^2}{2(\mathbf{k} - \mathbf{p})\pi} \left\{ \log \left[ 2k_0M + (\mathbf{k} - \mathbf{p}) \left( \sqrt{4(E + k_0)M} - \mathbf{k}^2 - \mathbf{p} \right) - 2Mp_0 \right] \right. \\ & \left. - \log \left[ 2M(k_0 - p_0) - (\mathbf{p} - \mathbf{k}) \left( -\mathbf{k} + \sqrt{-\mathbf{p}^2 + 4M(E + p_0)} \right) \right] \right\}. \end{aligned} \quad (\text{A-13})$$

Using the residue theorem and performing the integral over  $k_0 = \frac{-\mathbf{k}^2}{2M}$  and  $p_0 = \frac{-\mathbf{p}^2}{2M}$ , we get that:

$$\begin{aligned} i\mathcal{I}_B(E, \mathbf{k}, \mathbf{p}) = & \frac{iM^2}{2(\mathbf{k} - \mathbf{p})\pi} \left( \log \left[ \left( \sqrt{4ME - 3\mathbf{k}^2} - \mathbf{k} - 2\mathbf{p} \right) (\mathbf{k} - \mathbf{p}) \right] \right. \\ & \left. - \log \left[ (-\mathbf{k} + \mathbf{p}) \left( 2\mathbf{k} + \mathbf{p} - \sqrt{4ME - 3\mathbf{p}^2} \right) \right] \right). \end{aligned} \quad (\text{A-14})$$

## APPENDIX A. THE FADDEEV EQUATIONS THREE-BODY SCATTERING

---

Finally we get:

$$i\mathcal{I}_B(\mathbf{k}, \mathbf{p}) = \frac{M^2 \left( \arctan \left( \frac{2\mathbf{k}+\mathbf{p}}{\sqrt{3\mathbf{p}^2-4ME}} \right) - \arctan \left( \frac{\mathbf{k}+2\mathbf{p}}{\sqrt{3\mathbf{k}^2-4ME}} \right) \right)}{2\pi(\mathbf{k} - \mathbf{p})}. \quad (\text{A-15})$$

The one-nucleon exchange coupled to one photon exchange,  $K_b^{A,B}$  (Figure 3.8(b)), is given by:

$$\begin{aligned} K_b^{A,B}(\mathbf{k}, \mathbf{p}) &= \int \frac{d^4q}{(2\pi)^4} S(-k_0, -k) S(-p_0, -p) \mathcal{D}_{photon}(k + p + \mathbf{q}) \mathcal{D}_A(E + k_0, k) \times \\ &\quad \mathcal{D}_B(E + p_0, p) S(E - q_0, -\mathbf{q}) S(k_0 + q_0, k + \mathbf{q}) S(p_0 + q_0, p + \mathbf{q}) = \\ &= - \int \frac{d^3q}{(2\pi)^3} \frac{i\alpha M^2 \mathcal{D}_A \left( E - \frac{k^2}{2M}, k \right) \mathcal{D}_B \left( E - \frac{p^2}{2M}, p \right)}{(-ME + k^2 + k\mathbf{q} + \mathbf{q}^2) (-ME + p^2 + p\mathbf{q} + \mathbf{q}^2) [\lambda^2 + (k + p + \mathbf{q})^2]} \end{aligned} \quad (\text{A-16})$$

eq. (A-16) can be written as:

$$K_b^{A,B}(E, \mathbf{k}, \mathbf{p}) = \int \frac{d^3q}{(2\pi)^3} \frac{i\alpha M^2 D_A(E, k) D_B(E, p)}{A(\mathbf{q}) \cdot B(\mathbf{q}) \cdot C(\mathbf{q})} \quad (\text{A-17})$$

where

$$A(\mathbf{q}) = -ME + k^2 + k\mathbf{q} + \mathbf{q}^2 \quad (\text{A-18})$$

$$B(\mathbf{q}) = -ME + p^2 + p\mathbf{q} + \mathbf{q}^2 \quad (\text{A-19})$$

$$C(\mathbf{q}) = \lambda^2 + (k + \mathbf{p} + \mathbf{q})^2, \quad (\text{A-20})$$

using Feynman integrals we get:

$$K_b^{A,B}(\mathbf{k}, \mathbf{p}) = \int \frac{d^3q}{(2\pi)^3} \int_0^1 dx \int_0^{1-x} dy \frac{i\alpha M^2 D_A(E, k) D_B(E, p)}{(xA(\mathbf{q}) + yB(\mathbf{q}) + C(\mathbf{q}) \cdot (1 - x - y))^3}, \quad (\text{A-21})$$

and by performing a d-dimensional integrals in Minkowski space we get:

$$\begin{aligned}
 iK_b^{A,B}(E, \mathbf{k}, \mathbf{p}) &= \int_0^1 dx \int_0^{1-x} dy \alpha M^2 D_A(E, \mathbf{k}) D_B(E, \mathbf{p}) \times \\
 &\frac{1}{4\pi} \left\{ 2y [2ME - 2(\mathbf{k}^2 + \mathbf{k}\mathbf{p} + \mathbf{p}^2) + x(2\mathbf{k} + \mathbf{p})(\mathbf{k} + 2\mathbf{p})] + x [4ME - 4(\mathbf{k}^2 + \mathbf{k}\mathbf{p} + \mathbf{p}^2) \right. \\
 &\left. x(\mathbf{k} + 2\mathbf{p})^2] + y^2(2\mathbf{k} + \mathbf{p})^2 \right\}^{-3/2} = D_A(E, \mathbf{k}) \mathcal{I}_b(E, \mathbf{k}, \mathbf{p}) D_B(E, \mathbf{p}),
 \end{aligned} \tag{A-22}$$

where

$$\begin{aligned}
 \mathcal{I}_b(E, \mathbf{k}, \mathbf{p}) &= \frac{M^2 \alpha}{4(\mathbf{k}^2 - ME + \mathbf{k}\mathbf{p} + \mathbf{p}^2)} Q \left( \frac{\mathbf{k}^2 + \mathbf{p}^2 - ME}{\mathbf{k}\mathbf{p}} \right) \times \\
 &\left[ \frac{\arctan \left( \frac{\mathbf{k} + 2\mathbf{p}}{\sqrt{3\mathbf{k}^2 - 4ME}} \right) - \arctan \left( \frac{2\mathbf{k} + \mathbf{p}}{\sqrt{3\mathbf{p}^2 - 4ME}} \right)}{\mathbf{k} - \mathbf{p}} \right].
 \end{aligned} \tag{A-23}$$

$K_{c,d}^{A,B}$  (Figure 3.8(c, d)) is given by:

$$\begin{aligned}
 K_{c,d}^{A,B} &= - \int \frac{d^4 q}{(2\pi)^4} i \mathcal{D}_{photon}(-\mathbf{q}) \mathcal{D}^{A,B}(-p_0, -\mathbf{p}) S(-k_0, -\mathbf{k}) S(-q_0, -\mathbf{q}) \times \\
 &\mathcal{D}^{A,B}(E + k_0, \mathbf{k}) S(E + p_0, \mathbf{p}) S(k_0 - p_0 + q_0, \mathbf{k} - \mathbf{p} + \mathbf{q}) = \\
 &\int \frac{d^4 q}{(2\pi)^4} \frac{i \alpha M \mathcal{D}^{A,B} \left( E - \frac{\mathbf{p}^2}{2M}, -\mathbf{p} \right) \mathcal{D}^{A,B} \left( E - \frac{\mathbf{k}^2}{2M}, \mathbf{q} \right)}{(\lambda^2 + \mathbf{q}^2) (-ME + \mathbf{k}^2 + \mathbf{k}(\mathbf{q} - \mathbf{p}) + \mathbf{p}^2 - \mathbf{p}\mathbf{q} + \mathbf{q}^2)} = \\
 &- \int_0^1 dx \frac{\alpha M \mathcal{D}^{A,B} \left( E - \frac{\mathbf{p}^2}{2M}, -\mathbf{p} \right) \mathcal{D}^{A,B} \left( E - \frac{\mathbf{k}^2}{2M}, \mathbf{q} \right)}{4\pi \sqrt{4MEx + \mathbf{k}^2(x-4)x - 4\lambda^2 - 2\mathbf{k}\mathbf{p}(x-2)x + \mathbf{p}^2x^2 - 4\mathbf{p}^2x + 4\lambda^2x}} = \\
 &D_A(E, \mathbf{k}) \mathcal{I}_{c,d}(E, \mathbf{k}, \mathbf{p}) D_B(E, \mathbf{p}),
 \end{aligned} \tag{A-25}$$

where

$$\begin{aligned}
 \mathcal{I}_{c,d}(E, \mathbf{k}, \mathbf{p}) &= \frac{\alpha M^2}{8\pi(\mathbf{k} - \mathbf{p})\mathbf{k}\mathbf{p}} Q \left( \frac{\mathbf{k}^2 + \mathbf{p}^2 - ME}{\mathbf{k}\mathbf{p}} \right) \left[ \log(2ME - 2\mathbf{k}^2 + 2\mathbf{k}\mathbf{p} - 2\mathbf{p}^2) \right. \\
 &\left. - \log \left( -\mathbf{k}\sqrt{4ME - 3\mathbf{k}^2 + 2\mathbf{k}\mathbf{p} - 3\mathbf{p}^2} + \mathbf{p}\sqrt{4ME - 3\mathbf{k}^2 + 2\mathbf{k}\mathbf{p} - 3\mathbf{p}^2} + 2ME - \mathbf{k}^2 - \mathbf{p}^2 \right) \right].
 \end{aligned} \tag{A-26}$$

**b The Doublet channel for the  $p - d$  scattering**

$$\begin{aligned}
 (iT^{i,j})_{\alpha a}^{\beta b}(E; \mathbf{k}, \mathbf{p}) = & -i \frac{My_t^2}{2} (\sigma^j \sigma^i)_\alpha^\beta \delta_b^a \frac{1}{\mathbf{k}^2 + \mathbf{k}^2 + \mathbf{k} \cdot \mathbf{p} - ME} \\
 & - i \frac{My_t^2}{2} (\sigma^j \sigma^i)_\alpha^\beta \delta_b^a (i\mathcal{I}_b - \mathcal{I}_B(E, \mathbf{q}, \mathbf{p}) \mathcal{D}_{photon}(\mathbf{q} - \mathbf{p})) \\
 & + \frac{My_t^2}{2} \int \frac{d^3 \mathbf{q}}{(2\pi)^3} (\sigma^j \sigma^{\mathbf{k}})_\gamma^\beta \frac{iT^{ik}(E; \mathbf{q}, \mathbf{k})_{\beta b}^{\gamma c}}{\mathbf{q}^2 + \mathbf{p}^2 + \mathbf{q} \cdot \mathbf{p} - ME} D_t(E, \mathbf{q}) \delta_c^a \\
 & + \frac{My_t^2}{2} \int \frac{d^3 \mathbf{q}}{(2\pi)^3} (\sigma^j \sigma^{\mathbf{k}})_\gamma^\beta iT^{ik}(E; \mathbf{q}, \mathbf{k})_{\alpha b}^{\gamma c} D_t(E, \mathbf{q}) \delta_c^a i\mathcal{I}_b(E, \mathbf{q}, \mathbf{p}) \\
 & - \frac{My_t^2}{2} \int \frac{d^3 \mathbf{q}}{(2\pi)^3} T^{jk}(E; \mathbf{p}, \mathbf{k})_{\alpha b}^{\gamma c} D_t(E, \mathbf{q}) \delta^{ik} \delta_\gamma^\beta \left( \frac{1 + \tau^3}{2} \right)_c^a \mathcal{I}_B(E, \mathbf{q}, p) \mathcal{D}_{photon}(\mathbf{q} - \mathbf{p}) \\
 & + \frac{My_t y_s}{2} \int \frac{d^3 q}{(2\pi)^3} D_s^{np}(E, \mathbf{q}) (\sigma^{\mathbf{k}})_\gamma^\beta (\tau^3)_c^b (iS_{np}^i)_{\alpha a}^{\gamma c} \times \\
 & \quad \left( \frac{1}{\mathbf{q}^2 + \mathbf{q} \cdot \mathbf{p} + \mathbf{p}^2 - ME} + i\mathcal{I}_b(E, \mathbf{q}, \mathbf{p}) \right) \\
 & + \frac{My_t y_s}{2} \int \frac{d^3 q}{(2\pi)^3} D_{pp}(E, \mathbf{q}) (\sigma^{\mathbf{k}})_\gamma^\beta (\tau^{l=1-i \cdot 2})_c^b (iP^{bl})_{\alpha a}^{\gamma c} \\
 & \quad \left( \frac{1}{\mathbf{q}^2 + \mathbf{q} \cdot \mathbf{p} + \mathbf{p}^2 - ME} + i\mathcal{I}_c(E, \mathbf{q}, \mathbf{p}) \right)
 \end{aligned} \tag{A-27}$$



$$\begin{aligned}
 (iS_{np})_{\alpha\alpha}^{\beta b}(E; \mathbf{k}, \mathbf{p}) = & -\frac{iMy_t y_s}{2} (\sigma^i)_\alpha^\beta (\tau^3)_a^b \cdot \frac{1}{\mathbf{k}^2 + \mathbf{k} \cdot \mathbf{p} + \mathbf{p}^2 - ME} \\
 & - iy_s^2 \frac{1}{2} (\sigma^i)_\alpha^\beta (\tau^3)_a^b (i\mathcal{I}_b(E, \mathbf{k}, \mathbf{p}) - \mathcal{I}_B(E, \mathbf{k}, \mathbf{p}) \mathcal{D}_{photon}(\mathbf{k} - \mathbf{p})) \\
 & + \frac{My_t y_s}{2} \int \frac{d^3 q}{(2\pi)^3} D_t(E, \mathbf{q}) (\sigma^k)_\alpha^\gamma (\tau^3)_c^b (iT^{ik})_{\alpha a}^{\gamma c} \times \\
 & \quad \left( \frac{1}{\mathbf{q}^2 + \mathbf{q} \cdot \mathbf{p} + \mathbf{p}^2 - ME} + i\mathcal{I}_b(E, \mathbf{q}, \mathbf{p}) \right) \\
 & + \frac{My_s^2}{2} \int \frac{d^3 q}{(2\pi)^3} D_s^{np}(E, \mathbf{q}) \frac{(\tau^3)_c^b (\tau^3)_d^c}{\mathbf{q}^2 + \mathbf{q} \cdot \mathbf{p} + \mathbf{p}^2 - ME} (iS_{np}^i)_{\alpha a}^{\beta d} \\
 & + \frac{My_s^2}{2} \int \frac{d^3 q}{(2\pi)^3} (\tau^3)_c^b (\tau^3)_d^c (iS_{np})_{\alpha a}^{\beta d} D_t(E, \mathbf{q}) i\mathcal{I}_b(E, \mathbf{q}, \mathbf{p}) \\
 & - \frac{My_s^2}{2} \int \frac{d^3 \mathbf{q}}{(2\pi)^3} S_{np}^i(E; \mathbf{p}, \mathbf{k})_{\alpha b}^{\gamma c} D_t(E, \mathbf{q}) \delta_\gamma^\beta \left( \frac{1 + \tau^3}{2} \right)_c^a \mathcal{I}_B(E, \mathbf{q}, \mathbf{p}) \mathcal{D}_{photon}(\mathbf{q} - \mathbf{p}) \\
 & + \frac{My_s^2}{2} \int \frac{d^3 q}{(2\pi)^3} D_{pp}(E, \mathbf{q}) (\tau^{1-i \cdot 2})_c^b (\tau^3)_d^c (iP^i)_{\alpha a}^{\beta d} \times \\
 & \quad \left( \frac{1}{\mathbf{q}^2 + \mathbf{q} \cdot \mathbf{p} + \mathbf{p}^2 - ME} + i\mathcal{I}_c(E, \mathbf{q}, \mathbf{p}) \right), \tag{A-28}
 \end{aligned}$$

$$\begin{aligned}
 (iP^i)_{\alpha\alpha}^{\beta b}(E; \mathbf{k}, \mathbf{p}) = & -\frac{iMy_t y_s}{2} \cdot (\sigma^i)_\alpha^\beta (\tau^{B=1-i \cdot 2})_a^b \cdot \frac{1}{\mathbf{k}^2 + \mathbf{k} \cdot \mathbf{p} + \mathbf{p}^2 - ME} \\
 & + \frac{My_t y_s}{2} \int \frac{d^3 q}{(2\pi)^3} D_t(E, \mathbf{q}) (\sigma^k)_\alpha^\gamma (\tau^{B=1+i \cdot 2})_c^b (iT^{ik})_{\alpha a}^{\gamma c} \times \\
 & \quad \left( \frac{1}{\mathbf{q}^2 + \mathbf{q} \cdot \mathbf{p} + \mathbf{p}^2 - ME} + i\mathcal{I}_d(E, \mathbf{q}, \mathbf{p}) \right) \\
 & + \frac{My_s^2}{2} \int \frac{d^3 q}{(2\pi)^3} D_s^{np}(E, \mathbf{q}) (\tau^3)_c^b (\tau^{B=1-i \cdot 2})_d^c (iS_{np}^i)_{\alpha a}^{\beta d} \times \\
 & \quad \left( \frac{1}{\mathbf{q}^2 + \mathbf{q} \cdot \mathbf{p} + \mathbf{p}^2 - ME} + i\mathcal{I}_d(E, \mathbf{q}, \mathbf{p}) \right) \\
 & + \frac{My_s^2}{2} \int \frac{d^3 q}{(2\pi)^3} \mathcal{D}_{pp}(E - \frac{\mathbf{q}^2}{2M}, \mathbf{q}) (\tau^{1-i \cdot 2})_c^b (\tau^{B=1-i \cdot 2})_d^c (iP^i)_{\alpha a}^{\beta d} \times \\
 & \quad \left( \frac{1}{\mathbf{q}^2 + \mathbf{q} \cdot \mathbf{p} + \mathbf{p}^2 - ME} + i\mathcal{I}_b(E, \mathbf{q}, \mathbf{p}) \right) \tag{A-29}
 \end{aligned}$$

# Appendix B

## The analytic form of the NLO correction to the three-body force

Up to NLO, the three-body form has the form:

$$H(\Lambda) = H^0(\Lambda) + H^{(1)}(\Lambda) \quad (\text{B-1})$$

where the NLO correction,  $H^{(1)}(\Lambda)$ , is giving by [43, 44]:

$$\begin{aligned} H^{(1)}(\Lambda) = & \Lambda \left[ -3\pi \frac{1+s_0^2}{128} (\rho_t + \rho_s) \frac{1 - \left(1/\sqrt{1+4s_0^2}\right) \sin(2s_0 \log(\Lambda/\Lambda^*) + \arctan(1/2s_0))}{\sin^2(s_0 \log(\Lambda/\Lambda^*) - \arctan(s_0))} \right] - \\ & - \frac{3\pi(1+s_0^2)}{64} \left\{ \frac{1}{\sqrt{3}} (\rho_s + \rho_t) (a_s^{-1} + \gamma_t) |B_{-1}| \mathcal{G}_1(B_{-1}) - \frac{1}{2\sqrt{3}} (-\rho_s + \rho_t) (-a_s^{-1} + \gamma_t) |\tilde{B}_{-1}| \mathcal{G}_1(\tilde{B}_{-1}) + \right. \\ & \left. \frac{1}{2\sqrt{3}} (a_s^{-1} \rho_s + \rho_t \gamma_t) \mathcal{G}_1(0) - 0.1252 \right\} \sin^{-2} [s_0 \log(\Lambda/\Lambda^*) - \arctan(s_0)] , \quad (\text{B-2}) \end{aligned}$$

where:

$$B_{-1} = \frac{I(is_0 - 1)}{1 - I(is_0 - 1)} , \quad (\text{B-3})$$

$$\tilde{B}_{-1} = \frac{I(is_0 - 1)}{1 + \frac{1}{2}I(is_0 - 1)} , \quad (\text{B-4})$$

$$I(s) = \frac{8}{\sqrt{3}s} \frac{\sin(\frac{\pi s}{6})}{\cos(\frac{\pi s}{2})} , \quad (\text{B-5})$$

APPENDIX B. THE ANALYTIC FORM OF THE NLO CORRECTION TO THE  
THREE-BODY FORCE

---

and

$$\mathcal{G}(x) = \cos [\arg(x)] \log(\Lambda) - \frac{1}{2s_0} \sin \left[ 2s_0 \log\left(\frac{\Lambda}{\Lambda_*}\right) + \arg(x) \right] \quad (\text{B-6})$$

## The Hubbard-Stratonovich transformation with two-body electro-weak interaction

In this appendix, we present the Hubbard-Stratonovich (H-S) transformation for a  $\not\equiv$ EFT Lagrangian with an electro-weak interaction.

The two-body Lagrangian with electro-weak interaction has the form:

$$\mathcal{L} = \mathcal{L}_{\text{strong}} + \mathcal{L}_{\text{electroweak}}, \quad (\text{C-1})$$

where  $\mathcal{L}$  is two-body Lagrangian [27]:

$$\mathcal{L} = N^\dagger \left( i\partial_0 + \frac{\nabla^2}{2M} \right) N - \sum_{\mu} C_0^\mu \phi_\mu^\dagger \phi_\mu - \frac{MC_2^\mu}{2} [\phi_\mu^\dagger \mathcal{O}_D \phi_\mu + h.c.] , \quad (\text{C-2})$$

where:

$$(N^T P_{t,s} N) = \phi_{t,s} , \quad (\text{C-3})$$

$$\mathcal{O}_D = \left( i\partial_0 + \frac{\nabla^2}{4M} \right) , \quad (\text{C-4})$$

and (see for example [14]):

$$C_0^\mu = \frac{4\pi}{M} \frac{1}{\left( -\mu + \frac{1}{a_\mu} \right)} \quad (\text{C-5})$$

$$C_2^\mu = C_2^\mu = \frac{4\pi}{M \left( -\mu + \frac{1}{a_\mu} \right)^2} \frac{\rho_\mu}{2} . \quad (\text{C-6})$$

## APPENDIX C. THE HUBBARD-STRATONOVICH TRANSFORMATION WITH TWO-BODY ELECTRO-WEAK INTERACTION

---

$\mathcal{L}_{\text{electroweak}}$  is the electro-weak part of the  $\not{r}$ EFT Lagrangian:

$$\mathcal{L}_{\text{electroweak}}^\mu \propto \mathcal{A}_\mu = \mathcal{A}_\mu^{1\text{B}} + \mathcal{A}_\mu^{2\text{B}}. \quad (\text{C-7})$$

the two-body part of the electro-weak current,  $\mathcal{A}_\mu^{2\text{B}}$ , has the form:

$$\mathcal{A}_\mu = \sum_{\mu,\nu} L_{\mu\nu} \phi_\mu^\dagger \phi_\nu, \quad (\text{C-8})$$

where  $L_{\mu\nu}$  is the LEC that couples the two two-nucleon fields, e.g., for the weak interaction  $L_{\mu\nu} = L_{ts} = L_{1,A}$ . In order to find the right H-S transformation for  $\mathcal{L}$ , we assume that after applying the H-S transformation,  $\mathcal{L}$  is of the form:

$$\mathcal{L}_{\text{electroweak}}^{H-S} = \sum_{\mu,\nu=t,s} - \underbrace{\alpha_\mu (\mu^\dagger \phi_\mu + h.c)}_{\text{strong part}} - \underbrace{\mu^\dagger \beta_\mu \mu - \gamma_{\mu\nu} \phi_\nu^\dagger \mu - \gamma'_{\mu\nu} [\mu^\dagger \nu + h.c]}_{\text{electro-weak part}}, \quad (\text{C-9})$$

where the H-S transformation is defined such that:

$$\int dt \int ds \exp(-\mathcal{L}_{\text{electroweak}}^{H-S}) = \exp \left[ - \left( \sum_{\mu=t,s} A_\mu \phi_\mu^\dagger \phi_\mu + B_\mu \mathcal{O}_D \phi_\mu^\dagger \phi_\mu + L_{\mu\nu} \psi_\mu^\dagger \psi_\nu \right) \right]. \quad (\text{C-10})$$

By setting:

$$A_\mu = -C_0^\mu \quad (\text{C-11})$$

$$B_\mu = -\frac{C_2^\mu M}{2} \quad (\text{C-12})$$

and

$$\alpha_\mu = y_\mu \quad (\text{C-13})$$

$$\beta_\mu = \mathcal{O}_D - \sigma_\mu, \quad (\text{C-14})$$

we get that:

$$\gamma_{\mu\nu} = \frac{L_{\mu\nu}}{\sqrt{C_2^\mu M}} + c \frac{C_2^\mu}{C_0^\mu \sqrt{M C_2^\mu}} \quad (\text{C-15})$$

$$\gamma'_{\mu\nu} = \frac{L_{\mu\nu}}{\sqrt{C_2^\mu C_2^\nu M^2}} - c \left( \frac{C_0^\mu C_2^\nu}{C_0^\nu \sqrt{C_2^\mu C_2^\nu}} + \frac{C_0^\nu C_2^\mu}{C_0^\mu \sqrt{C_2^\mu C_2^\nu}} \right), \quad (\text{C-16})$$

## APPENDIX C. THE HUBBARD-STRATONOVICH TRANSFORMATION WITH TWO-BODY ELECTRO-WEAK INTERACTION

---

where  $c$  is an arbitrary constant that has to be determined by the original Lagrangian.



# Appendix D

## Appendix D - A Bayesian approach to estimate the convergence rate

In the following, we suggest an approach to study the truncation uncertainty and the size of the expansion parameter, of a set of observables whose expansion are  $\langle M_1 \rangle = \langle M_1 \rangle_{LO} \cdot (1 + c_{M_1}^{NLO} \delta + c_{M_1}^{N^2LO} \delta^2 + \mathcal{O}(\delta^3))$ .

### D.I The Bayesian probability distribution of the expansion parameter

We use information theory arguments to understand the expected behaviour of the expansion convergence rate. Let us look at the ratio of different expansion terms,

$$r_{k-l}^{M_1} \delta^{k-l} = \left| \frac{c_{M_1}^{N^kLO}}{c_{M_1}^{N^lLO}} \right|. \quad (D-1)$$

$\not\propto$ EFT formalism suggests that  $r_{k-l}^{M_1}$  should be a natural number. We interpret this as a statement regarding the nature of the distribution of these numbers. In laymen words, one would be surprised if these numbers deviate much from 1. In other words, these coefficients have some natural range of change  $\frac{1}{\alpha} < r_{k-l}^{M_1} < \alpha$ , where  $\alpha$  is a measure of naturalness. One can expect that  $\alpha$  is from a order of 2-3, while bigger variations are acceptable as long as they are rare. From a Bayesian point of view,  $r_{k-l}^{M_1}$  are independent and identically distributed random variable (i.i.d) with an average of about 1 and their logarithm has (unknown) standard deviation  $\log \alpha$ .

Information theory now states that the probability density function (pdf)  $f(r)$  should



## APPENDIX D. APPENDIX D - A BAYESIAN APPROACH TO ESTIMATE THE CONVERGENCE RATE

maximize the entropy  $S[f] = - \int dr f(r) \log f(r)$  subject to the constraints  $\overline{\log r} = 0$  and  $(\log r - \overline{\log r})^2 = \log \alpha$ . Thus, the log-average of  $r_{k-l}^{M_1} \delta^{k-l}$  should be the expansion parameter  $(k-l) \log \delta$ . These lead to a pdf  $f(r)$  which is a log-normal distribution.

One can now use a sample with size  $n$  to estimate the expansion parameter, i.e.,  $\overline{\log \delta} = \frac{1}{n} \sum_{i=1}^n \frac{1}{k-l} \log \left( r_{k-l}^{M_1(i)} \delta^{k-l} \right)$ . Then, by using Bayes theorem, the resulting distribution for the expansion parameter is Student's  $t$ -distribution with  $n-1$  degrees of freedom  $\frac{\log \delta - \overline{\log \delta}}{\sigma^2 / \sqrt{n}} \sim T(\sigma^2, n-1)$ .

### D.II The Bayesian probability distribution of the truncation error of an expansion, given a prior for the expansion parameter

A good estimate for the truncation error is the maximal coefficient in an expansion of order  $k$ , multiplied by  $\delta^{k+1}$ . In Refs. [102–104] a Bayesian probability distribution is calculated for the truncation error under the assumption of a natural expansion, albeit in the case where the expansion parameter  $\delta$  is known. In what follows, we combine their idea, with the probability distribution for the expansion parameter found above, to find the Bayesian probability distribution that the NLO result will deviate by  $\Delta$  from the true value. Then,

$$pr \left( \Delta \mid \left\{ a_{M_1^k}^{NLO} \right\}_{k=1}^n \right) = \int d\delta pr \left( \Delta \mid \left\{ c_{M_1^k}^{NLO} \right\}_{k=1}^n, \delta \right) \cdot pr \left( \delta \mid \left\{ a_{M_1^k}^{NLO} \right\}_{k=1}^n \right). \quad (\text{D-2})$$

$pr(\Delta \mid \left\{ c_{M_1^k}^{NLO} \right\}_{k=1}^n, \delta)$  is calculated in Ref. [102], and at NLO, is roughly constant for  $|\Delta| \leq R_\xi(\delta)$ , and decays as  $1/|\Delta|^3$  for  $|\Delta| \geq R_\xi(\delta)$ , where  $R_\xi(\delta) = \max \left( 1, \left\{ c_{M_1^k}^{NLO} \right\}_{n=1} \right) \delta^2$ . The exact functional form depends on the prior assumption for  $\left\{ c_{M_1^k}^{NLO} \right\}_{k=1}^n$ , but a common behavior to all the checked priors is that at degree of belief of  $\frac{k}{k+1}$  (translating to  $\approx 67\%$  for NLO calculations) the resulting truncation error is less than  $R_\xi(\delta) \delta^{k+1}$ .

As the pdf for  $\delta$ , we take the Student's  $t$ -distribution found in the previous subsection.

# Bibliography

- [1] John N. Bahcall and Robert M. May. The Rate of the Proton-Proton Reaction and Some Related Reactions. *apj*, 155:501, Feb 1969.
- [2] H. A. Bethe. Theory of the effective range in nuclear scattering. *Phys. Rev.*, 76:38–50, Jul 1949.
- [3] E. G. Adelberger et al. Solar fusion cross sections II: the pp chain and CNO cycles. *Rev. Mod. Phys.*, 83:195, 2011.
- [4] J. C. Hardy and I. S. Towner. Superaligned  $0^+ \rightarrow 0^+$  nuclear  $\beta$  decays: A new survey with precision tests of the conserved vector current hypothesis and the standard model. *Phys. Rev. C*, 79:055502, May 2009.
- [5] C. Amsler et al. Review of particle physics. *Physics Letters B*, 667(1):1 – 6, 2008. Review of Particle Physics.
- [6] Eric G. Adelberger et al. Solar fusion cross-sections. *Rev. Mod. Phys.*, 70:1265–1292, 1998.
- [7] A. Kurylov, M. J. Ramsey-Musolf, and P. Vogel. Radiative corrections to low-energy neutrino reactions. *Phys. Rev. C*, 67:035502, Mar 2003.
- [8] L. E. Marcucci, R. Schiavilla, and M. Viviani. Proton-proton weak capture in chiral effective field theory. *Phys. Rev. Lett.*, 110:192503, May 2013.
- [9] Doron Gazit, Sofia Quaglioni, and Petr Navrátil. Three-nucleon low-energy constants from the consistency of interactions and currents in chiral effective field theory. *Phys. Rev. Lett.*, 103:102502, Sep 2009.

- [10] B. Acharya, B.D. Carlsson, A. Ekström, C. Forssén, and L. Platter. Uncertainty quantification for proton-proton fusion in chiral effective field theory. *Physics Letters B*, 760:584 – 589, 2016.
- [11] Jiunn-Wei Chen, Takashi Inoue, Xiang-dong Ji, and Ying-chuan Li. Fixing two-nucleon weak-axial coupling  $L(1, A)$  from  $\mu - d$  capture. *Phys. Rev.*, C72:061001, 2005.
- [12] Paulo F. Bedaque and Ubirajara van Kolck. Effective field theory for few nucleon systems. *Ann. Rev. Nucl. Part. Sci.*, 52:339–396, 2002.
- [13] David B. Kaplan, Martin J. Savage, and Mark B. Wise. Nucleon-nucleon scattering from effective field theory. *Nuclear Physics B*, 478(3):629 – 659, 1996.
- [14] David B. Kaplan, Martin J. Savage, and Mark B. Wise. Two nucleon systems from effective field theory. *Nucl. Phys.*, B534:329–355, 1998.
- [15] David B. Kaplan, Martin J. Savage, and Mark B. Wise. A New expansion for nucleon-nucleon interactions. *Phys. Lett.*, B424:390–396, 1998.
- [16] David B. Kaplan, Martin J. Savage, and Mark B. Wise. A Perturbative calculation of the electromagnetic form-factors of the deuteron. *Phys. Rev.*, C59:617–629, 1999.
- [17] Evgeny Epelbaum, Hans-Werner Hammer, and Ulf-G. Meissner. Modern Theory of Nuclear Forces. *Rev. Mod. Phys.*, 81:1773–1825, 2009.
- [18] Sonia Bacca and Saori Pastore. Electromagnetic reactions on light nuclei. *J. Phys.*, G41(12):123002, 2014.
- [19] Daniel R. Phillips. Electromagnetic structure of two- and three-nucleon systems: An effective field theory description. *Annual Review of Nuclear and Particle Science*, 66(1):421–447, 2016.
- [20] J. A. Melendez, S. Wesolowski, and R. J. Furnstahl. Bayesian truncation errors in chiral effective field theory: nucleon-nucleon observables. *Phys. Rev.*, C96(2):024003, 2017.
- [21] Harald W. Griesshammer. Naive dimensional analysis for three-body forces without pions. *Nucl. Phys.*, A760:110–138, 2005.

## BIBLIOGRAPHY

---

- [22] Harald W. Griesshammer. Improved convergence in the three-nucleon system at very low energies. *Nucl. Phys.*, A744:192–226, 2004.
- [23] Lucas Platter. Low-Energy Universality in Atomic and Nuclear Physics. *Few Body Syst.*, 46:139–171, 2009.
- [24] Xinwei Kong and Finn Ravndal. Proton proton fusion in leading order of effective field theory. *Nucl. Phys.*, A656:421–429, 1999.
- [25] Jiunn-Wei Chen and Martin J. Savage.  $np \rightarrow \gamma$  for big bang nucleosynthesis. *Phys. Rev.*, C60:065205, 1999.
- [26] Gautam Rupak. Precision calculation of  $np \rightarrow \gamma$  cross-section for big bang nucleosynthesis. *Nucl. Phys.*, A678:405–423, 2000.
- [27] Jiunn-Wei Chen, Gautam Rupak, and Martin J. Savage. Nucleon-nucleon effective field theory without pions. *Nucl. Phys.*, A653:386–412, 1999.
- [28] Shung-ichi Ando and Chang Ho Hyun. Effective field theory on the deuteron with dibaryon field. *Phys. Rev.*, C72:014008, 2005.
- [29] Xinwei Kong and Finn Ravndal. Proton proton fusion in effective field theory. *Phys. Rev.*, C64:044002, 2001.
- [30] Malcolm Butler and Jiunn-Wei Chen. Proton-proton fusion in effective field theory to fifth order. *Physics Letters B*, 520(1-2):87 – 91, 2001.
- [31] R. Schiavilla, V. G. J. Stoks, W. Glöckle, H. Kamada, A. Nogga, J. Carlson, R. Machleidt, V. R. Pandharipande, R. B. Wiringa, A. Kievsky, S. Rosati, and M. Viviani. Weak capture of protons by protons. *Phys. Rev. C*, 58:1263–1277, Aug 1998.
- [32] S. Ando, J. W. Shin, C. H. Hyun, S. W. Hong, and K. Kubodera. Proton-proton fusion in pionless effective theory. *Phys. Lett.*, B668:187–192, 2008.
- [33] T.-S. Park, L. E. Marcucci, R. Schiavilla, M. Viviani, A. Kievsky, S. Rosati, K. Kubodera, D.-P. Min, and M. Rho. Parameter-free effective field theory calculation for the solar proton-fusion and hep processes. *Phys. Rev. C*, 67:055206, May 2003.

- [34] Martin J. Savage, Phiala E. Shanahan, Brian C. Tiburzi, Michael L. Wagman, Frank Winter, Silas R. Beane, Emmanuel Chang, Zohreh Davoudi, William Detmold, and Kostas Orginos. Proton-proton fusion and tritium  $\beta$  decay from lattice quantum chromodynamics. *Phys. Rev. Lett.*, 119:062002, Aug 2017.
- [35] V. A. Andreev et al. Muon Capture on the Deuteron – The MuSun Experiment. 2010.
- [36] W. T. Chou, E. K. Warburton, and B. Alex Brown. Gamow-Teller beta-decay rates for  $A \leq 18$  nuclei. *Phys. Rev.*, C47:163–177, 1993.
- [37] L.D. Faddeev and S.P. Merkuriev. *Quantum Scattering Theory for Several Particle Systems*. Springer, 1993.
- [38] Paulo F. Bedaque, H.-W. Hammer, and U. van Kolck. The Three boson system with short range interactions. *Nucl. Phys.*, A646:444–466, 1999.
- [39] Paulo F. Bedaque, H.-W. Hammer, and U. van Kolck. Effective theory of the triton. *Nucl. Phys.*, A676:357–370, 2000.
- [40] Gautam Rupak and Xin-Wei Kong. Quartet S wave p d scattering in EFT. *Nucl. Phys.*, A717:73–90, 2003.
- [41] Shung-Ichi Ando and Michael C. Birse. Effective field theory of  $^3\text{He}$ . *J. Phys.*, G37:105108, 2010.
- [42] J. Kirscher and D. Gazit. The Coulomb interaction in Helium-3: Interplay of strong short-range and weak long-range potentials. *Physics Letters B*, 755:253–260, April 2016.
- [43] Jared Vanasse, David A. Egolf, John Kerin, Sebastian Koenig, and Roxanne P. Springer.  $^3\text{He}$  and  $pd$  Scattering to Next-to-Leading Order in Pionless Effective Field Theory. *Phys. Rev.*, C89(6):064003, 2014.
- [44] C. Ji, D. R. Phillips, and L. Platter. The three-boson system at next-to-leading order in an effective field theory for systems with a large scattering length. *Annals of Physics*, 327:1803–1824, July 2012.
- [45] Sebastian Koenig and H.-W. Hammer. Low-energy p-d scattering and He-3 in pionless EFT. *Phys. Rev.*, C83:064001, 2011.

## BIBLIOGRAPHY

---

- [46] Sebastian Koenig, Harald W. Griesshammer, and H. W. Hammer. The proton-deuteron system in pionless EFT revisited. *J. Phys.*, G42:045101, 2015.
- [47] Sebastian Koenig, Harald W. Griesshammer, H.-W. Hammer, and U. van Kolck. Effective theory of  $^3\text{H}$  and  $^3\text{He}$ . *J. Phys.*, G43(5):055106, 2016.
- [48] Hilla De-Leon, Lucas Platter, and Doron Gazit. Calculation of  $A = 3$  bound state matrix element in pionless effective field theory. *In preparation*, 2018.
- [49] Hilla De-Leon and Doron Gazit. Precise and accurate calculation of low energy magnetic reactions in  $A \leq 3$  nuclear systems using effective field theory without pions. *In preparation*, 2018.
- [50] Jared Vanasse. Triton charge radius to next-to-next-to-leading order in pionless effective field theory. *Phys. Rev.*, C95(2):024002, 2017.
- [51] Hilla De-Leon, Lucas Platter, and Doron Gazit. Tritium  $\beta$ -decay in pionless effective field theory. *In preparation*, 2018.
- [52] Jared Vanasse. Charge and Magnetic Properties of Three-Nucleon Systems in Pionless Effective Field Theory. *Phys. Rev.*, C98(3):034003, 2018.
- [53] J. E. Purcell, J. H. Kelley, E. Kwan, C. G. Sheu, and H. R. Weller. Energy levels of light nuclei  $A = 3$ . *Nucl. Phys.*, A848:1–74, 2010.
- [54] P. J. Mohr and B. N. Taylor. CODATA recommended values of the fundamental physical constants: 1998. *Rev. Mod. Phys.*, 72:351–495, 2000.
- [55] AE Cox, SAR Wynchank, and CH Collie. The proton-thermal neutron capture cross section. *Nuclear Physics*, 74(3):497–507, 1965.
- [56] S. Ando, R. H. Cyburt, S. W. Hong, and C. H. Hyun. Radiative neutron capture on a proton at BBN energies. *Phys. Rev.*, C74:025809, 2006.
- [57] Silas R. Beane and Martin J. Savage. Rearranging pionless effective field theory. *Nucl. Phys.*, A694:511–524, 2001.
- [58] David B. Kaplan. More effective field theory for non-relativistic scattering. *Nuclear Physics B*, 494(1-2):471 – 483, 1997.

## BIBLIOGRAPHY

---

- [59] Xinwei Kong and Finn Ravndal. Coulomb effects in low-energy proton proton scattering. *Nucl. Phys.*, A665:137–163, 2000.
- [60] Xinwei Kong and Finn Ravndal. Proton proton scattering lengths from effective field theory. *Phys. Lett.*, B450:320–324, 1999.
- [61] Paulo F. Bedaque and Harald W. Griesshammer. Quartet S wave neutron deuteron scattering in effective field theory. *Nucl. Phys.*, A671:357–379, 2000.
- [62] Daniel R. Phillips, Gautam Rupak, and Martin J. Savage. Improving the convergence of N N effective field theory. *Phys. Lett.*, B473:209–218, 2000.
- [63] C. Van Der Leun and C. Alderliesten. The deuteron binding energy. *Nucl. Phys.*, A380:261–269, 1982.
- [64] J. J. de Swart, C. P. F. Terheggen, and V. G. J. Stoks. The Low-energy n p scattering parameters and the deuteron. In *3rd International Symposium on Dubna Deuteron 95 Dubna, Russia, July 4-7, 1995*, 1995.
- [65] S. R. Beane, P. F. Bedaque, W. C. Haxton, D. R. Phillips, and M. J. Savage. *From Hadrons to Nuclei: Crossing the Border*, pages 133–269. World Scientific Publishing Co, 2001.
- [66] J. R. Bergervoet, P. C. van Campen, W. A. van der Sanden, and Johan J. de Swart. Phase shift analysis of 0-30 MeV pp scattering data. *Phys. Rev.*, C38:15–50, 1988.
- [67] Daniel R. Phillips and T. D. Cohen. Deuteron electromagnetic properties and the viability of effective field theory methods in the two nucleon system. *Nucl. Phys.*, A668:45–82, 2000.
- [68] Mannque Rho. Effective field theory for nuclei, dense matter and the Cheshire Cat. *AIP Conf. Proc.*, 494:391–399, 1999.
- [69] Jared Vanasse. Fully Perturbative Calculation of  $nd$  Scattering to Next-to-next-to-leading-order. *Phys. Rev.*, C88(4):044001, 2013.
- [70] Harald W. Griesshammer. Naive dimensional analysis for three-body forces without pions. *Nucl. Phys.*, A760:110–138, 2005.

## BIBLIOGRAPHY

---

- [71] Harald W. Griesshammer, Matthias R. Schindler, and Roxanne P. Springer. Parity-violating neutron spin rotation in hydrogen and deuterium. *Eur. Phys. J.*, A48:7, 2012.
- [72] M. Blank and A. Krassnigg. Matrix algorithms for solving (in)homogeneous bound state equations. *Comput. Phys. Commun.*, 182:1391–1401, 2011.
- [73] C.H Llewellyn Smith. A relativistic formulation of the quark model for mesons. *Annals of Physics*, 53(3):521 – 558, 1969.
- [74] William H. Press, Saul A. Teukolsky, William T. Vetterling, and Brian P. Flannery. *Numerical Recipes 3rd Edition: The Art of Scientific Computing*. Cambridge University Press, New York, NY, USA, 3 edition, 2007.
- [75] Eric Braaten, Daekyoung Kang, and Lucas Platter. Universal Relations for Identical Bosons from 3-Body Physics. *Phys. Rev. Lett.*, 106:153005, 2011.
- [76] Sebastian Koenig. *Effective quantum theories with short- and long-range forces*. PhD thesis, Universität Bonn, Germany, August 2013.
- [77] Miroslav Pardy. The Cherenkov effect with massive photons. *Int. J. Theor. Phys.*, 41:887–901, 2002.
- [78] R. E. Cutkosky and M. Leon. Normalization of bethe-salpeter wave functions and bootstrap equations. *Phys. Rev.*, 135:B1445–B1446, Sep 1964.
- [79] J. Adam, Jr., Franz Gross, Cetin Savkli, and J. W. Van Orden. Normalization of the covariant three-body bound state vertex function. *Phys. Rev.*, C56:641–653, 1997.
- [80] Chen Ji and Daniel R. Phillips. Effective Field Theory Analysis of Three-Boson Systems at Next-To-Next-To-Leading Order. *Few Body Syst.*, 54:2317–2355, 2013.
- [81] H.-W. Hammer and Thomas Mehen. Range corrections to doublet s-wave neutron–deuteron scattering. *Physics Letters B*, 516(3):353 – 361, 2001.
- [82] Jiunn-Wei Chen, Gautam Rupak, and Martin J. Savage. Nucleon-nucleon effective field theory without pions. *Nucl. Phys.*, A653:386–412, 1999.



- [83] Johannes Kirscher, Ehoud Pazy, Jonathan Drachman, and Nir Barnea. Electromagnetic characteristics of  $A \leq 3$  physical and lattice nuclei. *Phys. Rev.*, C96(2):024001, 2017.
- [84] Jared Vanasse and Daniel R. Phillips. Three-nucleon bound states and the wigner-su(4) limit. *Few-Body Systems*, 58(2):26, Jan 2017.
- [85] Silas R. Beane, Emmanuel Chang, William Detmold, Kostas Orginos, Assumpta Parreño, Martin J. Savage, and Brian C. Tiburzi. *Ab initio* calculation of the  $np \rightarrow d\gamma$  radiative capture process. *Phys. Rev. Lett.*, 115:132001, Sep 2015.
- [86] S. R. Beane, E. Chang, S. Cohen, W. Detmold, H. W. Lin, K. Orginos, A. Parreno, M. J. Savage, and B. C. Tiburzi. Magnetic moments of light nuclei from lattice quantum chromodynamics. *Phys. Rev. Lett.*, 113(25):252001, 2014.
- [87] William Detmold, W. Melnitchouk, and Anthony William Thomas. Extraction of parton distributions from lattice QCD. *Mod. Phys. Lett.*, A18:2681–2698, 2003.
- [88] S. Athanassopoulos, E. Mavrommatis, K. A. Gernoth, and John Walter Clark. Nuclear mass systematics using neural networks. *Nucl. Phys.*, A743:222–235, 2004.
- [89] Emmanuel Chang, William Detmold, Kostas Orginos, Assumpta Parreno, Martin J. Savage, Brian C. Tiburzi, and Silas R. Beane. Magnetic structure of light nuclei from lattice QCD. *Phys. Rev.*, D92(11):114502, 2015.
- [90] S. R. Beane et al. Nucleon-Nucleon Scattering Parameters in the Limit of SU(3) Flavor Symmetry. *Phys. Rev.*, C88(2):024003, 2013.
- [91] S. R. Beane, E. Chang, S. D. Cohen, William Detmold, H. W. Lin, T. C. Luu, K. Orginos, A. Parreno, M. J. Savage, and A. Walker-Loud. Light Nuclei and Hypernuclei from Quantum Chromodynamics in the Limit of SU(3) Flavor Symmetry. *Phys. Rev.*, D87(3):034506, 2013.
- [92] Yu. A. Akulov and B. A. Mamyrin. Half-life and  $t_{1/2}$  value for the bare triton. *Phys. Lett.*, B610:45–49, 2005.
- [93] J. C. Hardy, I. S. Towner, V. T. Koslowsky, E. Hagberg, and H. Schmeing. Superaligned  $0^+ \rightarrow 0^+$  nuclear  $\beta$  decays: a Critical survey with tests of CVC and the standard model. *Nucl. Phys.*, A509:429–460, 1990.

## BIBLIOGRAPHY

---

- [94] J. J. Simpson. Half-life of tritium and the Gamow-Teller transition rate. *Phys. Rev.*, C35:752–754, 1987.
- [95] S. Eidelman et al. Review of particle physics. Particle Data Group. *Phys. Lett.*, B592:1–1109, 2004.
- [96] C. L. Morris et al. A new method for measuring the neutron lifetime using an in situ neutron detector. *Review of Scientific Instruments*, 88(5):053508, 2017.
- [97] M. Butler and J.-W. Chen. Elastic and inelastic neutrino-deuteron scattering in effective field theory. *Nuclear Physics A*, 675:575–600, August 2000.
- [98] John N. Bahcall. NEUTRINO ASTROPHYSICS. *CAMBRIDGE, UK: UNIV. PR. (1989) 567p*, 1989.
- [99] Q. R. Ahmad et al. Measurement of the rate of  $\nu_e + d \rightarrow p + p + e^-$  interactions produced by  $^8B$  solar neutrinos at the Sudbury Neutrino Observatory. *Phys. Rev. Lett.*, 87:071301, 2001.
- [100] Doron Gazit and Hilla De-Leon. Truncation error estimation and order-order by analysis for pionless eft observables. *In preparation*, 2018.
- [101] S. K. Bogner, R. J. Furnstahl, and A. Schwenk. From low-momentum interactions to nuclear structure. *Prog. Part. Nucl. Phys.*, 65:94–147, 2010.
- [102] Harald W. Griesshammer, Judith A. McGovern, and Daniel R. Phillips. Nucleon Polarisabilities at and Beyond Physical Pion Masses. *Eur. Phys. J.*, A52(5):139, 2016.
- [103] R. J. Furnstahl, N. Klco, D. R. Phillips, and S. Wesolowski. Quantifying truncation errors in effective field theory. *Phys. Rev. C*, 92:024005, Aug 2015.
- [104] Matteo Cacciari and Nicolas Houdeau. Meaningful characterisation of perturbative theoretical uncertainties. *Journal of High Energy Physics*, 2011(9):39, Sep 2011.
- [105] M. Butler, J.-W. Chen, and P. Vogel. Constraints on two-body axial currents from reactor antineutrino-deuteron breakup reactions. *Physics Letters B*, 549:26–31, November 2002.

## BIBLIOGRAPHY

---

- [106] Jiunn-Wei Chen, Karsten M. Heeger, and R. G. Hamish Robertson. Constraining the leading weak axial two-body current by recent solar neutrino flux data. *Phys. Rev. C*, 67:025801, Feb 2003.
- [107] V. A. Andreev et al. Muon Capture on the Deuteron – The MuSun Experiment. 2010.
- [108] Núria Vinyoles, Aldo M. Serenelli, Francesco L. Villante, Sarbani Basu, Johannes Bergström, M. C. Gonzalez-Garcia, Michele Maltoni, Carlos Peña-Garay, and Ningqiang Song. A new Generation of Standard Solar Models. *Astrophys. J.*, 835(2):202, 2017.
- [109] E. Tognelli, S. Degl’Innocenti, L.E. Marcucci, and P.G. Prada Moroni. Astrophysical implications of the proton–proton cross section updates. *Physics Letters B*, 742:189 – 194, 2015.